UNIVERSITÀ DELLA CALABRIA

**UNIVERSITA' DELLA CALABRIA**

Dipartimento di Fisica

**Dottorato di Ricerca in**

**SCIENZE E TECNOLOGIE FISICHE, CHIMICHE E DEI MATERIALI**

**CICLO**

**XXXII**

**TITOLO TESI**

# ACTIVE PLASMONIC NANOSTRUCTURES FOR BIOMEDICAL APPLICATIONS

**Settore Scientifico Disciplinare Fis07**

**Coordinatore:** Ch.mo Prof. Roberto Bartolino

Firma Firma oscurata in base alle linee guida del Garante della privacy

**Supervisore/Tutor**: Ch.mo Prof. (Prof. Giuseppe Strangi)

Firma Firma oscurata in base alle linee guida del Garante della privacy

**Dottorando:** Dott./ssa (Sharmistha Chatterjee)

Firma

Firma oscurata in base alle linee guida del Garante della privacy

**Dedicated**

**To all of my teachers**

**And**

**To my parents and late grandfather Jagannath Banerjee**

## Acknowledgements

I will never be able to thank Prof. Giuseppe Strangi, my supervisor and mentor, enough for believing in me and so unconditionally supporting me throughout the project period. I would like to thank him for guidance, encouraging my research and for allowing me to grow as a research motivated student. His advice on both research as well as on my career have been priceless. I also want to thank Dr. Loredana Ricciardi and Dr. Giovanna Palermo for helping me to learn and grow during my PhD period. Their love and support is precious for me when I am here far away from my home. I would like to thank all the faculty members and staffs of the department of physics for their constant motivation and support. I want to thank my lab mates Mohamed, Glynis, Ted, Dene, John, Adam, Giuseppe Lio, Wera, Tiziana, and Alexa for their constant help both in the University of Calabria, Italy and the Case Western Reserve University, USA. I would like to thanks also Rakesh Ji and Neha for the valuable time I spent with them here in the university. I am grateful to Alice and Pasquale for their help and support. Above all, I owe my deepest gratitude to my parents, my brother for their constant love, prayer, encouragement, support and for understanding my goals and aspirations. Last but not the least; I would like to thank to the Almighty, for giving me the opportunity to carry out research under one of the passionate researcher, Prof. Strangi, with some of the best co-workers and in renowned institutes like the University of Calabria, Italy and the Case Western Reserve University, USA.

# ABSTRACT (IN ITALIAN)

Il rilevamento in real-time e label-free di proteine a bassa concentrazione e allo stato naturale è considerato l' "Holy-Grail" nell'ambito della ricerca biomedicale. È possibile rilevare la presenza di una particolare infezione o malattia attraverso il monitoraggio di particolari marker proteici che risultano essere presenti nei fluidi corporei, come ad es. salive e sangue, anche già in uno stato iniziale di infezione o malattie. L'individuazione precoce della malattia permetterebbe di intervenire precocemente con le terapie, garantendo così un successo terapeutico che alla fine aumenterà i tassi di sopravvivenza e la qualità della vita. Il rilevamento di molecole non è solo legato all'ambito di ricerca biomedicale, ma è anche utile per il monitoraggio ambientale, la risposta alle emergenze e la sicurezza nazionale. Ma il rilevamento delle molecole proteiche nella fase iniziale di una malattia è estremamente difficile a causa della bassa concentrazione dei marcatori proteici nel fluido corporeo e delle loro dimensioni estremamente piccole (<3 nm). Un modo per superare questo ostacolo è utilizzare le straordinarie risposte elettromagnetiche delle nano-particelle ottenute a partire da metalli nobili (MNPs).

In questo lavoro sono state sintetizzate delle nano-stars di oro (AuNS) per usare le loro proprietà ottiche per il rilevamento di alcuni marker proteici. Per sintetizzare queste nano-particelle caratterizzate da una particolare forma, e che sono risultate estremamente stabili nel tempo (più di cinque mesi), è stato usato un metodo semplice e privo di tensioattivi. Sulla base della loro caratterizzazione e dell'analisi numerica condotta, è stato dimostrato che queste nano-antenne potrebbero essere un agente efficace per la diagnosi precoce delle malattie. Inoltre, per il rilevamento dei marcatori, le nano-gap eterodimeriche, creata tra una punta dell'antenna della nano-star e una nano-sfera di oro, sono risultate essere più efficienti delle nano-gap tra singole antenne nano-star a causa della loro capacità di mostrare un enhancement del campo elettrico, capace di creare hot-spots che fungono da sito di legame per la molecola da rilevare. Sia l'antenna nano-star che quella ibrida (nano-star/nano-sphere) potrebbero essere facilmente convertite in un biosensore, ancorando idonei anticorpi sulla loro superficie. Sorprendentemente, si è visto che queste antenne nano-star d'oro possiedono sia modi dipolari che i non-edge breathing mode. I modi dipolari saranno utili per il rilevamento di molecole proteiche usando il loro effetto localizzato di risonanza plasmonica di superficie (LSPR) che è uguale a qualsiasi convenzionale biosensore plasmonico. Ma i non-edge breathing mode dell'antenna nanostar saranno utili per determinare la massa

dell'analita adsorbito in base al cantilever principle. La stima della massa (con le informazioni sulla polarizzabilità e la dimensione) dei marker è cruciale poiché fornirebbe le informazioni sul numero di aminoacidi presenti in quella molecola che aiuteranno a comprendere meglio la sua struttura molecolare e quindi saranno utile per progettare il suo anti-agente. Queste efficienti acousto-plasmonic nano-antenna potrebbero quindi diventare un elemento chiave durante il monitoraggio della terapia. Per fare un passo avanti in quest'area di ricerca, il rilevamento basato sulla Fano-lineshape è stato ritenuto un'idea promettente. Da qui l'idea di riportate in una matrice polimerica termo-sensibile delle nanostrutture metalliche, in particolare nanorods da utilizzare per il rilevamento senza etichetta di molecole di proteine estranee con alta efficienza e per identificare il marker.

Nella seconda parte della tesi vengono discusse le proprietà ottiche di metasuperfici in Aluminium doped Zinc Oxide (AZO). Questo materiale è caratterizzato da basse perdite ottiche ed è popolare come materiale plasmonico alternativo ai metalli. In particolare sono state studiate le proprietà ottiche di un sistema di array di nanotubi di AZO altamente ordinato, impiegati per il rilevamento di gas. Sono state condotte delle prove per il rilevamento di gas $H_2$, che risulta essere utile sia in ambito industriale che in ambito biomedicale, ad esempio il rilevamento di gas $H_2$ a bassa concentrazione può favorire il rilevamento di batteri. In più, le matrici di nanopillar di AZO sono state caratterizzate con misure di angolo di Brewster che possono essere utili per molte applicazioni, inclusa la commutazione ottica.

Infine, alcuni lavori aggiuntivi sono stati descritti in breve. In questa sezione sono stati riportati studi teorici relativi a nanojet fotonici, comportamento asimmetrico della trasmissione del suono mostrato in metamateriali acustici stampati in 3D, tunabilità della lunghezza focale di metalli e per applicazioni della plasmonica nella cura del cancro.

# ABSTRACT (IN ENGLISH)

Real-time and label-free detection of protein molecules at ultralow concentration in their natural state is considered the “Holy-Grail” in biomedical research. Protein molecules pop up in the bodily fluids such as saliva, blood serum, at early stage of any infection or disease and circulate throughout the body. Therefore, the emergence of that particular infection or disease can be envisioned through the detection of the signature protein markers. The early detection of the disease would help to start the treatment early, and thus ensure therapeutic success which will eventually increase the survival rates and quality of life. The early detection of protein molecules is necessary for the diagnostics as well as for environmental monitoring, emergency response and homeland security. But the desired detection of protein molecules in the early stage is extremely challenging because of the ultralow concentration of the protein markers in the bodily fluid at the early stage and their acutely small size (< 3 nm). One way to overcome this hurdle is to use the extraordinary electromagnetic responses of noble metal nanoparticles (MNPs).

Here stable gold nanostars (AuNS) have been synthesized to use their property for sensing. A surfactant-free, simple, one step wet-chemistry method was used to synthesize these spiky nanoparticles, which were stable in aqueous media for more than five months. Based on their characterization and the numerical analysis, it has been realized that these nanoantennas could be an efficient agent for the early detection of disease. Furthermore, for the marker detection, the heterodimeric nanogap, created between a nanostar antenna tip and a gold nanosphere, was seen to be more effective than those single nanostar antennas because of their higher intensity enhancement capability and also the optimum electric field map at the hot-spots which acts as the binding site for molecule. Both the AuNS antenna and the hybrid one could be easily converted to a biosensor, by anchoring suitable anti-bodies on the surface of the nanoantenna. Surprisingly, these gold nanostar antennas were seen to have both the non-edge breathing modes and the well-known edge dipolar mode. The optically active edge dipolar mode will be useful for the detection of protein molecules by using their localized surface plasmon resonance (LSPR) effect which is same as any conventional plasmonic biosensor. But the non-edge breathing modes of nanostar antenna will be helpful to determine the mass of adsorbed analyte based on the cantilever principle. The mass estimation (having the information about the polarizability and the size) of the markers is very crucial because it would provide the information about the number of amino acids present in that molecule

which will help for better understanding of its molecular structure and thus will be useful for designing its anti-agent. This efficient acousto-plasmonic nanoantenna therefore could become a key element at a point of care. To go one step forward in this research area, Fano-lineshape based sensing was thought to be a promising idea. Here the reported Fano line-shape arises from the coupling of the gold nanorods dipped in thermo-responsive polymer matrix and a silver thin film. The Fano system was seen to respond to both the change in external temperature and the refractive index. This kind of Fano system will be helpful for the label-free detection of the foreign protein molecule with high efficiency and also for identifying the marker's thermodynamic state and reactions of the molecule which is crucial for protein engineering. All these constitute the base of the discussion of part I of the thesis which is about the light harvesting plasmonic nanoantennas.

In the $2^{nd}$ part of the thesis, AZO metasurfaces and their optical activities are discussed. Aluminium doped Zinc Oxide (AZO) is a low-loss material and popular as an alternate plasmonic material. The highly ordered AZO nanotubes array system has seen to have gas sensing capability. The reported $H_2$ gas detection within a very short time can make this system suitable for industrial application. The detection of $H_2$ gas of lower concentration with the help of these nanostructures is also useful to detect the presence of bacteria by tasting their exhaled $H_2$ gas. On the other hand, the AZO solid nanopillars arrays are seen to have generalized Brewster angle phenomena which can be useful for many applications including the optical switching.

Lastly, some additional works have been described in a brief way. In this section, photonic nanojet related theoretical study, asymmetric sound transmission behaviour shown in 3D printed acoustics metamaterials, focal-length tunability of metalens and plasmon assisted cancer therapy has been reported. As per my belief and understanding, all these studies reported in this thesis will enrich the related research areas.

# CONTENTS

**PART III: FEW ADDITIONAL WORKS DONE**

**CHAPTER I: TWIN PHOTONIC NANOJET**

**CHAPTER II: ACOUSTIC METAMATERIAL**

**CHAPTER III: PLASMONIC NANOANTENNA FOR CANCER THERAPY**

**CHAPTER IV: OPTICAL FOCAL LENGTH TUNABILITY OF META-LENS: EFFECT OF IMPLANTING LIQUID CRYSTAL INTO META-LENS (UNDER INVENTION DISCLOSURE)**

**CONCLUSION**

# LIST OF TABLES

PART I: LIGHT-HARVESTING PLASMONIC NANOANTENNA

# LIST OF FIGURES

PART – I: LIGHT-HARVESTING PLASMONIC NANOANTENNA

PART II: PLASMONIC METASURFACE AND THEIR OPTICAL ACTIVITY

# Outline of Thesis

## Part I: Light harvesting plasmonic nanoantenna

The first part of this thesis is all about the light harvesting properties of the plasmonic nanoantennas.

A brief overview on plasmonics will be discussed in the chapter I. To be more specific, here the following facts will be discussed: noble metals and their optical properties, plasmonic nanoparticles acting like an optical nanoantenna and the localized surface plasmon resonance (LSPR) effect connected with these plasmonic nanoantennas and lastly metallic thin films and the surface plasmon resonance (SPR) effect seen to occur in metallic thin films. This chapter will be concluded with a discussion of the active nature of nanoparticle based plasmonic systems.

The chapter II is all about the star shaped gold nanoparticle.

All the fabrication details of star shaped gold nanoparticle will be discussed in chapter IIA. These gold nanostar particles are promising candidates for protein sensing in many ways. The chapter IIA will start with a discussion on the fact that why protein sensing is necessary. This will be followed by the discussion on the different known nanoparticles suitable for protein sensing. There it will be very clear why some elongated nanoparticles especially star-shaped nanoparticles are beneficial in this field of sensing. Then the synthesis and characterization details of these gold nanostar particles will be discussed. Lastly, the light harvesting property of these nanostars particles will be written along with their applicability in the sensing field.

Chapter IIB is about the heterodimeric nanogap system composed of a gold nanostar particle and a gold nanosphere. Here design details of these nanogaps will be discussed first and then, their effectiveness in term of the sensitivity for protein sensing, will be given.

Chapter IIC is about the observation of breathing modes in gold nanostars and how these modes along with their popular dipolar mode will be useful for sensing. This chapter will start with a discussion of about breathing modes which originates from a different reason other than the popular edge modes such as dipolar, quadrupolar, and higher order multipolar modes. Then the experimental observation of both types' modes (breathing modes and dipolar edge modes) in these nanostars will be explained. Afterwards, some theoretical study will be given on both the breathing modes and edge mode to understand more carefully their

origin and shape in these nanostructures. This chapter will be ended with a discussion on the usefulness of these two types of modes of nanostars in protein sensing - both using optical signals as well as acoustic signals.

In chapter III, a system has been reported for both the detection of change in temperature and refractive index in the surrounding media. The chapter will start with a comparative study of asymmetric Fano line-shape and the symmetric Lorentzian dipolar line-shape and the reason for selecting Fano line-shape over the Lorentzian dipolar line-shape for detecting any changes in the surrounding environment. Then the origin of this Fano resonance will be discussed. In this case, the reported system shows a characteristic Fano line-shape which originates from the hybridization of narrower LSPR mode of gold nanoparticles and the wider background SPR mode of metallic thin film. Afterwards, the synthesis and characterization details of nanoparticle embedded polymer system will be given. The design details of metallic thin film and its characterization will be discussed subsequently. Later, description of our Fano system will be given including its schematic diagram, construction and characterization. Then, all the experimental results will be discussed about the detection of temperature change and the change in dielectric surrounding medium using this Fano system. The Finite Element Method (FEM) simulation done on this Fano system to understand the interaction of it with light will be discussed afterwards. The chapter will be concluded with a discussion of the effectiveness of this Fano system not only for protein sensing but also for temperature sensing. With the discussion of this last chapter part - I is completed.

# Part II: Plasmonic Metasurface and their optical activity

The second part of this thesis is about the plasmonic metasurface and their optical activity.

Chapter I discusses a brief overview on metasurface. Here, metamaterial, metasurface and meta-atom and their related important theoretical details is written briefly.

The chapter II is all about the aluminium-doped ZnO (AZO) nanopillar arrays based metasurface.

Chapter IIA is about hydrogen gas sensing using the Aluminium doped ZnO hollow nanopillars arrays based metasurface. At first, the motivation for gas sensing is explained. Then the importance of Aluminium-doped ZnO over well known noble metals is described along with the importance of these pillar structures for gas sensing. After that, all the fabrication and characterization details of aluminium-doped ZnO (AZO) nanopillars arrays are discussed here. Then, the details about the design of our gas sensor and our experimental set-up are given. Afterwards, all the gas-sensing experimental results and the related Finite Element Method (FEM) based Comsol simulation study results are given. Here, the applicability of solid and hollow AZO nanopillars arrays for gas sensing is also discussed.

Chapter IIB is about the Aluminium doped ZnO solid nanopillars arrays and their usefulness. At first generalized Brewster Phenomena and Perfect light absorption is discussed here. Then, all the relevant details about the experimental set-up and the experimental results are given. These AZO solid nanopillars arrays don't respond to $H_2$ gas but it shows the generalized Brewster angle effect over a range of angles. These arrays show the perfect light absorption characteristics over a wavelength range for a particular incidence angle. The difference in the optical characterises of the AZO solid pillars arrays are shown here for both air and Si as the host materials. Based on the optical characteristics, these solid pillars seem to be useful as optical switch by controlling polarization, incidence angle or wavelength.

With all these discussions, part - II is completed.

# Part III: Few additional works done

Part - III, is composed of few additional interesting projects which have been done during my PhD.

Chapter I is all about the numerical simulation done on photonic nanojet (PNJ) which is very well known phenomena related to dielectric microstructure. Here after introducing the PNJ effect, theoretical analysis about the twin-PNJ effect seen in our system, are described.

Chapter II discusses our results regarding the acoustics metamaterial. Like the plasmonic metamaterial acoustic metamaterial is also very important for various applications. This chapter begins with the general discussion about the acoustic metamaterials. Then, the design of our acoustic metamaterial, fabrication and the key experimental results are written briefly.

Chapter III is about the plasmonic nanoantennas for Cancer Therapy. The nanoshell antenna is well-known for its diagnostic application. But the heat generating property of these shell-like nanoantennas makes them very important for therapy also. The nanoshell combined with Ir-complex is able to destroy the glioblastoma cells completely. The results and discussion about this therapy are written briefly in this chapter.

The optical focal length tunability of flat Meta-lens with the help of liquid crystal is discussed (under invention disclosure) briefly in chapter IV of this part. Here, the meta-lens we used, the important facts related to the liquid crystal, and the way of injecting the liquid crystal into the meta-lens is written concisely along with a glimpse of the key experimental results.

With the discussion of all these chapters part III is completed.

# PART I

# LIGHT-HARVESTING PLASMONIC NANOANTENNA

# Chapter I

# Plasmonics: A Brief Overview

**I.1. Introduction:** Plasmonics is a fastly-growing field which falls at the boundary of physical optics and the condensed matter physics. It studies the effects of nanostructured metals. Nanostructured materials, in principle, are materials whose dimension is in between 1 to 100 nm at least in one dimension. When a material's size falls within that size limit then its behaviour gets changed compared to their bulk condition. Thus plasmonics studies the unusual and unknown behaviour of metal or metal-like nanostructures whose properties are far from their bulk properties. The "plasmonics" term is originating from the word "Plasmon" – The study of plasmons. The plasmon is the quantum of plasma oscillation. The quantum of light is known as photons, the quantum of mechanical vibration is known as phonons, in a similar way, the quantum of plasma oscillation is known as plasmon. These Plasmons are not a normal particle rather it's a quasi-particle because it arises from the quantization of plasma oscillation. Plasmons are the quantum of oscillation of the electron density with respect to the fixed ionic position in a metal. In metals electrons are free to move and all of them jointly behave like a sea of electrons which looks like the plasma. Now in presence of any external electric field, in order to cancel out the field inside the metal, all the electrons move in opposite direction of the externally applied electric field. If the electric field gets removed or pointed towards the other direction due to the repulsion among the electrons and the attraction of the positive ions the displaced electrons move towards their previous position. In this way the free conduction electrons oscillate back and forth in metals and plasmons are the quantization of this plasma oscillation. In a particular metal that oscillation happens with a particular frequency which is known as the plasma frequency that depends on the material property.

Plasmonics deals with the study of fabrication, properties and applications of plasmon supporting structures [1]. Although plasmonics talks about the optical properties of different nanostructured noble metals such as gold, silver, platinum, palladium, yet it is more confined in gold and silver nanostructures. Now-a-days because of a lot of applications (will be discussed later) this field is getting more and more attention. To know more about this plasmonics field of study we should first know about the important facts about the noble metals. In this chapter, after that discussion, the details about the nanostructured noble metals

will be discussed which will be connected to the study of plasmons. With all the study of noble metals in bulk as well as in nanostructured form, this chapter's discussion will be completed.

**I.2. Optical properties of noble metals:** The metal is a very well-known class of material which has a lot of distinguishing properties such as high reflectivity, good electronic conductivity, and high heat conductivity. Gold (Au), silver (Ag), platinum (Pt), palladium (Pd), copper (Cu), aluminium (Al) are examples of some popular metals. All the exciting properties of these noble metals originate from the same feature of the metal – the presence of free conduction electrons. To a good approximation, these free conduction electrons, which form apparently a plasma kind of state in a metal, oscillate in the background of the fixed positive ions of metals. This oscillation of the conduction electrons is known as the plasma oscillation. The frequency of this oscillation depends on the material itself, and it is unique for each material. This frequency is known as the plasma frequency and all the optical properties of the metals depend on this plasma frequency. The simplest known model which deals with this plasma frequency and therefore the optical properties of the noble metals is the popular "Drude model"

**Drude Model and the optical properties of metals**: According to the Drude model [2], the electric permittivity of the metal is given by

$$\varepsilon(\omega) = 1 - \frac{ne^2}{m\varepsilon_0}\frac{1}{\omega^2 + i\gamma_0\omega} \tag{I.1}$$

Where $n$ is the number density of the free electrons, $m$ is the free electron mass, $\gamma_0$is the damping term which depends on the free electron oscillation rate, and $\omega$ is the electron oscillation frequency. For most of the metals, $\gamma_0 \ll \omega$. In this case, the conduction electrons in a metal are considered not to be bound. Drude adapted the approach given in Lorentz model without the restoring force (i.e. $\omega_0 \approx 0$) and introduced this Drude model. If the response of the positive ions in metals will be included as a constant background with a real dielectric function then the modified Drude model would be

$$\varepsilon(\omega) = \varepsilon_\infty\left(1 - \frac{\omega_p^2}{\omega^2 + i\gamma_0\omega}\right) \tag{I.2}$$

Here $\varepsilon_\infty \geq 1$ and $\omega_p$ is the plasma frequency which is defined as

$$\omega_p = \sqrt{\frac{ne^2}{m_e\varepsilon_0\varepsilon_\infty}} \tag{I.3}$$

Here, $n$ is the electron number density, $e$ is the unit electronic charge, $m_e$ and $\varepsilon_0$ are the mass of the electron and the permittivity of the vacuum respectively.

From the previous expression of $\varepsilon(\omega)$, the real and imaginary parts of the permittivity of the metal according to the Drude model are

$$Re\big(\varepsilon(\omega)\big) = \varepsilon_\infty \left(1 - \frac{\omega_p^2}{\omega^2+\gamma_0^2}\right) \tag{I.4}$$

And

$$Im\big(\varepsilon(\omega)\big) = \frac{\varepsilon_\infty \omega_p^2 \gamma_0}{\omega(\omega^2+\gamma_0^2)} \tag{I.5}$$

Here $Re\big(\varepsilon(\omega)\big)$ decides the group velocity dispersion and $Im\big(\varepsilon(\omega)\big)$ regulates the dissipation of the energy of electrons in metals contributing to its absorption. This model can be well-connected to the experimental measurements of the optical constants of noble metals done by Johnson and Christy [3]. Although the Drude model fairly goes well with the experimental measurements done by Johnson and Christy for the higher wavelength range yet it is not consistent with the experimental findings in the lower wavelength range especially for the ultraviolet (UV) spectral region. The reason is the ignorance of the contribution coming from the bound electrons of metals towards their electric permittivity $\varepsilon\,(\omega)$ and their optical activity. In the following part, the description about the contribution of bound electrons in metals will be given which will complete the Drude model that took into account only the free electron contribution in metals to compute the metallic electric permittivity $\varepsilon\,(\omega)$. The extended expression of $\varepsilon\,(\omega)$ including the bound electron part then will be able to explain all the optical properties of the bulk metals even in the lower wavelength range including the UV region.

According to the Drude model, here it is very clear that, if $\omega_p$ will be in UV region, then $Re\big(\varepsilon(\omega)\big)$ of metals will be very small in the UV region and it will be close to zero there. Thus $Re\big(\varepsilon(\omega)\big)$ will be negative in the visible region and will be very negative in the IR region. This negative $Re\big(\varepsilon(\omega)\big)$ is the key feature of the metals in the optical range. Due to the existence of negative $Re\big(\varepsilon(\omega)\big)$ we can see the high reflectivity in metals and this is the origin of most of the plasmon related effects in bulk metals. Intra-band transitions, seen in metals, happen because of the electronic excitations within their conduction band, can also find explanation from the Drude model. There are few additional and important processes which seen to occur in real metals such as Landau damping and interband transitions. These

processes also contribute to the optical properties of the real metals. Interband transition compared to the Landau damping is more important to understand the optical properties of the real metals because this kind of transition seen to occur in most of the metals in many cases and because of this phenomena their electric permittivity and thus their optical properties gets perturbed. Inter-band transitions originate from the optical excitations of the bound electrons, approximated as the collection of Lorentz oscillators, to higher energy band. The contribution of the inter-band transition and thus the bound electrons modifies the electric permittivity expression of metals in the following manner

$$\varepsilon(\omega) = \varepsilon_b(\omega) + \varepsilon_\infty - \frac{\omega_p^2}{\omega^2 + i\gamma_0\omega} \qquad \text{(I.6)}$$

Here $\varepsilon_b(\omega)$ is originating from the inter-band transitions and thus from bound electrons. This is modifying the classically known expression of the electric permittivity of metals derived from the Drude model written with only the free electron contribution in metals. The inter-band contribution $\varepsilon_b(\omega)$ does not strongly affect the optical properties of metals if the inter-band transition energy falls in the UV range. But for some metals like gold (Au) the inter-band transitions falls very close to or just below the plasma frequency. Therefore, for those cases, the electric permittivity of metals (like Au) which decides their optical properties must include the term $\varepsilon_b(\omega)$.

With all these discussions, the above section is able to give an idea about the noble metals and their optical properties with the details about their origin. The above discussion is true for bulk metals but if one goes from the bulk to the nanostructures metals then all the properties of the bulk metals will get modified for its confinement over the nanometer (nm) region. Because of their modified and useful features these nanostructured metals are very beneficial compared to the bulk metals in many applications and thus deserve a brief discussion. In the following section some useful details about these nanostructured metals and their applications will be given. The work done during my PhD is based on the usefulness of these nanostructured materials and thus the following discussion about the nanostructures will be very beneficial for understanding the successive chapters of the PhD thesis project works.

**Nanostructured Materials:** From the above discussion it is very clear that how a metal behaves in its bulk condition, its optical properties and the origin of the optical properties. It is worth to mention here that in general, a material behave differently at the different size scales. When a material instead of its bulk state, gets confined over some nanometer scale (1 nm-100 nm) in any dimension (or more than one dimension) then due to the confinement of

the conduction electrons the energy levels gets modified and in that condition it's behaviour gets changed compared to the bulk counterpart. There is a famous fragment of sentence by Richard Feynman – "Plenty of rooms at the bottom" which describes the possibilities and powers of this miniaturization that cannot be seen at the macroscale. Metals are also size and shape dependent. When the metals get confined over the nanometer region in one dimension or more than one dimension, then those nanoscale metals behave differently with respect to their known bulk properties and also the nanoscale metals have modified optical properties than their bulk form. In recent years, metal nanostructures become very popular because of their usefulness in both the fundamental research areas as well as their technological applications. Because of the unique physical and chemical properties along with their functionalities compared to their bulk properties, these metal nanostructures are acquiring more attentions. The plasmonics field of study is emerged to spot-light these plasmon driven unique optical properties of the metal nanostructures which are the most exciting and fascinating properties of the metals confined in the nanometer size scale.

At nanoscale, the noble metals such as gold (Au), silver (Ag) posses high absorption in the visible range which depends on different parameters of that nano structured metals. The different absorption in different types of metal nanostructures (with variable size, shape and material) can be observed by the different colours associated with them. This high absorption originates from the collective oscillations of the conduction electrons in a confined region of nanometer size, in response to the electric field of the interacting electromagnetic (em) radiation of the light.

The importance of Ag and Au among all the other metals is because of the possibility of getting any colour and absorption band almost in any part of the visible region by controlling their shape and size. These Ag and Au nanostructures are also well-known for their chemical stability and biocompatibility nature. Since the ancient ages people are using the different kinds of remarkable features of these metal nanoparticles in different fields but the oldest example till date is the use of metal nanoparticle to process different colours by Romans during 1000-1200 BC. The popular Lycurgus cup ($4^{th}$ century AD) carries the unique feature of the colour change using the nanoparticles that can be seen by experiencing its different colours depending on the direction and angle of interaction of the incident light [4].

Now-a-days, because of the significant improvement in the plasmonics field of research, people are able to fabricate metal nanoparticle of different shape such as nanosphere, nanoshell, nanorod, rice grain type of nanoellipsoid, nanowires, nanoprisms, nanocages,

nanocubes, nanoplates, nanotriangles, nanostars and hexagonal nanoparticles and many more including the coupled nanoparticles with the possibility of size tunability [5-12]. Because of the ease of fabrication of these metal nanostructures, the unique features of all these different kinds of metal nanoparticles (MNPs) and their usefulness, MNPs and thus plasmonics finds a large variety of interdisciplinary applications [13], such as biomedicine [5], energy application, surface enhanced Raman spectroscopy (SERS) [14-15], sensing, [16-17] cloaking which can make the things invisible [18], subwavelength imaging [19], photocatalysis [20], photovoltaics [21-22], photo-therapies [23], quantum technologies, and miniaturized photonic circuits, and for on-chip integration of photonic and electronic systems [24-25].

The secret of all the astounding optical properties of the metal nanoparticles which makes them very useful in diversified field is their ability to confine light at the sub-wavelength scale [26-31]. The domain of this plasmonics field is standing over these unique light interaction properties of the metallic nanostructures and the metallic thin films. Therefore, these two sections, metal nanostructures and the metallic thin film deserve a brief discussion along with their distinctive light interaction and confinement properties. In the following sections all the important details about the metal nanoparticles and metallic thin film along with their light interactivity are given which will be helpful for understanding different features of the following chapters containing the PhD thesis projects works.

### I.3. Metal nanoantennas and discussion about localized surface plasmon resonance:

Metal nanoparticles (MNPs) interacting with the incident electromagnetic (em) light behaves differently than the bulk metal and are able to confine the light very tightly near its surface in some specific regions. In this case we are considering the MNPs of size comparable to or smaller than the wavelength of the incident em wave so that in that size limit we can safely consider the electric field of the incoming light interacting with the MNP is fairly constant over their volume. When em wave interacts with such a MNP, its free electron clouds gets excited and because of the interaction with the electric field of the incident em wave the free electron clouds move back and forth in the metal nanostructure. This movement, rather the oscillation of these free electrons within the MNPs are terms as the localized surface plasmon (LSP) oscillations as the oscillation of the plasmons here is confined over the closed surface of MNPs (the oscillation of free electrons in bulk metals is known as the plasmons). Because of these oscillations of the charged particles in MNPs, they start to radiate.

This radiation is function of the size, shape, material type of the MNP as well as the type of dielectric surroundings in which that metal nanostructure is submerged [5, 8, 11, 26-28, 33]. The outgoing radiation field intensity originating from the oscillation of LSPs varies at different regions of the MNP surface because of the different local curvatures in the surface of the nanoparticle. It is a very well-known fact that the electric field of any em radiation should be perpendicular to the local surface of the interacting structure. The different curvature at different position of MNPs surface decides the electric field lines density of the outgoing radiation field and because of this light gets confined over some particular area very densely compared to the other regions. These regions because of the existence of the higher electric field lines density turns out to be brighter compared to the other sections. These brighter regions at the surface of the MNPs characterized by the highest confinement of the outgoing radiation electric field and are termed as the Hot-spots areas. The electric field confinement in the hot-spot area can be changed by changing the curvature at that particular area which can be done by modifying the size and shape of the MNPs. Also by changing the material property of the MNPs (i.e. by choosing different types of metals with different electron number density, *n*) and their dielectric environment, the confinement and the electric field map can be modified.

The frequency, with which the LSPs in a MNP oscillate, is unique for a particular nanoparticle. When the incident em field has that particular frequency during interaction with the MNP then the interaction results in the highest confinement and thus the highest enhancement in the electric field intensity. That particular frequency of a particular MNP is known as the localized surface plasmon resonance (LSPR). This LSPR depends on the size, shape, material of the MNP and also on its dielectric environment as it is connected with the oscillation of free electrons in that particular confined structure [5, 8, 11, 26-28, 33].

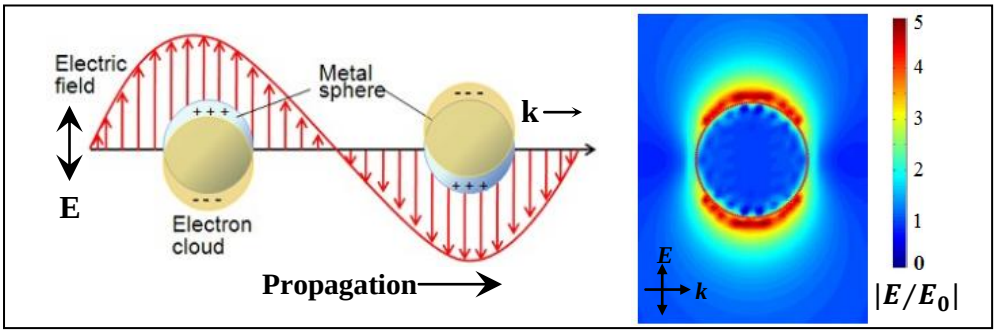


Figure I.1. Sketch of the mechanism of LSPRs of spherical MNPs and the resultant electric field confinement at the surface of the nanoparticle after interacting with the em light.

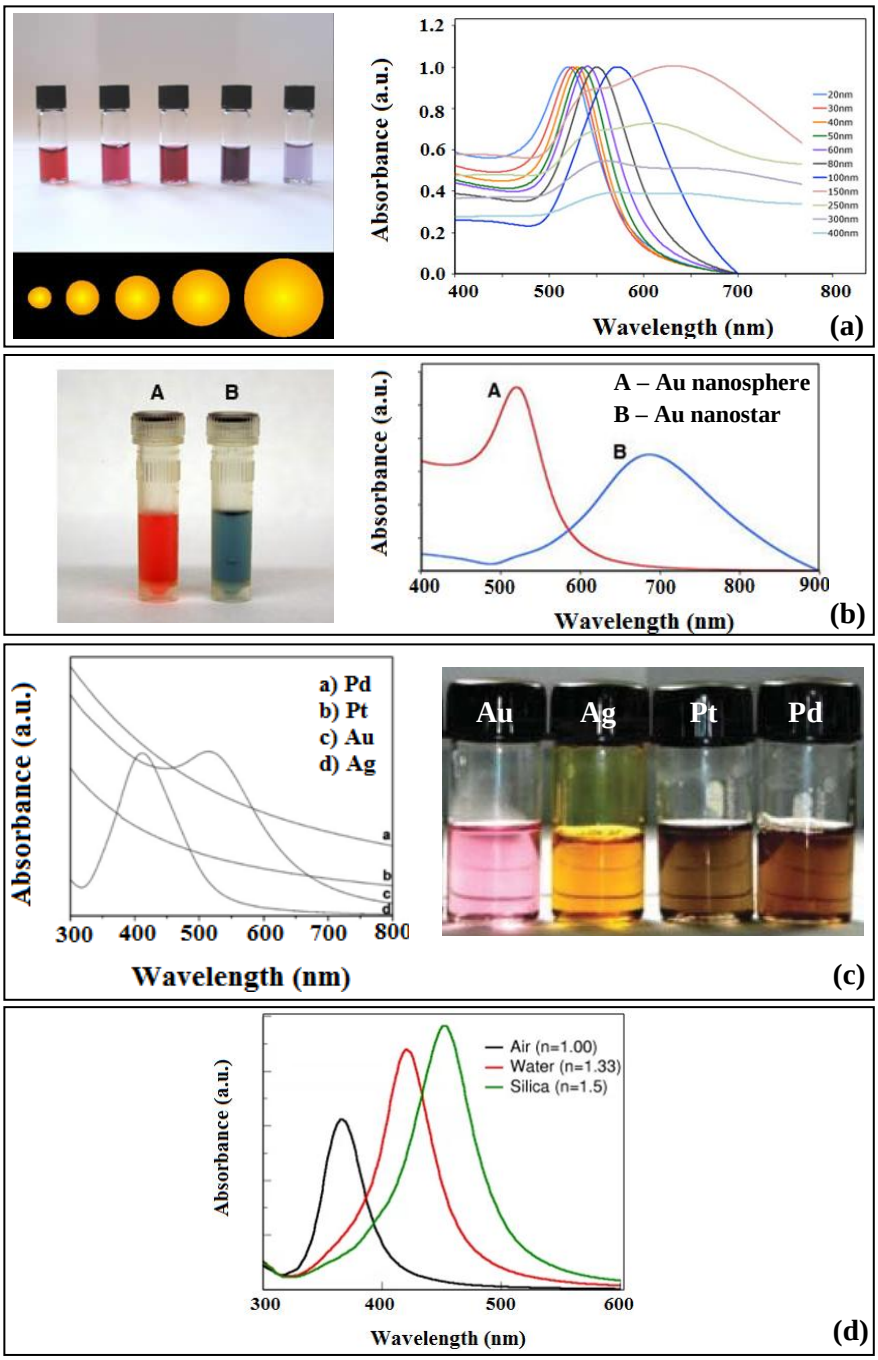


Figure I.2. Effect of different parameters on absorbance of MNPs and their LSPR spectra: (a) The variation of absorption of the Au NPs of different size giving rise to different colours and the different LSPRs, bigger size has red-shift in absorption maxima. (b) The variation of absorption and thus colours of Au NPs of two different shapes – nanosphere and nanostars, with two different LSPRs. (c) The variation of absorption and thus colours and LSPRs of NPs of different material (Ag, Au, Pt, Pd). Here same size of the spherical metal nanoparticles is taken [33]. (d) The variation of absorption and thus LSPRs of 50 nm of Ag nanospheres in different surrounding media (nanoComposix website).

The figure above is giving some idea about all the known parameters which can control the LSPR of MNPs and the light confinement and thus intensity enhancement by those particles.

In the figure I.2, panel (a) is describing how the absorption of metal nanoparticle (in this case Au nanosphere) will be modified for its different size. The different absorption can be visualized externally by seeing their respective colours. The difference in the absorption will be clear when we will measure the absorption characteristics (or extinction) by using a UV-VIS-NIR spectrophotometer. Here the different absorption maxima, which are known as LSPR, for different size of the MNPs is describing the MNP size effect. Panel (b) is describing how the absorption property and thus colour and the LSPR will be modified for different shape of the metal nanoparticle. For this case, Au nanoparticle of spherical shape and star shape are considered for comparison and in both the cases water is chosen as the media. Panel (c) is describing the effect of different kinds of material on their absorption properties [33]. For this comparison four types of metals have been chosen – gold (Au), silver (Ag), Platinum (Pt), and palladium (Pd). All the MNPs are of same size and same shape – spherical shape. Water is chosen as the media in each case. The different absorption nature with different LSPR and colours are describing here the effect of material property on their optical activity. Lastly in panel (d) the effect of different dielectric surrounding media [nanoComposix website] has been described. For this study 50 nm of Ag nanosphere has been taken and those NPs have been submerged in different surround media with different dielectric constants – air ($\varepsilon = 1.00$), water ($\varepsilon = 1.33$), and silica glass ($\varepsilon = 1.50$). The red shift in the LSPR of this MNP for the media with higher value of dielectric constant is describing the effect of surrounding dielectric media. Thus summarizing all the above details we can say that the features of the LSPR (its position), absorption of the MNPs, electric field map, light confinement and the electric field enhancement near the MNP surface depends on the four factors – size, shape, material and the nature of the dielectric environment [5, 8, 11, 26-28, 33]. The enhancement in the radiation field and the light confinement becomes maximum at the LSPR of the MNPs. The electric field intensity enhancement at the hot spots is different for different excitation wavelength, because of the strong dependence of the electric permittivity of the plasmonic particles on the excitation wavelength. Here it is worth to mention that all the above features of MNPs can be understood with the help of dipolar model.

Figure I.1 is depicting the sketch of the mechanism of light interaction with spherical MNP which helps to realize the LSPR of spherical MNP (which can be applied in general for any size, shape, material, and surrounding media of any MNP) and the resultant electric field confinement at the surface of the nanoparticle when it interacts with the em light.

Using the unique light interaction nature and the LSPR properties of metal nanoparticles we can use these MNPs in many areas of application which is written in the previous section already. Thus it is necessary to study the optical properties [electric field at their hot spots and localised surface plasmon resonance (LSPR) wavelength] in detail of these MNPs. The following theoretical sections regarding the MNPs will help us to understand the light interactivity, the absorption property, the LSPR wavelength, light confinement and intensity enhancement by a specific metal nanoparticle with particular size, shape, material and surrounding media.

**Theoretical methods:** Theoretically we can estimate the LSPR wavelength of MNPs and the electric field enhancement at their hot spots, using following methods.

**Mie theory (for spherical particles):** In 1908, Mie introduced a procedure to calculate the scattering, absorption and extinction properties of spherical particle in a homogeneous medium. In that case plane wave illumination is considered [32]. The scattered and internal fields are calculated to be the infinite series of vector spherical harmonic functions which are designated as $M_{emn}$, $N_{emn}$, $M_{omn}$ and $N_{omn}$ where the indices *o* and *e* designates the odd and even functions and the indices *n* and *m* are correlated with the Legendre functions of degree *n* and order *m*. The vector functions are calculated from the following two relations

$$\boldsymbol{M} = \nabla \times \left( \mathbf{r} \psi \right) \tag{I.7}$$

$$\boldsymbol{N} = \frac{\nabla \times \boldsymbol{M}}{k} \tag{I.8}$$

Where **r** is a constant vector and $\psi$ is a scalar wave function which satisfies the well known Helmholtz equation.

The internal fields of sphere of radius *a* and complex refractive index $\tilde{n}_1$ ($=\sqrt{\varepsilon_1 \mu_1}$) due to the plane wave illumination $\boldsymbol{E}_i = \hat{e}_x \boldsymbol{E}_0 \exp\left[ i\left( \boldsymbol{k} \cdot \boldsymbol{r} - \omega t \right) \right]$ will be

$$\boldsymbol{E}_1 = \sum_{n=1}^{\infty} \frac{i^n E_0 \left( 2n+1 \right)}{n\left( n+1 \right)} \left( c_n M_{o1n}^{(1)} - i d_n N_{o1n}^{(1)} \right) \tag{I.9}$$

$$\boldsymbol{H}_1 = -\frac{k_1}{\omega \mu_1} \sum_{n=1}^{\infty} \frac{i^n E_0 \left( 2n+1 \right)}{n\left( n+1 \right)} \left( d_n M_{o1n}^{(1)} + i c_n N_{o1n}^{(1)} \right) \tag{I.10}$$

Here, $k_1 = k_0 \tilde{n}_1$ and $k_0$ is the propagation constant of the incident em field in vacuum. Thus he scattered fields will be

$$\boldsymbol{E}_s = \sum_{n=1}^{\infty} \frac{i^n E_0 (2n+1)}{n(n+1)} \left( i a_n N_{o1n}^{(3)} - b_n M_{o1n}^{(3)} \right) \tag{I.11}$$

$$\boldsymbol{H}_s = \frac{k}{\omega\mu} \sum_{n=1}^{\infty} \frac{i^n E_0 (2n+1)}{n(n+1)} \left( i b_n N_{o1n}^{(3)} + a_n M_{o1n}^{(3)} \right) \tag{I.12}$$

Here index (3) is connected to radial dependence of generating functions associated with the Hankel functions of first order $h_n^{(1)}$. The values of all the coefficients $a_n$, $b_n$, $c_n$ and $d_n$ are correlated with the spherical Bessel and Hankel functions and are known as the scattering and internal field coefficients [32]. The estimation of these coefficients using appropriate boundary conditions will help us to calculate the scattering and the extinction cross sections which are given below [26-27]

$$C_{sca} = \frac{2\pi}{k^2} \sum_{n=1}^{\infty} (2n+1) \left( |a_n|^2 + |b_n|^2 \right) \tag{I.13}$$

$$C_{ext} = \frac{2\pi}{k^2} \sum_{n=1}^{\infty} (2n+1) \Re (a_n + b_n) \tag{I.14}$$

The absorption cross section of the sphere can be estimated using the relation

$$C_{abs} = C_{ext} - C_{sca} \tag{I.15}$$

All these relations will help us to see the absorption, scattering and extinction properties of spherical particles as function of the photon wavelength of the incident em light. The wavelength of photon at which one can have the highest absorption, scattering and extinction intensity by using a plasmonic nanosphere, is its LSPR wavelength and at this particular excitation wavelength the most efficient excitation of localised surface plasmons will take place giving the highest light localization. Because of this, the electric field intensity enhancement at any of the hot spot of the plasmonic particles would be optimized.

Bohren and Huffman wrote FORTRAN codes to calculate the Mie scattering coming from a homogeneous sphere, a coated sphere, and an infinite cylinder. Despite the computational complexity of these algorithms, it is possible only to have the cross sections of single spherical particle. Thus the Mie theory is unable to calculate the scattering coefficients and the LSPRs of MNPs of the different other shapes such as – core shell particle, ellipsoidal and rod shaped elongated structures and different other structures like star shape. The details about the relevant theoretical processes for calculating the different cross-sections and the LSPRs of those MNPs of different shapes are given below.

**Quasi-static theory (for nanosphere and nanoshell and elongated particles):** The theory is for particles of dimensions much smaller than the excitation wavelength ( $D \le \lambda/10$ ) [30]. In presence of em radiation the MNPs (in general for NPs) behave as simple radiating dipoles. The dimension of the NPs is small enough and thus we can consider the phase of the incident electric field fairly constant inside the particle. This field can be estimated by using the expression of the electrostatic potential which is $\boldsymbol{E} = -\nabla\psi$ [30].

**Spherical nanoarticles**: For the nanosphere of radius $a$ and dielectric constant $\varepsilon_1$ kept in a homogeneous dielectric medium of dielectric constant $\varepsilon_2$ if we consider the incoming em field as

$$\boldsymbol{E}_0(\boldsymbol{r},t) = \boldsymbol{E}_0(\boldsymbol{r})\exp(-i\omega t) \tag{I.16}$$

Then, the expressions of the internal electric field $\boldsymbol{E}_1$ and the external electric field $\boldsymbol{E}_2$ of the spherical particle, estimated by solving the Laplace equation in spherical harmonics are given by [30]

$$\boldsymbol{E}_1 = \frac{3\varepsilon_2}{\varepsilon_2 + 2\varepsilon_1}\boldsymbol{E}_0 \tag{I.17}$$

$$\boldsymbol{E}_2 = \boldsymbol{E}_0 + \frac{3\boldsymbol{n}(\boldsymbol{n}\cdot\boldsymbol{p}) - \boldsymbol{p}}{r^3}\frac{1}{4\pi\varepsilon_1} \tag{I.18}$$

Here $\boldsymbol{n}$ is unit vector in the direction of point of observation at a distance $\boldsymbol{r}$ from the dipole (i.e. the sphere) and $\boldsymbol{p}$ is the induced dipole moment of the nanosphere which is given by

$$\boldsymbol{p} = \alpha\varepsilon_1\boldsymbol{E}_0 = 4\pi a^3\frac{\varepsilon_2 - \varepsilon_1}{\varepsilon_2 + 2\varepsilon_1}\varepsilon_1\boldsymbol{E}_0 \tag{I.19}$$

Thus now the absorption, scattering and extinction cross sections of the nanosphere can be written as [26, 28]

$$\sigma_{abs} = k\Im\left[\alpha(\omega)\right] \tag{I.20}$$

$$\sigma_{scat} = \frac{k^4}{6\pi}\left|\alpha(\omega)\right|^2 \tag{I.21}$$

$$\sigma_{ext} = \sigma_{abs} + \sigma_{scat} \tag{I.22}$$

Thus the scattering, absorption, and extinction cross sections are seen to be strongly dependent on polarizability. The polarizability will go to maximum value when denominator of equation (I.19) will be zero [i.e. $\varepsilon_1(\omega) = -\varepsilon_2/2$ ]. This condition is popular as the Frölich

resonance condition. At the frequency where that resonance condition will be satisfied, the optical properties such as absorption and scattering will reach to the maximum.

**Core-Shell nanoparticles**: The scattering, absorption, extinction properties of single spherical core-shell particles can be estimated by using the equations (I.20), (I.21), and (I.22). In this case, the expression of the polarizability ($\alpha$) of the spherical nanoparticle given in equation (I.19) should be replaced by the proper expression of $\alpha$ for the nanoshell found elsewhere [31].

**Elongated nanoparticles:** Elongated nanoparticles such as nanorod, nanoellipsoid when interacts with em radiation having polarization along their semi-major axis then a huge electric field develops because of their stronger light confinement capability at their tips. This light confinement and thus electric field enhancement is higher than that of a nanosphere. This is happening for the case of the elongated particles due to the lightning rod effect along with their LSPR effect. The effect of LSPR for the light confinement and electric field enhancement for elongated particles follows the same mechanism for the other particles which has been discussed already. Here the discussion will be given about the lightening rod effect which makes these elongated particles different than the spherically symmetric NPs by helping them to achieve way more intensity enhancement at their hot-spots. This effect is very much effective at tips of those elongated particles because of the high radius of curvature at tips where the electrical charge density is expected to be preferably very high. The total electric field at the tip of the elongated nanoparticles is [26, 30]

$$E_{tip} = \gamma E_{dip} + E_i \tag{I.23}$$

Where, $E_i$ *and* $E_{dip}$ are the incident electric field and the induced dipole electric field respectively. Here $\gamma$ is the shape factor for a nanoparticle which is given by [26],

$$\gamma = \frac{3}{2}\left(a/b\right)^2\left(1-\mathrm{A}_a\right) \tag{I.24}$$

Here 2*a* is the length (along the incident electric field direction) and 2*b* is the breadth of the elongated nanoparticle. The depolarization factor '$\mathrm{A}_a$' is therefore given by

$$\mathrm{A}_a = \left(\frac{1-e^2}{e^2}\right)\left[\frac{1}{2e}\ln\left(\frac{1+e}{1-e}\right)-1\right] \tag{I.25}$$

Here, $e^2 = 1-\left(1/r^2\right)$ and $r = a/b$. The maximum strength of the dipole electric field developed at the tip of an elongated structure is as follows [26]

$$E_{tip} = 2\frac{P}{a^3} \tag{I.26}$$

Where

$$P = \left(\frac{V}{4\pi}\right)\left[\frac{\varepsilon_2 - \varepsilon_1}{\varepsilon_1 + (\varepsilon_2 - \varepsilon_1)A_a}\right]E_{inc} \qquad \text{(I.27)}$$

Here the volume of the elongated particle is denoted by *V*.

According to the above discussion, for an elongated nanostructure *a/b* ratio is higher than that for the spherically symmetric nanostructures. Because of that the shape factor ($\gamma$) is of higher magnitude for the elongated NPs compared to the spherical NPs. This is the reason for having stronger light confinement at the tips of the elongated NPs compared to the spherical NPs which helps to have the higher electric field intensity enhancement at the respective positions than that of a nanosphere.

This quasi-static method is simpler but it has the following problems

i. Valid for smaller NPs only ($D \leq \lambda/10$).
ii. Not valid for complex nanostructures (such as nanostar, nanotriangle).
iii. Considers the dipolar field only (ignoring the effect of higher order multipoles)
iv. Optical properties of the nanoparticles are considered to be independent of their size.

To avoid these difficulties one may consider the Finite Difference Time Domain (FDTD) method [34-35] and Finite Element Method (FEM) [36]. With those numerical methods one may calculate the LSPRs and electric field enhancement by any kind of NPs with any size and shape. The theoretical study will take into account also the material property of both the NP and the surrounding medium. With these method the analysis can be done not only for the spherically symmetric NPs and known simple elongated NPs such as nanorods and nanoellipsoid, but this method could also be applied for any arbitrary shaped (such as nanostars, nanocubes, nanotriangle, hexagonal shaped NPs and many others) NPs. These methods take into consideration the size effect during the numerical evaluation of the optical properties of the NPs but there is no restriction on the NPs size, i.e. applicable to any size scale. These methods consider dipolar and also higher order multipolar modes to have the result and thus the effect is more general one compared to the other theoretical processes.

Now we have all the required details about the optical properties of the MNPs –how the metal NPs interact with the incoming em wave and what happens during that interaction, then resonance effect, i.e. their LSPR and also how to estimate their LSPR and the corresponding electric field intensity enhancement. These details are sufficient to understand the different kinds of plasmonic effect occurring in MNPs and will be useful for later discussion. Now the

only remaining important part is – "Metallic thin film and its light interaction". That discussion will complete this chapter and is given in the following section.

**I.4. Metallic thin film and discussion about Surface Plasmon Polaritons (SPPs):**

Surface plasmons become an important event when we consider the light interaction with a metal-dielectric interface. Surface plasmons (SPs) are the coherent delocalized electron oscillations which exists at the interface between metal and dielectric where the real part of the dielectric function changes its sign across the interface (metal has a negative $Re(\varepsilon(\omega))$ and for dielectric $Re(\varepsilon(\omega))$ is positive).The surface plasmons existing at the metal-dielectric interface cannot propagate in absence of any em wave. When the em wave interacts with the metal-dielectric interface, the interaction between the surface charge density (or surface plasmons) and the incoming em field (or photon) generates the quasi-particle surface plasmon polaritons (SPPs) which are able to propagate in the interface. The dispersion relation followed by this SPP wave is given below

$$k_{sp} = k_i \sqrt{\frac{\varepsilon(\omega)\varepsilon_{diel}}{\varepsilon(\omega)+\varepsilon_{diel}}} \qquad \text{(I.28)}$$

Here $\varepsilon(\omega)$ is the frequency dependent electric permittivity of metals, $\varepsilon_{diel}$ is the dielectric constant of the surrounding medium, $k_i$ (= $\omega/c$) and $k_{sp}$ are the momentum of the em wave in free space and that of the SPP wave respectively. The dispersion of SPP wave is plotted in the figure I.3 along with the schematic of the mechanism of SPP wave generation. There we can see that for a particular frequency of the incoming light, the momentum of the SPP wave is larger than that of the em wave in free space. This mismatch requires the presence of particular kind of structures (for example – grating, Kretschmann geometry, Otto geometry etc) to couple the em photons to the surface plasmons and to excite the SPP waves in the metal-dielectric interface. SPPs are also able to enhance optical near-field like the LSPs in MNPs. SPPs were first demonstrated by Wood in 1902. After that lots of fundamental as well as application oriented researches have been done on SPP based structures [37-39]. The SPP based nanostructures can found many applications such as surface enhanced Raman spectroscopy (SERS), data storage, solar cells, bio-chemical sensors, miniaturized photonic circuits, [37-39] and in many other fields by using their unique optical interaction properties.

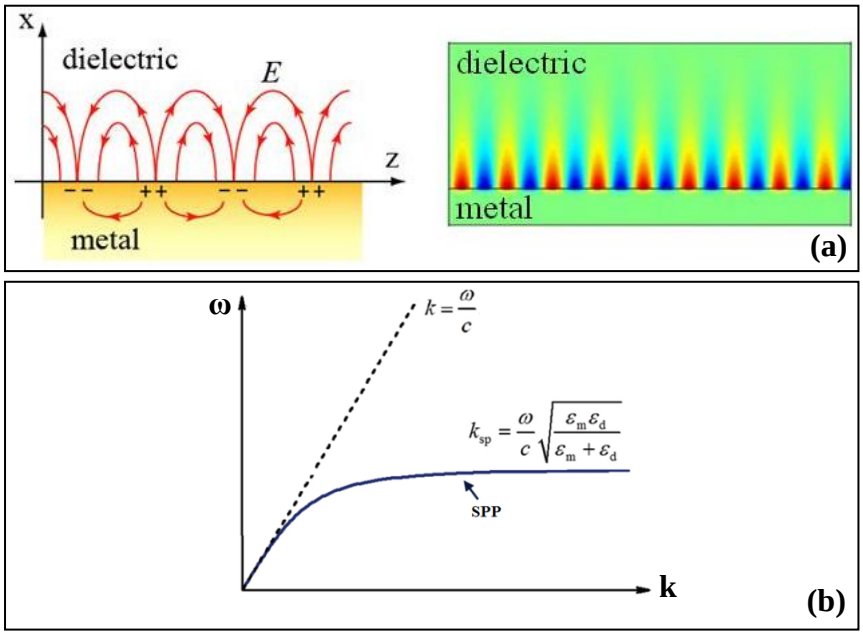


Figure I.3. (a) The schematic of the mechanism of SPP wave generation. (b) The dispersion of SPP waves.

To understand the SPP waves more carefully along with their origin and nature for different kinds of polarization (TE and TM) we need some theoretical study which is given below.

**Surface Plasmon Polaritons (SPPs) and the related important theory:**

As already explained, the surface plasmon polaritons (SPPs) are the electromagnetic excitations that propagate at the metal-dielectric interface, and are confined evanescently in the perpendicular direction. The propagation of the SPPs can be understood classically with the help of following approach.

To understand the physical properties of the SPPs, let us first consider the popular Helmholtz equation [29].

$$\nabla^2 \boldsymbol{E} + k_0^2 \varepsilon \boldsymbol{E} = 0 \qquad \text{(I.29)}$$

Where, the wave vector of the propagating em wave in vacuum is given by

$$k_0 = \omega/c \qquad \text{(I.30)}$$

The Helmholtz equation is acquired from the well-known Maxwell's equations and considering some assumptions which are

- Absence of any kind of external charge, i.e., $\nabla . \boldsymbol{D} = 0$
- The time-dependent electromagnetic field $\boldsymbol{E}(\boldsymbol{r}, t) = \boldsymbol{E}_0(\boldsymbol{r}) e^{-i\omega t}$ event at a single interface.

Here we consider $\varepsilon = \varepsilon(z)$, i.e., $\varepsilon$ depends only on one spatial coordinate as we are considering one dimensional problem. In this case the propagation of the electromagnetic wave is along the x-direction and thus don't show any spatial variation along the y-direction. At this moment we are considering the Cartesian coordinate system. One more point, here, $z = 0$ plane is the metal-dielectric interface.

Now considering all the previous conditions the electric field expression comes out to be

$$\boldsymbol{E}(x, y, z) = \boldsymbol{E}(z)e^{i\beta x} \tag{I.31}$$

Therefore, now the Helmholtz equation can be written as

$$\frac{\partial^2 \boldsymbol{E}(z)}{\partial z^2} + (k_0^2\varepsilon - \beta^2)\boldsymbol{E}(z) = 0 \tag{I.32}$$

With the help of this equation one can determine the spatial field profile of SPPs and the dispersion of its propagating waves. The different field components of the electric field, ***E*** and the magnetic field, ***H*** can also be found out from this expression.

If we consider the Maxwell's equation and take curl of it taking into account few facts such as,

- There is no external charge present in the system we are considering.
- $\left(\frac{\partial}{\partial t} = -i\omega\right)$ for the harmonic time dependence
- $\left(\frac{\partial}{\partial x} = i\beta\right)$, for the propagation along the x-direction.
- $\left(\frac{\partial}{\partial y} = 0\right)$ i.e., the system is homogeneous along the y-direction.

Considering all the conditions we get the following sets of equations which are given below

$$\frac{\partial E_y}{\partial z} = -i\omega\mu_0 H_x \tag{I.33a}$$

$$\frac{\partial E_x}{\partial z} - i\beta E_z = i\omega\mu_0 H_y \tag{I.33b}$$

$$i\beta E_y = i\omega\mu_0 H_z \tag{I.33c}$$

$$\frac{\partial H_y}{\partial z} = i\omega\varepsilon_0\varepsilon E_x \tag{I.33d}$$

$$\frac{\partial H_x}{\partial z} - i\beta H_z = -i\omega\varepsilon_0\varepsilon E_y \tag{I.33e}$$

$$i\beta H_y = -i\omega\varepsilon_0\varepsilon H_z \tag{I.33f}$$

The above sets of equations give two sets of solutions for two different polarizations of the propagating waves – transverse magnetic mode (TM) and transverse electric mode (TE).

For TM mode, $E_x \neq 0$, $E_z \neq 0$, and $H_y \neq 0$.

And for TE mode, $H_x \neq 0$, $H_z \neq 0$, and $E_y \neq 0$.

For TM modes, from the equations (d) and (f) we can get the following expressions

$$E_x = -i\frac{1}{\omega\varepsilon_0\varepsilon}\frac{\partial H_z}{\partial z} \tag{I.34a}$$

$$E_z = -\frac{\beta}{\omega\varepsilon_0\varepsilon}H_y \tag{I.34b}$$

Here $E_x$ and $E_z$ are expressed as the functions of $H_y$. Now $H_y$can be derived from the solution of the TM wave equation which is given by

$$\frac{\partial^2 H_y}{\partial z^2} + (k_0^2\varepsilon - \beta^2)H_y = 0 \tag{I.34c}$$

On the other hand, for transverse electric (TE) mode, the required sets of equations are

$$H_x = i\frac{1}{\omega\mu_0}\frac{\partial E_y}{\partial z} \tag{I.35a}$$

$$H_z = -\frac{\beta}{\omega\mu_0}E_y \tag{I.35b}$$

Here $H_x$ and $H_z$ are expressed as the functions of $E_y$. Now $E_y$ can be derived from the solution of the TE wave equation which is given by

$$\frac{\partial^2 E_y}{\partial z^2} + (k_0^2\varepsilon - \beta^2)E_y = 0 \tag{I.35c}$$

All these expressions are describing the nature of SPPs at a single, flat metal-dielectric interface. Propagating SPP waves which is seen at the metal-dielectric interface has a characteristics evanescent decay of intensity in the z-direction, perpendicular to the direction of propagation of SPP waves. Here for this system, half space in $z > 0$ is considered as of dielectric nature where $Re(\varepsilon(\omega)) > 0$, and half space in $z < 0$ is considered as of conducting metallic nature where $Re\big(\varepsilon(\omega)\big) < 0$. Propagation of SPPs is of different nature for the two different polarization TE and TM case which are described in the following section.

➢ **TM Polarization:** For TM polarization, the solution of the equation gives the following field components which are describing the nature of the SPP propagation in the x-direction and the nature of the exponential decay of SPP wave along the z-direction.

$$H_y(z) = A_2 e^{i\beta x} e^{-k_2 z} \tag{I.36a}$$

$$E_x(z) = iA_2 \frac{1}{\omega \varepsilon_0 \varepsilon_2} k_2 e^{i\beta x} e^{-k_2 z} \tag{I.36b}$$

$$E_z(z) = -iA_2 \frac{\beta}{\omega \varepsilon_0 \varepsilon_2} e^{i\beta x} e^{-k_2 z} \tag{I.36c}$$

When, $z > 0$. And for $z < 0$

$$H_y(z) = A_1 e^{i\beta x} e^{k_1 z} \tag{I.37a}$$

$$E_x(z) = -iA_1 \frac{1}{\omega \varepsilon_0 \varepsilon_1} k_1 e^{i\beta x} e^{k_1 z} \tag{I.37b}$$

$$E_z(z) = -A_1 \frac{\beta}{\omega \varepsilon_0 \varepsilon_1} e^{i\beta x} e^{k_1 z} \tag{I.37c}$$

Here, for the above sets of equations $A_1$ and $A_2$ are the magnetic field amplitudes and $k_1$ and $k_2$ are the wave vectors in the two media.

The evanescent decay length of the SPP fields is defined as the length in the perpendicular direction with respect to the metal-dielectric interface at which the electric field amplitude decays over the exponential times of the electric field amplitude at the metal-dielectric interface. It can be calculated from the following relation

$$\hat{z} = \frac{1}{|k_z|} \tag{I.38}$$

Where $\hat{z}$ is the evanescent decay length of SPPs electric field perpendicular to the metal-dielectric interface and $k_z$ is the wave vector component perpendicular to the interface between the two media. The evanescent decay length gives an idea about the confinement of the SPP wave in the interface.

To satisfy the continuity equation of $H_y, E_x$ and $E_z$ at the metal-dielectric interface where we consider $z = 0$ we should have

$$A_1 = A_2 \tag{I.39}$$

And

$$\frac{k_2}{k_1} = -\frac{\varepsilon_{diel}}{\varepsilon(\omega)} \tag{I.40}$$

For this case of TM polarization the confinement to the metal dielectric interface demands the following condition

$$Re\big(\varepsilon(\omega)\big) < 0 \text{ While } \varepsilon_{diel} > 0$$

Therefore, for TM polarization, the surface SPP waves can exist only if the interface will comprise of two materials for which the real part of dielectric permittivity will change its sign across the interface, such as the interface between a conductor and an insulator. Additionally, to have certain specific characteristics of $H_y$ we have to have the following conditions too.

$$k_1^2 = \beta^2 - k_0^2\varepsilon(\omega) \quad \text{(I.41)}$$

$$k_2^2 = \beta^2 - k_0^2\varepsilon_{diel} \quad \text{(I.42)}$$

Now if we combine all the above three relations connecting $k_1$ and $k_2$, then the most useful result of this section regarding the SPPs, which is the dispersion relation of the SPPs waves will come out. The dispersion relation for TM polarization of the propagating surface plasmon polaritons (SPP) wave confined at the metal-dielectric interface will be expressed by the following relation

$$\beta = k_0\sqrt{\frac{\varepsilon(\omega)\varepsilon_{diel}}{\varepsilon(\omega)+\varepsilon_{diel}}} \quad \text{(I.43)}$$

The above expression is valid for both the real and complex type of dielectric permittivity $\varepsilon(\omega)$, i.e., for the conductors without and with the attenuation.

- **TE Polarization:** For TE polarization, the field components of the SPP wave can be expressed as

$$E_y(z) = A_2 e^{i\beta x} e^{-k_2 z} \quad \text{(I.44a)}$$

$$H_x(z) = -iA_2 \frac{1}{\omega\mu_0} k_2 e^{i\beta x} e^{-k_2 z} \quad \text{(I.44b)}$$

$$H_z(z) = A_2 \frac{\beta}{\omega\mu_0} e^{i\beta x} e^{-k_2 z} \quad \text{(I.44c)}$$

For $z > 0$, and for $z < 0$ those field components of the SPP wave will be reduced to the following forms

$$E_y(z) = A_1 e^{i\beta x} e^{k_1 z} \quad \text{(I.45a)}$$

$$H_x(z) = iA_1 \frac{1}{\omega\mu_0} k_1 e^{i\beta x} e^{k_1 z} \quad \text{(I.45b)}$$

$$H_z(z) = A_1 \frac{\beta}{\omega\mu_0} e^{i\beta x} e^{k_1 z} \quad \text{(I.45c)}$$

For the above sets of equations, $A_1$ and $A_2$ are the electric field amplitudes.

In this TE polarization case the demand of continuity of $E_y$ and $H_x$ at the interface demand two conditions which are

$$A_1 = A_2 \quad \text{(I.46)}$$

And

$$A_1(k_1 + k_2) = 0 \quad \text{(I.47)}$$

The above condition will be fulfilled only if

$$A_1 = 0 \quad \text{(I.48)}$$

This means that, in such situation $A_2 = 0$ because we know that $A_1 = A_2$.

This means that no surface modes can exist in case of TE polarization.

In case of the multilayer structures, like metamaterials, which consists of alternating conducting and dielectric thin films, every single metal-dielectric interface supports bound SPPs. If the separations between the adjacent interfaces are $\leq$ the decay length $\hat{z}$ of the interface mode then the interaction among all those penetrating SPP modes into the structure activate the coupled mode. These coupled modes are very important modes in case of the metamaterials comprises of metal and dielectric thin film stack and will be discussed in the later chapter dedicated for the overview of metamaterial only.

This completes the discussion about the metallic thin film and its interaction with the incoming em light which also includes the generation and properties of the very important and useful SPP waves for different light polarization.

**I.5. Conclusion:** In summary, here in this chapter the usefulness of the nanostructured metals are described compared to their bulk characteristics. The interaction of the bulk metals with light is explained which is helpful for understanding the different behaviours of metals. The light interaction in case of metal nanoparticles and the metallic thin films which can generate LSPs and SPPs respectively are also given. The information about the LSPR and SPR along with their behaviour has been discussed. All the discussion will help to have idea about the light confinement and enhancement ability using these nanostructures which will be useful for the preceding chapters.

**I.6. References:**

[1] E. Le, R. Pablo Etchegoin, Principles of Surface-Enhanced Raman Spectroscopy, 1st edition. Elsevier Science, 2008.

[2] P. Drude, Zur elektronentheorie der metalle. Annalen der Physik 1900, 306 (3), 566-613.

[3] P. B. Johnson, and R. W. Christy. Optical Constants of the Noble Metals. Phys. Rev. B 1972, 6, 4370-4379.

[4] I. Freestone, N. Meeks, M. Sax, and C. Higgitt. The Lycurgus cup a roman nanotechnology. Gold Bulletin 2007, 40 (4), 270-277.

[5] P. K. Jain, K. S. Lee, I. H. El-Sayed, and M. A. El-Sayed. Calculated absorption and scattering properties of gold nanoparticles of different size, shape, and composition: applications in biological imaging and biomedicine. The Journal of Physical Chemistry B, 2006, 110 (14), 7238-7248.

[6] M. A. Garcia. Surface plasmons in metallic nanoparticles: fundamentals and applications. Journal of Physics D: Applied Physics, 2011, 44 [28], 283001.

[7] J. N. Anker, W. P. Hall, O. Lyandres, N. C. Shah, J. Zhao, and R. P. Van Duyne. Biosensing with plasmonic nanosensors. Nat. Mater. 2008, 7 (6), 442-453.

[8] C. Noguez. Surface plasmons on metal nanoparticles: the influence of shape and physical environment. The Journal of Physical Chemistry C 2007, 111 (10), 3806-3819.

[9] A. Moores, and F. Goettmann. The plasmon band in noble metal nanoparticles: an introduction to theory and applications. New J. Chem. 2006, 30, 1121-1132.

[10] H. A. Atwater. The promise of plasmonics. Scientific American 2007, 296 (4), 56-62.

[11] S. Underwood, and P. Mulvaney. Effect of the solution refractive index on the color of gold colloids. Langmuir 1994, 10 (10) 3427-3430.

[12] M. Hu, J. Chen, Z. –Y. Li, L. Au, G. V. Hartland, X. Li, M. Marquez, and Y. Xia. Gold nanostructures: engineering their plasmonic properties for biomedical applications. Chem. Soc. Rev. 2006, 35, 1084-1094.

[13] Schuller, J.A.; Barnard, E.S.; Cai, W.S.; Jun, Y.C.; White, J.S.; Brongersma, M.L. Plasmonics for Extreme Light Concentration and Manipulation. Nat. Mater. 2010, 9, 193–204.

[14] Sharma, B.; Frontiera, R.R.; Henry, A.I.; Ringe, E.; Van Duyne, R.P. SERS: Materials, Applications, and The Future. Mater. Today 2012, 15, 16–25.

[15] Nie, S.M.; Emery, S.R. Probing Single Molecules and Single Nanoparticles by Surface-Enhanced Raman Scattering. Science 1997, 275, 1102–1106.

[16] Willets, K.A.; Van Duyne, R.P. Localized Surface Plasmon Resonance Spectroscopy and Sensing. Annu. Rev. Phys. Chem. 2007, 58, 267–297.

[17] Sreekanth, K.V.; Alapan, Y.; ElKabbash, M.; Ilker, E.; Hinczewski, M.; Gurkan, U.A.; De Luca, A.; Strangi, G. Extreme Sensitivity Biosensing Platform Based on Hyperbolic Metamaterials. Nat. Mater. 2016, 15, 621–627.

[18] W. Cai, U. K. Chettiar, A.V. Kildishev, and V. M. Shalaev. Optical Cloaking with Metamaterials. Nat. Photon 2008, 1, 224-227.

[19] Sekhon, J.S.; Malik, H.K.; Verma, S.S. DDA Simulations of Noble Metal and Alloy Nanocubes for Tunable Optical Properties in Biological Imaging and Sensing. RSC Adv. 2013, 3, 15427–15434.

[20] Hou,W.B.; Cronin, S.B. A Review of Surface Plasmon Resonance Enhanced Photocatalysis. Adv. Funct. Mater. 2013, 23, 1612–1619.

[21] Reineck, P.; Lee, G.P.; Brick, D.; Karg, M.; Mulvaney, P.; Bach, U. A Solid-State Plasmonic Solar Cell Via Metal Nanoparticle Self-Assembly. Adv. Mater. 2012, 24, 4750–4755.

[22] Chen, H.C.; Chou, S.W.; Tseng, W.H.; Chen, I.W.P.; Liu, C.C.; Liu, C.; Liu, C.L.; Chen, C.H.; Wu, C.I.; Chou, P.T. Large Au-Ag Alloy Nanoparticles Synthesized in Organic Media Using a One-Pot Reaction: Their Applications for High-Performance Bulk Heterojunction Solar Cells. Adv. Funct. Mater. 2012, 22, 3975–3984.

[23] Kelkar, S.S.; Reineke, T.M. Theranostics: Combining Imaging and Therapy. Bioconj. Chem. 2011, 22, 1879–1903.

[24] Barnes,W.L.; Dereux, A.; Ebbesen, T.W. Surface Plasmon Subwavelength Optics. Nature 2003, 424, 824–830.

[25] Ozbay, E. Plasmonics: Merging Photonics and Electronics at Nanoscale Dimensions. Science 2006, 311, 189–193.

[26] Bohren, C. F.; Huffman, D. R. Adsorption and Scattering of Light by Small Particles; Wiley-VCH: New York, 1983.

[27] van de Hulst, H. C. Light Scattering by Small Particles; Dover: New York, 1981.

[28] Maier, S. A. Plasmonics: Fundamentals and Applications; Springer: Berlin, 2007.

[29] Novotny, L.; Hecht, B. Principles of Nano-Optics 2nd edn; Cambridge University Press: Cambridge, 2012.

[30] Jackson, J. D. Classical Electrodynamics*;* Wiley: New York, 1999.

[31] Purcell, E. M.; Pennypacker, C. R. Astrophys. *J*. 1973, 186, 705-714.

[32] Mie, G. Beitrage zur optik truber medien, speziell kolloidaler metallosungen. Annalen der Physik. 1908, 330 (3), 377–445.

[33] Water-solubilized aminoclay–metal nanoparticle composites and their novel properties

K. K. R. Datta, M. Eswaramoorthy and C. N. R. Rao . J. Mater. Chem., 2007, 17, 613–615.

[34] Yee, K. IEEE Trans. Antennas Propag. 1966, 14, 302-307

[35] Taflove, A.; Hagness, S. C. Computational Electrodynamics: The Finite-Difference Time-Domain Method; MA: Artech House: Boston, 2004.

[36] Jin, J. M. The Finite Element Method in Electromagnetics 2nd edn; Wiley: New York, 2002.

[37] M. Born and E. Wolf. Principle of optics: electromagnetic theory of propagation, interference and diffraction of light. Cambridge university press, 1999.

[38] J. Zhang, L. Zhang, and W. Xu. Surface plasmon polaritons: physics and applications. Journal of Physics D: Applied Physics 2012, 45 (11) 113001.

[39] W. L. Barnes, A. Dereux, and T. W. Ebbesen. Surface Plasmon Subwavelength Optics. Nature 2003, 424, 824-830.

# CHAPTER II:

# STAR-SHAPED METALLIC NANOPARTICLE

# Chapter IIA

# Fabrication of star-shaped metallic nanoparticle for sensing

## IIA.1. Motivation for Sensing

Real-time and label-free detection and sizing of protein molecules at ultralow concentration in their natural state is considered a longstanding need in biomedical research as these protein markers could be an indicator of a particular infection or the reemergence of a disease which would allow the identification of the onset of cancers and many other dangerous diseases before they become clinically relevant. This kind of early detection will help to monitor disease progression and evaluate therapeutic success, thereby increasing survival rates and quality of life [1]. This kind of detection is also useful for environmental monitoring, emergency response, and homeland security.

At very early stage of disease, the signature protein markers circulate throughout the human body by mixing with the bodily fluids such as saliva, blood serum etc. But at that early stage, the concentration of those protein markers in the bodily fluids are very low and unfortunately, the mass of most of the protein molecules is typically lower than 5 attogram. So, not only the ultralow concentration in the bodily fluid but also the acutely small size (<3 nm) of the protein markers create extreme challenges in the real-time and label-free detection and sizing of single protein molecules at their early stage of infection [2]. Moreover, size estimation of the markers is very crucial because it would provide the information about the molecular weight and number of amino acids present in that molecule. All these will help for better understanding of the molecular structure of that marker and will be helpful for making its anti-agent.

One way to detect these proteins is to use the unusual electromagnetic responses of electron clouds of noble metal nanoparticles, which lead to the well-known localized surface plasmon resonance (LSPR) effect. The LSPR effect of the plasmonics nanoantenna in various nanoplasmonic sensors is an efficient way for the real-time label-free detection of single protein molecules [3].

Because of the inherent LSPR effect nanoantennas create hot-spot when it interacts with light. When a protein molecule comes nearby the nanoparticle in presence of light, the bio-molecule feels a huge attraction to the hot-spots of the nanoplasmonic antenna due to the

creation of a huge light force at those hot-spot areas. Because of this attraction when the protein molecule gets adsorbed onto the surface of the nanoantenna, the evanescent field of the resonance mode starts to polarize the dielectric bionanoparticle. During this process, as the mode has to do some work to polarize that bionanoparticle its energy gets reduced. Experimentally, this situation can be visualised as a shift of the previously observed LSPR mode of the nanoantenna which is actually a narrow dip in the transmission spectrum or sharp peak in the elastic spectrum along the wavelength axis [3-6].

The fractional wavelength shift of the LSPR mode due to the adsorption of a single protein molecule obeys the following relation [6].

$$\frac{\Delta\lambda_r}{\lambda_r} \propto \frac{\int_{molecule} \Delta\varepsilon \boldsymbol{E}_a(\boldsymbol{r}_p)^* \boldsymbol{E}_b(\boldsymbol{r}_p) dV}{\int \varepsilon_r(\boldsymbol{r}) \left|\boldsymbol{E}(\boldsymbol{r})\right|^2 dV} \tag{1.1}$$

Where, $\Delta\lambda_r$ is the wavelength shift, $\lambda_r$ is the LSPR mode of the unperturbed nanoantenna, $\boldsymbol{E}_a(\boldsymbol{r}_p)^* \cdot \boldsymbol{E}_b(\boldsymbol{r}_p)$ is the product of the field within the perturbing volume before (*b*) and after (*a*) the bio-molecule is put into the hot-spot area, $\Delta\varepsilon$ is the change in permittivity of the surrounding medium in presence of an analyte. Here $\varepsilon_r(\boldsymbol{r})$ and **E**(***r***) are respectively the electric permittivity and electric field of the nanoparticle at its hot-spot area when the antenna interacts with light in absence of any molecule. As the bio-molecule is nothing but a Rayleigh particle whose dimension is much smaller than the free space excitation wavelength, therefore the shape of wave function or the evanescent field of the nanoantenna can be assumed to be fairly constant within the interacting molecule during the detection process. Applying this approximation the above equation can be written as [6]

$$\frac{\Delta\lambda_r}{\lambda_r} \propto \frac{\mathrm{Re}[\alpha_{ex}]\boldsymbol{E}_0^2(\boldsymbol{r_p})}{\int \varepsilon_r(\boldsymbol{r}) \left|\boldsymbol{E}_0(\boldsymbol{r})\right|^2 dV} \tag{1.2}$$

Here, $\mathrm{Re}[\alpha_{ex}]$ is the real part of the excess polarization of the bio-analyte which depends on the size and thus mass of the molecule. So from this equation it can be understood that for a single protein molecule with ultra-low mass it is very hard to have a significant wavelength shift and thus a good signal to noise (S/N) ratio which limits the practical real-time label-free detection of single protein molecule at ultra-low concentration. In the above equation, the numerator and the denominator represent here the excess polarization energy of the particle

and energy of the LSPR mode of the nanoantenna, respectively. $\boldsymbol{E_0(r_p)}$ is the electric field amplitude of the LSPR mode at the location of the protein adsorption $\boldsymbol{r_p}$, and $\boldsymbol{E_0(r)}$ is the magnitude of the electric field of the LSPR mode at the hot-spot area of the nanoparticle interacting with light in absence of any molecule. From the above relation it can be realized that for the real-time label-free detection of a single protein molecule of smaller mass and thus smaller value of $\mathrm{Re}[\alpha_{ex}]$ in ultra-low concentration one has to increase the $\boldsymbol{E_0(r_p)}$ to have a significant wavelength shift ($\Delta\lambda_r$) and thus a good signal-to -noise (S/N) ratio. Thus the enhancement in the experimental signal, which is the experimental wavelength shift, majorly depends on the field at the hotspots of the nanoantenna. The dipolar electric field at the hot-spot of the nanoantenna created during its interaction with electromagnetic wave for light confinement in the nanoparticle at its LSPR can be tuned by controlling the nanoparticle size, shape, electric permittivity of that nanoantenna and dielectric matrix in which the plasmon nanostructure is located [7, 8]. By the suitable selection of a nanoparticle, one can reach to the enhancement of the dipolar electric field up to the order of 1000 easily. Therefore, here it seems that the label-free detection of single protein molecule could be possible by amplifying the signal in the above discussed way.

## IIA.2. Comparison of all the known nanoparticles suitable for protein sensing using plasmonic biosensor: Why star-shaped nanoparticles are better for sensing:

Among different suitable nanoplasmonic antenna Core shell nanoparticles are better than rigid spherical nanoparticles for their higher tunability and electric field enhancement capability [9]. However, it has been observed that NPs with sharp edges, such as nanoellipsoid [10], nanotriangles [11], nanocubes [12, 13], nanorods [14, 15], nanostars [16-19], or octahedral nanoparticles [20, 21], have a higher capability of confining light in ultra-small regions compared to the non-spiky spherically symmetric NPs. A comparison table (Table. 1) is given below which bears an idea about the electric field enhancement by the popular nanoantennas which can be used to build different kind of nanoplasmonic sensor. Based on that data one can choose the most efficient nanoantennas.

Here it can be seen that a giant dipole electric field (with respect to the non-spiky spherically symmetric nanoparticle such as nanosphere, nanoshell) develops at the tips of nanostar spikes (also true for other spiked antennas such as nanocubes and octahedral nanoparticle), corners of nanotriangles and tips of nanorod and nanoellipsoid, when they interact with

electromagnetic wave. This kind of enhanced electromagnetic energy concentration at the hot spots of spiky NPs is due to the plasmonic resonance effect, which is more effective than the non-spiky nanoparticles (nanosphere, nanoshell) because of their lightning rod effect [22-26] and the small radius of curvature of the edges, which results in the enhancement of the local electric field, distributed over the hot spot area of those nanostructure.

Among all the spiky nanoparticles if we compare star-shaped nanoantennas (and nanocubes, nanotriangle and octahedral nanoparticle) with nanorod and nanoellipsoid then star-shaped antennas (also true for nanocubes, nanotriangle and octahedral nanoparticle) will be more beneficial for the nanoplasmonic sensor because of the following reasons:

I. For the case of a nanorod and nanoellipsoid [27-32] to get the maximum electric field enhancement generated due to the lightning rod effect at its hotspots, the incident electric field of the incoming electromagnetic wave should be in parallel direction with the length (major axis) of the nanorod and nanoellipsoid type of elongated nanoantennas. But, we don't have any control on the orientation of the nanostructure with respect to the electric field of the incoming light wave. Therefore, it is very difficult to optimize the electric field enhancement at the hot spot of the nanorod and nanoellipsoid type of particles. But for nanostar (true for nanocubes, nanotriangle and octahedral nanoparticle) this type of problem will not occur as these particles have their spikes arranged more symmetrically over their surface and any of the spikes can generate the hot-spot depending on the direction of the incoming electric field.

II. Although the electric field enhancement is almost same for nanostar like the nanoellipsoid and nanorod yet the probability of getting at least one hot spot for any kind of incoming electromagnetic wave with random electric field makes these star shaped nanoantennas suitable for nanoplasmonic sensor. Nanotriangle, like nanostar has the advantage of having higher probability of generating hot-spots for any random incoming electric field yet here it is worth to mention that a single nanotriangle shaped particle is not able to create the field enhancement like a nanorod, nanoellipsoid or nanostar. Among all the possible spiked antennas such as the nanoellipsoid and the nanorod, which can concentrate light like nanostars [27–32], nanostars with a random distribution of spikes over their core have the advantage of having hot spots excited by any kind of polarization of the incident light, being polarization-insensitive. The higher probability of generation of a few

hot spots irrespective of incident light polarization as well as the creation of huge intensity enhancement in the hot spots make these highly tunable nanostars very promising in the field of real-time biosensing at a point of care with respect to gold nanorods and nanoellipsoides.

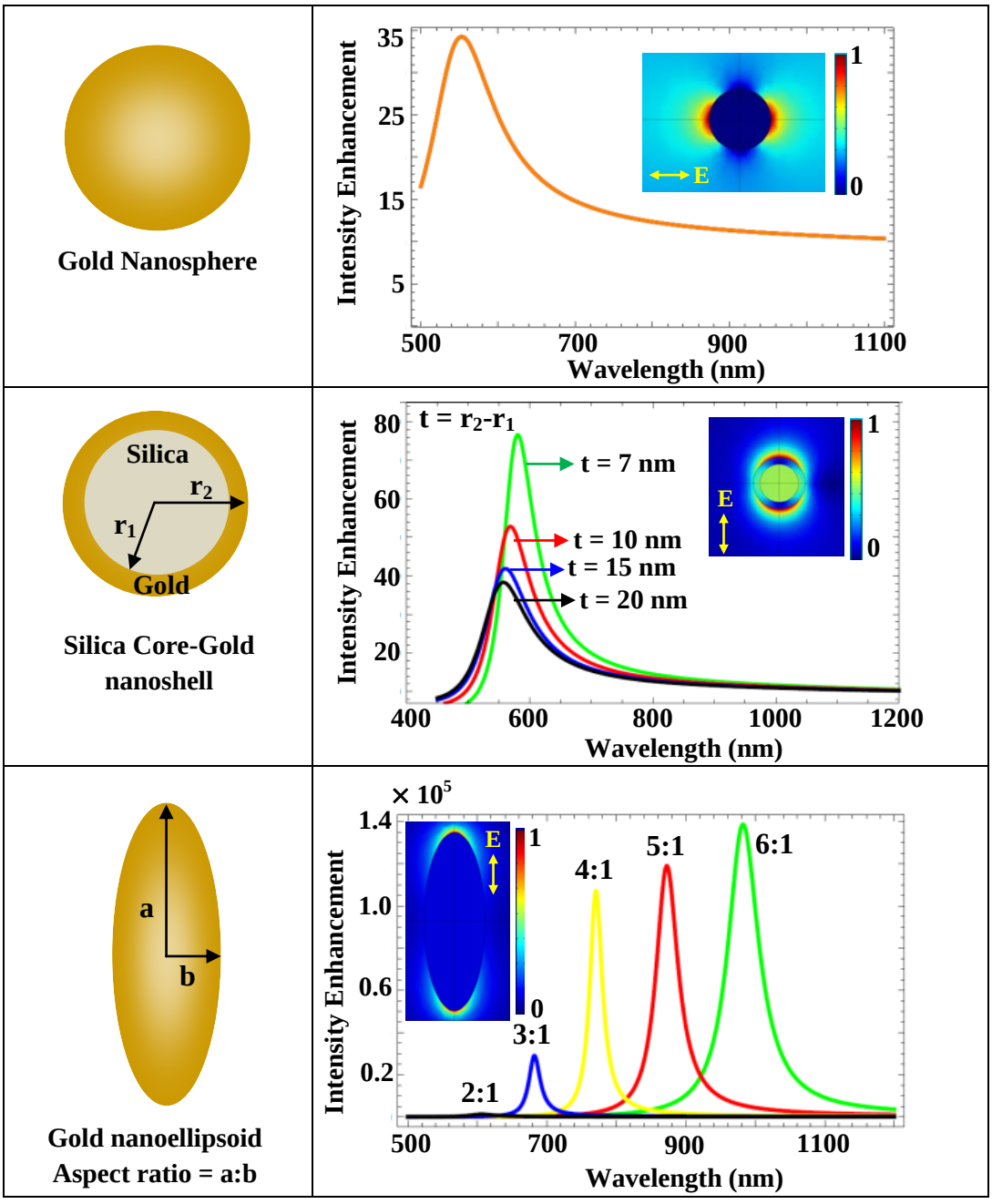

| | |
|---|---|
| 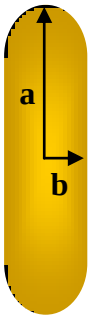 <br>**Gold nanorod**<br>**Aspect ratio = a:b** | 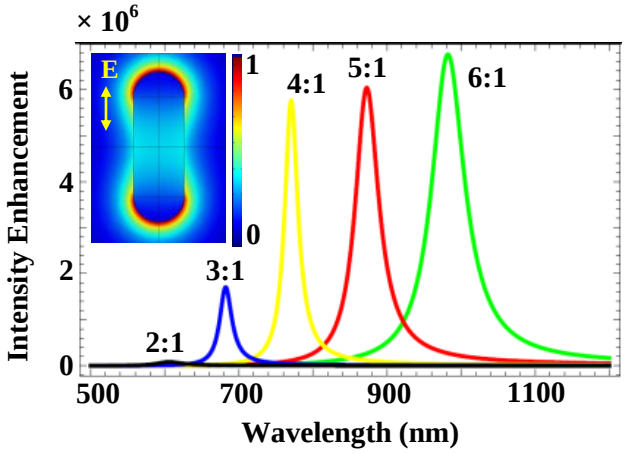 |
| 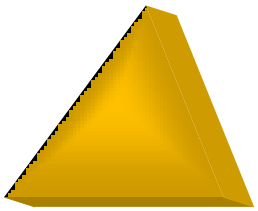 <br>**Gold nanotriangle**<br>**Side length = 60 nm**<br>**Thickness = 5 nm** | 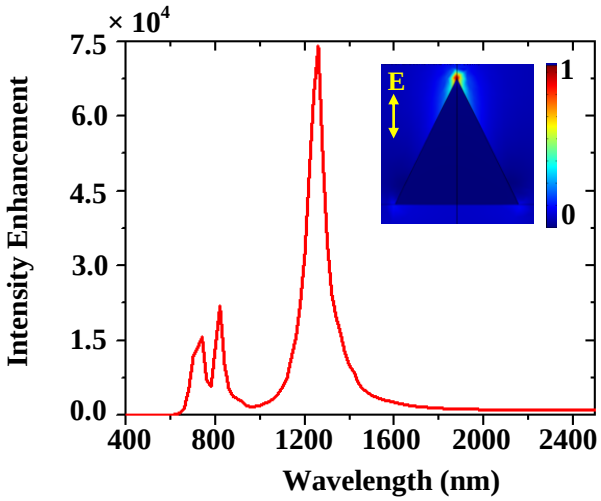 |
|  <br>**Gold nanostar**<br>**Spike length = 90 nm**<br>**Tip Radius = 5 nm**<br>**Core size = 60 nm** | 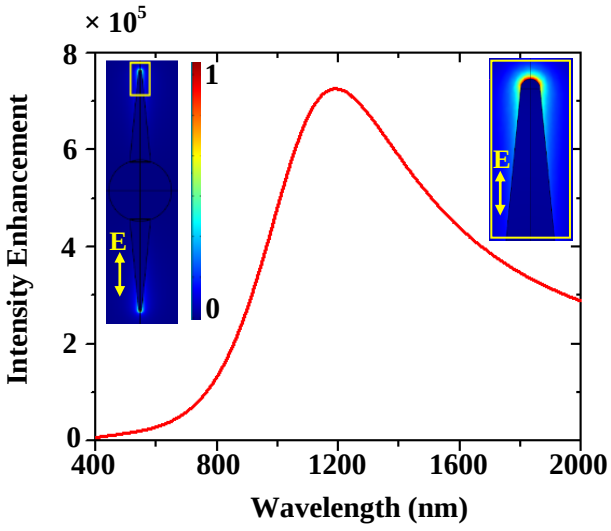 |

Table 1: Here electric field intensity enhancement by different nanoantenna such as gold nanosphere, silica core-gold nanoshell, gold nanoellipsoid, nanorod, nanotriangle, and nanostar are shown. From this comparison table it is clear that a single gold nanoellipsoid or nanorod or nanostar antenna is better than a single gold nanotriangle or nanosphere or silica core gold nanoshell antenna. All these theoretical analysis has been done by comsol 5.4. The details about the numerical analysis method will be described in later section.

So after comparing all the possible shape it seem that the nanostar, nanocubes and octahedral nanoparticles with lots of spikes arranged in their surface symmetrically, having at least one hot spot with the maximum intensity enhancement will be more appropriate than nanorod and nanoellipsoid for a nanoplasmonic sensor. Because of the wide application of those mentioned spiked NPs, the effective and controlled synthesis parameters that can tune LSPRs along with the ability to manipulate hot spot landscapes has become an important research field.

Recently, significant efforts have been devoted to achieve novel nanomaterials that allow for the manipulation of the interaction of light at the nanoscale. Gold is the most widely used noble metal for biomedical applications due to its well-known low toxicity, biocompatibility, chemical stability and tunability.

By considering all the above points and several advantages and possibilities of gold nanostars (AuNS), these efficient nanoantennas have been synthesized here using a new synthesis route and well characterized with different experimental facilities. The details about the synthesis procedures and characterization of the synthesized nanoparticles are given below. This chapter also contains detail about the numerical simulation on the gold nanostar which describes its usefulness as a nanoplasmonic sensor.

## IIA.3. Synthesis of Gold Nanostar (AuNS) Antennas:

The popular wet-chemistry method represents a largely used bottom-up approach for NP synthesis among many other possible routes. In 2006, Nehl et al first synthesized nanostar gold particles by wet-chemistry method via a two step seed mediated growth process and characterized its optical properties. In this case the overall size of a typical nanostar was 100 nm and the number of spikes of each nanostar varies from 3 to 8. Synthesized gold nanostars had a good plasmon tunability and higher reproducibility but the yield of the synthesis was not good (9% - 14%), the size distribution of star shaped nanoparticles is also large and the spikes were not so sharp [33]. Later, Kumar et al. in 2008 improved the yield of the gold nanostar synthesis [34]. Later many research groups synthesized gold nanostar antenna in their own unique way to improve the quality, monodispersity and yield. Many of them also adapted the green synthesis route for gold nanostars [35]. Moukarzel et al. synthesized gold nanostars with a seed-less amino-sugar mediated method in 2011 [36]. Yuan et al, in 2012, for the first time, synthesized gold nanostars in a surfactant-free wet chemistry method. Until that time, the researchers were using a surfactant for synthesizing gold nanostar particle to

restrict the growth of the nanoparticle size. But, Yuan et al were successful to synthesize smaller gold nanostars using their process without any surfactant where the quality of the nanostar, their yield and monodispersity was also found to be good. But that synthesis process was a two-step seed mediated growth method [37]. Later, Kedia et al. introduced the process of reshaping a gold nanostar and its corresponding plasmon tuning mechanism [38]. Recently, Minati et al synthesized star shaped gold nanoparticles via a one-step reduction process where the size of the nanostar was small [39]. But, for our case to have a good plasmonic biosensor we need a star shaped gold nanoparticle which can produce high electric field enhancement and according to the lightning rod effect, thus we should have gold nanostar antenna with a sharper and elongated spikes. In addition, the size of the gold nanostars has to be beyond 100 nm, to have more scattering cross section than the absorption cross section. Furthermore, a larger gold nanostar antenna (> 100 nm) having several elongated sharper spikes randomly distributed over its surface synthesized via a surfactant-free route will be beneficial not only for in vitro sensing but also for in vivo testing. Synthesizing gold nanostars without a surfactant is beneficial because during synthesis, we can avoid the phenomena of attachment of the surfactant atoms (used to restrict the nanoparticle growth) on the nanoparticle surface which will have better biocompatibility with respect to those nanoparticles synthesized using a surfactant-assisted way. Moreover depending on the surfactant layer thickness on the nanoparticle, the electric field at the binding site could be fainted which may not be sufficient to polarize the adsorbed protein molecule due to the rapid decay of the dipole electric field intensity.

It has been already mentioned that very few research groups have synthesized spiked gold nanostar antennas via a surfactant-free wet-chemistry route although different research groups have synthesized AuNS in many different ways. So there is still a need for a low-cost, simple, surfactant-free wet chemistry method for synthesizing these highly efficient spiked nanoplasmonic antennas with high yield. Here, we report a simple, one-step surfactant-free wet chemistry method for synthesizing Au nanostructures with high stability and yield. This improves on our previously reported AuNS synthesis method [40], where the stability was poor and the control of the nanostar synthesis parameters was not possible. Synthesis as well as optical and electron spectroscopy characterization of these highly stable nanoparticles (stability > 5 months in aqueous solution) indicate that these nanoparticles have remarkable plasmonic features. Here the synthesis details of the gold nanostar (AuNS) particle are described along with its numerical investigation. But the characterization details of those AuNS antenna are described in following chapters based on their particular application.

## Materials Used For AuNS Synthesis:

Gold (III) chloride trihydrate ($HAuCl_4$, $3H_2O$), silver nitrate (AgNO3), ascorbic acid (AA), hydrochloric acid (HCl) (35–37%), and polyvinylpyrrolidone (PVP) were purchased from Sigma Aldrich (Milan, Italy)and used as received without further purification. The water used throughout this synthesis process was reagent-grade, produced using a Milli-Q SP ultrapure-water purification system.

## Synthesis Process of the Stabilized AuNS:

Here gold nanostars were synthesized in a simple, one-step (without seed), surfactant free wet-chemistry method. First, 10 mL of 0.25 mM chloroauric acid ($HAuCl_4$) solution [in presence of 10 $\mu$l of 1 M HCl solution] was taken in a 20 mL glass vial. The solution was stirred at room temperature under moderate stirring (700 rpm). Then, 100 $\mu$l of $AgNO_3$ solution of 1mM concentration and 50 $\mu$l of AA solution of 100 mM concentration were added simultaneously with the above chloroauric acid solution at room temperature under moderate stirring (700 rpm). The color of the solution rapidly became blue within 30 s and after 2 min from the addition of the AA and $AgNO_3$, 5 mL of polyvinylpyrrolidone (PVP) solution of 2 mM concentration was added and the solution was stirred for 8 min. After 10 min as a whole, the reaction was completed and the solution was kept for another 3 h at room temperature at rest. After that, one centrifugal wash had been done at 4000 rcf for 20 min in a 15 mL tube to wash out the extra PVP. After centrifugation, the liquid containing extra PVP and the other chemicals was collected as much as possible, and the precipitate was redispersed in DI water. In this way, we got our stabilized AuNSs dispersed in DI water and kept it at room temperature for future use. Here in this synthesis process, the length and number of spikes of nanostars could be easily adjusted by varying pH, stirring speed, and concentration ratios of the ingredients. Here we have maintained a constant stirring speed throughout the synthesis process. The synthesized AuNSs were well characterized and these details are given in the following chapters based on their particular application.

## Results and Discussions:

To obtain nanostars in aqueous suspension with high yield and stability, there are parameters that need to be precisely controlled during synthesis. These parameters are summarized in this section.

One of these parameters is the relative amount of reducing agent to the gold precursor. Here, ascorbic acid (AA, $C_6H_8O_6$) was used as the reducing agent, and chloroauric acid ($HAuCl_4$) was used as the gold precursor. The ratio of AA to chloroauric acid was maintained to be 1.5–2.0 to reduce all $HAuCl_4$ molecules present in the solution completely.

Secondly, the presence of Ag+ ($AgNO_3$) was necessary in this synthesis process for the nanostar formation. During synthesis, the main function of $Ag^+$ was to expedite the anisotropic growth of Au branches on certain crystallographic facets [37]. The synthesis procedure will only yield polydispersed nanorods and nanospheres in the absence of Ag+ ($AgNO_3$). Increasing the amount of $AgNO_3$ during the synthesis will increase the length and the number of spikes of the AuNS. Here figure IIA.1 describes the morphology of gold nanoparticles prepared without $AgNO_3$ (figure IIA.1 a) and with 100 $\mu$l $AgNO_3$ solution of 1 mM concentration (figure IIA.1 b). Here it can be seen that the synthesis process is giving only polydispersed nanorods and nanospheres in absence of Ag+ ($AgNO_3$). But in presence of $AgNO_3$ the synthesis route is giving spiky gold nanostars (AuNS).

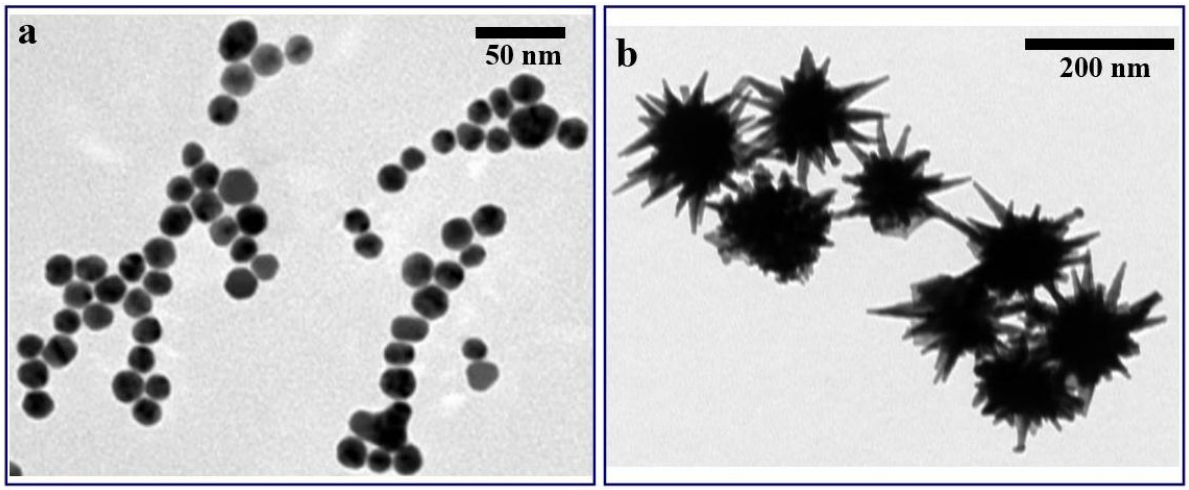


Figure IIA.1. Effect of Adding Silver Nitrate ($AgNO_3$) During Nanoparticle Synthesis: (a) A typical lower magnification randomly selected Transmission Electron Microscopy (TEM) image of a collection of Au nanoparticles produced without adding $AgNO_3$. (b) A typical lower magnification randomly selected TEM image of a collection of Au nanoparticles produced in presence of $AgNO_3$. Here we can see that synthesized gold nanoparticles in absence of $AgNO_3$ are mostly of spherical shape whereas in presence of $AgNO_3$ the nanoparticles turn out to be of star shape. This is showing that the presence of Ag+ ($AgNO_3$) is necessary in this synthesis process for the nanostar formation.

The third factor was the presence of HCl. A small amount of HCl helped in this case to slightly decrease the pH of the solution and to get a red-shifted plasmon band.

The fourth factor was the simultaneous injection of AA and $AgNO_3$, in the $HAuCl_4$ solution (in the presence of HCl), because this will significantly influence the polydispersity, yield, and quality of the nanostars.

The fifth factor was the stirring speed. A study was carried out to probe the best stirring speed for the AuNS synthesis process which reveals that 700 rpm is the best stirring speed for a successful AuNS synthesis as the measured extinction cross section for the AuNS solution is highest for that speed. The Figure below is showing the experimental extinction spectra for the AuNS solutions prepared using different stirring speed.

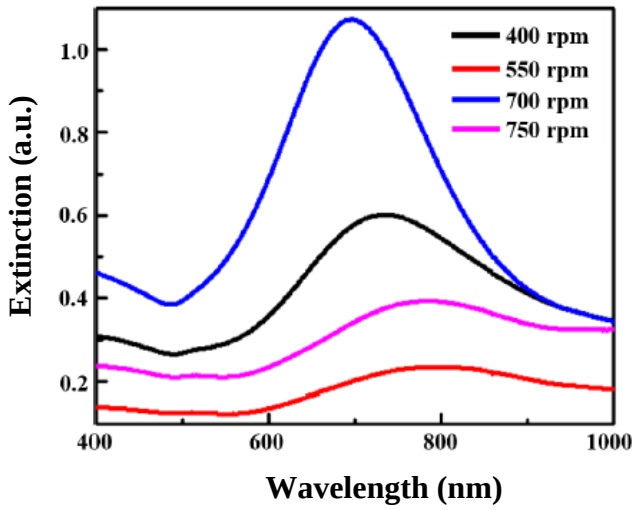


Figure IIA.2. Study on the Stirring Speed During the Synthesis Process: Comparison of different experimental UV-Vis-NIR spectra of the synthesized AuNS solutions produced using different stirring speeds. Here it can be seen that 700 rpm is the best stirring speed for a successful synthesis as the measured extinction cross section for that specific AuNS solution is highest.

The sixth factor was the proper injection time of polyvinylpyrrolidone (PVP). To investigate the best injection time of PVP for a successful AuNS synthesis three AuNS solution has been prepared. The extinction spectra of all those three solutions are given in the Figure below. In this figure the black curve is for that AUNS solution where PVP was added just before the addition of the ascorbic acid (AA) (before reduction). The red curve is for that AuNS solution where the PVP was added during the addition of AA (during reduction). The blue curve is for the AUNS solution where PVP was added after 2 minutes from the time of simultaneous injection of AA and $AgNO_3$ (after reduction). This AuNS solution (blue curve) is seen to have the highest extinction cross section implying that the best injection time of PVP for a successful synthesis is after 2 min from the time of simultaneous injection of AA and $AgNO_3$, because by that time the reduction process had quite enough time to be completed and was

not affected by the PVP addition by any means. Here, PVP concentration was taken lower so that the reduction kinetics was not affected. PVP is added in this process only to create a hindrance to the nucleation process among the nanostars for a highly stable AuNS aqueous suspension. Here, the inset picture of the figure IIA.3 is showing the colour of the synthesized AuNS solution after centrifugation.

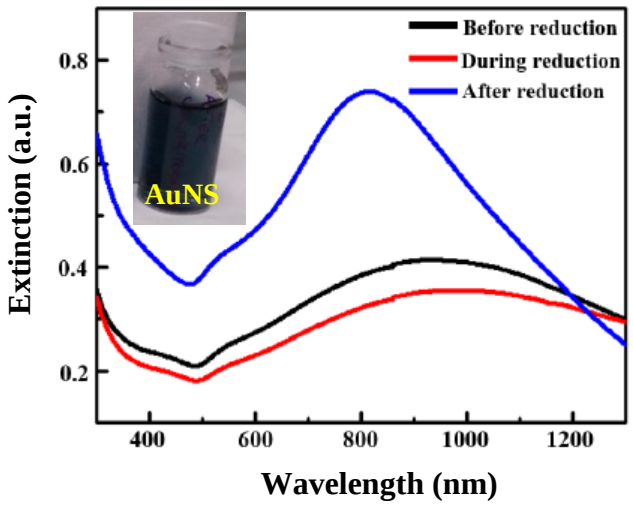


Figure IIA.3. Study on the Best Injection Time of Polyvinylpyrrolidone (PVP) During Synthesis: Comparison of different experimental UV-Vis-NIR spectra of the synthesized AuNS solutions is given where variation of PVP injection time has been taken into account. Here it can be seen that the best injection time of PVP for a successful synthesis is after 2 minutes from the time of simultaneous injection of AA and $AgNO_3$ not before or during the synthesis as the measured extinction cross section for that specific AuNS solution is highest. The inset picture is showing the synthesized AuNS aqueous solution after centrifugation.

The gold nanostars prepared by our method maintaining all the previously discussed important parameters were found to be stable in aqueous solution for more than five months. During AuNS synthesis and the study of different synthesis parameters, the effect of slight variations in temperature was neglected, as the temperature was never above $60^{o}C$, so any observable effect on the synthesis end product due to temperature variation was not expected [41].

After preparing these spiky gold nanostar antenna it is very essential to know how much efficient these antenna will be for biosensing. For that we investigated theoretically the electric field intensity enhancement by these antennas when it interacts with light. Sensitivity has also been calculated for various AuNS with different spike length. All these have been done using the commercial software package Comsol 5.4 which is based on Finite Element

Method (FEM). The details about the numerical investigation method and the results are discussed below.

### IIA.4. Numerical Study:

**Numerical Simulation Method:** FEM based Comsol simulations are used here to study the interaction of a single AuNS with photons. All the data regarding nanostars spikes and their cores are taken from the TEM studies (discussed in the following chapter) to have an idea about the possible intensity enhancement by these synthesized star nanoantennas. Intensity enhancement study will tell about the sensitivity of these antennas as a plasmonic biosensor as the signal to noise (S/N) ratio or in other words the sensitivity depends on the intensity enhancement at the hot-spots of these antennas. The simulation has been done using the Radio Frequency (RF) module of Comsol 5.4 [42-44]. During simulation the nanostructure's surface has been discretized with tetrahedral mesh elements with a typical maximum and minimum side lengths of 24.5 and 1.05 nm, respectively. Here the electric field was mapped in the entire space. Different cross sections (Scattering, Absorption and Extinction) of those nanoantennas were also examined. For these optical simulations the definitions in the Comsol material library are used for all the optical and physical properties of the surrounding media. During sensitivity calculation, we considered first air ($\varepsilon = 1.0$) and then water ($\varepsilon = 1.7689$) as the homogeneous surrounding media. In all simulations, the wavelength-dependent permittivity of the gold was taken from [45]. Here, plane waves are used as the excitation source. Electric field polarization of incident light is always chosen along the semi major axis of the AuNS spikes during extinction and electric field mapping. We also calculated the shift in LSPR of the single AuNS and the AuNS-nanosphere heterodimer when a BSA molecule (of 0.11 attogram mass ~ 66.5 kDa) is coupled in the hot spot region of those nanoantennas immersed in water medium. During simulation, a BSA protein molecule was taken as a dielectric particle of cylindrical shape with a permittivity of 2.25, with a characteristic height of 3.4 nm and a 6.8 nm short cylinder diameter [46].

**Numerical Simulation Results:**

Our synthesized AuNSs have lots of sharp spikes on its surface as is seen from the TEM images (already shown). So it is quite expected that these spikes will be able to localize the incident light very tightly and will create huge intensity enhancement at their hot-spots after resonant light illumination. Our comsol simulation results agree with these thoughts. Here in figure IIA.4 below the numerical results regarding the light interaction of AuNS is described.

Panel (a) reports how a single plasmonic nanostar antenna behaves when it interacts with photons in water. Panel (b) shows how the situation is modified if a BSA molecule is located in close proximity to the tip. For this investigation, the incident light polarization has been assumed to be along the z-direction (i.e. along the length or semi major axis of the spike of AuNS), whereas the propagation direction has been assumed to be the +y-direction. The yellow dotted lines are the external boundaries of the nanostructure depicted for clear understanding. The extinction properties corresponding to a single AuNS plasmonic antenna immersed in water in the presence and absence of a BSA molecule are shown in figures IIA.5.

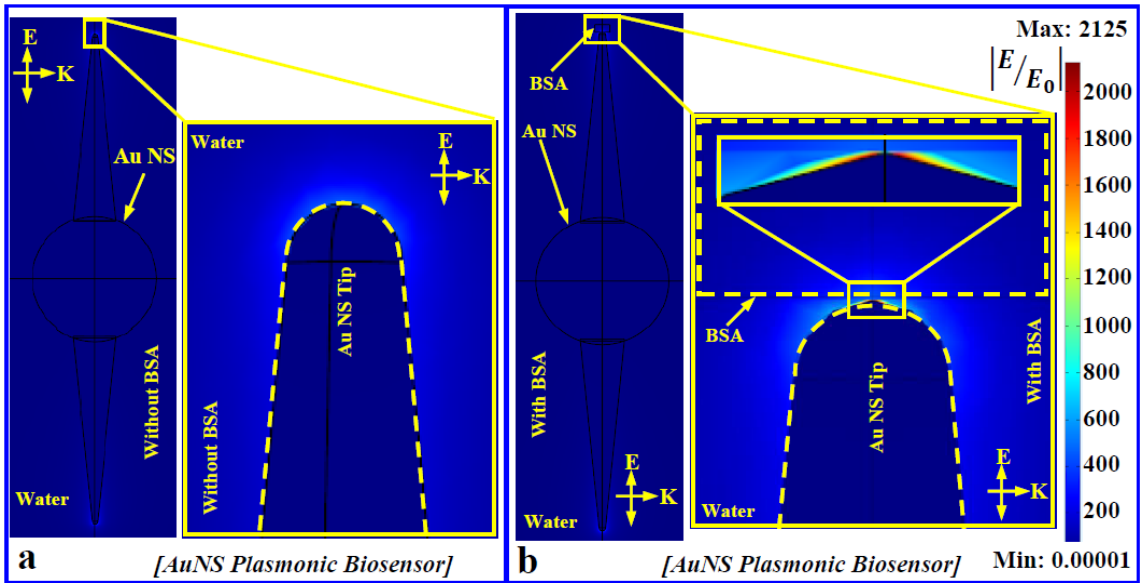


Figure IIA.4. Numerical Simulation Results on Field Enhancement: (a) Interaction of single AuNS plasmonic biosensor dispersed in water with incident light in the absence of a BSA molecule. The zoomed portion of the yellow box shows the intensity enhancement at the pinnacle of the spike. (**b**) Interaction of a single AuNS plasmonic biosensor with incident light in the presence of BSA in water media. Here in all cases, the incident light wave has polarization along the z-axis (i.e. along the length or semi-major axis of the spike) and propagation along the +y direction. The AuNS has a spike length of 88 nm and a 60 nm core, a value taken from the TEM images during experimental measurements.

In the above simulation results, the enhancement factor is given in term of the quantity$|E/E_0|$. However, the shift in the wavelength due to the adsorption of the protein molecule is proportional to the light intensity ($\frac{I}{I_0} = \left|\frac{E}{E_0}\right|^2$) at the binding site. The intensity enhancement by a smaller spike, 33 nm AuNS spike (smallest spike length) in water is approximately $1.6\times10^3$ whereas the intensity enhancement for 88 nm spikes (the AuNS in the

above figure which is one of the AuNS that has larger spike length) is approximately $2.5\times10^5$ in water which is equivalent to the electric field enhancement of 500 times as shown in the panel (a) of figure IIA.4. This panel (a) describes the enhancement factor in absence of any protein molecule. Here for numerical simplicity we consider only 2 spikes of AuNS but can be generalized for other cases too which has to deal with AuNS with a lot of spikes. In panel (b) the intensity enhancement in presence of Bovine serum Albumin (BSA) molecule becomes $2\times10^6$ times which is quite high with respect to the panel (a) case. This happens because the molecule is a dielectric particle. Upon protein adsorption on the tip of the AuNS, light at the hot-spot become more localized as the molecule is a denser light medium than the surroundings. And because of this drastic further localization of hot-spot area of the nanoantenna in presence of analyte the field intensity enhanced to even higher but within very small region. The zoomed portion in panel (b) is describing this effect.

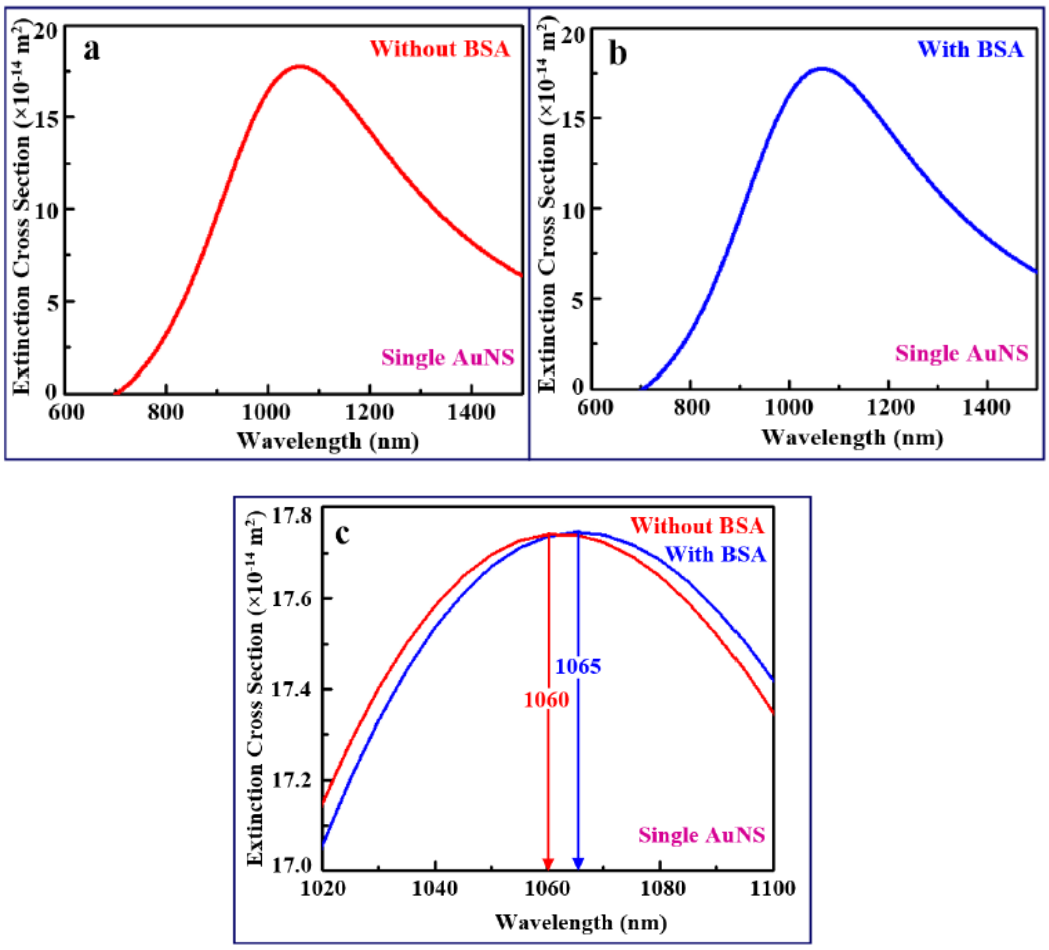


Figure IIA.5. Numerical Simulation Results on Extinction Property: (a) Extinction property of single AuNS dispersed in water in absence of BSA molecule is shown here. (b) Extinction property of single AuNS in presence of BSA in water media. (c) Comparison between both the situation of single AuNS, in absence and presence of BSA molecule. Here 5 nm of

wavelength shift is predicted according to the theoretical analysis for the adsorption of single BSA molecule at the AuNS tip.

FEM simulation on the extinction property of the AuNS of 60 nm core and 88 nm spike is calculated here which is shown in Figure IIA.5 above. Here the two situations have been considered – one is in absence of any protein molecule (panel a) and the other one is for the presence of a single Bovine Serum Albumin (BSA) molecule on the AUNS hot spot at its tip (panel b). According to the shown FEM analysis, the LSPR of a single AuNS plasmonic antenna immersed in water is found to occur at 1060 nm in absence BSA molecule. In presence of the single BSA molecule at AuNS tip the LSPR shifts to 1065 nm. So, according to the theoretical investigation, 5 nm of wavelength shift is expected for adsorption of single BSA molecule (molecular weight ~ 66.5 kDa) for this AuNS tip. During this FEM analysis also the incident light wave has polarization along z axis, propagation along +y direction and the orientation of the 88 nm spikes of the AuNS is taken along the axis of polarization. In this study also the wavelength dependent permittivity of gold is taken from the Johnson and Christy measurements [45]. Here for this type of single AuNS antenna according to our numerical investigation it is expected that the sensitivity can reach of about 1940 nm/RIU which is pretty high as a single plasmonic biosensor [48].

The following figure describes the working principle of a single AuNS based plasmonic biosensor.

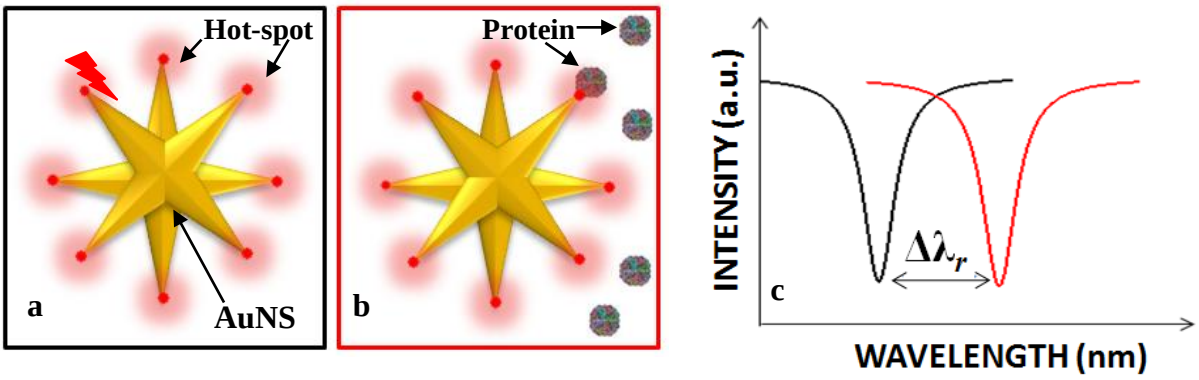


Figure IIA.6. Schematic diagram of AuNS based plasmonic biosensor: Panel (a) shows schematic diagram of single dipole stimulated plasmonic AuNS antenna based biosensor. Here this antenna has multiple hot-spots near the pinnacle of its tips which has been generated from the interaction with light. In this case no analyte is present. Panel (b) shows the modified scenario in presence of protein molecule. Panel (c) shows the wavelength shift of the LSPR mode of AuNS (black curve) upon adsorption of single protein molecule (red curve) at any one of the hotspots of the nanoantenna. By measuring this significant wavelength shift $\Delta\lambda_r$ one can detect the presence of an analyte using this plasmonic biosensor.

For large protein molecules (>1 MDa), energy loss to polarize the molecule is higher, so a larger LSPR shift that is easy enough to detect occurs; however, for the case of a protein molecule of ultrasmall molecular weight and thus smaller polarizability, the loss of energy of the LSPR shift becomes difficult to detect. Recently, single protein molecule detection has been reported using a plasmonic biosensor based on nanorods [47]. The reported S/N was very low, as the FWHM line width of the LSPR spectrum was larger (~50 nm) than the average wavelength shift (~0.1 nm) produced due to the adsorption of a molecule on the surface of the nanoplasmonic particle [47]. Therefore, real-time (label-free) detection of protein molecules of lower molecular weight (e.g., the Thyroglobulin molecule of a 660 kDa molecular weight and a BSA molecule of a 66.5 kDa molecular weight) in ultralow concentration appears to be forbidden with current technologies. Moreover the expected shift of resonance wavelength due to the adsorption of single protein molecule may be perturbed from laser wavelength fluctuations which can worsen the situation.

Recently, by using thermal-stabilized reference interferometer, a research group from CALTECH made possible to beat down the experimental noise to 0.2 fm by cancelling the laser wavelength fluctuations and they have detected a single polystyrene particle of mass 9 ag with a S/N just greater than one. But, actually this polystyrene particle has larger mass than most of the single protein molecule.

Therefore, for the detection of single protein molecule with ultra-low polarizability and thus mass, one of the possible ways is to amplify the signal (according to the equation 1.2) and this can be done by using a spiky gold nanostar plasmonic antenna. Figure IIA.4 is describing the high intensity enhancement ($2.5\times10^5$) capability of this single AuNS.

Figure IIA.6 is describing the principle of the AuNS based plasmonic biosensor. In this schematic diagram panel (a) describes the interaction of AuNS antenna with electromagnetic (em) wave. Here due to the light interaction the localized surface plasmon of AuNS antenna gets excited and starts oscillating. These oscillations of plasmons generate multiple hot spots in AuNS which are created at the tip of its different spikes. Here, the electric field intensity at the hot spots would be higher than excitation electric field intensity. Panel (b) is describing the protein interaction with AuNS antenna in presence of light. Due to the huge light confinement at the hot-spots light force is created. Because of this light force in the hot-spots areas the protein molecules feel attraction towards those areas and when it gets adsorbed at any one of the hot spots of AuNS it produce wavelength shift. This situation appears as a clear step in the wavelength trace (dip trace) as shown in the panel (c). This red-shift in

wavelength signifies a decrease in energy of the LSPR mode of single AuNS. When the analyte comes in vicinity of the hot-spots of AuNS, the evanescent field of the AuNS LSPR mode starts to polarize that dielectric foreign particle and in that process it loose energy which is seen here as a red-shift in the wavelength axis. In this way one can detect the presence of single protein molecule in ultra-low condition flowing through the bodily fluid at very early stage by using a single AuNS antenna based plasmonic biosensor. Moreover, this AuNS can be converted to a sensor by immobilizing a capture molecule (probe) at its tip to specifically recognize molecules at a point of care.

**IIA.5. Conclusion:**

In summary, here it was seen that single AuNS antenna based plasmonic biosensor has the capability to detect the presence of single protein molecule at ultra-low condition in real-time label-free method at very early stage of infection with a possibility to convert it to a sensor for the specific bio-molecule detection. Although the single AuNS has the capability to detect single protein molecule with high sensitivity yet the high localization of light at the tip of the nanostar may create some problem in some specific cases. For example for those molecules which is bigger in size with respect to the area of the hot-spots of AuNS it may have some issues. Due to the steep radius of curvature at the tip of the nanostar the intense dipole electric field intensity at the surface of the AuNS tips decreases rapidly with the distance away from the pinnacle and vanishes within few nanometres because of the smaller tip size (typically 5 nm) of the AuNS. In this case it may have problem for the bigger molecules (size > 10 nm). Moreover, in order to convert this device as a single molecule biosensor, the AuNS tip surface has to be functionalized with suitable anti-bodies. If we functionalize the AuNS tip surface with anti-bodies for specific detection of single protein molecules, then most of this intense dipole field would strongly interact with the anti-bodies and a very faint electric field will polarize the protein molecule, which would be adsorbed on the anti-bodies. Due to this, the magnitude of the wavelength shift would become very low; sometimes it would be still within the experimental noise. For this reason, the sensitivity or performance of the sensor would become very poor.

To overcome this problem, during the project period, we analyzed the activity of heterodimeric plasmonic nanoantenna. These efficient plasmonic nanoantennas will not only have higher intensity enhancement but also an optimum spreading of this strong electric field in their hot-spot regions which will help to polarize the protein molecule completely and in a stronger way. The details about these AuNS based heterodimers are given in the next chapter.

Characterization details of our synthesized AuNS are also given in the following chapter which is helpful to fabricate an efficient and novel plasmonic AuNS based heterodimeric nanogap biosensor.

**IIA.6. Reference:**

[1] Rezaei, N. Cancer Immunology; Springer: New York, NY, USA, 2014.

[2] Prasad, P.N. Introduction to Biophotonics; John Wiley & Sons: Hoboken, NJ, USA, 2003.

[3] Schuller, J.A.; Barnard, E.S.; Cai, W.S.; Jun, Y.C.; White, J.S.; Brongersma, M.L. Plasmonics for Extreme Light Concentration and Manipulation. Nat. Mater. 2010, 9, 193–204.

[4] Willets, K.A.; Van Duyne, R.P. Localized Surface Plasmon Resonance Spectroscopy and Sensing. Annu. Rev. Phys. Chem. 2007, 58, 267–297.

[5] Sreekanth, K.V.; Alapan, Y.; ElKabbash, M.; Ilker, E.; Hinczewski, M.; Gurkan, U.A.; De Luca, A.; Strangi, G. Extreme Sensitivity Biosensing Platform Based on Hyperbolic Metamaterials. Nat. Mater. 2016, 15, 621–627.

[6] Arnold, S.; Khoshsima, M.; Teraoka, I.; Holler, S.; Vollmer, F. Shift of whispering-gallery modes in microspheres by protein adsorption Opt. Lett. 2003, 28 (4), 272-274.

[7] Kelly, K.L.; Coronado, E.; Zhao, L.L.; Schatz, G.C. The Optical Properties of Metal Nanoparticles: The Influence of Size, Shape, and Dielectric Environment. J. Phys. Chem. B 2003, 107, 668–677.

[8] Scholl, J.A.; Koh, A.L.; Dionne, J.A. Quantum Plasmon Resonances of Individual Metallic Nanoparticles. Nature 2012, 483, 421–427.

[9] Baniukevic, J.; Hakki Boyaci, I.; Goktug Bozkurt, A.; Tamer, U.; Ramanavicius, A.; Ramanaviciene, A. Magnetic gold nanoparticles in SERS-based sandwich immunoassay for antigen detection by well oriented antibodies. Biosensors and Bioelectronics 2013, 43, 281–288.

[10] M. Du; G.H. Tang, Plasmonic nanofluids based on gold nanorods / nanoellipsoids / nanosheets for solar energy harvesting. Solar Energy 2016, 137, 393–400.

[11] Nelayah, J.; Kociak, M.; Stephan, O.; Garcia de Abajo, F.J.; Tence, M.; Henrard, L.; Taverna, D.; Pastoriza-Santos, I.; Liz-Marzan, L.M.; Colliex, C. Mapping Surface Plasmons on a Single Metallic Nanoparticle. Nat. Phys. 2007, 3, 348–353.

[12] Rycenga, M.; Xia, X.; Moran, C.H.; Zhou, F.; Qin, D.; Li, Z.-Y.; Xia, Y. Generation of Hot Spots with Silver Nanocubes for Single-Molecule Detection by Surface-Enhanced Raman Scattering. Angew. Chem. Int. Ed. 2011, 50, 5473–5477.

[13] Sun, Y.G.; Xia, Y.N. Shape-Controlled Synthesis of Gold and Silver Nanoparticles. Science 2002, 298, 2176–2179.

[14] Chen, H.J.; Shao, L.; Li, Q.; Wang, J.F. Gold Nanorods and Their Plasmonic Properties. Chem. Soc. Rev. 2013, 42, 2679–2724.

[15] Lee, S.J.; Moskovits, M. Remote Sensing by Plasmonic Transport. J. Am. Chem. Soc. 2012, 134, 11384–11387.

[16] Rodríguez-Lorenzo, L.; Alvarez-Puebla, R.A.; Pastoriza-Santos, I.; Mazzucco, S.; Stéphan, O.; Kociak, M.; Liz-Marzán, L.M.; García de Abajo, F.J. Zeptomol Detection through Controlled Ultrasensitive Surface-Enhanced Raman Scattering. J. Am. Chem. Soc. 2009, 131, 4616–4618.

[17] Liao, H.-G.; Jiang, Y.-X.; Zhou, Z.-Y.; Chen, S.-P.; Sun, S.-G. Shape-Controlled Synthesis of Gold Nanoparticles in Deep Eutectic Solvents for Studies of Structure-Functionality Relationships in Electrocatalysis. Angew. Chem. Int. Ed. 2008, 47, 9100–9103.

[18] Wu, H.-L.; Chen, C.-H.; Huang, M.H. Seed-Mediated Synthesis of Branched Gold Nanocrystals Derived from the Side Growth of Pentagonal Bipyramids and the Formation of Gold Nanostars. Chem. Mater. 2008, 21, 110–114.

[19] Liu, X.-L.;Wang, J.-H.; Liang, S.; Yang, D.-J.; Nan, F.; Ding, S.-J.; Zhou, L.; Hao, Z.-H.;Wang, Q.-Q. Tuning Plasmon Resonance of Gold Nanostars for Enhancements of Nonlinear Optical Response and Raman Scattering. J. Phys. Chem. C 2014, 118, 9659–9664.

[20] Zhang, J.; Gao, Y.; Alvarez-Puebla, R.A.; Buriak, J.M.; Fenniri, H. Synthesis and SERS Properties of Nanocrystalline Gold Octahedra Generated from Thermal Decomposition of HAuCl4 in Block Copolymers. Adv. Mater. 2006, 18, 3233–3237.

[21] Li, C.R.; Lu, N.P.; Mei, J.; Dong, W.J.; Zheng, Y.Y.; Gao, L.; Tsukamoto, K.; Cao, Z.X. Polyhedral to Nearly Spherical Morphology Transformation of Silver Microcrystals Grown from Vapor Phase. J. Cryst. Growth 2011, 314, 324–330.

[22] Sarid, D.; Challener,W. Modern Introduction to Surface Plasmons: Theory, Mathematica Modeling, and Applications; Cambridge University Press: Cambridge, UK, 2010.

[23] Giannini, V.; Rodríguez-Oliveros, R.; Sánchez-Gil, J.A. Surface Plasmon Resonances of Metallic Nanostars/Nanoflowers for Surface-Enhanced Raman Scattering. Plasmonics 2010, 5, 99–104.

[24] Alvarez-Puebla, R.; Liz-Marzan, L.M.; García de Abajo, F.J. Light Concentration at the Nanometer Scale. J. Phys. Chem. Lett. 2010, 1, 2428–2434.

[25] Etchegoin, P.G.; Le Ru, E.C. Surface Enhanced Raman Spectroscopy: Analytical, Biophysical and Life Science Applications. Chapter I—"Basic Electromagnetic Theory of SERS"; WILEY-VCH Verlag GmbH & Co. KGaA: Weinheim, Germany, 2010.

[26] S. Chatterjee, M. Tech. Thesis, 2015, IIT patna.

[27] Bohren, C.F.; Huffman, D.R. Adsorption and Scattering of Light by Small Particles; Wiley-VCH: New York, NY, USA, 1983.

[28] Jackson, J.D. Classical Electrodynamics; Wiley: New York, NY, USA, 1999.

[29] Maier, S.A.; Atwater, H.A. Plasmonics: Localization and Guiding of Electromagnetic Energy in Metal/Dielectric Structures. J. Appl. Phys. 2005, 98, 0111011.

[30] Wang, H. Brandl, D.W.; Le, F.; Nordlander, P.; Halas, N.J. Nanorice: A Hybrid Plasmonic Nanostructure. Nano Lett. 2006, 6, 827–832.

[31] Liaw, J.W.; Kuo, M.K.; Liao, C.N. Plasmon Resonances of Spherical and Ellipsoidal Nanoparticles. J. Electromagn. Waves Appl. 2005, 19, 1787–1794.

[32] Mohamed, M.B.; Volkov, V.; Link, S.; El-Sayed, M.A. The 'Lightning' Gold Nanorods: Fluorescence Enhancement of over a Million Compared to the Gold Metal. Chem. Phys. Lett. 2000, 317, 517–523.

[33] Colleen, L.N.; Liao, H.; Hafner, J.H. Optical Properties of Star-Shaped Gold Nanoparticles. Nano Lett. 2006, 6, 683–688.

[34] Kumar, P.S.; Pastoriza-Santos, I.; Rodriguez-Gonzalez, B.; García de Abajo, F.J.; Javier, F.; Liz-Marzan, L.M. High-Yield Synthesis and Optical Response of Gold Nanostars. Nanotechnology 2008, 19 (1), 0156061- 0156066.

[35] Chen, Q.; Kaneko, T.; Hatakeyama, R. Green Tea Induced Gold Nanostar Synthesis Mediated by Ag(I) Ions Condens. Mater. 2014, 1585, 1401–1417.

[36] Moukarzel,W.; Fitremann, J.; Marty, J.D. Seed-Less Amino-Sugar Mediated Synthesis of Gold Nanostars. Nanoscale 2011, 3, 3285–3290.

[37] Yuan, H.; Khoury, C.G.; Hwang, H.; Wilson, C.M.; Grant, G.A.; Vo-Dinh, T. Gold Nanostars: Surfactant-Free Synthesis, 3D Modelling, and Two-Photon Photoluminescence Imaging. Nanotechnology 2012, 23, 075102 – 075117.

[38] Kedia, A.; Kumar, P.S. Controlled Reshaping and Plasmon Tuning Mechanism of Gold Nanostars. J. Mater. Chem. C 2013, 1, 4540–4549.

[39] Minati, L.; Benetti, F.; Chiappini, A.; Speranza, G. One-Step Synthesis of Star-Shaped Gold Nanoparticles. Physicochem. Eng. Asp. 2014, 441, 623–628.

[40] Chatterjee, S.; Ringane, A.B.; Arya, A.; Das, G.M.; Dantham, V.R.; Laha, R.; Hussain, S. A High-Yield, One-Step Synthesis of Surfactant-Free Gold Nanostars and Numerical Study for Single Molecule SERS Application. J. Nanopart. Res. 2016, 18, 242–249.

[41] Morla-Folch, J.; Guerrini, L.; Pazos-Perez, N.; Arenal, R.; Alvarez-Puebla, R.A. Synthesis and Optical Properties of Homogeneous Nanoshurikens. ACS Photonics 2014, 1, 1237–1244.

[42] Comsol Multiphysics Structural Mechanics—User's Guide, Comsol, 2012, Version: 4.3.

[43] T. Schumacher, M. Brandstetter, D. Wolf, K. Kratzer, M. Hentschel, H. Giessen and M. Lippitz, Appl. Phys. B: Lasers Opt., 2016, 122, 1–11.

[44] L. Wang, T. Sagaguchi, T. Okuhata, M. Tsuboi and N. Tamai, ACS Nano, 2017, 11, 1180–1188.

[45] Johnson, P.B.; Christy, R.W. Optical Constants of the Noble Metals. Phys. Rev. B **1972**, 6, 4370–4379.

[46] Dantham, V.R.; Holler, S.; Barbre, C.; Keng, D.; Kolchenko, V.; Arnold, S. Label-Free Detection of Single Protein using a Nanoplasmonic-Photonic Hybrid Microcavity. Nano Lett. 2013, 13, 3347–3351.

[47] Ament, I.; Prasad, J.; Henkel, A.; Schmachtel, S.; Sönnichsen, C. Single Unlabeled Protein Detection on Individual Plasmonic Nanoparticles. Nano Lett. **2012**, 12, 1092–1095.

[48] Chatterjee, S.; Ricciardi, L.; Deitz, J. I.; Williams, R. E. A.; McComb, D. W.; Strangi, G. Heterodimeric Plasmonic Nanogaps for Biosensing. Micromachines 2018, 9, 664.

# Chapter IIB

# Heterodimeric nanoplasmonic gap for sensing

## IIB.1. Design of the nanogap between a gold nanostar antenna and a gold nanosphere:

**Introduction:** In this chapter study of heterodimeric plasmonic nanogaps created between gold nanostar (AuNS) tips and gold nanosphere is reported. As already told in the previous chapter that for a plasmonic biosensor not only the electric field intensity enhancement by a nanoantenna is important for real-time label-free detection of the protein molecule but also the electric field distribution is very important. A wide distribution of electric field which mean a comparatively week localization in the hot-spot area is not good for plasmonic biosensing as the intensity enhancement is lower there resulting in the lower sensitivity or the lower S/N ratio (according to equation 1.2). While very much localized electric field originating in the hot-spots areas of spiky nanoantennas (like our synthesized AuNS) of spikes with high curvature area sometimes fail to penetrate the adjacent analyte completely, depending on the size of the analyte resulting again difficulty in protein detection. The possible solution is to choose a plasmonic antenna with high intensity enhancement efficiency which contains also an optimum distribution of the electric field in its hot-spot area. Heterodimers based on the synthesized AuNS can solve this purpose as AuNS will be able to hike the incident electric field which will be further increased by the presence of the other nanoantenna. Moreover, for the interaction of both the nanoantennas this stronger electric field will be distributed over a larger area than the case for only the AuNS plasmonic antenna which will be better for the complete interaction with any nearby analyte. As the first step to construct a heterodimer based on the AuNS, gold nanosphere was chosen for its simplicity, capability to spread its hot-spot area and its spherical symmetry. To construct the heterodimer the selective binding is realized by properly functionalizing the two nanostructures – AuNS tip and the gold nanosphere; in particular, the hot electrons injected at the nanostar tips trigger a regio-specific chemical link with the functionalized nanospheres. The AuNSs synthesized via our simple, one-step, surfactant-free, high-yield wet-chemistry method (discussed in previous chapter IIA) is used for this purpose. The high aspect ratio of the sharp nanostar tip collects and concentrates intense electromagnetic fields in ultrasmall surfaces with small curvature radius. The extremities of these surface tips become plasmonic hot spots, allowing significant intensity enhancement of local fields and hot-electron

injection. The presence of gold nanosphere helps to increase the field enhancement further and modifies also the electric field-lines arrangement in the hot-spot area. Electron energy-loss spectroscopy (EELS) was performed to spatially map local plasmonic modes of the nanostar. The presence of different kinds of modes at different position of these nanostars makes them one of the most efficient, unique, and smart plasmonic antennas. These modes are harnessed to mediate the formation of heterodimers (nanostar-nanosphere) through hot-electron-induced chemical modification of the tip. For an AuNS-nanosphere heterodimeric gap, the intensity enhancement factor in the hot-spot region was determined to be $10^6$, which is an order of magnitude greater than the single nanostar tip and further improvement is possible by considering different radius of the nanosphere antenna and the gap between them. The intense local electric field within the nanogap results in ultra-high sensitivity for the presence of bioanalytes captured in that region. In case of a single BSA molecule (66.5 KDa), the sensitivity was evaluated to be about 1940 nm/RIU for a single AuNS, but was 5800 nm/RIU for the AuNS-nanosphere heterodimer. This indicates that this heterodimeric nanostructure can be used as an ultrasensitive plasmonic biosensor to detect single protein molecules or nucleic acid fragments of lower molecular weight with high specificity in real-time.

**Design details of AuNS-nanosphere heterodimers:**

For fabricating the AuNS-nanosphere heterodimer, at first the two basic components – AuNS plasmonic antennas and the gold nanosphere antennas are synthesized via our simple, one-step, surfactant-free low-cost and high yield weight chemistry method as described in the previous chapter (chapter IIA) which are stable in the aqueous solution for more than 5 months [1]. Then optical and electron spectroscopy characterization of these highly stable AuNS particles has been done. The optical characterization provides information regarding the collective behaviour of the nanostars present in the aqueous solution, whereas electron energy-loss spectroscopy (EELS) investigations performed in the scanning transmission electron microscope (STEM) allows for high-resolution spatial determination of the local plasmonic response such as the tip, the core of the nanostar, and different portions of the spike. EELS reveal the presence of different kinds of modes in these AuNSs, which makes them unique and more efficient than the existing nanoantennas. On the other hand gold nanosphere is spherically symmetric and very well known and it has only one kind of plasmonic mode unlike the gold nanostar with different modes in different regions of AuNS. Based on this information, heterodimeric nanogaps can be created at any region of the

nanostars by merely choosing the specific mode of that region. For this synthesized AuNS antenna here not only the presence of the well-known dipolar plasmonic edge mode arising out of the oscillations of localized surface plasmon is seen but also the presence of breathing modes that originate from the confinement of surface plasmons by the geometrical boundaries of a nanoparticle have been observed. These acoustic breathing modes are very efficient for any kind of near field coupling because of their higher optical mode density and are thus important for the desired sensing experiments [2]. Previously, several groups have reported EELS measurements on various nanoantennas including nanostars, but none of them reported about the breathing modes of the nanostars [3-16]. The exciting details about the existence of both these plasmonic edge and acoustic breathing modes in AuNS will be discussed in the following chapter but here for this chapter the information about the different modes at different regions of AuNS will be discussed as it is crucial for the fabrication of AuNS based heterodimers. In the following section EELS studies and the relevant numerical investigations are discussed which have provided key information for designing controlled heterodimeric nanogaps by using a regio-selective surface chemistry method mediated by hot electrons, which was introduced by Cortés, E. et al. [17] Theoretical investigations confirms both the collective as well the individual AuNS behaviour in aqueous solution. Moreover, the maximum intensity enhancement and the sensitivity comparison of the single AuNS and the hybrid AuNS-nanosphere system reveal the usefulness of the heterodimeric system.

**Experimental Section:**

**Characterization of AuNS:** UV-Vis-NIR spectroscopy (Agilent, Cary, NC, USA) and transmission electron microscopy TEM (FEI, Hillsboro, OR, USA) were applied to characterize the synthesized nanoparticles to have specific information about AuNS useful for fabricating AuNS based heterodimers.

**UV-Vis-NIR Spectra:** A Perkin Elmer Lambda 900 spectrophotometer (Perkin Elmer, Shelton, CT, USA) was used to obtain the UV-Vis-NIR spectra of the synthesized gold nanostars solution, which describes the extinction property of this nanostar solution in a wavelength range of 400–1300 nm.

**High-Resolution STEM, EDS, and EELS Measurements:** Scanning transmission electron microscopy (STEM, FEI Thermo Fisher Scientifics, Hillsboro, OR, USA) (monochromated, aberration-corrected FEI Titan3 G2 STEM) was used to probe the size and shape of the synthesized gold nanoparticles. Low-loss Electron Energy Loss Spectroscopy (EELS) was

employed to elucidate the electronic structure of the synthesized gold nanoparticles, while X-ray energy dispersive spectroscopy (XEDS or EDS) was used to determine the weight percentage of the gold present in the solution. Samples were prepared by depositing aqueous suspension containing the synthesized gold nanoparticles on a standard holey carbon film supported by a TEM grid which was left drying in air one day before the STEM measurements. All work was performed at 60 kV with a high collection angle (approximately 25 mrad) to minimize Cherenkov radiation in the EELS signal [18]. The convergence angle was 13.2 mrad, and the probe size was approximately 1.3 angstrom. The EELS energy resolution was approximately 150 meV (full width at half-maximum of the zero-loss peak). Spectrum imaging was used to spatially resolve the EELS signal along and across each nano object, and all EELS data were processed using the Gatan Digital Micrograph software package. During the EEL spectra acquisition, there was no evidence of irradiation damage in the AuNS samples. The zero-loss peak for each spectrum was removed using the standard reflected tail method, which reflects the tail on the energy-gain side of the spectrum onto the energy-loss side, typically with a predefined scaling factor, and subtracts it [19-22].

**Experimental results on AuNS and the Fabrication of AuNS-nanosphere heterodimer:**

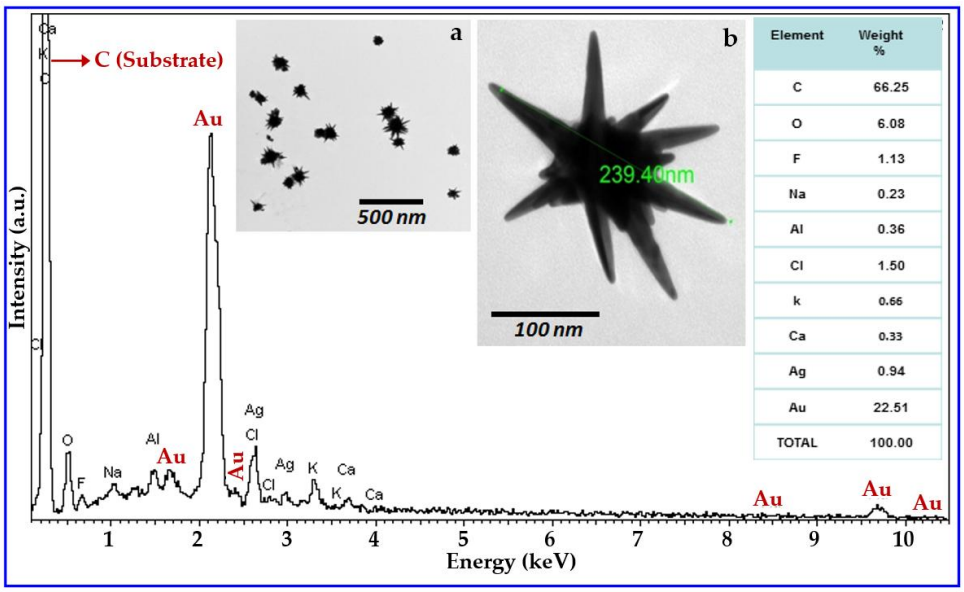


**Figure IIB.1.** X-ray energy dispersive spectroscopy (XEDS) of the synthesized AuNS solution dispersed on a carbon tape. The inset table shows the weight percentages of the elements present in the sample. Inset Figure ‘a’ shows a typical lower magnification TEM image of a collection of Au nanoparticles, showing that the majority of nanostructures have some spiked areas, confirming the relatively high yield of the synthesis method. Inset Figure ‘b’ is a typical higher magnification transmission electron microscopy (TEM) image of the synthesized nanostructure.

Synthesized AuNS were characterized using TEM to see their shape, size, material and the variation in their structure parameter which is needed for the heterodimer fabrication. Figure IIB.1 shows the X-ray energy dispersive spectroscopy (XEDS) of the synthesized AuNS solution. In the spectrum, the most intense peak corresponds to carbon due to the carbon tape substrate used. The peak corresponding to Au is the second most intense peak in the spectrum, and the weight percentage of the gold present in our synthesized gold nanoparticle solution is 22.51%. Panel (a) shows a typical lower magnification TEM image where almost all nanoparticles are found to have at least one spike in their surface confirming the relatively high yield of the synthesis method. Panel (b) shows a randomly selected higher magnification TEM image of a gold nanoparticle.

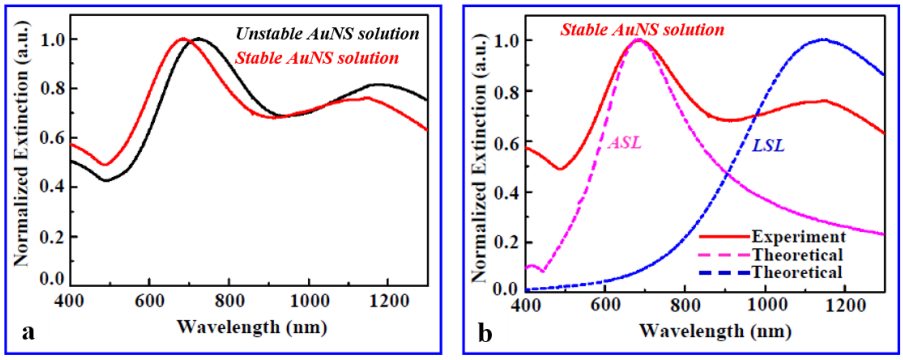


**Figure IIB.2.** (a) The UV-Vis-NIR spectra of the synthesized AuNS solution in both stable and unstable condition. (b) Normalized experimental extinction cross section of stabilized AuNS solution and the relevant theoretical investigation of the extinction property of AuNSs with two different spike lengths. The largest spike length (LSL) and average spike length (ASL) were calculated based on the collected TEM information.

After the above morphological study of the synthesized nanostructures, to have the other crucial information for heterodimer formation, UV-Vis-NIR spectroscopic measurements have been done. Here the information regarding collective modes of the nanoparticles present in the aqueous solution is given. Panel (a) shows two extinction spectra for both the stabilized AuNS solution and the AuNS solution that is not stabilized. Panel (b) shows the difference between the normalized experimental extinction characteristics of the stabilized AuNS solution and the corresponding theoretical investigations. Here, two modes are distinctive in the experimental extinction spectrum. As per the data collected from the TEM images of several AuNSs, the average spike length (ASL) of the nanostars was about 63 nm, taking into account all possible spike lengths from the smallest spike length (SSL) of 33 nm to the largest

spike length (LSL) of 90 nm, and the average diameter of the core was almost 60 nm. Depending on the length of the spike, the tip radius varied from 5 to 1 nm. FEM simulations were performed for two AuNSs with ASL and LSL spike lengths and with the same core diameter of 60 nm to determine their extinction characteristics. The purple and blue curves in panel (b) represent the normalized extinction spectra of the theoretical AuNS with ASL and LSL spike lengths, respectively. By considering the convolution of both theoretical curves, we can conclude that the resultant theoretical extinction characteristics match well with the experimental curve profile and the LSP resonances.

Although experimental and theoretical studies of the extinction properties of the AuNS solution provided relevant information about the ensemble behaviour of AuNSs in aqueous solution, to move towards a controlled construction of hybrid plasmonic nanogaps for sensing, local information regarding the plasmonic field distribution and resonance frequencies is necessary. To use the regio-specific surface chemistry method based on hot electron injection introduced by Cortés et al. [17] for the creation of heterodimeric nanogaps between AuNSs and Au nanospheres, STEM-EELS investigations of the nanostructure were performed to gain precise information about single AuNS plasmonic modes. Figure IIB.3 illustrates the EELS analysis of the synthesized AuNS.

Here panel (a) shows a STEM-HAADF image of the AuNS that was used for EELS analysis. The boxes on the image indicate the regions from which the EELS spectrum images were acquired. Here in panel (b), (c), (d) are the different spectrum images of the core of the nanostar (the black box in panel (a)) and the different regions of the spike of the nanostar antenna are shown. In the core region of the AuNS 3 different position (A, B, C) have been chosen and for all those 3 position the energy-loss spectrum exhibits one major peak at 2.2 eV (~564 nm). From the STEM images it has been seen that the size of the AuNS core is almost 60 nm in all the cases. To verify the fact that 2.2 eV mode is originating only from the contribution of the core LSPR mode of the AuNS, numerical investigation based on FEM has seen done. The result of these FEM based Comsol simulation is given in figure IIB.4. Here, numerical investigation on the extinction property of the Au nanosphere with a 60 nm diameter shows LSPR at 550 nm suggesting that the 2.2 eV mode is associated with the LSPR at the core of AuNS. During this FEM study, the surrounding media was taken as the water media, the incident light polarization was taken along z axis (parallel to the semi-major axis of the spike) and propagation direction along +y axis. In this study the wavelength dependent permittivity of gold is taken from the Johnson and Christy measurements [26].

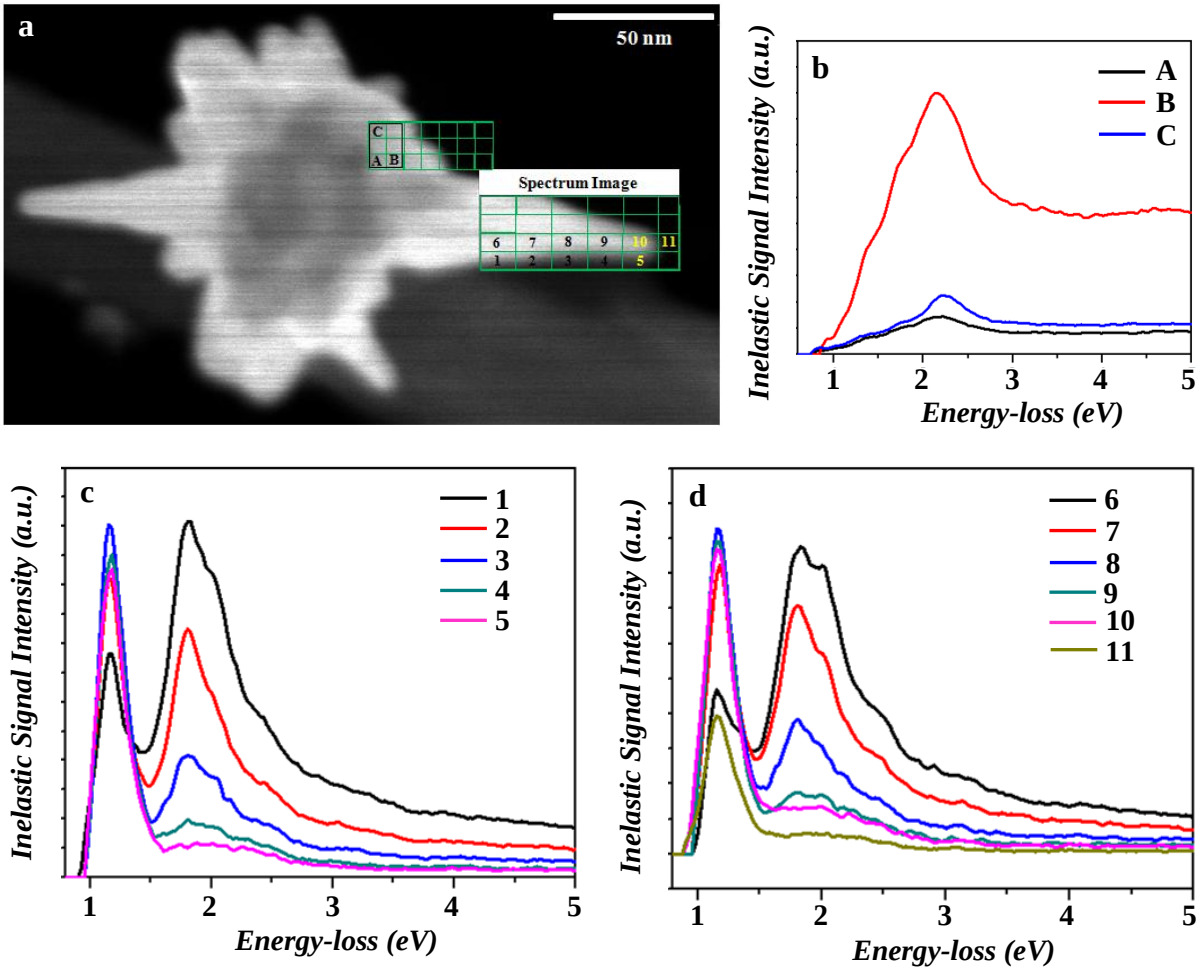


Figure IIB.3. Electron energy loss spectroscopy (EELS) characterization of the AuNS: (a) AuNS image with relative areas of investigation; (b) EELS spectra of core of the AuNS; (c) and (d) EELS spectra of different regions of the spike of the AuNS.

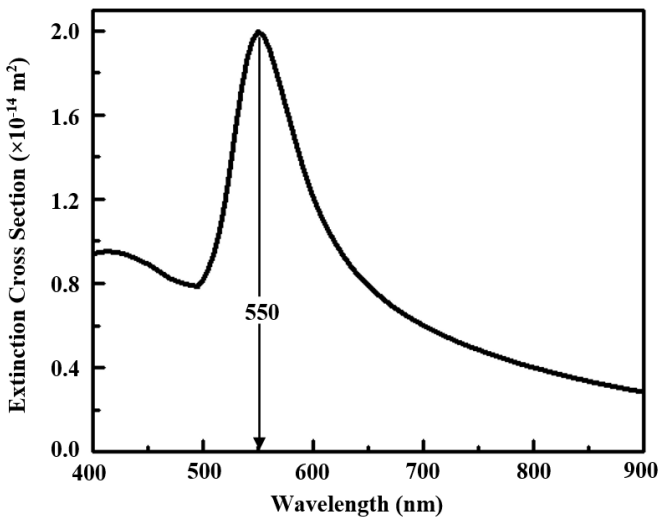


**Figure IIB.4.** FEM analysis on light interaction of single Au nanosphere of size 60 nm immersed in water is shown here. The LSPR of 60 nm Au nanosphere is seen to occur at 550 nm.

After the analysis of the core region of AuNS the spikes of the nanostructures have been examined. The energy-loss spectra from different regions of the AuNS spike have been shown in figure IIB.3(c) and IIB.3 (d). For these regions, the energy-loss spectra along with the AuNS core mode (2.2 eV) exhibit two major peaks at 1.2 eV (~1033 nm) and 1.8 eV (~689 nm). Here it can be seen that the 1.2 eV mode shows a maximum intensity at a position approximately halfway along the length of the spike, although the presence of the 1.8 eV mode cannot be ignored at that location. At the pinnacle of this AuNS spike of length 88 nm (the 5th, 10th, and 11th region of the AuNS spike), the major plasmonic resonance is at 1.2 eV and the presence of 2.2 eV mode (AuNS core mode) can also be seen here. On the other hand, the 1.8 eV mode exhibits maximum intensity at a location closer to the core of the nanostar. FEM investigation is carried out to see the LSPR of this AuNS and it has been shown in the following figure IIB.5.

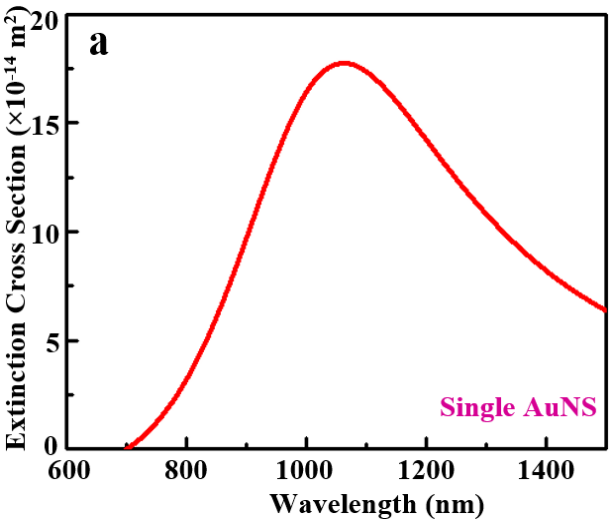


Figure IIB.5. (a) Extinction property of single AuNS is shown here.

FEM investigation on the extinction properties for this AuNS with 88 nm spike length and 60 nm core shows that the LSPR occurs at 1060 nm shown in the above figure. Both the numerical result and the EELS investigation indicate that the mode that is predominating in an AuNS tip region is 1.2 eV, which is crucial information to design regio-specific interactions that allow selected nanostructures to be bound at the tip of the AuNS via the non-localized surface chemistry method. The following figure IIB.6 shows how a regio-specific interaction—driven by hot-electron injection—can promote the formation of a heterodimeric (nanostar-nanosphere) nanostructure for plasmonic biosensing via the method introduced by Cortés et al. [17].

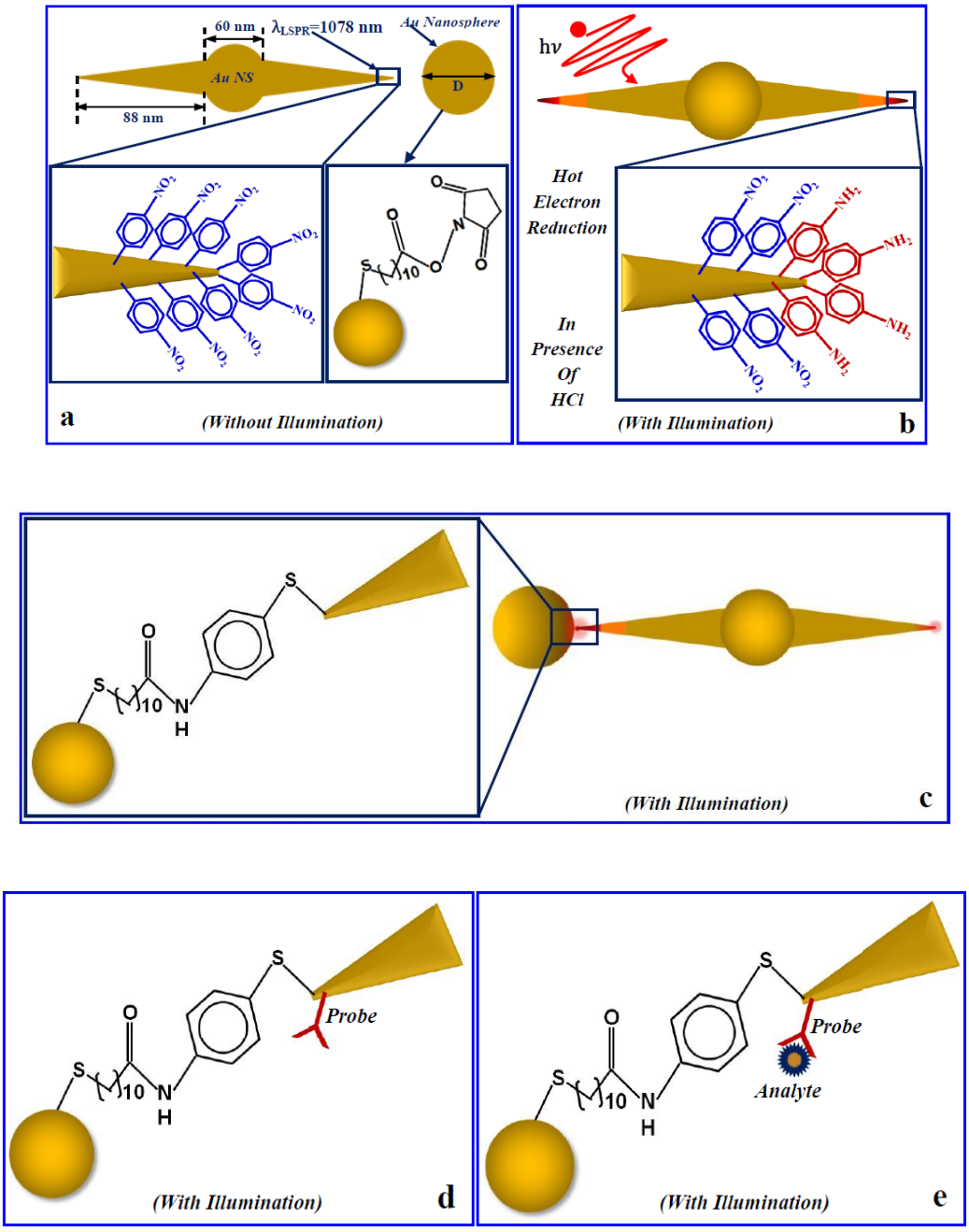


Figure IIB.6. Design of a hybrid AuNS-nanosphere plasmonic antenna via the local surface chemistry modification method. (a) AuNS surface modified by 4-NTP and Au nanosphere coated with 11-mercaptoundecanoic acid (MUA) are shown. (b) Hot electron injection after light illumination on a 4-NTP-coated AuNS antenna at LSPR wavelength (1078 nm) in the presence of HCl; (c) The formation of a hybrid nanoantenna where the Au nanosphere is coupled to the AuNS tip. This happened when the activated and purified Au nanospheres left in contact with the hot-electron-converted AuNS antennas. (d) The hybrid plasmonic antenna converted as a sensor by only attaching a suitable probe to this system. (e) The plasmonic heterodimer sensor in the presence of a bioanalytes.

Here it is worth to mention that instead of AuNS tip, if one wants to choose different region of the AuNS for the binding of the other nanoantenna (here Au nanosphere) to make the hybrid structure, he can just choose a particular excitation frequency, $\nu$ (given in the EELS spectra of different regions in figure IIB.3) and only that area will be active which will be helpful to make those highly selective heterodimeric structures.

After having all the characterization details of AuNS, helpful for making the AuNS-nanosphere hybrid structure and the detailed steps of making this hybrid plasmonic antenna via the local surface chemistry modification method we should also have the idea about the local electric field intensity enhancement by this hetero-dimeric antenna at its hot-spot which is very essential for a good plasmonic biosensor and also the electric field pattern, the important parameter for which we thought this structure would be better than the existing single nanoantennas. To have that knowledge, theoretical study has been done by FEM based Comsol 5.4 software package which is discussed in the next section.

**IIB.2. Numerical simulation on the sensitivity of the nanoplasmonic gap:**

The plasmonic biosensor detection mechanism has already been discussed. According to that for a plasmonic biosensor to have a good sensitivity and S/N ratio one should have higher electric field intensity enhancement at the hot-spot regions of the nanoantenna. That is why to examine how efficient these hybrid structures will be, the intensity enhancement, electric field pattern and the sensitivity has been calculated using comsol and the details about the method and the results are given below.

**Numerical Simulation Method:** Finite Element Method (FEM) simulations are carried out using Comsol 5.4 [23-25] here to study the interaction of a plasmonic biosensor of a single AuNS and a hybrid AuNS-nanosphere with photons to compare their sensitivity. All the data regarding nanostars spikes and their cores are taken from the TEM studies. The nanostructure's surface is discretized with tetrahedral mesh elements with a typical maximum and minimum side lengths of 24.5 and 1.05 nm, respectively. During simulations, the electric field was mapped in the entire space. Photon interaction with single AuNS and AuNS-nanosphere heterodimer with a different nanosphere size and a gap distance were studied. Different cross sections (Scattering, Absorption and Extinction) of those nanoantennas were also examined. During sensitivity calculation, we considered first air ($\varepsilon = 1.0$) and then water ($\varepsilon = 1.7689$) as the homogeneous surrounding media. In all simulations, the wavelength-dependent permittivity of the gold was taken from Johnson and Christy measurements [26].

The wavelength shift in LSPR of the single AuNS and the AuNS-nanosphere heterodimer has been calculated considering a BSA molecule (of 0.11 attogram mass ~ 66.5 kDa) is coupled in the hot spot region of those nanoantennas immersed in water medium. During simulation, a BSA protein molecule was taken as a dielectric particle of cylindrical shape with a permittivity of 2.25, a characteristic height of 3.4 nm and a 6.8 nm short cylinder diameter [27-28].

**Numerical Simulation Results:**

A hybrid plasmonic nanogap constructed by coupling Au nanosphere at the tip of the AuNS via the above-mentioned hot electron mediated method realizes an excellent nanoscale detector for single small protein molecules. This hybrid nanogap can be converted to a sensor by immobilizing a capture molecule (probe) at the nanogap to specifically recognize molecules at a point of care.

Here in the following figure IIB.7 the interaction of a single plasmonic nanogap with light photon has been shown to have the info about its intensity enhancement capability and electric filed pattern which will tell the efficiency of this heterodimeric nanogap as a plasmonic biosensor and also a comparison is done with respect to the single dipole stimulated spiky AuNS plasmonic antenna. Here Panel (a) reports how a single plasmonic nanostar antenna behaves when it interacts with photons. Panel (b) shows how the situation is modified if a BSA molecule is located in close proximity to the tip. Panel (c) is similarly describing the photon interaction of a heterodimer composed of a nanostar with 88 nm spike length, 60 nm core and a 100 nm gold nanosphere separated by a distance of 3.4 nm distance in water. Panel (d) shows the same interaction in presence of a single BSA protein molecule situated in the heterodimeric nanogap. For this investigation, the incident light polarization has been assumed to be along the z-direction (parallel to the spike length or the semi-major axis of the AuNS spike), whereas the propagation direction has been assumed to be the +y-direction.

In this case, the local field of the nanogap behaved like a single AuNS tip in the presence of the bio-nanoparticle. The energy of the hybrid mode of the heterodimeric nanogap reduces in presence of a foreign molecule. This reduction in the energy of the hybrid mode was realized from its shift in the transmission spectrum and thus can be used for molecular detection. Here, because of the high electric field enhancement at the binding site (nanogap) and the optimum distribution of the field, the gap mode shift for a single (or a few) molecule

of lower molecular weight (such as the BSA protein molecule with 66.5 kDa) is detectable (numerical investigation supports this claim). This detection could be even more specific by attaching a probe molecule at the gap.

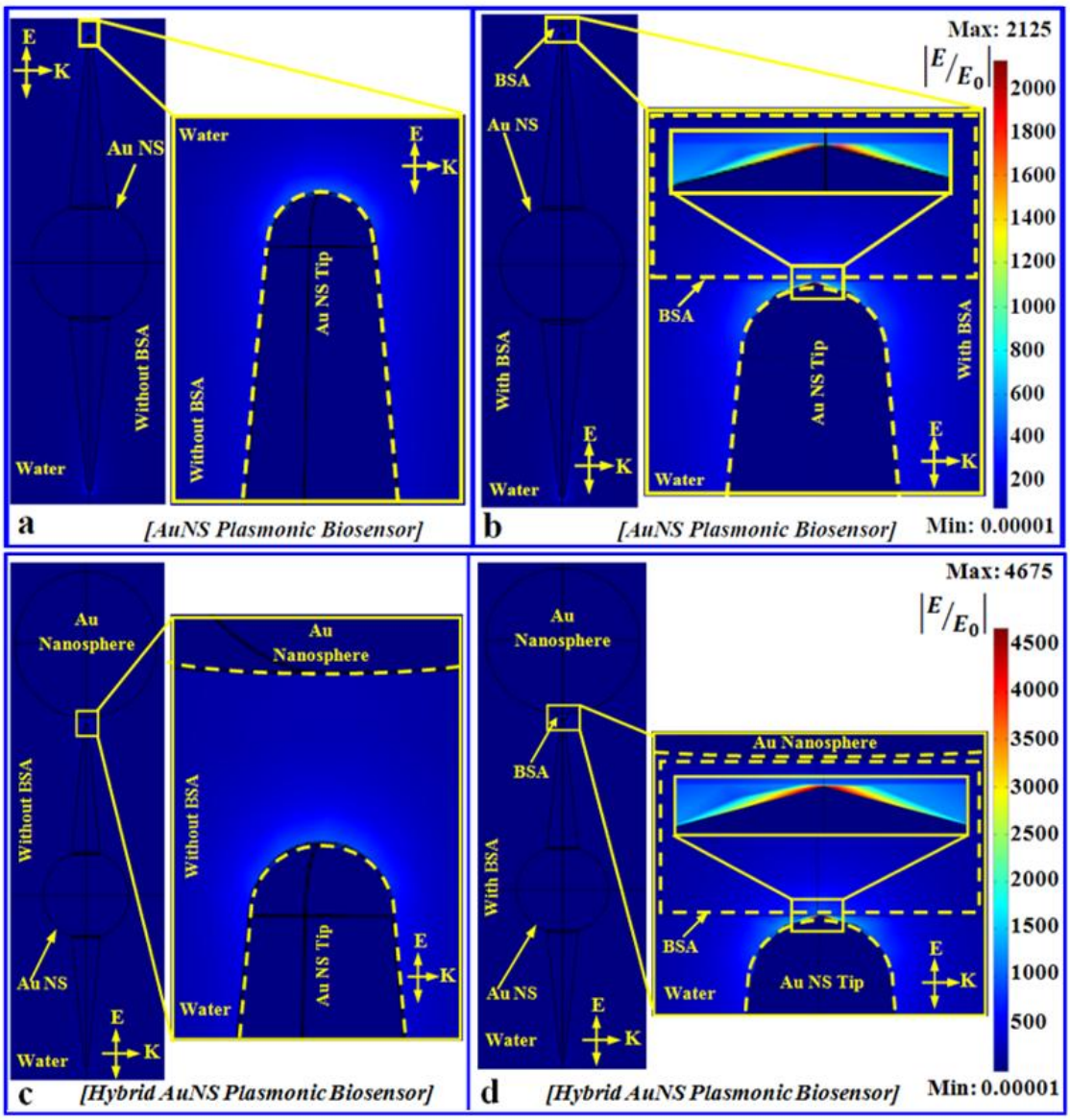


Figure IIB.7. (a) Interaction of single AuNS plasmonic biosensor dispersed in water with incident light in the absence of a BSA molecule. The zoomed portion of the yellow box shows the intensity enhancement at the pinnacle of the spike. (b) Interaction of a single AuNS plasmonic biosensor with incident light in the presence of BSA in water media. (c) Photon interaction of a hybrid plasmonic biosensor developed from a single AuNS and an Au nanosphere in the absence of BSA immersed in water. (d) Interaction of a hybrid plasmonic sensor with incident light in the presence of BSA in water media. Here in all cases, the incident light wave has polarization along the z-axis and propagation along the +y direction. The AuNS has a spike length of 88 nm and a 60 nm core, and the size of the Au nanosphere is 100 nm.

In the above FEM simulation results, the enhancement measurement is given in terms of the quantity $|E/E_0|$. However, the shift in the wavelength due to the adsorption of the protein molecule is proportional to the light intensity ($I/I_0 = |E/E_0|^2$) at the binding site. That is why it is better to interpret the results in terms of the light intensity enhancement. Here the intensity enhancement by a AuNS with 88 nm spike and 60 nm core is approximately $2.5 \times 10^5$ in water. It is worth noticing that the remarkable tenfold increase of the light intensity enhancement in the absence of protein molecules within the heterodimeric gap with respect to a single nanostar spike. Strikingly, for a 3.4 nm heterodimeric gap (100 nm gold nanosphere-88 nm AuNS spike with 60 nm core), the intensity enhancement was found to be $2.3 \times 10^6$ in the absence of a BSA molecule in water. Hence, such a heterodimeric plasmonic sensor can detect a single BSA molecule with higher sensitivity. The electric field pattern is also seen to be more dispersed with more strength for this heterodimer with respect to the single AuNS tip which will be better for complete interaction of the dielectric analyte and the enhanced electric field in the hot-spot area of the antennas. For both the antennas (single AuNS and the AuNS-nanosphere heterodimer) in presence of bioanalytes the field is seen to be more localized almost in the same manner with respect to the absence of protein.

To know the sensitivity of these heterodimers the extinction properties corresponding to a AuNS-nanosphere heterodimer plasmonic biosensor immersed in water in the presence and absence of a BSA molecule is calculated which is shown in the following figure IIB.8. The sensitivity of the heterodimeric nanogap can be easily calculated based on these simulation and can be compared with the single AuNS tip sensitivity based on the FEM simulation results of previous chapter.

For the FEM based Comsol simulation on the extinction property of the AuNS-Au nanosphere shown in figure IIB.8 the diameter of the AuNS core is chosen 60 nm and the spike length is considered to be 88 nm. The diameter of the Au nanosphere is 100 nm and 3.4 nm gap is maintained along the z-axis between these two antennas. The LSPR of that hetero-dimer immersed in water is found to occur at 1250 nm in absence BSA molecule (panel (a)) whereas the LSPR of the structure is found to be at 1265 nm in presence of the single BSA molecule at the hot spot created at the nanogap between the AuNS tip and Au nanosphere (panel (b)). So, according to this theoretical analysis 15 nm wavelength shift is expected for adsorption of single BSA molecule (molecular weight ~ 66.5 kDa) for this AuNS-Au nanosphere hetero-dimer plasmonic biosensor. Hence, such a heterodimeric plasmonic sensor can detect a single BSA molecule with a sensitivity of about 5800 nm/RIU, and its sensitivity

is expected to increase further by decreasing the size of the asymmetric tip-sphere nanogap. As is reported, in the previous chapter the sensitivity of the single AuNS antenna with 88 nm spike and 60 nm core is 1940 nm/RIU for a single BSA protein molecule, we can safely declare that the sensitivity of the heterodimeric nanogap is more with respect to that of the single AuNS.

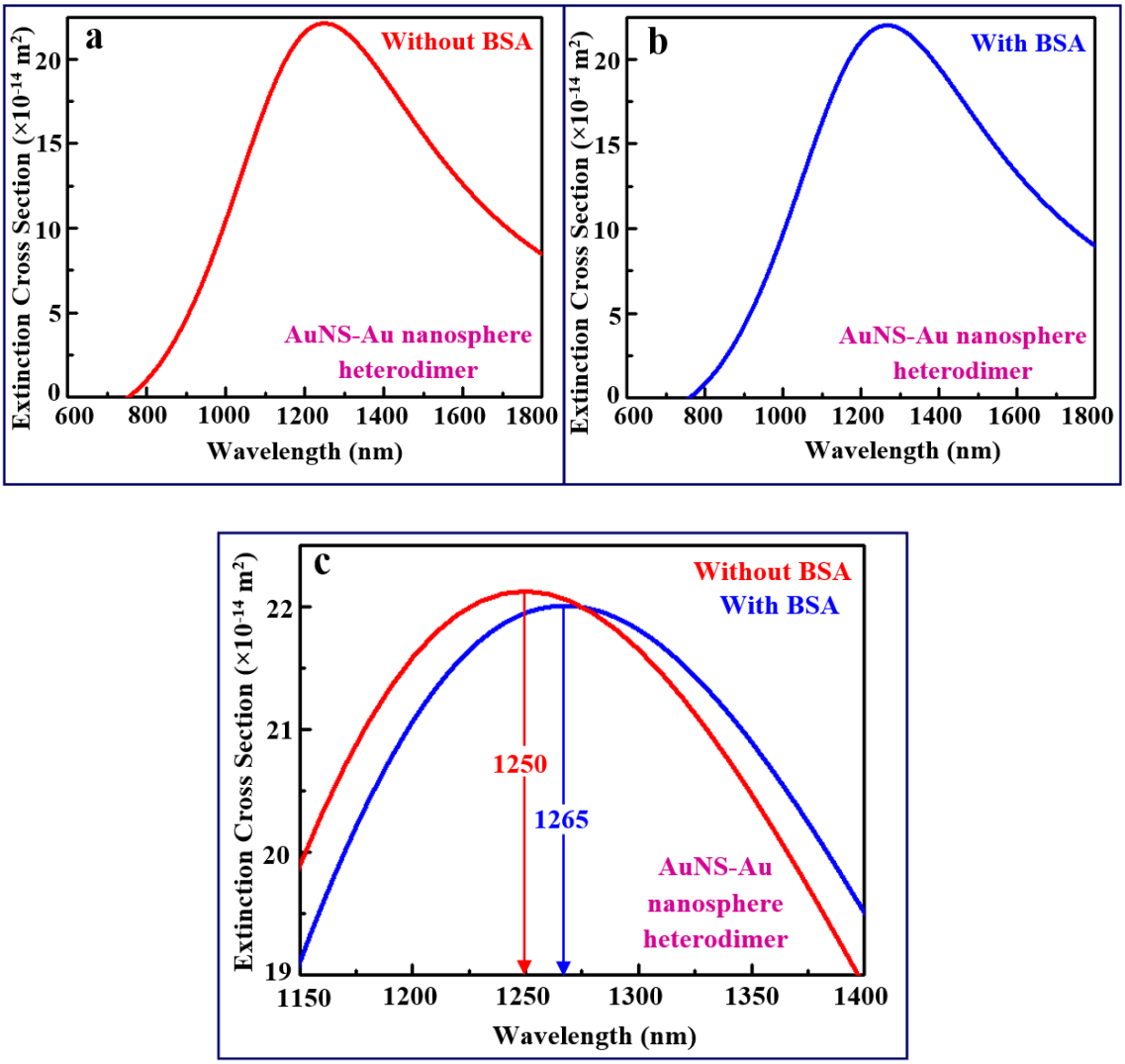


Figure IIB.8. (a) Extinction property of AuNS-Au nanosphere hetero-dimer plasmonic biosensor dispersed in water media in absence of BSA molecule. (b) Extinction property of AuNS-Au nanosphere hetero-dimer plasmonic biosensor in presence of BSA. (c) Comparison between both the situation of heterodimeric plasmonic biosensor, in absence and presence of BSA molecule. Here, according to the theoretical analysis 15 nm shift is predicted for the adsorption of single BSA molecule at the hot spot created at the nanogap between AuNS tip and Au nanosphere.

During the above FEM analysis, the incident light wave has polarization along z axis, propagation along +y direction and the orientation of the 88 nm spikes of the AuNS is taken

along the axis of polarization. In this study the wavelength dependent permittivity of gold is taken from the Johnson and Christy measurements [26] and the specification of the BSA is taken from the reference [27-28].

## IIB.3. Conclusion

To summarize, we reported the study of heterodimeric nanostructures for plasmonic sensing based on the formation of nanogaps between nanostar tips and nanospheres. The stable, highly tunable AuNSs were synthesized here via a simple, one-step, surfactant-free, wet-chemistry method with high yield and characterized via optical and EELS spectroscopic investigations. The formation of the nanogap is controlled and triggered by exploiting the light-induced hot-electron injection at the tip of the nanostars through the localized surface chemistry method. These hybrids and asymmetric plasmonic nanogaps can dramatically confine the incident electromagnetic field at their hot spots, irrespective of the incident light polarization. The numerical investigation supports the experimental results and predicted an ultrahigh sensitivity of this single molecule plasmonic biosensor (>5000 nm/RIU). This result will allow for the fabrication of nanogap sensors with high sensitivity and specificity for proteins and nucleic acids tests, which can find large use in point-of-care diagnostic technologies based on an easy and accurate optical readout.

## IIB.4. References

[1] Chatterjee, S.; Ricciardi, L.; Deitz, J. I.; Williams, R. E. A.; McComb, D. W.; Strangi, G. Heterodimeric Plasmonic Nanogaps for Biosensing. Micromachines 2018, 9, 664.

[2] Krug, M.K.; Reisecker, M.; Hohenau, A.; Ditlbacher, H.; Trugler, A.; Hohenester, U.; Krenn, J.R. Probing Plasmonic Breathing Modes Optically. Appl. Phys. Lett. 2014, 105, 1711031–1711033.

[3] Chu, M.W.; Myroshnychenko, V.; Chen, C.H.; Deng, J.P.; Mou, C.Y.; García de Abajo, F.J. Probing Bright and Dark Surface-Plasmon Modes in Individual and Coupled Noble Metal Nanoparticles Using an Electron Beam. Nano Lett. 2009, 9, 399–404.

[4] Wang, H.; Wu, Y.; Lassiter, B.; Nehl, C.L.; Hafner, J.H.; Nordlander, P.; Halas, N.J. Symmetry Breaking in Individual Plasmonic Nanoparticles. Proc. Natl. Acad. Sci. USA 2006, 103, 10856–10860.

[5] Koh, A.L.; Bao, K.; Khan, I.; Smith, W.E.; Kothleitner, G.; Nordlander, P.; Maier, S.A.; McComb, D.W. Electron Energy-Loss Spectroscopy (EELS) of Surface Plasmons in Single

Silver Nanoparticles and Dimers: Influence of Beam Damage and Mapping of Dark Modes. ACS Nano 2009, 3, 3015–3022.

[6] Morla-Folch, J.; Guerrini, L.; Pazos-Perez, N.; Arenal, R.; Alvarez-Puebla, R.A. Synthesis and Optical Properties of Homogeneous Nanoshurikens. ACS Photonics 2014, 1, 1237–1244.

[7] Wu, Y.; Li, G.; Cherqui, C.; Bigelow, N.W.; Thakkar, N.; Masiello, D.J.; Camden, J.P.; Rack, P.D. Electron Energy Loss Spectroscopy Study of the Full Plasmonic Spectrum of Self-Assembled Au–Ag Alloy Nanoparticles: Unravelling Size, Composition, and Substrate Effects. ACS Photonics 2016, 3, 130–138.

[8] Mazzucco, S.; Stéphan, O.; Colliex, C.; Pastoriza-Santos, I.; Liz-Marzan, L.M.; García de Abajo, F.J.; Kociak, M. Spatially Resolved Measurements of Plasmonic Eigenstates in Complex-Shaped, Asymmetric Nanoparticles: Gold Nanostars. Eur. Phys. J. Appl. Phys. 2011, 54, 335121–335129.

[9] García de Abajo, F.J.; Kociak, M. Probing the Photonic Local Density of States with Electron Energy Loss Spectroscopy. Phys. Rev. Lett. 2008, 100, 1068041–1068044.

[10] Myroshnychenko, V.; Nelayah, J.; Adamo, G.; Geuquet, N.; Rodriguez-Fernandez, J.; Pastoriza-Santos, I.; MacDonald, K.F.; Henrard, L.; Liz-Marzan, L.M.; Zheludev, N.I.; et al. Plasmon Spectroscopy and Imaging of Individual Gold Nanodecahedra: A Combined Optical Microscopy, Cathodoluminescence, and Electron Energy-Loss Spectroscopy Study. Nano Lett. 2012, 12, 4172–4180.

[11] Losquin, A.; Zagonel, L.F.; Myroshnychenko, V.; Rodriguez-Gonzalez, B.; Tencé, M.; Scarabelli, L.; Förstner, J.; Liz-Marzan, L.M.; García de Abajo, F.J.; Stephan, O.; Kociak, M. Unveiling Nanometer Scale Extinction and Scattering Phenomena through Combined Electron Energy Loss Spectroscopy and Cathodoluminescence Measurements. Nano Lett. 2015, 15, 1229–1237.

[12] Myroshnychenko, V.; Rodríguez-Fernández, J.; Pastoriza-Santos, I.; Funston, A.M.; Novo, C.; Mulvaney, P.; Liz-Marzán, L.M.; García de Abajo, F.J. Modelling the Optical Response of Gold Nanoparticles. Chem. Soc. Rev. 2008, 37, 1792–1805.

[13] Novikov, S.M.; Sánchez-Iglesias, A.; Schmidt, M.K.; Chuvilin, A.; Aizpurua, J.; Grzelczak, M.; Liz-Marzán, L.M. Gold Spiky Nanodumbbells: Anisotropy in Gold Nanostars. Part. Part. Syst. Charact. 2014, 31, 77–80.

[14] Koh, A.L.; Fernández-Domínguez, A.I.; McComb, D.W.; Maier, S.A.; Yang, J.K.W. High-Resolution Mapping of Electron-Beam-Excited Plasmon Modes in Lithographically Defined Gold Nanostructures. Nano Lett. 2011, 11, 1323–1330.

[15] Cube, F.V.; Niegemann, J.; Irsen, S.; Bell, D.C.; Linden, S. Angular-Resolved Electron Energy Loss Spectroscopy on a Split-Ring Resonator. Phys. Rev. B 2014, 89, 1154341–1154345.

[16] Nelayah, J.; Kociak, M.; Stephan, O.; Garcia de Abajo, F.J.; Tence, M.; Henrard, L.; Taverna, D.; Pastoriza-Santos, I.; Liz-Marzan, L.M.; Colliex, C. Mapping Surface Plasmons on a Single Metallic Nanoparticle. Nat. Phys. 2007, 3, 348–353.

[17] Cortes, E.; Xie, W.; Cambiasso, J.; Jermyn, A.S.; Sundararaman, R.; Narang, P.; Schlucker, S.; Maier, S.A. Plasmonic Hot Electron Transport Drives Nano-Localized Chemistry. Nat. Commun. 2017, 8, 1–10.

[18] Stoger-Pollach, M. Optical Properties and Bandgaps from Low Loss EELS: Pitfalls and Solutions. Micron 2008, 39, 1092–1110.

[19] Deitz, J.I.; Karki, S.; Marsillac, S.X.; Grassman, T.J.; McComb, D.W. Bandgap Profiling in CIGS Solar Cells via Valence Electron Energy-Loss Spectroscopy. J. Appl. Phys. 2018, 123, 1157031–1157036.

[20] Contreras, M.; Tuttle, J.; Du, D.; Qi, Y.; Swartzlander, A.; Tennant, A.; Noufi, R. Graded Band-Gap Cu(In,Ga)Se2 Thin-Film Solar Cell Absorber with Enhanced Open Circuit Voltage. Appl. Phys. Lett. 1993, 63, 1824–1826.

[21] Williams, D.B.; Carter, C.B. Transmission Electron Microscopy: A Textbook for Materials Science; Springer: New York, NY, USA, 2009.

[22] Digital Micrograph EELS Analysis User’s Guide—EELS Analysis User Guide; Gatan, Inc.: Pleasanton, CA, USA, 2003.

[23] Comsol Multiphysics Structural Mechanics—User's Guide, Comsol, 2012, Version: 4.3.

[24] T. Schumacher, M. Brandstetter, D. Wolf, K. Kratzer, M. Hentschel, H. Giessen and M. Lippitz, Appl. Phys. B: Lasers Opt., 2016, 122, 1–11.

[25] L. Wang, T. Sagaguchi, T. Okuhata, M. Tsuboi and N. Tamai, ACS Nano, 2017, 11, 1180–1188.

[26] Johnson, P.B.; Christy, R.W. Optical Constants of the Noble Metals. Phys. Rev. B 1972, 6, 4370–4379.

[27] Dantham, V.R.; Holler, S.; Barbre, C.; Keng, D.; Kolchenko, V.; Arnold, S. Label-Free Detection of Single Protein using a Nanoplasmonic-Photonic Hybrid Microcavity. Nano Lett. 2013, 13, 3347–3351.

[28] Ament, I.; Prasad, J.; Henkel, A.; Schmachtel, S.; Sönnichsen, C. Single Unlabeled Protein Detection on Individual Plasmonic Nanoparticles. Nano Lett. 2012, 12, 1092–1095.

# Chapter IIC

# Breathing modes of gold nanostars and its usefulness in sensing

## IIC.1. Breathing modes in nanoparticles - A brief discussion:

Label-free detection of protein molecules in their natural state at ultralow concentration is considered as the holy grail of biomedical research [1]. But, because of the acutely small size (<3 nm) of single protein molecules, their detection becomes exceptionally challenging [2]. One method to deal with this problem is to use the well-known localized surface plasmon effect of noble metal nanoparticles (NPs) which has been used for a wide variety of applications [3-7] including sensing [8-10], imaging [11], surface enhanced Raman spectroscopy (SERS) [12-13], quantum technologies and miniaturized photonic circuits [14-15]. Localized surface plasmon resonance (LSPR) of noble metal NPs can be tuned by changing their size, shape, material and the surrounding dielectric matrix [16-17]. NPs with sharp corners like nanotriangles [18], nanocubes [19-20], nanorods [21-22] nanostars [23-26] or octahedral nanoparticles [27-28] are able to confine light in ultrasmall regions tightly because of the lightning rod effect and the plasmonic resonance effect, resulting in higher electromagnetic energy concentration and thus higher electric field intensity at their hot-spots compared to the non-spiky NPs [29–31]. Thus spiky gold nanoparticles are ideal for plasmonic sensing because of their biocompatibility tunability and the large field enhancement at their hotspots. A small change in the surrounding dielectric media after the adsorption of protein molecules at the hot-spots results in a shift of the NP LSPR and thus helps to detect the presence of biomolecules. This opens new opportunities for design of next generation nano-devices for sensing applications.

Surface plasmons confined within the geometrical boundaries of flat nanoparticles give rise to radially symmetric plasmonic breathing modes [32-33]. A flat metal NP not only has edge modes [34] (dipolar, quadrupolar and higher order multipolar modes) because of LSPR, but also supports film modes. Breathing modes are dark modes that cannot be detected by photons as their net dipole moment is zero. However such modes can be detected by inelastic electron scattering in electron energy-loss spectroscopy as the electron wavelength is much smaller than the nanoparticle size [35-36]. The breathing modes are very important for near field coupling effects as they have a very high optical mode density. Several groups have investigated breathing modes of different metal nanostructures such as nanodisk [32, 35, and

37] nanoplates [36], core–shell nanoparticles [38-39], nanotriangles [40], nanowires [41-42] nanosphere-nanodisk trimers [43], metal oligomers [44], and graphene nanoellipses [45] but breathing modes of AuNSs have never been reported before.

AuNSs, because of having several polarization insensitive hot-spots generated after the interaction of light at the tip of the spikes randomly distributed over their core, are more advantageous than the other spiked nanoantennas like nanoellipsoides and nanorods [46-51] which have the ability to concentrate light like nanostars. AuNSs which are well known for their biomedical applications due to their low-toxicity, biocompatibility, high tunability and high electric field intensity enhancement at their hot-spots [46-49] have been synthesized using nano-chemistry strategies, including environmentally sensitive "green" synthesis routes [52-58] and surfactant-free routes. Here, for our study we have synthesized these highly tunable, stable, efficient AuNSs using a low-cost, simple, one-step (seedless), surfactant-free, high-yield wet chemistry method [59].

In this contribution we report experimental evidence of both the plasmonic edge modes and acoustic breathing modes in AuNSs. Results of optical and electron spectroscopy characterization of these highly stable nanoparticles (stability > 5 months in aqueous solution) are reported. Optical characterization provided integrated information regarding the collective behaviour of AuNSs in aqueous suspension while electron energy-loss spectroscopy (EELS), performed using a scanning transmission electron microscope (FEI Titan3 G2 STEM), provided local plasmonic responses of a single AuNS with high spatial resolution. Several groups have investigated plasmonic nanostructures including AuNSs via EELS [60–74] but this high resolution, low-loss EELS investigation of these synthesized AuNSs has shown the presence of regular edge plasmon modes along with radial breathing modes, irrespective of the spike length.

This study is also supported by extensive theoretical investigations. The effect of tip displacement in response to excitation of the breathing modes has been calculated using the structural mechanics model of Comsol 5.4 which is based on the Finite Element Method. The maximum intensity enhancement of a single AuNS antenna has been calculated using the Radio Frequency (RF) module of Comsol 5.4. All these results indicate the possibility of creating a device based on the acousto-plasmonic AuNS antenna which will be useful for two-step clinical diagnostics.

## IIC.2. Experimental and theoretical evidence of edge dipolar modes and non-edge breathing modes in gold nanostar

**Experimental Methods used:**

**Characterization:** The synthesized nanoparticles are characterized using UV-Vis-NIR spectroscopy and scanning transmission electron microscopy.

**UV-Vis-NIR spectroscopy:** The UV-Vis-NIR spectra of the synthesized gold nanostar solution were obtained using a PerkinElmer Lambda 900 spectrophotometer. The extinction properties of the nanostar solution were measured in a wavelength range of 400 nm to 1300 nm.

**STEM and EELS measurements:** To probe the size and shape of the synthesized nanoparticle, a STEM (monochromated, image-corrected FEI Titan3 G2 STEM) was used. The electronic structure of the synthesized AuNSs was investigated with the help of low-loss EELS. Sample preparation was done one day before the STEM measurements by drop casting and then drying the aqueous solution of gold nanoparticles on a standardized holey carbon film supported on a TEM grid. All experiments were performed at 60 kV with a high collection angle (~ 25 mrad) to minimize the influence of Cherenkov radiation on the EELS signal [84]. The convergence angle and the probe size were measured to be approximately 13.2 mrad and 1.3 angstrom, respectively. The EELS energy resolution which is equivalent to the full width at half-maximum of the zero-loss peak was approximately 150 meV. To resolve the EELS signal spatially along and across each nano-object, spectrum imaging was used. All the EELS data were treated using the Gatan Digital Micrograph software package. No evidence of irradiation impairment was observed in the sample during EEL spectra acquisition. The zero-loss peak for each spectrum was removed using the standard reflected tail method which reflects the tail on the energy gain side of the spectrum onto the energy-loss side, typically with a pre-defined scaling factor, and subtracts it [85–88].

**Numerical Simulation Method:** FEM simulations are used here to find a correlation between the experimental data and the predicted properties of extinction (optical module) and acoustic modes (structural mechanics module) of AuNSs. During simulation, data regarding the different sizes and shapes of AuNS spikes and their cores are obtained from the STEM studies. The study is carried out to map the electric field for plasmonic modes and structural modification of the nanoantennas for phononic modes. The relative pressure due to the excitation of the breathing modes of AuNSs was calculated using the structural mechanics

module of COMSOL 5.4 [75-77] where the mode frequency was obtained from the experimental EELS information. The Radio Frequency (RF) module of Comsol 5.4 is used to investigate the plasmonic modes. Scattering, absorption and extinction cross-sections of the AuNS plasmonic antennas are also calculated here. For the optical simulations the definitions in the Comsol material library are used for all the optical and physical properties of the surrounding media. Simulations considering both air ($\varepsilon = 1.0$) and water ($\varepsilon = 1.77$) as the homogeneous surrounding media are performed here. During this numerical investigation, the wavelength dependent permittivity of gold is obtained from the Johnson and Christy measurements [89] and linearly polarized plane waves are used as the excitation source. Electric field polarization of incident light is always chosen along the semi major axis of the AuNS spikes during extinction and electric field mapping. For the simulation of acoustic modes performed in air the material mechanical properties of Au are defined according to the bulk values. Physics controlled free tetrahedral meshes with an extremely fine mesh size for the AuNSs and for surrounding media mesh of normal size have been chosen for all analysis. For the simulation of acoustic modes, performed in air, the material mechanical properties of Au are defined according to the bulk values (Young's modulus = 79 GPa, Poisson's ratio = 0.4, and density = 19300 kg $m^{-3}$). For that simulation the longitudinal speed of sound in gold is taken as 3240 m $s^{-1}$.

**Experimental and Theoretical Results and Discussions:**

For this study Gold nanostars (AuNSs) were synthesized using our own one-step (without seed) surfactant-free wet chemistry method as described in the previous chapter [59]. Here figure IIC.1 (a) shows a typical high magnification TEM image of a synthesized gold nanoparticle while panel (b) shows a low magnification TEM image where almost all the nanoparticles have at least one spike on their surface, confirming the relatively high yield of the synthesis method. The X-ray energy dispersive spectroscopy (XEDS) study of the synthesized AuNSs which confirms the presence of Au in the aqueous nanostars solution and thus the biocompatibility of the synthesized nanoparticle solution is also given in the previous chapter IIB.

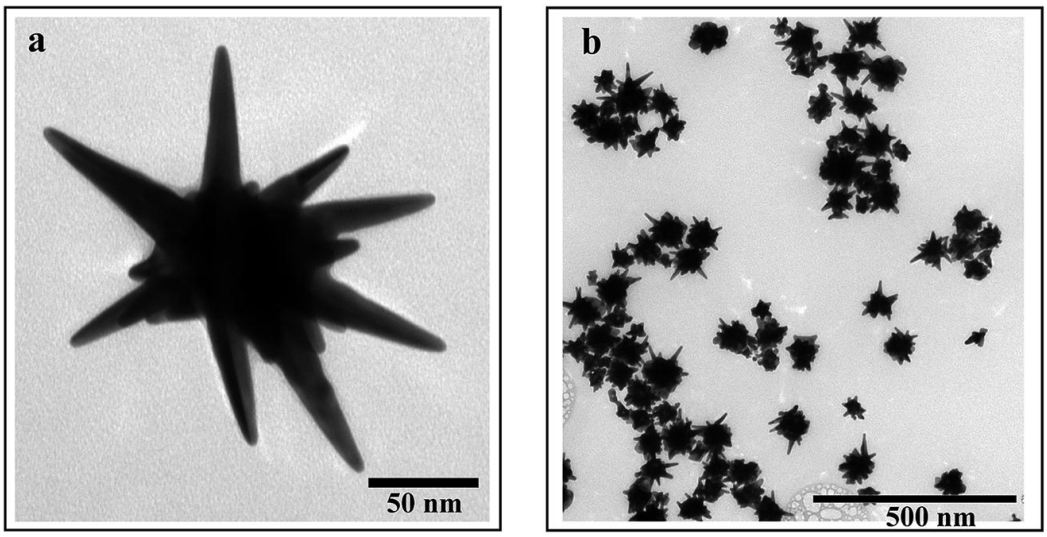


Figure IIC.1. (a) A high magnification TEM image of a randomly selected gold nanoparticle is shown. (b) A low magnification TEM image is shown here which is representative of almost all the nanoparticles observed.

Figure IIC.2 (a) shows a comparative study between the normalized experimental extinction spectra of the stable AuNS solution collected using a PerkinElmer Lambda 900 spectrophotometer and the corresponding theoretical investigations. Notably, in the experimental extinction spectra two major modes can be seen. The histogram for spike lengths of synthesized AuNSs is shown in panel (b). The average spike length (ASL) of the nanostars was measured and averaged from TEM images of nearly 100 AuNS nanoparticles and was found to measure approximately 70 nm while the average diameter of the core measured almost 60 nm. The tip radius of the AuNS spike is varied here from 5 nm to 1 nm depending on the spike length. From the histogram in panel (b) one may observe that the AuNSs with an ASL of approximately 70 nm are dominant in solution. AuNSs with a large spike length (LSL) of nearly 90 nm are the second most dominant type of nanostar in the solution. Panel (c) and (d) are showing the representative of these two kinds of nanostars - AuNS with ASL and AuNS with LSL respectively, observed during the STEM measurements. Therefore, the histogram in panel (b) supports the origin of the two peaks observed in the experimental extinction spectra. Complementarily, Finite Element Method (FEM) simulations were performed using Comsol 5.4 for the AuNSs with an ASL of 70 nm and LSL of 90 nm and the same core diameter (60 nm), permitting determination of extinction characteristics. The red and blue curves, shown in panel (a), represent the theoretically calculated normalized extinction spectra for AuNSs of spike lengths 70 nm and 90 nm respectively, the convolution of which gives the resultant normalized theoretical

extinction spectra of the AuNS solution. From this figure we can conclude that the resultant theoretical extinction characteristics match well with the experimental ones, thus confirming our hypothesis.

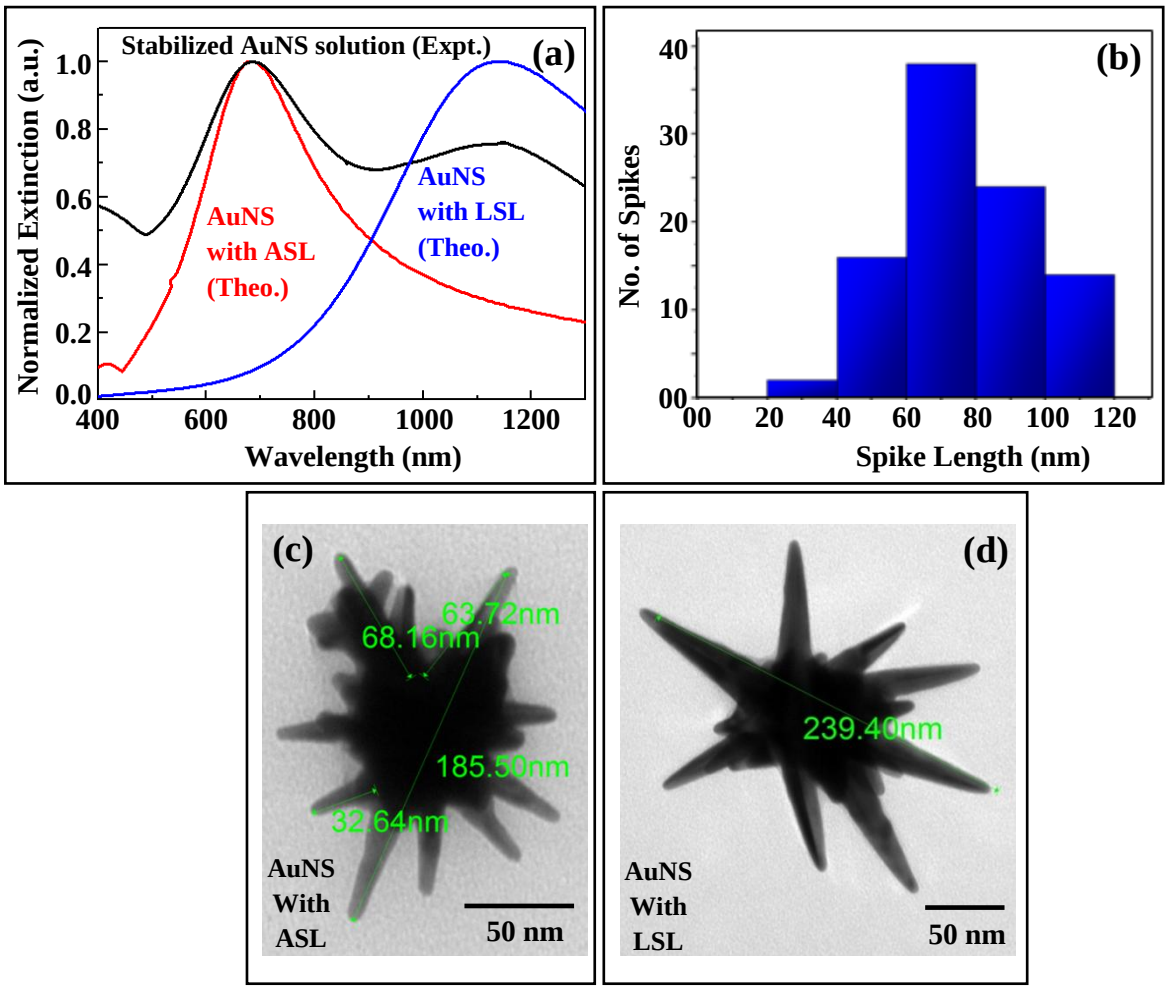


Figure IIC.2. (a) Comparison of the normalized experimental extinction spectrum of the synthesized stabilized AuNS solution and the relevant theoretical investigation conducted on the extinction properties of AuNSs of two different spike lengths. Large spike length (LSL) and average spike length (ASL) are obtained based on the collected TEM information. (b) Histogram of the spike lengths of synthesized AuNSs is shown based on the collected TEM images of nearly 100 NPs. (c) A high magnifications TEM image of a gold nanostar particle with ASL is shown. (d) A high magnification TEM image of a gold nanostar particle with LSL is shown.

Although optical and computational studies of AuNSs dissolved in aqueous solution provided integrated information about the ensemble behaviour of AuNSs, STEM-EELS measurements revealed localized information about the plasmonic field distribution and resonances for different locations across a single nanostructure. Figure IIC.3 illustrates the EELS analysis for synthesized AuNSs with a LSL. EELS experiments allowed mapping of plasmonic edge

modes in AuNSs and also the excitation and observation of optically dark radial breathing modes. The STEM-HAADF (High Angle Annular Dark Field) image of an AuNS with the LSL which was used for EELS analysis is shown in panel (a). The regions from which the EELS spectra were mapped and acquired are indicated by the colored boxes on the STEM image.

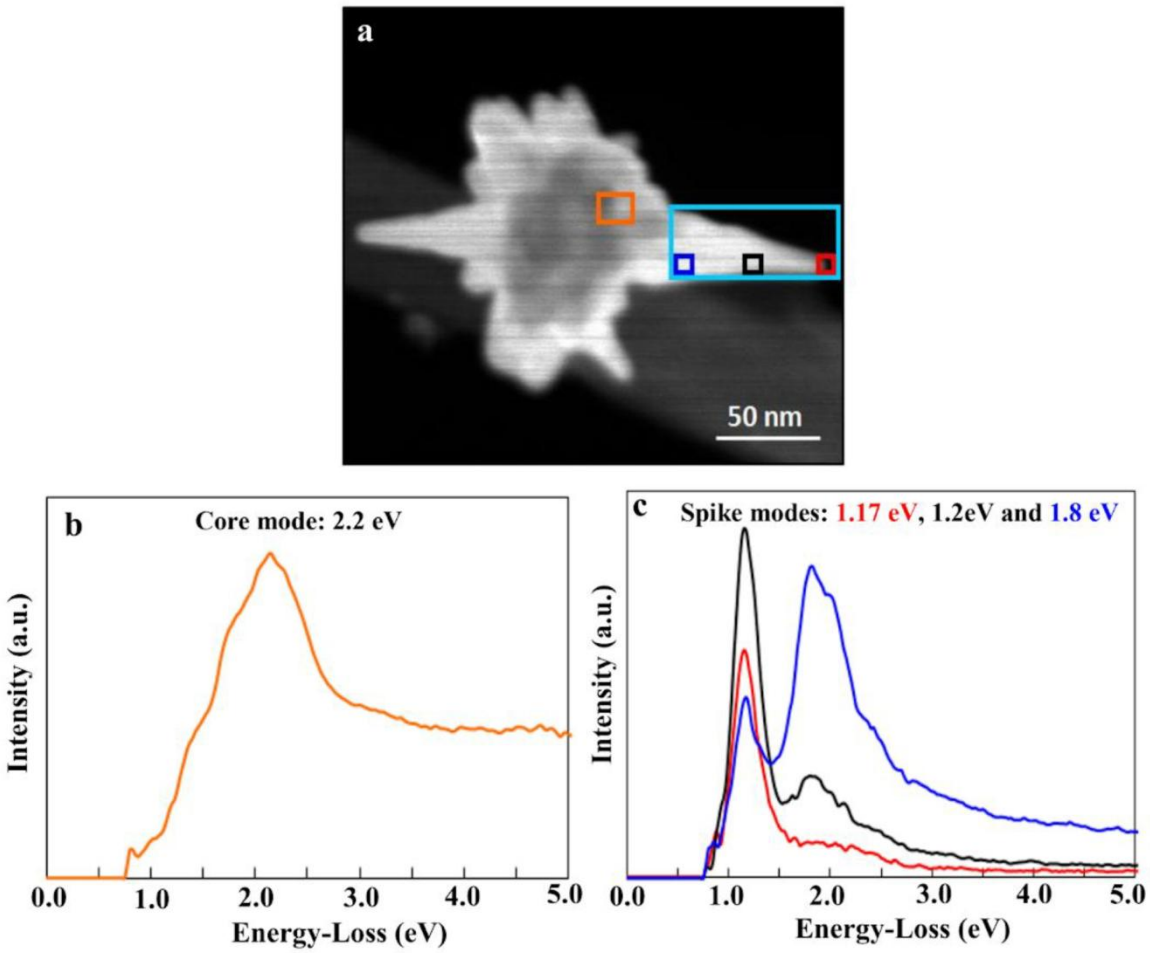


Figure IIC.3. EELS characterization of AuNSs with a LSL: (a) AuNS with relative areas of investigation indicated by different colored boxes. (b) EELS spectrum of the AuNS core. (c) EELS spectra of different regions of the AuNS spike.

Here in the above figure panel (b) and (c) show the EELS spectra taken at the nanostar core and the nanostar spike. Panel (b) shows a peak at 2.2 eV, which corresponds to the core mode of the AuNS as confirmed by the FEM simulation (figure IIC.4. (a) ), which shows LSPR at 550 nm (2.2 eV) for a gold core of 60 nm. The strongest mode observed, at the pinnacle of the AuNS spike, was 1.17 eV, corresponding with one extinction peak from the UV-Vis-NIR spectra. FEM simulations carried out on similar types of AuNSs, having an 88 nm spike

length and 60 nm core, indicate that the LSPR is expected to occur at 1060 nm (1.17 eV) and thereby confirm the dipolar (bright) edge mode nature at the pinnacle (figure IIC.4. (b) ).

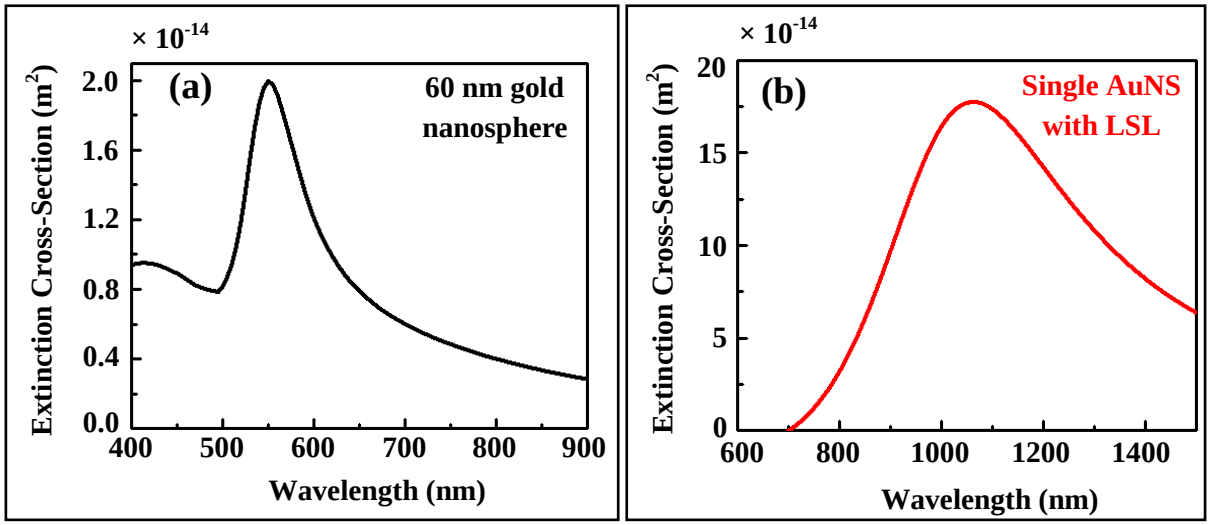


Figure IIC.4. (a) Extinction cross-section of 60 nm Au nanosphere is shown. The theoretical LSPR is seen to occur here at 550 nm. (b) Extinction property of single LSL AuNS where the LSPR is at 1060 nm.

The EELS intensity maps for 1.2 eV and 1.8 eV mode, shown in figure IIC.5 (b) and (c), confirm their non-plasmonic non-edge nature observed at the spike of this AuNS.

During STEM-EELS mapping, a 1.2 eV mode (figure IIC.5 (b)) was excited and observed in the central region of the spike. This mode shows a very different spatial and intensity distribution with respect to the edge mode. In addition, further away from the pinnacle, a similarly structured mode was observed at 1.8 eV. The comparison of the optical and EELS spectra of several nanostar spikes (with small and large spike lengths) shows that the modes in the body of the spike are dark modes, since they cannot be excited by light and they are not observed in the optical spectra. To further confirm their non-plasmonic edge mode character a computational study was performed using FEM based Comsol 5.4 by analysing the mode shape at each mode frequency. Comsol simulations confirmed that the 1.2 eV mode possesses all the features of a radial breathing mode (figure IIC.7) and it does not present the characteristic spatial distribution of plasmonic edge modes (dipolar, quadrupolar and higher order modes). However, the EELS maps were obtained by exciting the entire AuNS with a defocused electron beam, unlike the spectra in figure IIC.3, obtained by spectrum imaging (SI) with a sub-nm electron probe. EELS intensity maps at 1.2 eV and 1.8 eV clearly show the mode localization away from the AuNS tip.

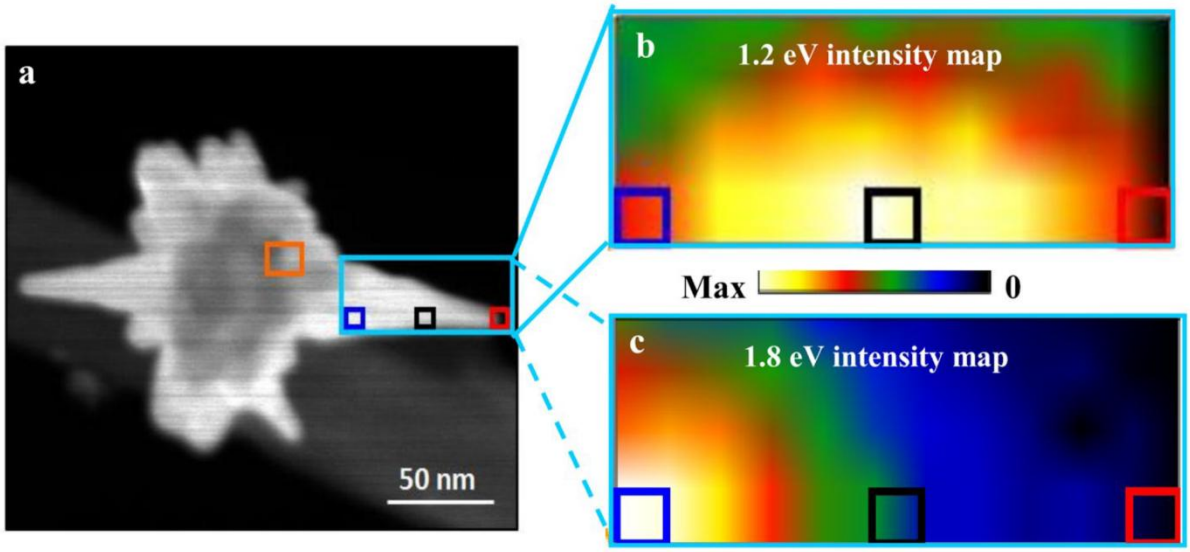


Figure IIC.5. EELS intensity maps of different dominant modes in spikes of AuNSs with a LSL: (a) AuNS with relative areas of investigation indicated by different colored boxes. (b) EELS intensity map at 1.2 eV mode. (c) EELS intensity map at 1.8 eV mode. Here 1.2 eV and 1.8 eV modes are the major plasmonic modes located at the AuNS spike with LSL.

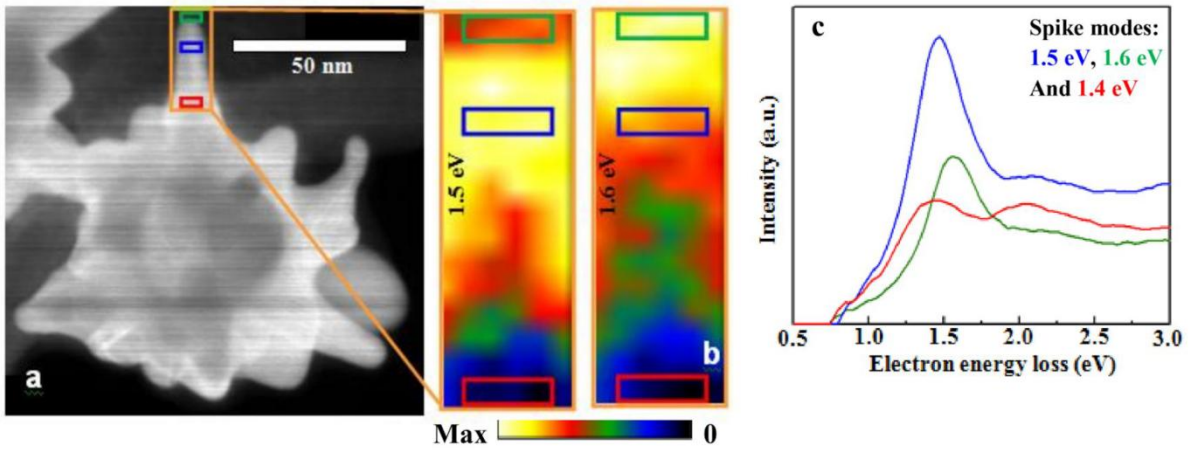


Figure IIC.6. EELS of an AuNS with short spike length (SSL): (a) AuNS image with relative areas of investigation (coloured boxes). (b) Intensity maps of major plasmonic modes at 1.5 eV and 1.6 eV located at the AuNS spike. (c) EELS spectra of different regions of the AuNS spike. The dominant mode at the pinnacle of the spike is 1.6 eV. The 1.6 eV EELS intensity map confirms its edge mode nature by showing a maximum intensity at the tip of the spike (green box area), whereas the 1.5 eV mode, which is dominant in the body of the spike (blue box region) confirms its non-plasmonic nature.

The presence of radial breathing modes and a dipolar edge mode is more evident for short spike than for long spike AuNSs, because of its larger interaction volume. The details of the EELS analysis of the AuNS with a small spike length (SSL) are shown in figure IIC.6 and the relevant numerical results are given in figure IIC.7.

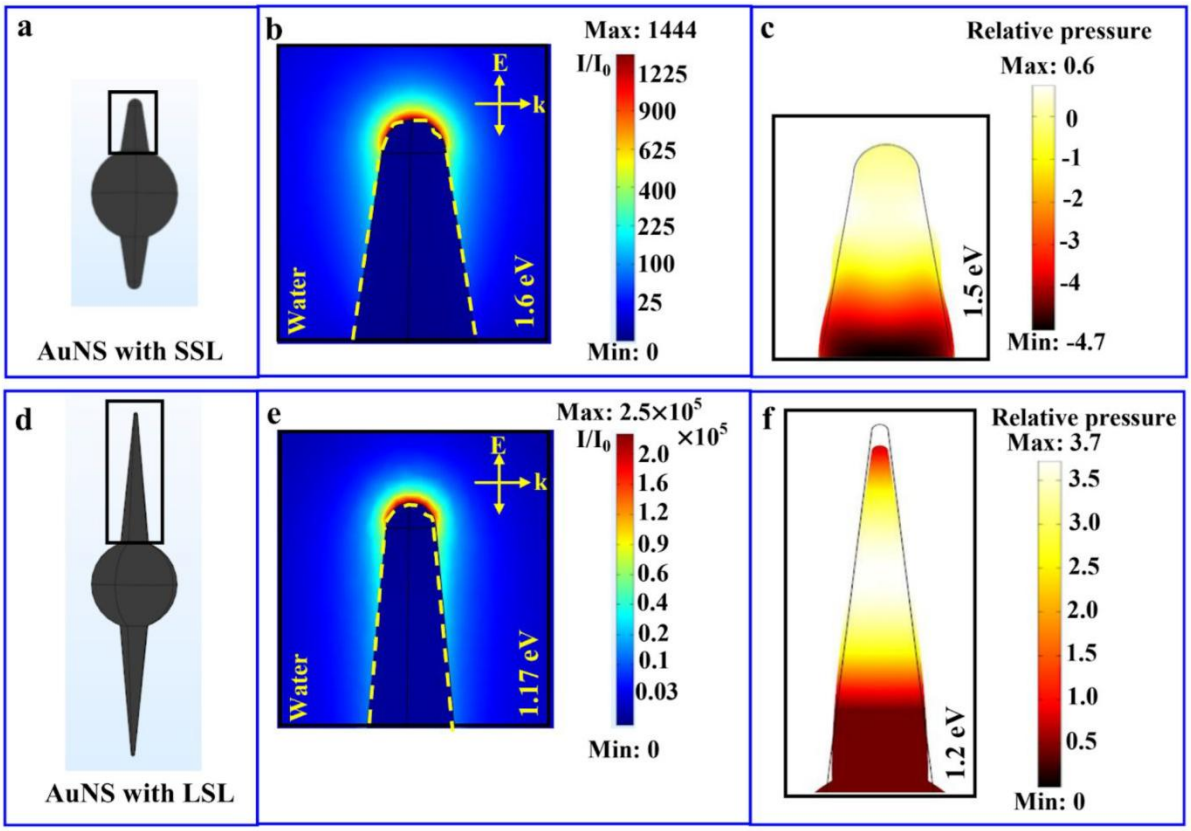


Figure IIC.7. (a) Single AuNS with a small spike length (SSL) is shown here. The enlarged portion of the black box shows different responses at different modes and thus is useful theoretically to predict the nature of the mode (either plasmonic edge mode or radial breathing mode). (b) Behaviour of a single AuNS with a SSL at 1.6 eV. (c) Behaviour of a single AuNS with a SSL at 1.5 eV. (d) Single AuNS with a LSL is shown. The enlarged portion of the black box shows different responses at different modes. (e) Behaviour of a single AuNS with a LSL at 1.17 eV. (f) Behaviour of a single AuNS with a LSL at 1.2 eV.

Figure IIC.7 illustrates the numerical study performed for the various observed modes, both edge and non-edge modes, in a single AuNS with a large spike length (LSL) and a small spike length (SSL), when excited by light and electron beams. Here panel (a) shows an illustration of a plasmonic SSL nanostar antenna determined by the quantitative parameters measured from the STEM images. Panel (b) shows the resultant mode distribution at 1.6 eV when excited by light; the mode has its highest intensity at the pinnacle of the AuNS spike, as also observed in the EELS intensity map (figure IIC.6 (b) ). Considering that the skin depth of gold in the wavelength range of 400 - 1200 nm is smaller than 5 nm, any plasmonic edge mode is not expected to penetrate into the body of the nanoparticle; rather it is confined at the metal–dielectric interface. Moreover, extinction studies also confirm the LSPR of this structure at 1.6 eV; thereby, this mode is a dipolar edge mode. Of note, the yellow dashed

line in figure IIC.7 (b) represents the nanoparticle edge and does not appear to show evidence of structural modification. The intensity map in figure IIC.6 (b) exhibits an unexpected shape for the 1.5 eV modes; this mode was not observed in the optical extinction spectra, thereby indicating that it is formed by a non-plasmonic nature, as also supported by the simulations. The hypothesis that these modes are of an acoustic nature originated from multiple observations: the appearance of the highest intensity position away from the metal–dielectric interface, the radially symmetric nature of the mode and the corresponding absence of this mode in the extinction spectra, both for theoretical and experimental studies. To confirm this hypothesis, the mode at 1.5 eV of the SSL AuNS was investigated numerically using the structural mechanics module of Comsol 5.4 (the parameters for the simulation are given in the numerical simulation section) [75–77]. In figure IIC.7, panel (c) shows the 1.5 eV mode shape and distribution obtained via Comsol simulations for the SSL AuNS. The map of the relative pressure calculated via the structural mechanics module shows that the mode has the familiar, radial symmetry of a typical breathing mode [32–34]. The black contour line, shown in panel (c), represents the unperturbed morphology of the SSL AuNS, whereas the color map shows the relative pressure distribution at 1.5 eV and the modification of the structure because of the acoustic mode. Similarly, panel (f) here shows the simulation obtained via Comsol of the LSL AuNS for the anomalous mode at 1.2 eV, as also shown in figure IIC.5 (b). Notably, the relative pressure is highest in the middle of the spike of the AuNS resulting in a significant contraction of the same structure. The map of the relative pressure, as calculated by structural mechanics, shows that the 1.2 eV mode exhibits the radial symmetry of a typical breathing mode, [32–34] again supporting the acoustic nature of the 1.2 eV mode of the LSL AuNS. Panel (e) of the above figure conversely shows the results for the analysis of the mode at 1.17 eV of the LSL AuNS, as reported in figure IIC.3. The 1.17 eV mode has its highest intensity at the pinnacle of the AuNS spike, as observed in the EELS spectra (figure IIC.3 (c) ). The 1.17 eV mode is a plasmonic edge mode, since its dipolar nature has been confirmed by calculating the LSPR from the extinction spectra and the electric field mapping using the RF module of Comsol 5.4.

Continued analysis of SI data for breathing modes revealed that the 1.5 eV mode is located along the spike where the diameter measured 7.4 nm (figure IIC.6), whereas for the LSL AuNS the breathing mode at 1.2 eV is located along the spike where the diameter is 21.4 nm (figure IIC.5). For any specific, non-symmetric structure, theoretical calculation of acoustic mode frequency is tedious [78-79] yet Lamb introduced a very simple relationship between

the acoustic breathing mode frequency and the size of the structure [80]. According to Lamb's relationship, the acoustic breathing mode frequency varies inversely with the diameter of the spherically symmetric structures. If the spikes of the AuNS are considered to be a parallel combination of many disks, [81] - the Lamb principle is also verified here for the two breathing modes - as the mode frequencies vary inversely with the structure diameter.

The plasmonic edge and breathing modes of AuNSs can be synergistically employed to determine the size and mass of target molecules, respectively, by combining the reactive sensing principle for plasmonic biosensing [82-83] and a nano-cantilever mechanism. According to the numerical investigation, the field intensity enhancement was found to be approximately $2.5\times10^5$ in water media for the LSL AuNS at its LSPR (1060 nm). This indicates that the acousto-plasmonic AuNS based nanoantenna - supporting both plasmon edge and breathing modes – can be useful for two-step label free molecular detection at a point-of-care.

## IIC.3. Conclusion

To summarize, we report the experimental evidence of both plasmonic edge and acoustic breathing modes in gold nanostars (AuNSs). For this work, AuNSs are synthesized via our own simple, one-step, surfactant-free wet chemistry method with high yield and stability and characterized via optical spectroscopy and EELS. Optical extinction measurements of AuNSs confirm the presence of localized surface plasmon resonances (LSPRs), while electron energy-loss spectroscopy (EELS) using a scanning transmission electron microscope (STEM) shows the spatial distribution of LSPRs and reveals the presence of acoustic breathing modes. Plasmonic hot-spots generated at the pinnacle of the sharp spikes, due to the optically active dipolar edge mode, allow significant intensity enhancement of local fields and hot-electron injection, and are thus useful for detection of small protein molecules. The breathing modes observed away from the apices of the nanostars are identified as stimulated dark modes - they have an acoustic nature - and likely originate from the confinement of the surface plasmon by the geometrical boundaries of a nanostructure. Thus based on the information provided by the low-loss EELS about the local plasmonic edge modes of different regions of the nanostars and the presence of optically dark breathing modes, one can use the plasmonic edge and acoustic breathing modes of these synthesized AuNSs to determine the size and mass of adsorbed analyte based on both a plasmon resonance sensing mechanism and the cantilever principle, irrespective of the molecular shape. This experimental study is also supported by the numerical investigations performed by FEM based Comsol 5.4 which confirms the

presence of both plasmonic edge and breathing modes in different AuNSs with different spike lengths. The numerical study predicts that for this kind of AuNS plasmonic antenna the field-intensity enhancement factor in the hot-spot region can reach around $10^5$. So the presence of both these modes and the high intensity enhancement capability offer the possibility of designing a nanoplasmonic antennas based on these efficient acousto-plasmonic AuNSs, which can provide information on mass and polarizability of biomolecules using a two-step label-free molecular detection process for clinical diagnostics.

## IIC.4. References


[1] N. Rezaei, Cancer Immunology, Springer, New York, 2014.

[2] P. N. Prasad, Introduction to Biophotonics, John Wiley & Sons, New Jersey, 2003.

[3] J. A. Schuller, E. S. Barnard, W. S. Cai, Y. C. Jun, J. S. White and M. L. Brongersma, Nat. Mater., 2010, 9, 193-204.

[4] W. B. Hou and S. B. Cronin, Adv. Funct. Mater., 2013, 23, 1612-1619.

[5] P. Reineck, G. P. Lee, D. Brick, M. Karg, P. Mulvaney and U. Bach, Adv. Mater., 2012, 24, 4750-4755.

[6] H. C. Chen, S. W. Chou, W. H. Tseng, I. W. P. Chen, C. C. Liu, C. Liu, C. L. Liu, C. H. Chen, C. I. Wu and P. T. Chou, Adv. Funct. Mater., 2012, 22, 3975-3984.

[7] S. S. Kelkar and T. M. Reineke, Bioconjugate Chem., 2011, 22, 1879-1903.

[8] K. A. Willets and R. P. Van Duyne, Annu. Rev. Phys. Chem., 2007, 58, 267-297.

[9] K. V. Sreekanth, Y. Alapan, M. ElKabbash, E. Ilker, M. Hinczewski, U. A. Gurkan, A. De Luca and G. Strangi, Nat. Mater., 2016, 15, 621-627.

[10] K. V. Sreekanth, Y. Alapan, M. ElKabbash, A. M. Wen, E. Ilker, M. Hinczewski, U. A. Gurkan, N. F. Steinmetz and G. Strangi, Adv. Opt. Mater., 2016, 4, 1767-1772.

[11] J. S. Sekhon, H. K. Malik and S. S. Verma, RSC Adv., 2013, 3, 15427-15434.

[12] B. Sharma, R. R. Frontiera, A. I. Henry, E. Ringe and R. P. Van Duyne, Mater. Today, 2012, 15, 16-25.

[13] S. M. Nie and S. R. Emery, Science, 1997, 275, 1102-1106.

[14] W. L. Barnes, A. Dereux and T. W. Ebbesen, Nature, 2003, 424, 824-830.

[15] E. Ozbay, Science, 2006, 311, 189-193.

[16] K. L. Kelly, E. Coronado, L. L. Zhao and G. C. Schatz, J. Phys. Chem. B, 2003, 107, 668-677.

[17] J. A. Scholl, A. L. Koh and J. A. Dionne, Nature, 2012, 483, 421-428.

[18] J. Nelayah, M. Kociak, O. Stephan, F. J. Garcia de Abajo, M. Tence, L. Henrard, D. Taverna, I. Pastoriza-Santos, L. M. Liz-Marzan and C. Colliex, Nat. Phys., 2007, 3, 348-353.

[19] M. Rycenga, X. Xia, C. H. Moran, F. Zhou, D. Qin, Z. Y. Li and Y. Xia, Angew. Chem., Int. Ed., 2011, 50, 5473-5477.

[20] Y. G. Sun and Y. N. Xia, Science, 2002, 298, 2176-2179.

[21] H. J. Chen, L. Shao, Q. Li and J. F. Wang, Chem. Soc. Rev., 2013, 42, 2679-2724.

[22] S. J. Lee and M. Moskovits, J. Am. Chem. Soc., 2012, 134, 11384-11387.

[23] L. Rodr´ıguez-Lorenzo, R. A. Alvarez-Puebla, I. Pastoriza-Santos, S. Mazzucco, O. St´ephan, M. Kociak, L. M. Liz-Marz´an and F. J. Garc´ıa de Abajo, J. Am. Chem. Soc., 2009, 131, 4616-4618.

[24] H. G. Liao, Y. X. Jiang, Z. Y. Zhou, S. P. Chen and S. G. Sun, Angew. Chem., Int. Ed., 2008, 47, 9100-9103.

[25] H. L. Wu, C. H. Chen and M. H. Huang, Chem. Mater., 2008, 21, 110-114.

[26] X. L. Liu, J. H. Wang, S. Liang, D. J. Yang, F. Nan, S. J. Ding, L. Zhou, Z. H. Hao and Q. Q. Wang, J. Phys. Chem. C, 2014, 118, 9659-9664.

[27] J. Zhang, Y. Gao, R. A. Alvarez-Puebla, J. M. Buriak and H. Fenniri, Adv. Mater., 2006, 18, 3233-3237.

[28] C. R. Li, N. P. Lu, J. Mei, W. J. Dong, Y. Y. Zheng, L. Gao, K. Tsukamoto and Z. X. Cao, J. Cryst. Growth, 2011, 314, 324-330.

[29] V. Giannini, R. Rodr´ıguez-Oliveros and J. A. S´anchez-Gil, Plasmonics, 2010, 5, 99-104.

[30] R. Alvarez-Puebla, L. M. Liz-Marzan, and F. J. Garc´ıa de Abajo, J. Phys. Chem. Lett., 2010, 1, 2428-2434.

[31] P. G. Etchegoin and E. C. Le Ru, Surface Enhanced Raman Spectroscopy: Analytical, Biophysical and Life Science Applications, Chapter I – “Basic Electromagnetic Theory of SERS”, WILEY-VCH Verlag GmbH & Co. KGaA, Weinheim, 2010.

[32] F. P. Schmidt, H. Ditlbacher, U. Hohenester, A. Hohenau, F. Hofer and J. R. Krenn, Nano Lett., 2012, 12, 5780.

[33] A. Chakrabarty, F. Wang, F. Minkowski, K. Sun and Q. H. Wei, Opt. Express, 2012, 20, 11615.

[34] F. P. Schmidt, H. Ditlbacher, U. Hohenester, A. Hohenau, F. Hofer and J. R. Krenn, Nat. Commun., 2014, 5, 3604.

[35] F. P. Schmidt, A. Losquin, F. Hofer, A. Hohenau, J. R. Krenn and M. Kociak, ACS Photonics, 2018, 5, 861.

[36] M. Zhao, M. Bosman, M. Danesh, M. Zeng, P. Song, Y. Darma, A. Rusydi, H. Lin, C. W. Qiu and K. P. Loh, Nano Lett., 2015, 15, 8331.

[37] M. K. Krug, M. Reisecker, A. Hohenau, H. Ditlbacher, A. Trugler, U. Hohenester and J. R. Krenn, Appl. Phys. Lett., 2014, 105, 1711031-1711033.

[38] J. E. Sader, G. V. Hartland and P. Mulvaney, J. Phys. Chem. B, 2002, 106, 1399.

[39] J. H. Hodak, A. Henglein and G. V. Hartland, J. Phys. Chem. B, 2000, 104, 5053.

[40] A. Campos, A. Arbouet, J. Martin, D. G´erard, J. Proust, J. Plain and M. Kociak, ACS Photonics, 2017, 4, 1257.

[41] N. Large, L. Saviot, J. Margueritat, J. Gonzalo, C. N. Afonso, A. Arbouet, P. Langot, A. Mlayah and J. Aizpurua, Nano Lett., 2009, 9, 3732.

[42] K. Yu, T. A. Major, D. Chakraborty, M. S. Devadas, J. E. Sader and G. V. Hartland, Nano Lett., 2015, 15, 3964.

[43] S. Tripathy, R. Marty, V. K. Lin, S. L. Teo, E. Ye, A. Arbouet, L. Saviot, C. Girard, M. Y. Han and A. Mlayah, Nano Lett., 2011, 11, 431.

[44] C. Cherqui, N. W. Bigelow, A. Vaschillo, H. Goldwyn and D. J. Masiello, ACS Photonics, 2014, 1, 1013.

[45] W. Wang and Z. Song, Phys. B, 2017, 530, 142.

[46] S. A. Maier and H. A. Atwater, J. Appl. Phys., 2005, 98, 0111011.

[47] H. Wang, D. W. Brandl, F. Le, P. Nordlander and N. J. Halas, Nano Lett., 2006, 6, 827-832.

[48] J. W. Liaw, M. K. Kuo and C. N. Liao, Journal of Electromagnetic Waves and Applications, 2005, 19, 1787-1794.

[49] M. B. Mohamed, V. Volkov, S. Link and M. A. El-Sayed, Chem. Phys. Lett., 2000, 317, 517-523.

[50] C. F. Bohren and D. R. Huffman, Adsorption and Scattering of Light by Small Particles, Wiley-VCH, New York, 1983.

[51] J. D. Jackson, Classical Electrodynamics, Wiley, New York, 1999.

[52] L. N. Colleen, H. Liao and J. H. Hafner, Nano Lett., 2006, 6, 683-688.

[53] P. S. Kumar, I. Pastoriza-Santos, B. Rodriguez-Gonzalez, F. J. Garc´ıa d´e Abajo, F. Javier and L. M. Liz-Marzan, Nanotechnology, 2008, 19, 0156061-0156066.

[54] Q. Chen, T. Kaneko and R. Hatakeyama, Condens. Matter, 2014, 1585, 1401-1417.

[55] W. Moukarzel, J. Fitremann and J. D. Marty, Nanoscale, 2011, 3, 3285-3290.

[56] H. Yuan, C. G. Khoury, H. Hwang, C. M. Wilson, G. A. Grant and T. Vo-Dinh, Nanotechnology, 2012, 23, 075102-075117.

[57] A. Kedia and P. S. Kumar, J. Mater. Chem. C, 2013, 1, 4540-4549.

[58] S. Chatterjee, A. B. Ringane, A. Arya, G. M. Das, V. R. Dantham, R. Laha and S. Hussain, J. Nanopart. Res., 2016, 18, 242–249.

[59] S. Chatterjee, L. Ricciardi, J. I. Deitz, R. E. A. Williams, D. W. McComb and G. Strangi, Micromachines, 2018, 9, 664.

[60] M. W. Chu, V. Myroshnychenko, C. H. Chen, J. P. Deng, C. Y. Mou and F. J. Garc´ıa d´e Abajo, Nano Lett., 2009, 9, 399-404.

[61] J. Nelayah, M. Kociak, O. Stephan, F. J. Garc´ıa d´e Abajo, M. Tence, L. Henrard, D. Taverna, I. Pastoriza-Santos, L. M. Liz-Marzan and C. Colliex, Nat. Phys., 2007, 3, 348-353.

[62] H. Wang, Y. Wu, B. Lassiter, C. L. Nehl, J. H. Hafner, P. Nordlander and N. J. Halas, Proc. Natl. Acad. Sci. U. S. A., 2006, 103, 10856-10860.

[63] A. L. Koh, K. Bao, I. Khan, W. E. Smith, G. Kothleitner, P. Nordlander, S. A. Maier and D. W. McComb, ACS Nano, 2009, 3, 3015-3022.

[64] J. Morla-Folch, L. Guerrini, N. Pazos-Perez, R. Arenal and R. A. Alvarez-Puebla, ACS Photonics, 2014, 1, 1237-1244.

[65] Y. Wu, G. Li, C. Cherqui, N. W. Bigelow, N. Thakkar, D. J. Masiello, J. P. Camden and P. D. Rack, ACS Photonics, 2016, 3, 130-138.

[66] S. Mazzucco, O. St´ephan, C. Colliex, I. Pastoriza-Santos, L. M. Liz-Marzan, F. J. Garc´ıa d´e Abajo and M. Kociak, Eur. Phys. J.: Appl. Phys., 2011, 54, 335121-335129.

[67] F. J. Garc´ıa d´e Abajo and M. Kociak, Phys. Rev. Lett., 2008, 100, 1068041-1068044.

[68] V. Myroshnychenko, J. Nelayah, G. Adamo, N. Geuquet, J. Rodriguez-Fernandez, I. Pastoriza-Santos, K. F. MacDonald, L. Henrard, L. M. Liz-Marzan, N. I. Zheludev, M. Kociak and F. J. Garc´ıa d´e Abajo, Nano Lett., 2012, 12, 4172-4180.

[69] A. Losquin, L. F. Zagonel, V. Myroshnychenko, B. Rodriguez-Gonzalez, M. Tence, L. Scarabelli, J. F¨orstner, L. M. Liz-Marzan, F. J. Garc´ıa de Abajo, O. Stephan and M. Kociak, Nano Lett., 2015, 15, 1229-1237.

[70] J. A. Scholl, A. L. Koh and J. A. Dionne, Nature, 2012, 483, 421-427.

[71] V. Myroshnychenko, J. Rodr´ıguez-Fern´andez, I. Pastoriza-Santos, A. M. Funston, C. Novo, P. Mulvaney, L. M. Liz-Marz´an and F. J. Garc´ıa d´e Abajo, Chem. Soc. Rev., 2008, 37, 1792-1805.

[72] S. M. Novikov, A. S´anchez-Iglesias, M. K. Schmidt, A. Chuvilin, J. Aizpurua, M. Grzelczak and L. M. Liz-Marz´an, Part. Part. Syst. Charact., 2014, 31, 77-80.

[73] A. L. Koh, A. I. Fern´andez-Dom´ınguez, D. W. McComb, S. A. Maier and J. K. W. Yang, Nano Lett., 2011, 11, 1323-1330.

[74] F. V. Cube, J. Niegemann, S. Irsen, D. C. Bell and S. Linden, Phys. Rev. B: Condens. Matter Mater. Phys., 2014, 89, 1154341-1154345.

[75] Comsol Multiphysics Structural Mechanics—User's Guide, Comsol, 2012, Version: 4.3.

[76] T. Schumacher, M. Brandstetter, D. Wolf, K. Kratzer, M. Hentschel, H. Giessen and M. Lippitz, Appl. Phys. B: Lasers Opt., 2016, 122, 1-11.

[77] L. Wang, T. Sagaguchi, T. Okuhata, M. Tsuboi and N. Tamai, ACS Nano, 2017, 11, 1180-1188.

[78] W. M. Visscher, A. Migliori, T. M. Bell and R. A. Reinert, J. Acoust. Soc. Am., 1991, 90, 2154.

[79] L. Saviot and D. B. Murray, Phys. Rev. B: Condens. Matter Mater. Phys., 2009, 79, 214101-214111.

[80] H. Lamb, Proc. London Math. Soc., 1882, 13, 189.

[81] N. Large, L. Saviot, J. Margueritat, J. Gonzalo, C. N. Afonso, A. Arbouet, P. Langot, A. Mlayah and J. Aizpurua, Nano Lett., 2009, 9, 3732-3738.

[82] V. R. Dantham, S. Holler, C. Barbre, D. Keng, V. Kolchenko and S. Arnold, Nano Lett., 2013, 13, 3347-3351.

[83] I. Ament, J. Prasad, A. Henkel, S. Schmachtel and C. S¨onnichsen, Nano Lett., 2012, 12, 1092-1095.

[84] M. Stoger-Pollach, Micron, 2008, 39, 1092-1110.

[85] J. I. Deitz, S. Karki, S. X. Marsillac, T. J. Grassman and D. W. McComb, J. Appl. Phys., 2018, 123, 1157031-1157036.

[86] M. Contreras, J. Tuttle, D. Du, Y. Qi, A. Swartzlander, A. Tennant and R. Noufi, Appl. Phys. Lett., 1993, 63, 1824-1826.

[87] D. B. Williams and C. B. Carter, Transmission Electron Microscopy: A Textbook for Materials Science, Springer, New York, 2009.

[88] Digital Micrograph EELS Analysis User's Guide – EELS Analysis User Guide, Pleasanton, CA, 2003.

[89] P. B. Johnson and R. W. Christy, Phys. Rev. B: Solid State, 1972, 6, 4370-4379.

[90] S. Chatterjee, L. Ricciardi, J. I. Deitz, R. E. A. Williams, D. W. McComb, and G. Strangi, Nanoscale Adv., 2019, 1, 2690-2698.

# Chapter III

# Fano resonance for detection of both change in temperature and refractive index in surrounding medium

**III.1. Introduction:** Localized surface plasmon resonances (LSPRs) arising from the collective electron oscillations in metal nanoparticles (MNPs) have attracted tremendous interests for its ability to concentrate and manipulate light in nanoscale regime. The strong electromagnetic field enhancement arising due to the LSPR can boost many linear and non-linear optical processes and is useful in different practical applications [1]. In the previous chapters (IIA, IIB, IIC) the LSPR effect of the spiky gold nanostar (AuNS) particle has been discussed. The manipulation of the incident electromagnetic light allows these antennas to be one of the efficient nanoantennas as it can enhance the electric field at its hot-spots arising at the AuNS tip. Not only this single AuNS is useful but also it has been seen that the heterodimeric nanogap created between the AuNS and gold nanosphere can be even more sensitive with respect to the single AuNS because of its higher intensity enhancement capability and the optimum electric field mapping in the gap region. Both the single AuNS and heterodimeric nanogap seems to be an efficient plasmonic biosensor. Other than the edge dipolar mode arising out of the LSPR of the single AuNS, the breathing acoustic modes of these antennas, discussed in chapter IIC also seems to be very interesting and useful as acousto-plasmonic biosensor.

Although the LSPR of the nanoantennas are well-known and find application in many different areas yet, recently Fano resonance in plasmonic systems have attracted a lot of attention compared to the LSPR of MNPs. The “Fano resonance” is named after the famous Italian-American physicist Ugo Fano [2, 3] This particular resonance is a resonant scattering effect which gives wise to an asymmetric line-shape unlike the symmetric dipolar line-shape arising from the LSPR effect in MNPs. The Fano resonances, identified by their characteristic asymmetric lineshape were first discovered in atomic systems, experiencing interference between discrete and continuum states. Analogously Fano resonances in plasmonic systems originate from the interference between a bright mode (superradiant), and a dark mode (subradiant) via near field coupling. In other words, the interference between a broad background and a resonant scattering process can produce the asymmetric Fano line-shape. A

Fano peak is a consequence of constructive interference between such modes, whereas a Fano dip arises as the two modes interfere destructively.

Explanation of Fano resonance: The Fano resonance originates from the interference between two scattering amplitudes – scattering from a continuum of states (the background process with a characteristic broad mode) and the scattering coming from the excitation of a discrete state (a resonant process with a characteristics narrow mode). For the Fano resonance to occur, the resonant state energy should fall in the energy range of the background continuum state. The background scattering changes slowly with energy near the resonant mode but the resonant scattering changes both in amplitude and phase very quickly with the input energy. This kind of variation in behaviour of both the background and the resonant scattering process creates the Fano asymmetric profile.

When the incident em energy is much higher than the resonant scattering energy the background scattering process dominates and one can see a broad mode. The Fano resonance occurs when the phase of the resonant scattering amplitude changes by **π** and it happens when the input energy, $E < 2\Gamma_{res}$, where $\Gamma_{res}$ is the line width of the resonant scattering mode energy. The Fano resonance asymmetric line-shape is only originating from this rapid variation in phase of the resonant process. According to Ugo Fano, the total scattering cross-section $\sigma$ of this Fano scattering process is

$$\sigma \approx \frac{(q\Gamma_{res}/2+E-E_{res})^2}{(\Gamma_{res}/2)^2+(E-E_{res})^2} \qquad \text{(III.1)}$$

Where $q$ is the Fano parameter which depends on the ratio of the resonant scattering amplitude to the direct or background scattering amplitude and this parameter decides the strength of this Fano process. When the direct scattering amplitude vanishes the $q \to \infty$ and then the Fano formula reduces to the usual Breit-Wigner (Lorentzian) formula:

$$\frac{(\Gamma_{res}/2)^2}{(\Gamma_{res}/2)^2+(E-E_{res})^2} \qquad \text{(III.2)}$$

Fano resonance is found to exist in many areas of application of physics, such as atomic physics, nuclear physics, condensed matter physics, circuits, microwave engineering, nonlinear optics, nanophotonics and plasmonics, magnetic metamaterials [4], and in mechanical waves [5]. The figure below shows the asymmetric Fano line-shape.

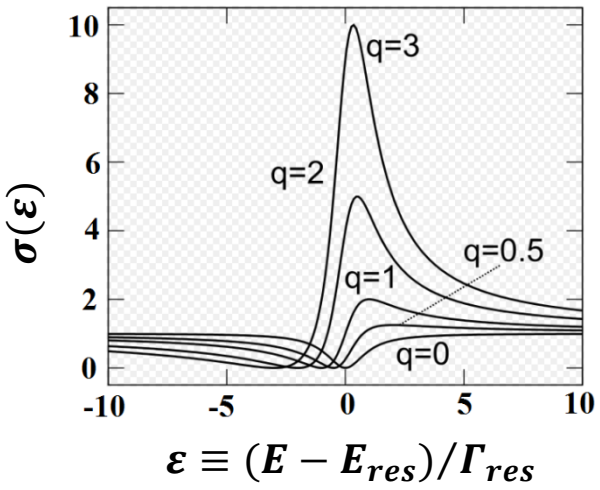


Figure III.1. Asymmetric Fano line-shape for variable q where scattering cross-section is plotted against normalized energy.

Compared to the symmetric Lorentzian characteristic lineshape of the well-known dipolar edge mode Fano line-shape is more useful due to some of its unique properties such as a narrow asymmetric line-shape, stronger electromagnetic field intensity enhancement, more light confinement to the nanometer scale, and high spectral sensitivity to changes in the local dielectric environment [6]. Because of the ability to confine light more tightly and efficiently and its steeper dispersion compared to the known plasmon resonances Fano resonance become promising for nanoscale sensing particularly for refractive index sensing [7], temperature sensing [8], plasmon rulers [9], surface enhanced Raman spectroscopy (SERS) [10], switching [11, 12], and lasing, nonlinear and slow-light devices and many other applications [13-14]. The observation of this kind of asymmetric Fano line-shape in optics is first observed by Wood [15]; however it took some time to understand the phenomena clearly [16]. After that Fano resonance has been observed in many different systems such as prism-coupled square micro pillars [17], photonic crystal [18], Plasmonic nanostructures, subwavelength apertures, coupled clusters of nanoparticles, ring-disc cavities, and metallic films along with metamaterials [19-38]. The Fano resonance in plasmonic systems arises from the coupling of a non-radiative mode with a continuum of radiative electromagnetic waves and is used in different sections depending on the strength of the coupling between its components. In the weak coupling regime, where the radiative losses of the dark mode gets suppressed the Fano is used for the nanoscale plasmon rulers to quantify nanometre displacement. In intermediate regime, the field intensity enhancement capability reaches maximum which is good for second harmonic generation, SERS, antenna based trapping, and refractive index sensing. Finally, for stronger coupling, the specific features of Fano

resonances are altered [39]. The Fano resonance in plasmonic structures can be tuned by tuning various parameters to break the symmetry, such as inter-particle separation, particle size, film to particle separation, phase of different elements [40-42].

Here in this chapter a system has been experimentally demonstrated whose characteristic line-shape is of Fano type. This Fano resonance is originating from the interference of resonance mode arising from the gold nanorods dipped in polymer matrix and silver thin film. It has been seen that this Fano resonance can efficiently respond to the change in both external temperature and refractive index simultaneously. Because of the pronounced asymmetric spectral lineshape and highly enhanced local fields, this plasmonic Fano resonance can be effectively exploited for applications ranging from chemical and biological sensors, to surface enhanced Raman spectroscopy (SERS) and nonlinear optics. Until now Fano line shape has been used for label-free detection of protein molecule with high sensitivity [7] and also for external temperature sensing [8]. But there is no report in the literature about a Fano resonant structure for measuring the change in both external temperature and refractive index simultaneously [43]. Relevant numerical investigation has also been done here based on finite element method (FEM). In the following section all the details about the Fano system and the related experimental and theoretical results are given.

## III.2. Results and discussion

**III.2.a. Fabrication of the Fano system:** The schematic diagram of our Fano system is shown in the figure below.

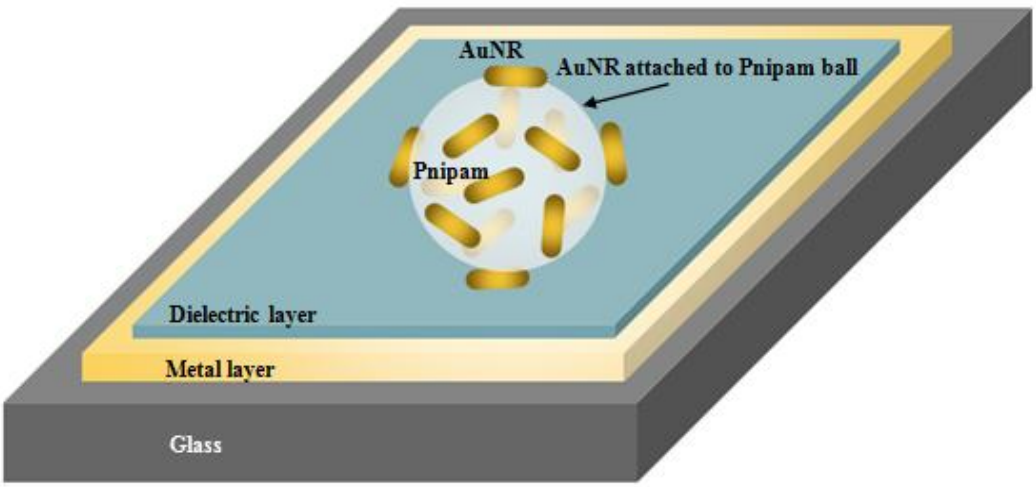


Figure III.2: Schematic diagram of the plasmonic Fano system.

Here, it can be seen that the Au nanorods (AuNRs) are attached on the surface of Pnipam polymer which is separated from 80 nm Ag thin film by $SiO_2$ dielectric spacer layer. The Fano resonance is originating from the hybridization of the localized surface plasmons (LSPs) of AuNRs and surface plasmons (SPs) of Ag thin film.

The Fabrication of the aqueous solution of AuNRs dipped in the thermo-responsive Pnipam polymer has been done following the process specified in ref [44]. The details about the characterization are shown below.

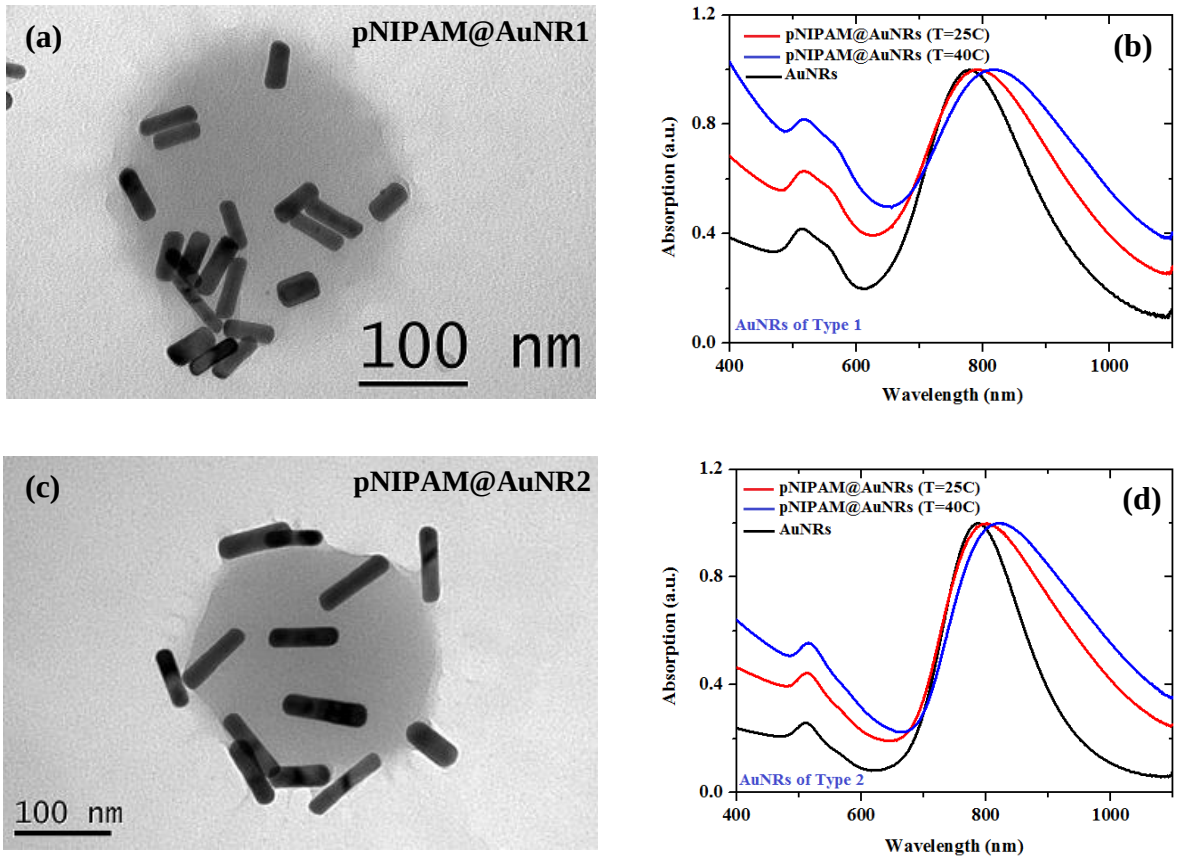


Figure III.3. (a) STEM image of AuNRs in pNIPAM polymer matrix is shown where the AuNRs are of aspect ratio 3.6. (b) The UV-Vis-NIR spectra of aqueous solution of AuNRs of type 1 with aspect ratio 3.6. Here the absorption spectra of AuNRs in pNIPAM matrix for swollen (red curve) and collapsed state (blue curve) are also included. (c) STEM image of AuNRs of type 2 with aspect ratio 3.9 in pNIPAM polymer matrix is shown. (b) The UV-Vis-NIR spectra of aqueous solution of AuNRs of type 2 along with the absorption spectra of AuNRs in pNIPAM matrix for both thermodynamic states are also included here.

Poly (N-isopropylacrylamide) (pNIPAM) is a well-known thermo-responsive polymer. The hydrodynamic diameter of this polymer is 544.2±7 nm at 25$^{o}$C, while that hydrodynamic diameter reduces down to 306.3±4 nm when it is heated to 40$^{o}$C and above because of the

dehydration. The state with higher hydrodynamic diameter at the room-temperature is known as the swollen state and the state with lower hydrodynamic diameter at higher temperature is known as the collapsed state. When pNIPAM is heated, it expels all its liquid contents and reaches to the collapsed state with lower hydrodynamic diameter. The phase transition from a swollen hydrated state to a shrunken dehydrated state is reversible.

For this kind of experiments two types of AuNRs with two different aspect ratios are taken which are synthesized by following the route described in ref [44]. The AuNRs of type 1 has the length (L) and width (W) of approximately 54 ($\pm$6) nm and 15 ($\pm$2) nm. Thus the aspect ratio (L/W) of these NRs is 3.6. The localized surface plasmon resonance (LSPR) of these antennas is found to be 780 nm from their absorption characteristics in aqueous media. The AuNRs of type 2 has seen to have the length (L) and width (W) of approximately 74 ($\pm$7) nm and 19 ($\pm$3) nm. Thus the aspect ratio (L/W) of these NRs is 3.9. The LSPR of these nanostructures is 790 nm in aqueous media found from their absorption characteristics. The scanning tunnelling electron microscopy (STEM) images of AuNRs of aspect ratio 3.6 and 3.9 dipped in polymer matrix are given in the figure III.3 (a) and (c) respectively. These two figures are describing the morphology of these nanoantennas as well as their arrangements in the polymer matrix. The UV-Vis-NIR spectra of the aqueous solution of both these two types of AuNRs are given in panel (b) and (d) respectively where all the absorption characteristics of AuNRs aqueous solution, AuNRs in pNIPAM at two different thermodynamic states (25$^{o}$C and 40$^{o}$C) are also given.

The thin silver film (Ag-film) is deposited over glass slide (Micro slides, Corning) by the thermal evaporation technique. Here 80 nm thickness of the Ag –film has been chosen to have a nearly a complete reflection from this metal film. During the metal film deposition 0.5 $As^{-1}$ deposition rate is maintained. To ensure a good adhesion of the Ag to the glass slide 0.5 nm Ge is deposited before the deposition of the silver film using the electron beam evaporation technique. After deposition of Ge and the Ag layer, $SiO_2$ layer of variable thickness is deposited using the electron beam evaporation technique. For all these fabrication the materials were purchased from Kurt J. Lesker Company.

After fabricating the $SiO_2$-Ag thin film, 12 µl of aqueous solution of pNIPAM @ AuNRs of both kinds are drop casted and left till drying. For both AuNRs of aspect ratio 3.6 and 3.9 three types of thin film platform has been chosen with same thickness of Ag layer but of variable $SiO_2$ spacer layer thickness – 10 nm, 20 nm, and 30 nm. This is how the Fano system has been fabricated.

### III.2.b. Experimental characterization and theoretical analysis methods used:

**Experimental Characterization:** The synthesized nanoparticles are characterized using UV-Vis-NIR spectroscopy and scanning transmission electron microscopy (STEM), spectroscopic ellipsometer.

**UV-Vis-NIR spectroscopy:** The UV-Vis-NIR spectra of the pnipam @ AuNRs and AuNRs aqueous solution were obtained using a PerkinElmer Lambda 900 spectrophotometer. The extinction properties of the solution helped us to have their LSPRs.

**STEM measurements:** To probe the size and shape of the synthesized nanoparticle, a scanning tunneling electron microscopy (STEM) was used. Sample preparation was done before the STEM measurements by drop casting and then drying the aqueous solution of gold nanoparticles on a standardized holey carbon film supported on a TEM grid.

**Ellipsometric reflection measurement method:** A high-resolution variable-angle spectroscopic ellipsometry (SE) (J. A. Woollam Co., Inc., V-VASE) is used to experimentally measure all types of angular reflection data. The low-power spectroscopic ellipsometer has high precision and it is non-destructive and thus preferable for the optical characterization of nanostructures. This variable-angle spectroscopic ellipsometer is used to measure the reflectivity R ($\lambda$, $\phi$) at different angle of incidence, $\phi$, in the desired wavelength range, $\lambda$. The maximum resolution of this ellipsometer is 0.03 nm but for our measurements 1 nm resolution is maintained throughout all the experiments. To measure the angular reflection R ($\lambda$, $\phi$) at variable external temperature the Calctec Hs unit (a Peltier-controlled sample heating stage) sample heating stage is used for our measurements.

**Numerical Simulation Method:** Finite element method (FEM) based Comsol simulations are used here to find the electric field enhancement at the $SiO_2$ spacer layer of this Fano system. During simulation, data regarding the different sizes and shapes of AuNRs are obtained from the STEM studies. The thickness of the $SiO_2$ layer and the Ag layer is taken from the profilometer study. The study is carried out to map the electric field for plasmonic modes. The Radio Frequency (RF) module of Comsol 5.4 is used to investigate the plasmonic modes, the electric field pattern and its enhancement in the spacer layer and the reflection characteristics of this Fano system. For the optical simulations the definitions in the Comsol material library are used for all the optical and physical properties of the surrounding media. Simulations considering air ($\varepsilon = 1.0$) as the homogeneous surrounding media are performed. During this numerical investigation, the wavelength dependent permittivity of gold (Au) and

silver (Ag) are obtained from the Johnson and Christy measurements [45] and linearly polarized plane waves are used as the excitation source. Both kinds of incident light polarization have been analyzed. Physics controlled extra-fine meshes are used for all analysis.

### III.2.c. Discussion about the Experimental and Theoretical Results:

The reflection characteristics of pNIPAM deposited on the glass slide and the $SiO_2$-Ag film are shown in the figure below.

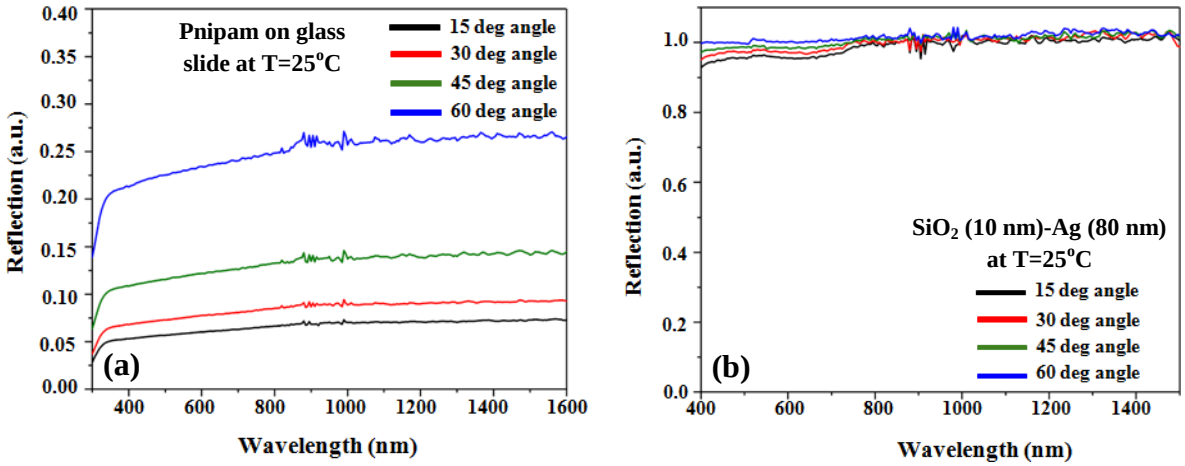


Figure III.4. (a) Reflection of drop-casted Pnipam film on Glass slide at room temperature for variable angle. (b) Reflection of $SiO_2$ (10 nm)-Ag (80 nm) thin film on Glass slide at room temperature for variable angle.

The figure above shows the reflection characteristics of the Pnipam film drop-casted on a glass slide (panel a) and the $SiO_2$ (10 nm)-Ag (80 nm) thin film deposited on glass slide (panel b). The measurements are taken at the room temperature for variable measurement angle. For Ag film the reflection is almost 100% over the desired wavelength range and is almost flat, which is quite obvious. For the pNIPAM film although reflection is less than the Ag films yet the trend is similar to a metal film.

Now both of the pNIPAM @ AuNRs film and the $SiO_2$-Ag film characteristics are far from the fano response. But when both these components interact (which is done by drop-casting the Pnipam @ AuNRs sample on top of $SiO_2$-Ag film) the Fano line-shape gets generated. The figure III.5 shows this Fano response for variable $SiO_2$ spacer layer thickness.

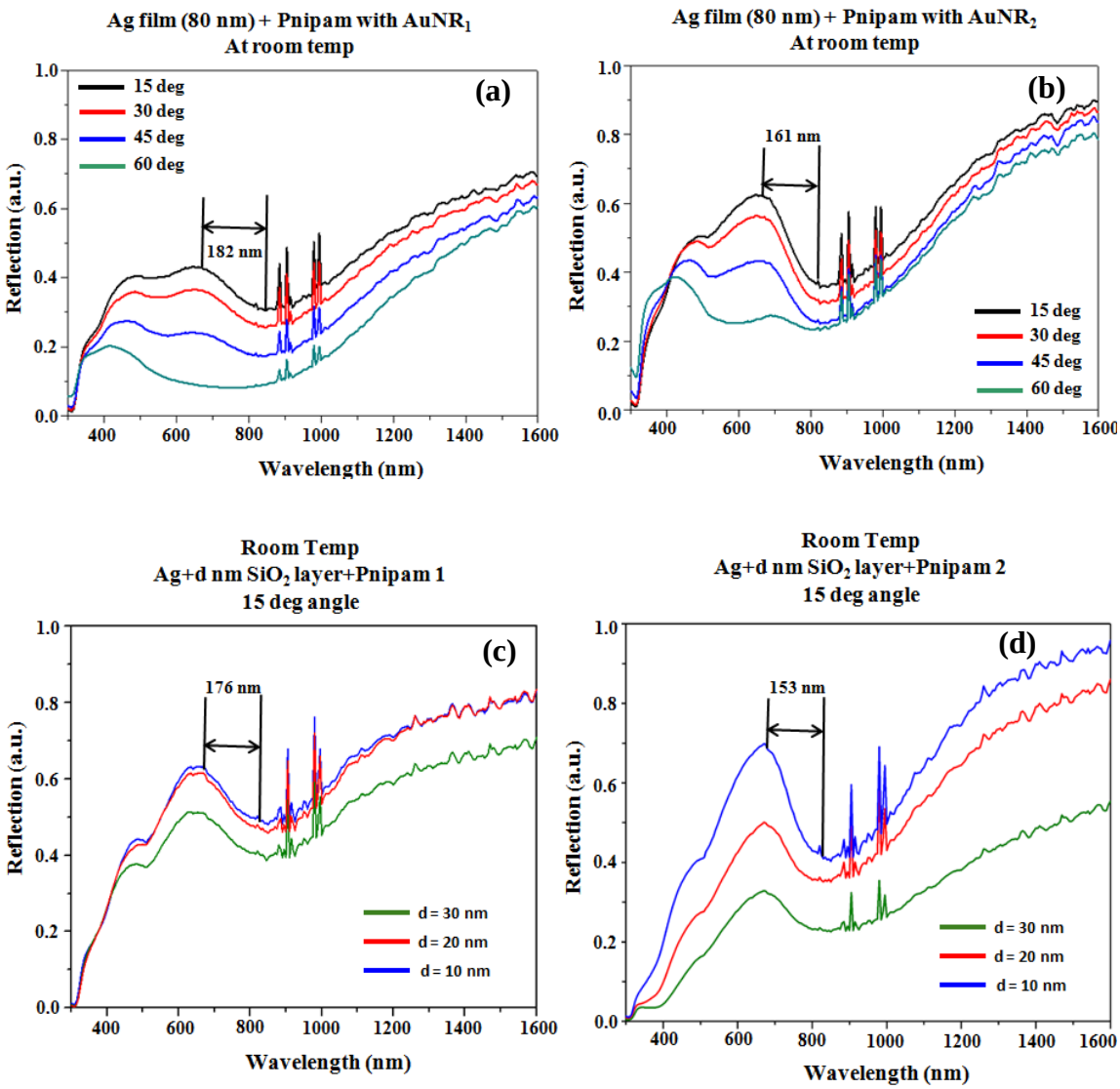


Fig. III.5. Reflection characteristics of (a) pNIPAM @ AuNRs1 and (b) pNIPAM @ AuNRs2 deposited on Ag film without any spacer layer. These two types of measurements are taken at room temperature and for variable angle. Reflection characteristics of (c) pNIPAM @ AuNRs1 and (d) pNIPAM @ AuNRs2 deposited on Ag film with the $SiO_2$ spacer layer of variable thickness. The measurement is done at room temperature and the angle of measurement foe these cases are 15 degree. Here for all the cases 80 nm thickness of Ag film is considered. For all these cases the variation of the Fano line-shape in room temperature is indicating the importance of different parameter, such as angle of measurements, aspect ratios of the AuNRs, different dielectric spacer layer thickness.

Here in the figure above we can see the Fano line-shape arising out of the interaction between the pNIPAM @ AuNRs and the Ag film in room-temperature. In panel (a) the reflection property of pNIPAM @ AuNRs1 (aspect ratio – 3.6) deposited on Ag film is shown. Here the base is 80 nm fully reflective Ag thin film. For this measurement there is no spacer dielectric layer in between the AuNRs and the Ag film. The measurement is done for variable collection angle among which 15 degree seems to give the stronger and steeper Fano line-

shape where the difference between the dip and the peak is approximately 182 nm. The same kinds of results are shown in panel (b) but in this case the AuNRs are of higher aspect ratio (3.9). Because of the higher aspect ratio of the AuNRs these are capable of localizing the incident electric field more densely and thus they have stronger interaction with the underlying Ag film compared to that in the panel (a). Thus in this case the Fano line-shape becomes steeper and stronger. In this case the dip-to-peak difference becomes 161 nm for 15 deg angle. For both the measurements shown in panel (a) and panel (b) for AuNRs1 and AuNRs2 respectively the measurement angle of 15 deg gives the stronger interaction. Thus to see the effect of insertion of dielectric spacer layer of variable thickness we chose 15 deg as the measurement angle. In panel (c) and (d) the effect of spacer layer thickness variation on Fano line-shape are shown. In later section numerical results will also be shown to give the idea about the effect for variable dielectric spacer layer thickness. For panel (c) and (d) the AuNRs of type 1 and type 2 are considered respectively. For the smallest dielectric spacer layer thickness the Fano response becomes the strongest one among the other for both kinds of AuNRs as that ensures the highest interaction in the given environment. Here also AuNRs of type 2 give the steeper Fano shape (dip-to-peak = 153 nm for 10 nm spacer thickness) with respect to the AuNRs of type 1 (dip-to-peak = 176 nm for 10 nm spacer thickness) because of the above said reason. If we compare here the strength of the Fano line shape shown in panel (a) and panel (c) for same kind of AuNRs then it is very clear that the insertion of the dielectric spacer layer gives more strength to the Fano response including a better control over tunability. The increase in the Fano strength can be realized from the comparison of dip-to peak parameter which is 182 nm without a spacer layer for 15 deg angle and with 10 nm of dielectric spacer layer for the same measurement angle that parameter goes down to 176 nm. The same is true for AuNRs of type 2 if we compare panel (b) and (d). Here the dip-to peak parameter is 161 nm without a spacer layer for 15 deg angle and with 10 nm of dielectric spacer layer for the same measurement angle that parameter is 153 nm. Here as all the measurements are taken at room temperature the effect of inter particle distance variation between the different AuNRs in the polymer matrix is neglected as in this condition the hydrodynamic diameter of Pnipam is conserved. So for this case (room temperature condition) the generation of the Fano line-shape and its variation is not controlled by the inter-AuNRs distance variation in the polymer matrix.

From these results it is very clear that the Fano system can respond to the changes in the refractive index of its surroundings. If we see the Fano response at room temperature without

any spacer layer and with the spacer layer of three different thicknesses for a particular angle and a particular type of AuNR then the line-shape variation is telling its sensitiveness towards the surrounding refractive index and the optical density variation near its vicinity. Thus this Fano system has a very good refractive index sensing capability. The numerical results described in later section will give an idea about the light field intensity enhancement factor for this Fano system and the electric field mapping which will indicate the hot-spot area. We already know that for refractive index sensing the intensity enhancement factor at the binding site of the analyte decide how sensitively the detection process can be done. According to the theoretical analysis (described later) this Fano system also is capable to have a giant intensity enhancement at the hot-spot region and thus expected to have a good sensitivity for the foreign molecule detection based on its capability to respond to the refractive index change.

Now this Fano line-shape can also be perturbed by varying the external temperature. The figure above shows all the results for room temperature and all those are useful for understanding our Fano system's capability to respond to the refractive index change in the surrounding media. The figure III.6 is describing the variation in the Fano response for different temperature which will be useful to have an idea about its sensitivity towards the change in external temperature.

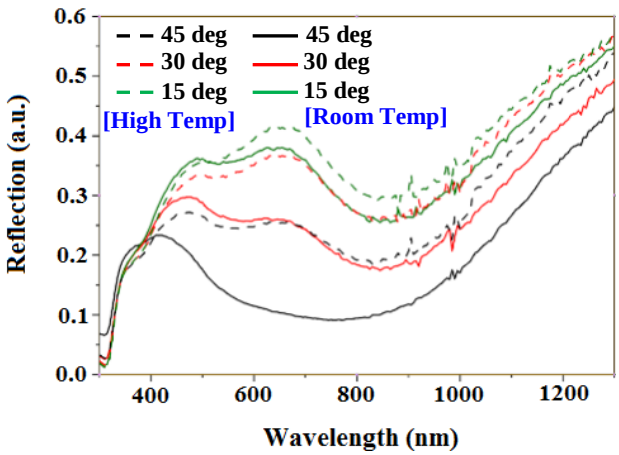


Fig. III.6. Variation of Fano line shape for varying temperature at different angle of measurements. Here the measurement angle is varied from 15 deg to 45 deg and for each case the change in variation of the Fano line-shape for room temperature and at 45$^{o}$C temperature (high temperature) has been recorded.

The figure III.6 is showing how the variation of external temperature affects the Fano line-shape for different measurement angle. Although for 15 deg measurement angle the Fano line-shape is steeper and stronger with respect to the other measurement angle, yet the change

in the Fano response for variation in external temperature becomes clearer for higher measurement angle. Here, for 45 deg angle, the change is highest, as for this angle in room temperature there is almost no Fano response but when the temperature reaches to 45$^{o}$C, a clear Fano response appears. Here it is worth to mention that the response shown in the figure III.6 is for the AuNRs of type 1. For AuNRs of type 2 the results of the temperature variation are of same trend. It has been seen that the Fano line-shape change due to the change in external temperature is clearer for AuNRs of type 1 than the type 2. This is because due to the smaller aspect ratio of type 1 AuNRs (L=54 nm; W=15 nm) the inter-particle separation of AuNRs in the polymer matrix is larger and they have more freedom for their arrangements in the matrix. Therefore, for this case when the hydrodynamic diameter of the polymer decreases due to the increase in external temperature, a noticeable difference in the Fano line-shape has been seen. On the other hand for AuNRs for type 2 due to their larger aspect ratio (L=74 nm; W=19 nm) they have less freedom in the polymer matrix upon temperature increase. When the temperature increases, the hydrodynamic diameter of the Pnipam polymer decreases and the attached AuNRs of type 2 come closer to each other and form a pseudo-metallic film over a wide wavelength range and a less steep Fano response, which is hard to detect. Thus for temperature sensing AuNRs of type 1 is better than the other while for refractive index sensing type 2 AuNRs with higher aspect ratio and higher capability of intensity enhancement is better. But here for both the temperature and refractive index sensing type 1 AuNRs seems to work better but optimization of AuNRs aspect ratio can be done later.

For all these reflection measurements at variable temperature a Calctec Hs unit is used as a Peltier heater which was installed on the sample stage of a variable angle spectroscopic ellipsometer during measurements. Because of this additional stage installation there is a decrease in the reflection intensity compared to the case of without the heating stage. That is why a small difference in the fano response has been seen in room temperature with and without this external heating stage.

Here Pnipam base is used to build this Fano plasmonic system to include the system's sensitivity towards the change in external temperature. The Pnipam has two thermodynamic states – swollen and collapsed state – with higher and lower hydrodynamic diameter – at room temperature and 40$^{o}$C and above respectively. That is why our Fano system also shows two distinctive states – at room temperature and around 40$^{o}$C. If one will opt a thermodynamically active base with more dynamic temperature controlling capability, then

the base as well as our system will have a lot of thermodynamic states at different temperature. In this way one can add tunability for the temperature variation where a small variation in the temperature can be detected. The two thermodynamic state of the Pnipam @AuNRs are shown in the figure below.

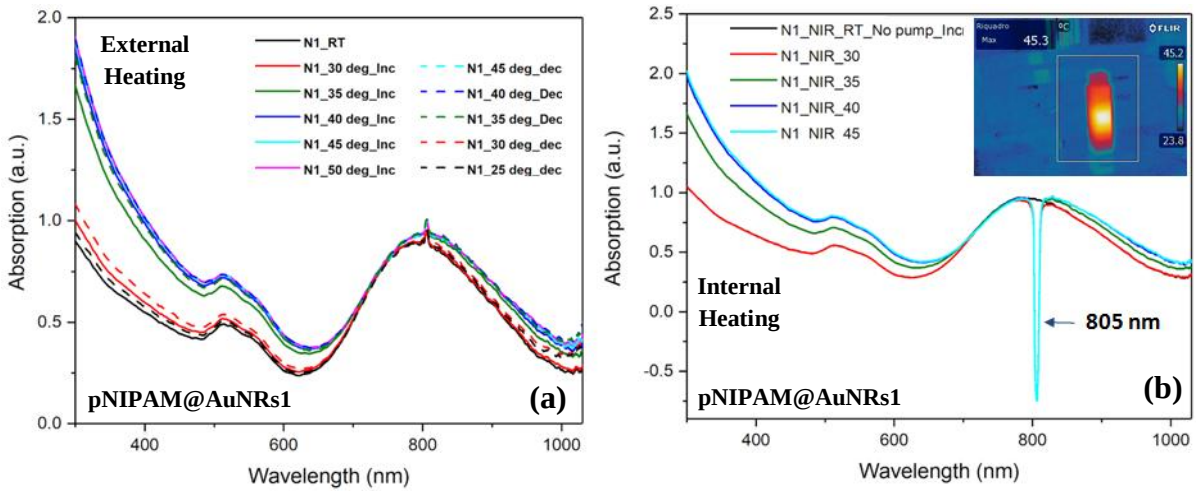


Figure III.7. (a) Response of pNIPAM @AuNRs1 aqueous solution at different temperatures. Here external heating source is used. The temperature is varied from 25$^{o}$C (RT: room temperature) to 50$^{o}$C by 5$^{o}$C. The absorption spectra are measured both for increasing and decreasing temperature. (b) Response of pNIPAM @AuNRs1 aqueous solution at different temperatures. Here laser is used to heat the sample over a much localized region and thus it is marked as internal heating. The temperature is varied from 25$^{o}$C (RT: room temperature) to 45$^{o}$C by 5$^{o}$C. The NIR laser (wavelength – 805 nm) is used for this internal heating. The inset figure shows a picture of the cuvette containing the pnipam@AuNRs1 sample during internal laser heating where the scale is describing the temperature of the sample

In the figure III.7 the two hydrodynamic state of the pnipam@AuNRs1 aqueous solution is very clear for both the external and the internal laser heating. For the external heating measurements here a temperature controlled TC125 by Quantum North-West is used that contains a Peltier-controlled cuvette holder (temperature-controlled range to -55 °C to +150 °C). For internal heating the sample is illuminated orthogonally by a continuous NIR laser at λ= 805 nm, with a beam diameter of (2.25 ± 0.22) mm. As the laser heating is much localized it is named as the internal heating. The photo-induced temperature variation was monitored by using a thermo-camera (E40 by FLIR) characterized by a sensitivity of 0.07 °C and a spatial resolution of 2.72 mrad. The camera control parameters were appropriately set to consider both environmental and materials properties (room temperature, level of humidity in the room, emissivity of the material). By detecting the highest temperature value T, corresponding to the central pixel of each hot-spot shown in the thermo graphic images, it

was possible to detect the characteristic temperature variation $\Delta T = T - T_0$ respect to the room temperature.

So till now from all the experimental results it is very clear that our Fano plasmonic system is capable to detect the change in the surrounding refractive index as well as the temperature. As this Pnipam sample has two stable thermodynamic states it can only sense these two temperature state. Instead of taking Pnipam if one takes any other polymer which can change their property over broad range of temperature (or any other physical parameters like stress, strain etc) continuously then that system may give response for a slight change in the external temperature or some other stimuli. But Pnipam is good for protein state identification as protein has similar kind of coil to globule transition property based on their thermodynamic condition. Although now we know the response of the Fano line-shape for the surroundings refractive index change and temperature change, yet to have idea about its sensitivity for the detection, we should be conscious about its capability to concentrate the electric field lines and thus the intensity enhancement at its hot spots. For this reason finite element method (FEM) based theoretical analysis has been done which is given below.

Numerical investigations based on FEM have been done to see the effect on coupling of AuNRs and Ag thin film upon changing the dielectric spacer layer thickness which is giving an idea about the Fano strength. The numerical investigation results are described in figure III.8 and III.9. In figure III.8 the electric field intensity enhancement capability of a single AuNR antenna of type 1 (L – 54 nm; W - 15 nm; aspect ratio 3.6:1) is shown.

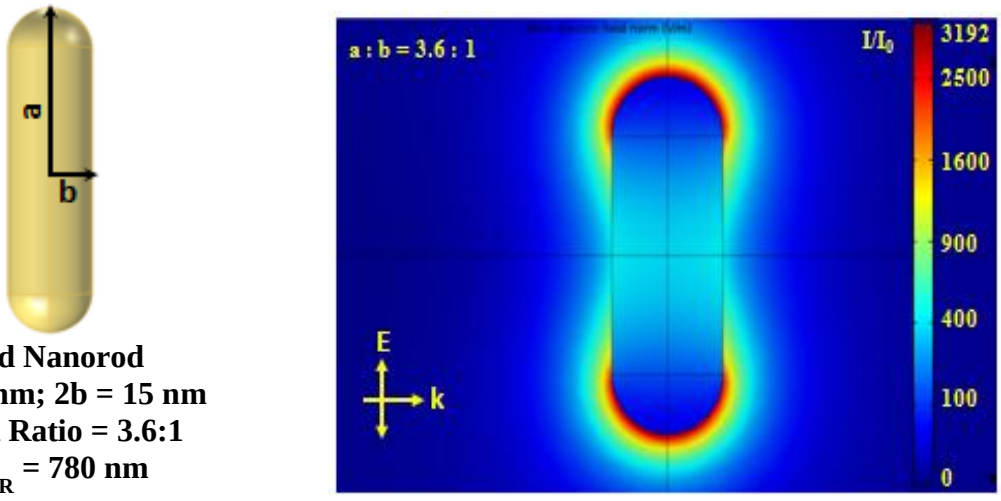


Figure III.8. Electric field intensity enhancement by a single AuNR antenna of type 1 which has length – 54 nm, width – 15 nm and thus the aspect ratio – 3.6:1. The intensity enhancement reaches to 3192 at its LSPR – 780 nm.

Here for AuNR1, the intensity enhancement goes upto 3192 times the incident intensity at its LSPR which is 780 nm. During this evaluation incident electric field is considered along the semi-major axis of the AuNR.

In figure III.9 the numerical simulation results for the Fano system is described. Here one can see that, for the Fano response arising from the interaction between the AuNRs (aspect ratio – 3.6:1) and the Ag thin film (majorly) the intensity enhancement can goes upto $10^{12}$ times (as $E/E_0 \sim 10^6$ and $I/I_0 = |E/E_0|^2$) which is way larger than the intensity enhancement by a single AuNR antenna of type 1 (aspect ratio - 3.6:1). Here for Fano line-shape the interaction between the AuNRs also play a role but the effect is less significant compared to the strength of interaction between the AuNRs and the Ag film. In figure III.9, the electric field mapping is plotted for four cases. Panel (a) describes the light interaction of the Fano system in absence of any spacer dielectric layer while panel (b), (c), and (d) describes the same in presence of 10 nm, 20 nm and 30 nm of $SiO_2$ spacer layer respectively. In each case 2 measurement angle has been chosen – 15 deg and 30 deg to show the angular light interaction dependence of the Fano system. From the figure below it is very clear that the plasmonic field strength is higher in the spacer layer. For 10 nm $SiO_2$ layer the field strength is higher than the 20 nm and 30 nm $SiO_2$ layer which can be verified also from the experimental results described in figure III.5. This is happening because of the decrease in the coupling strength for larger spacer layer thickness. If one compares the results shown in panel (a) and (b) then it becomes very clear that the presence of $SiO_2$ spacer layer is more useful than the case of "no spacer layer". The spacer layer helps to strengthen the localization of the field over a significant area (for the no spacer layer case the hot spot areas are more pointed compared to the case when the spacer layer is present) in between the AuNRs and Ag thin film which helps to get a stronger Fano resonance and thus steeper response. This fact can also be verified from the experimental results shown in figure III.5. The angular dependence becomes clearer for the higher thickness of the dielectric layer (20 nm and 30 nm) compared to the 10 nm dielectric layer thickness and also to the case when dielectric layer is absence. This is quite obvious and can be correlated with the experimental results. As the system is 3D symmetric, during FEM simulations it has been analyzed in 2D axisymmetrically to minimize the calculation time. The wavelength dependent optical constants of metals are taken from the Johnson and Christy measurements [45]. Here it is worth to mention that the wavelength at which these electric field mapping has been done is chosen from on the calculated reflection spectra. The reflection spectra of the Fano system with different spacer layer thickness are

shown in the figure III.10. In that figure for each case of dielectric spacer layer thickness, the asymmetric response is very clear and the Fano line-shape is seen to have a blue-shift upon increase in the spacer thickness describing the lower coupling between the two Fano components (AuNRs and Ag thin film).

So, all these results are indicating the usefulness of our Fano plasmonic system for detecting both the changes in refractive index and temperature of the surrounding media. Due to the extreme intensity enhancement capability in the spacer layer, this Fano line-shape is able to detect the presence of smaller protein molecule (in the spacer layer) along with the possibility of detecting their thermodynamic state helpful for protein engineering.

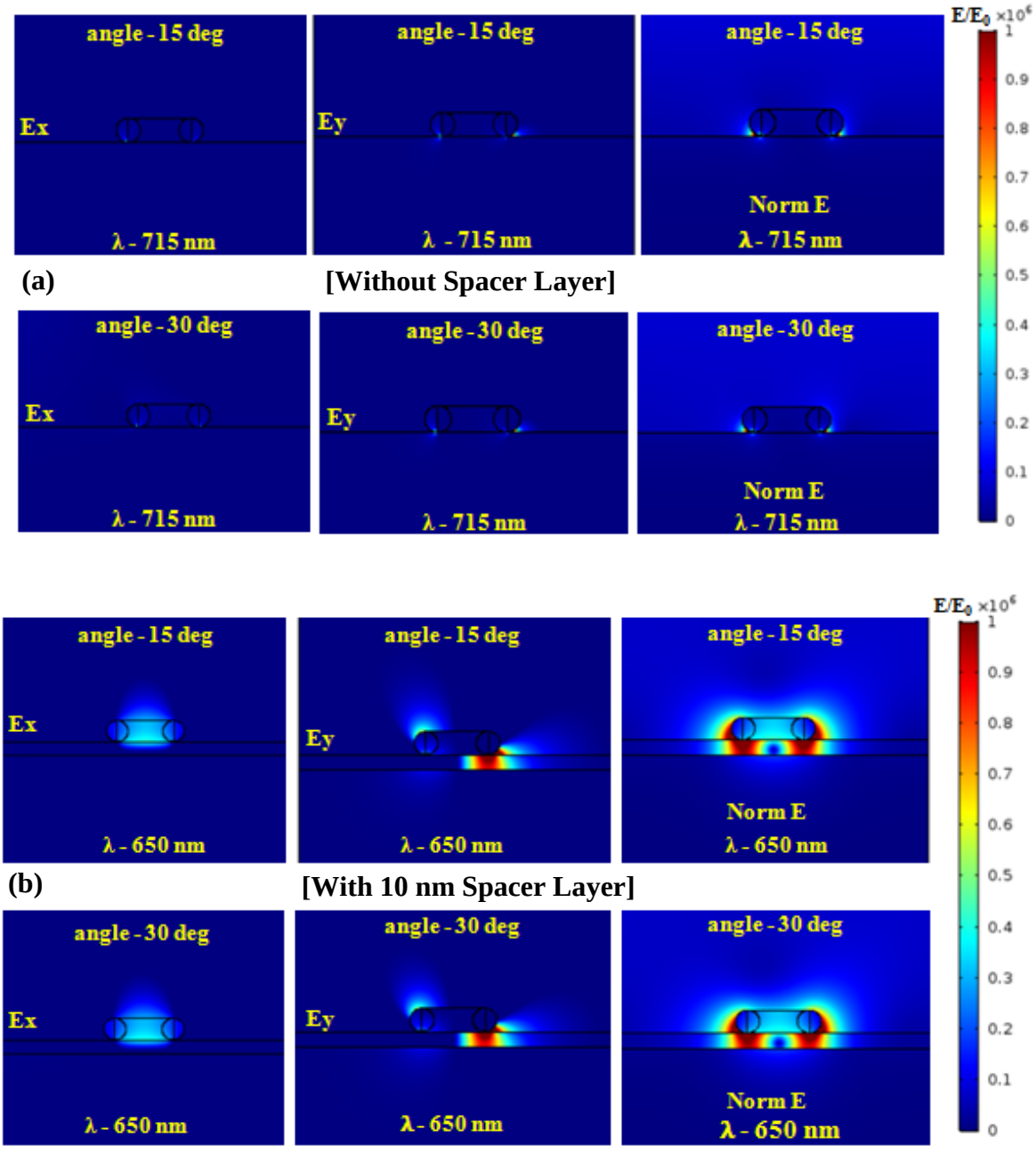

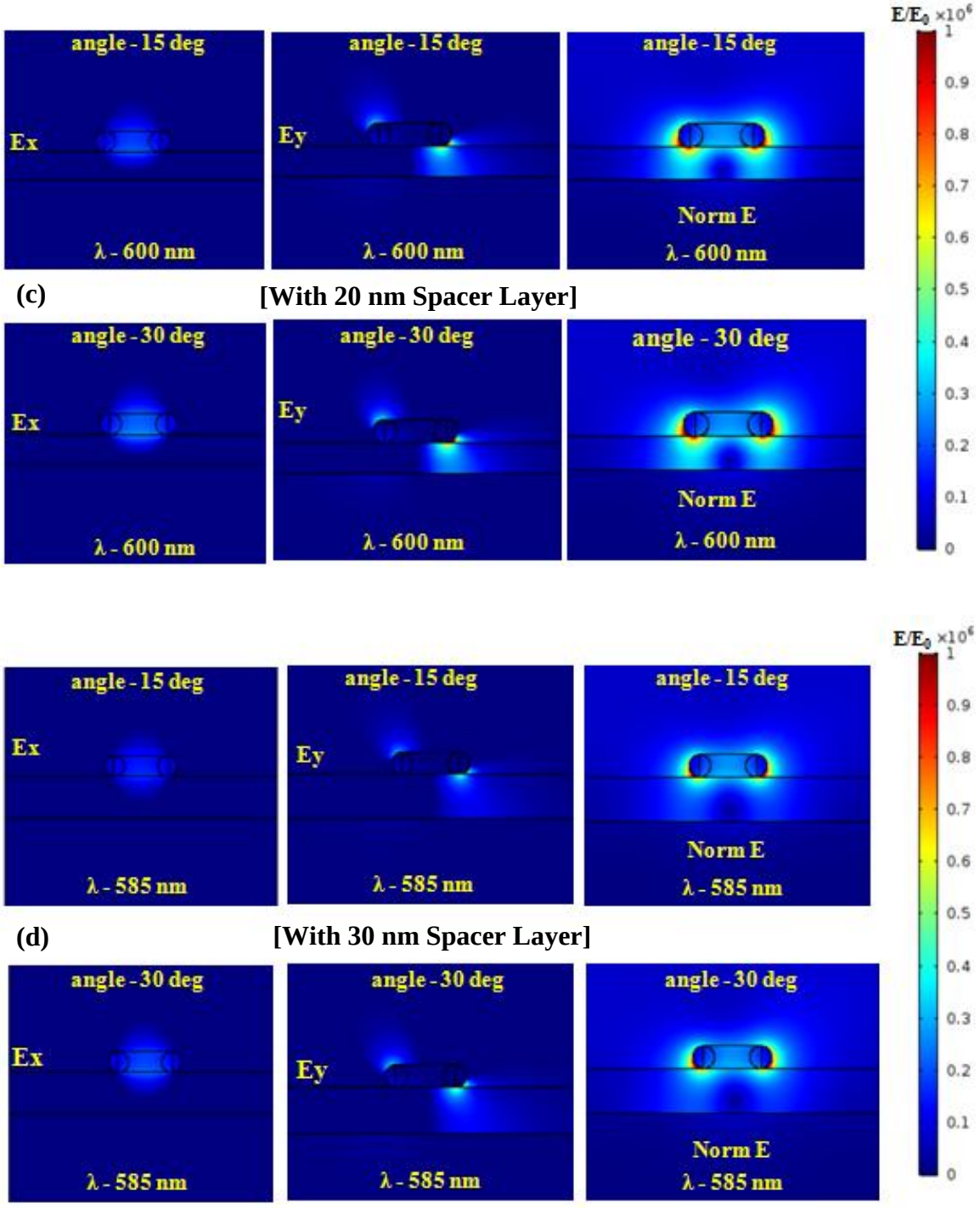


Figure III.9. FEM based comsol simulations for electric field mapping. The elctric field mappling for our Fano system (a) in absence of any dielectric spacer layer, (b) in presence of 10 nm of $SiO_2$ (c) 20 nm of $SiO_2$, and (d) 30 nm of $SiO_2$ spacer layer are described here. Every calculation is done here for both 15 deg and 30 deg incidence angle. The asymmetry in the electric field map here is pointing out towards its non-dopolar nature which is quite obvious as the system shows Fano response both experimentally and theoretically (figure III.10).

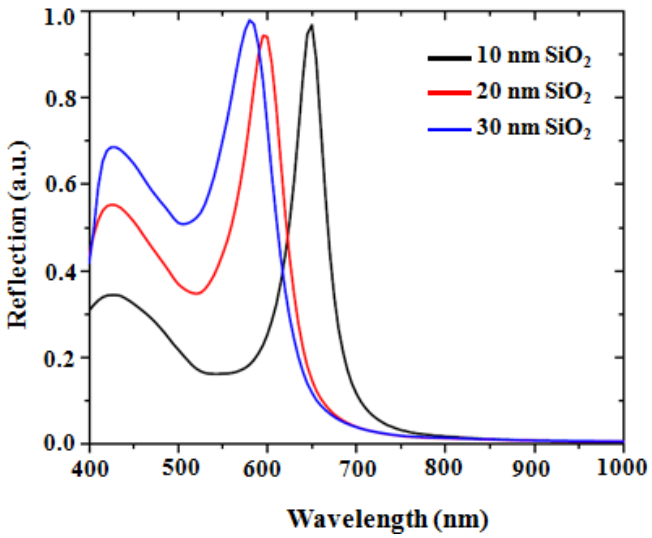


Figure III.10. Numerically evaluated reflection spectra of the plasmonic Fano system for variable spacer dielectric ($SiO_2$) layer thickness.

### III.3. Conclusion

In summary, we report experimental demonstration of a system whose characteristic line-shape is of Fano type. The system found to be capable of simultaneous realization of change in external temperature and refractive index. The Fano resonant structure has been made by depositing a hybrid nano-composite on silver thin film. The study has also been done by adding a dielectric silica spacer layer between the hybrid nano-composite and silver thin film. In the hybrid nano-composite plasmonic gold nanorods are synergistically integrated with Pnipam, a thermo-responsive polymer. Here Fano resonance arises from the near field coupling of narrow localised surface plasmon (LSP) mode of gold nanorods and broad surface plasmon (SP) mode of silver thin film. The coupling strength and thus the Fano line shape which depends on the separation between the two plasmonic systems is seen to be changed by incorporating the dielectric silica spacer layer and by changing the hydrodynamic diameter of the Pnipam with the variation of the external temperature. This indicates that the mentioned hybrid system has the capability to sense change in external temperature and refractive index simultaneously. Furthermore we have done numerical investigation based on finite element method (FEM) to see the effect on coupling of gold nanorods and silver thin film upon changing the separation distance between them which is giving an idea about the Fano strength variation. All these are suggesting that this system will not only help for the label-free detection of the foreign protein molecule but also for identifying the different thermodynamic states and reactions of the molecule which is crucial for protein engineering.

## III.4. References

[1] J. A. Schuller, E. S. Barnard, W. S. Cai, Y. C. Jun, J. S. White, and M. L. Brongersma, “Plasmonics for Extreme Light Concentration and Manipulation,” Nat. Mater., vol. 9, pp. 193−204, 2010.

[2] A. Bianconi Ugo Fano and shape resonances in X-ray and Inner Shell Processes" AIP Conference Proceedings (2002): (19th Int. Conference Roma June 24–28, 2002).

[3] Fano, U. (15 December 1961). "Effects of Configuration Interaction on Intensities and Phase Shifts". Physical Review. American Physical Society (APS). 124 (6): 1866–1878.

[4] Luk'yanchuk, Boris; Zheludev, Nikolay I.; Maier, Stefan A.; Halas, Naomi J.; Nordlander, Peter; Giessen, Harald; Chong, Chong Tow (23 August 2010). "The Fano resonance in plasmonic nanostructures and metamaterials". Nature Materials. Springer Nature. 9 (9): 707–715.

[5] Martínez-Argüello, A. M.; Martínez-Mares, M.; Cobián-Suárez, M.; Báez, G.; Méndez-Sánchez, R. A. (1 May 2015). "A new Fano resonance in measurement processes". EPL (Europhysics Letters). IOP Publishing. 110 (5): 54003.

[6] B. Luk'yanchuk, N. I. Zheludev, S. A. Maier, N. J. Halas, P. Nordlander, H. Giessen, and C. T. Chong, “The Fano Resonance in Plasmonic Nanostructures and Metamaterials,” Nat. Mater., vol. 9, pp. 707–715, 2010.

[7] B. Gallinet, and O. J. F. Martin, “Refractive Index Sensing with Subradiant Modes: A Framework To Reduce Losses in Plasmonic Nanostructures,” ACS Nano, vol. 7, no. 8, pp. 6978-6987, 2013.

[8] Y. Kong, Q. Wei, C. Liu, and S. Wang “Nanoscale temperature sensor based on Fano resonance in metal–insulator–metal waveguide,” Opt. Comm., vol. 384, pp. 85-88, 2017.

[9] N. Liu, M. Hentschel, T.Weiss, A. P. Alivisatos, and H. Giessen, “Three-dimensional plasmon rulers,” Science 332, 1407–1410 (2011).

[10] J. Ye, F. Wen, H. Sobhani, J. B. Lassiter, P. V. Dorpe, P. Nordlander, and N. J. Halas, “Plasmonic nanoclusters: Near field properties of the fano resonance interrogated with sers,” Nano Lett. 12, 1660–1667 (2012).

[11] T. T. Hoang, Q. M. Ngo, D. L. Vu, H. P. T. Nguyen. Controlling Fano resonances in multilayer dielectric gratings towards optical bistable devices Scientific Reports 2018, 8,

16404.

[12] X. Zhao, Z. Zhang, S. Yan. Tunable Fano Resonance in Asymmetric MIM Waveguide Structure. Sensors 2017, 17, 1494.

[13] C. Wu, A. B. Khanikaev, and G. Shvets, “Broadband Slow Light Metamaterial Based on a Double-Continuum Fano Resonance,” Phys. Rev. Lett. 106, 107403 (2011).

[14] B. Lukyanchuk, N. I. Zheludev, S. A. Maier, N. J. Halas, P. Nordlander H. Giessen and C. T. Chong. The Fano resonance in plasmonic nanostructures and metamaterials. Nature Materials 2010, 9, 707-715 (Review Article).

[15] Hessel, A. & Oliner, A. A. A new theory of Wood’s anomalies on optical gratings. Appl. Opt. 4, 1275–1297 (1965).

[16] Sarrazin, M., Vigneron, J. P. & Vigoureux, J. M. Role of Wood anomalies in optical properties of thin metallic films with a bidimensional array of subwavelength holes. Phys. Rev. B 67, 085415 (2003).

[17] Lee, H-T. & Poon, A. W. Fano resonances in prism-coupled square micropillars. Opt. Lett. 29, 5–7 (2004).

[18] Rybin, M. V. et al. Fano resonance between Mie and Bragg scattering in photonic crystals. Phys. Rev. Lett. 103, 023901 (2009).

[19] Tribelsky, M. I., Flach, S., Miroshnichenko, A. E., Gorbach, A. V. & Kivshar, Y. S. Light scattering by a finite obstacle and Fano resonances. Phys. Rev. Lett. 100, 043903 (2008).

[20] Miroshnichenko, A. E. et al. Fano resonances: A discovery that was not made 100 years ago. Opt. Phot. News 19, 48 (2008).

[21] Hao, F. et al. Symmetry breaking in plasmonic nanocavities: Subradiant LSPR sensing and a tunable Fano resonance. Nano Lett. 8, 3983–3988 (2008).

[22] Hao, F., Nordlander, P., Sonnefraud, Y., Van Dorpe, P. & Maier, S. A. Tunability of subradiant dipolar and Fano-type plasmon resonances in metallic ring/disk cavities: Implications for nanoscale optical sensing. ACS Nano 3, 643–652 (2009).

[23] Mirin, N. A., Bao, K. & Nordlander, P. Fano resonances in plasmonic nanoparticle aggregates. J. Phys. Chem. A 113, 4028–4034 (2009).

[24] Verellen, N. et al. Fano resonances in individual coherent plasmonic nanocavities. Nano Lett. 9, 1663–1667 (2009).

[25] Maier, S. A. The benefits of darkness. Nature Mater. 8, 699–700 (2009).

[26] Y. Sonnefraud, N. Verellen, H. Sobhani, G. A. E. Vandenbosch, V. V. Moshchalkov, P. Van Dorpe, P. Nordlander, and S. A. Maier, "Experimental realization of subradiant, superradiant, and fano resonances in ring/disk plasmonic nanocavities," ACS Nano 4, 1664–1670 (2010).

[27] Liu, N. et al. Plasmonic analogue of electromagnetically induced transparency at the Drude damping limit. Nature Mater. 8, 758–762 (2009).

[28] A. E. Miroshnichenko, S. Flach, and Y. S. Kivshar, "Fano resonances in nanoscale structures," Rev. Mod. Phys. 82, 2257–2298 (2010).

[29] S. Collin, G. Vincent, R. Haidar, N. Bardou, S. Rommeluere, and J.-L. Pelouard, "Nearly Perfect Fano Transmission Resonances Through Nanoslits Drilled in a Metallic Membrane," Phys. Rev. Lett. 104, 027401 (2010).

[30] F. J. Garcia-Vidal, L. Martin-Moreno, T. W. Ebbesen, and L. Kuipers, "Light Passing Through Subwavelength Apertures," Rev. Mod. Phys. 82, 729–787 (2010).

[31] N. A. Mirin, K. Bao, and P. Nordlander, "Fano Resonances in Plasmonic Nanoparticle Aggregates," J. Phys. Chem. A 113, 4028–4034 (2009).

[32] N. Verellen, Y. Sonnefraud, H. Sobhani, F. Hao, V. V. Moshchalkov, P. Van Dorpe, P. Nordlander, and S. A. Maier, "Fano resonances in individual coherent plasmonic nanocavities," Nano Lett. 9, 1663–1667 (2009).

[33] F. Hao, P. Nordlander, Y. Sonnefraud, P. Van Dorpe, and S. A. Maier, "Tunability of Subradiant Dipolar and Fano-Type Plasmon Resonances in Metallic Ring/Disk Cavities: Implications for Nanoscale Optical Sensing," ACS Nano 3, 643–652 (2009).

[34] C. Wu, A. B. Khanikaev, R. Adato, N. Arju, A. A. Yanik, H. Altug, and G. Shvets, "Fano-resonant asymmetric metamaterials for ultrasensitive spectroscopy and identification of molecular monolayers," Nat. Mater. 11, 69–75 (2012).

[35] J. A. Fan, C. Wu, K. Bao, J. Bao, R. Bardhan, N. J. Halas, V. N. Manoharan, P. Nordlander, G. Shvets, and F. Capasso, "Self-assembled plasmonic nanoparticle clusters," Science 328, 1135–1138 (2010).

[36] R. Singh, I. A. I. Al-Naib, M. Koch, and W. Zhang, “Sharp Fano Resonances in THz Metamaterials,” Opt. Express 19, 6320–6327 (2011).

[37] K. Bao, N. A. Mirin, and P. Nordlander, “Fano Resonances in Planar Silver Nanosphere Clusters,” Appl. Phys. A-Mater. Sci. Process. 100, 333–339 (2010).

[38] M. Hentschel, D. Dregely, R. Vogelgesang, H. Giessen, and N. Liu, “Plasmonic Oligomers: The Role of Individual Particles in Collective Behavior,” ACS Nano 5, 2042–2050 (2011).

[39] Benjamin Gallinet. Fano Resonances in Plasmonic Nanostructures: Fundamentals, Numerical Modeling and Applications. Doctoral Thesis, EPFL, 2012.

[40] Martin Frimmer and A. Femius Koenderink Spontaneous Emission Control in a Tunable Hybrid Photonic System arXiv:1212.6396v1 [physics.optics] 27 Dec 2012.

[41] Mustafa Yorulmaz, Anneli Hoggard, Hangqi Zhao, Fangfang Wen, Wei-Shun Chang, Naomi J. Halas, Peter Nordlander, and Stephan Link Absorption Spectroscopy of an Individual Fano Cluster. Nano Lett. 2016, 16, 6497−6503.

[42] Ryan T. Hill, Jack J. Mock, Yaroslav Urzhumov, David S. Sebba, Steven J. Oldenburg, Shiuan-Yeh Chen, Anne A. Lazarides, Ashutosh Chilkoti, and David R. Smith. Leveraging Nanoscale Plasmonic Modes to Achieve Reproducible Enhancement of Light. Nano Lett. 2010, 10, 4150–4154.

[43] S. Chatterjee, G. Palermo, T. Letsou, G. Lio, A. De Luca, and G. Strangi. Fano Resonance for simultaneous measurement of change in External Temperature and Refractive index. Proceedings of the 3rd International Conference of Theoretical and Applied Nanoscience and Nanotechnology (TANN'19) Ottawa, Canada – June 13-14, 2019 Paper No. 111.

[44] Y. N. Montecelo, M. C. Hermo, X. T. Kong, B. R. González, Z. Wang, M. P. Lorenzo, A. O. Govorov, and M. A. C. Duarte, “Traveling hot-spots in plasmonic photocatalysis: Manipulating interparticle spacing for real-time control of electron injection,” ChemCatChem., vol. 10, pp. 1-7, 2018.

[45] Johnson, P.B.; Christy, R.W. Optical Constants of the Noble Metals. Phys. Rev. B 1972, 6, 4370–4379.

# PART II

# PLASMONIC METASURFACE AND THEIR OPTICAL ACTIVITY

## Chapter I

## Metamaterials: A brief overview

**I.1. Introduction:** The light propagation in a material is controlled by the Refractive index ($n$). The refractive index (r.i.), $n$ is in general a complex number and is described by

$$n = n_1 + in_2 \qquad \text{(I.1)}$$

Where the real part of the refractive index $n_1$ controls the phase velocity of light in material and the imaginary part $n_2$ govern the optical losses in the medium [1]. Refractive index depends on two basic parameters – one is the electric permittivity, ε and the other one is the magnetic permeability, $\mu$ ($n^2 = \varepsilon\mu$). These two parameters, ε and $\mu$ control the coupling of the material with the electric and magnetic field lines of the incoming light respectively. Therefore, electric permittivity $\varepsilon$ and magnetic permeability $\mu$ are the two basic components of material which will decide the interaction of electric and magnetic lines of force of an incident electromagnetic (em) wave inside the material media and its nearby region. Based on the different values of permittivity and permeability all the materials can be classified into the following four general categories which is described in the figure I.1.

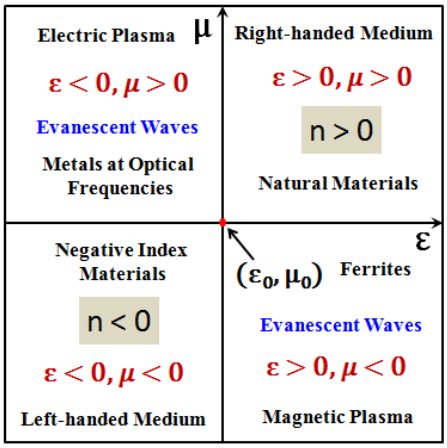


Figure I.1. Classification of materials on the basis of magnetic permeability ($\mu$) and electric permittivity ($\varepsilon$).

As depicted in the above figure the four types of material media are

i) **Natural Materials**: All the common natural materials belong to this class. These materials are also known as the right handed materials (RHM) For the materials of this category, $\varepsilon > 0$ and $\mu > 0$, resulting in the positive effective refractive index of the materials, i.e., $n > 0$. Depending on the value of positive $n$ the velocity of

the light inside the medium will be decided. Refractive index, *n* will also decide the bending of the em light when it will enter the material media. For a higher value of *n*, the propagation speed of the light will be slower inside the material and that will also help to have stronger deflection of light when it will enter the media. All the dielectric materials with positive real value of *n* possess this quality [2]. According to Maxwell, as these materials have $\varepsilon > 0$ and $\mu > 0$, electric field, E**,** magnetic field, H, and wave vector k can form a right-handed system, which can support forward propagating waves.

**ii)** **Electric Plasma:** All the known noble metals which have the metallic properties at the optical frequencies belong to this class. For these materials, $\varepsilon < 0$ and $\mu > 0$, resulting in the complex effective refractive index of the materials, i.e. $n = n_1 + in_2$ . Depending on the values of *n* here evanescent waves can also be generated for particular frequency of the incoming light. These materials are also known as epsilon-negative (ENG) materials or electrical metamaterials. In particular frequency ranges, other than noble metals (at optical wavelengths) few more natural materials can posses the electric plasma and thus belong to this category. Those materials are - some ferroelectric materials and doped semiconductors at specific frequencies below their plasma frequency $\omega_p$.

**iii)** **Negative Index Materials:** No natural materials belong to this class. This type of materials has been demonstrated only by constructing the artificial structures. These materials are also known as the left handed materials or left handed metamaterials (LHM). They are also popular as double-negative (DNG) materials. For such materials, $\varepsilon < 0$ and $\mu < 0$, resulting in the negative effective refractive index of the materials, i.e. $n < 0$. Because of their negative effective refractive index light behaves peculiarly inside and near the surface of the materials belong to this class. Here for these materials due to $n < 0$, phase velocity inside the material is negative. For these materials, E, H, and k form a left-handed system, which results in the opposite orientation of wave-vector k and Poynting vector S. These kinds of artificial materials were first proposed theoretically by Veselago and thus also popularly known as Veselago materials [3] or negative index materials (NIMs). But Sir John Pendry first proposed to use these materials for perfect lensing by using their extra-ordinary em properties [4]. That opened up a new fascinating research area – Metamaterials. After that by using their negative

refractive index property these artificial materials have been used for a variety of applications such as superlensing, cloaking, sensing, and many more which will be discussed in the later section (metamaterial section).

iv) **Magnetic Plasma:** Some natural ferrite materials or gyro-tropic materials (beyond optical frequencies) belong to this class. For these materials, $\varepsilon > 0$ and $\mu < 0$, resulting in the complex effective refractive index of the materials as $n = \sqrt{\varepsilon\mu}$. Depending on the value of the frequency of the incoming light evanescent waves can also be generated using these materials. These materials are also known as Mu-negative (MNG) materials or magnetic metamaterials. No natural material can possess all these features at the optical frequencies. The magnetic response of these materials quickly dies away beyond the microwave frequency range.

Here it is worth to mention that $(\varepsilon_0, \mu_0)$ is denoting a case where $\varepsilon \to 0$ and $\mu \to 0$. This situation can be achieved by constructing an artificial structure belonging to the metamaterial class. In that case, near-zero refractive index or zero refractive index can be achieved. Light inside these materials will have no spatial phase shift and will travel with an extremely large phase velocity. This kind of material will be useful for many different applications such as – for directional emission, tunneling waveguides, em cloaks, for making large-area single-mode devices etc. Inside these zero-refractive index materials, there is no phase change of the interacting em wave. Therefore, the light maintains a constant phase in this case and can be thought of as stretched out infinitely in space for long wavelengths. This uniform phase maintenance capability allows these materials to stretch or squash and twist or turn the interacting light without losing the energy which makes them useful for many applications especially for quantum computing.

The above discussion gives a brief idea about all the known class of materials. In this chapter Metamaterials and their unique features will be discussed which will be useful for the preceding chapters. The chapter contains also some brief discussion about the metasurface and the meta-atom. All those useful details about the metamaterials, metasurfaces and meta-atoms are given in the following sections.

**I.2. Metamaterial:**

A metamaterial is a heterogeneous hybrid artificial material which is fabricated and manipulated to have some extraordinary properties arising from the combination of its structure and composition beyond the classical material properties. The unit blocks of the

metamaterial structure should be of subwavelength size. No natural material belongs to this unique class of material. “Meta” is a Greek word which means “beyond” or “more than”. Thus the name itself is carrying the hidden powers of these materials with properties beyond traditional materials.

The metamaterials have several key features which are

(i) Metamaterials are artificial composite materials composed of different meta-atoms or meta-molecules (building blocks). Those meta-atoms or meta-molecules are either periodically or randomly (amorphous) arranged. Those unit structures are sometimes layered with or embedded into dielectric matrix;

(ii) The meta-atoms are smaller than the incident wavelength; therefore, metamaterials can be treated as homogeneous materials effectively at the operation frequency and can have effective material parameters. In other words an artificial material can be treated as metamaterials only when the operating frequency is maintained below a certain limit).

(iii) Metamaterials exhibit neither the properties of its constituent materials nor the properties of any known natural material (excluding some very specific, rare, and usually unstable substances such as plasma)

(iv) Metamaterials are naturally of dispersive nature provided some active elements are incorporated.

The above discussion is helpful to understand the metamaterials and their properties.

The metamaterial was first proposed theoretically by Victor Veselago [3]. But Sir John Pendry first demonstrated experimentally these materials [4-5] and also highlighted their application as a perfect lens. Later Smith and his co-workers demonstrated NIMs in microwave which is the first demonstration of NIMs in that optical range [6-7]. But for these materials negative ε and μ did not reach to a single point. After that a lot exciting metamaterials along with their application in different areas have been reported [8, 9]. In the following years, the optical metamaterials with negative refractive index in optical frequency range was reported for two kinds of metal-dielectric arrangements – one with the metallic rods immersed in the dielectric matrix environment [10, 11] and the other one with the metal-dielectric multilayer [8]. To overcome the optical losses in metamaterials mainly introduced by the metallic part in these materials people used a lot of tricks – incorporation of gain media, electromagnetic induced transparency (EIT) and searching many alternating materials (such as AZO, ITO etc) instead of metals [11-17]. To fabricate metamaterials researchers

adopted both top-down and bottom-up approaches, including self assembling of nanostructures [17-20]. Recently hyperbolic metamaterials with the characteristic hyperbolic dispersion become very popular. These kinds of materials have been fabricated by either constructing metal-dielectric stacks or using metallic nanorods (or nanowires) dipped in dielectric host [23-29]. These different kinds of metamaterials because of their special light manipulation properties become very much useful in different areas of applications such as cloaking, magnetic resonance imaging, perfect lensing, waveguiding, imaging, sensing, superlensing etc [2, 4, 5, 9, 12, 16-17, 21-23, 25-30].

Few examples of the different kinds of artificially designed metamaterials are given in the following figure (figure I.2).

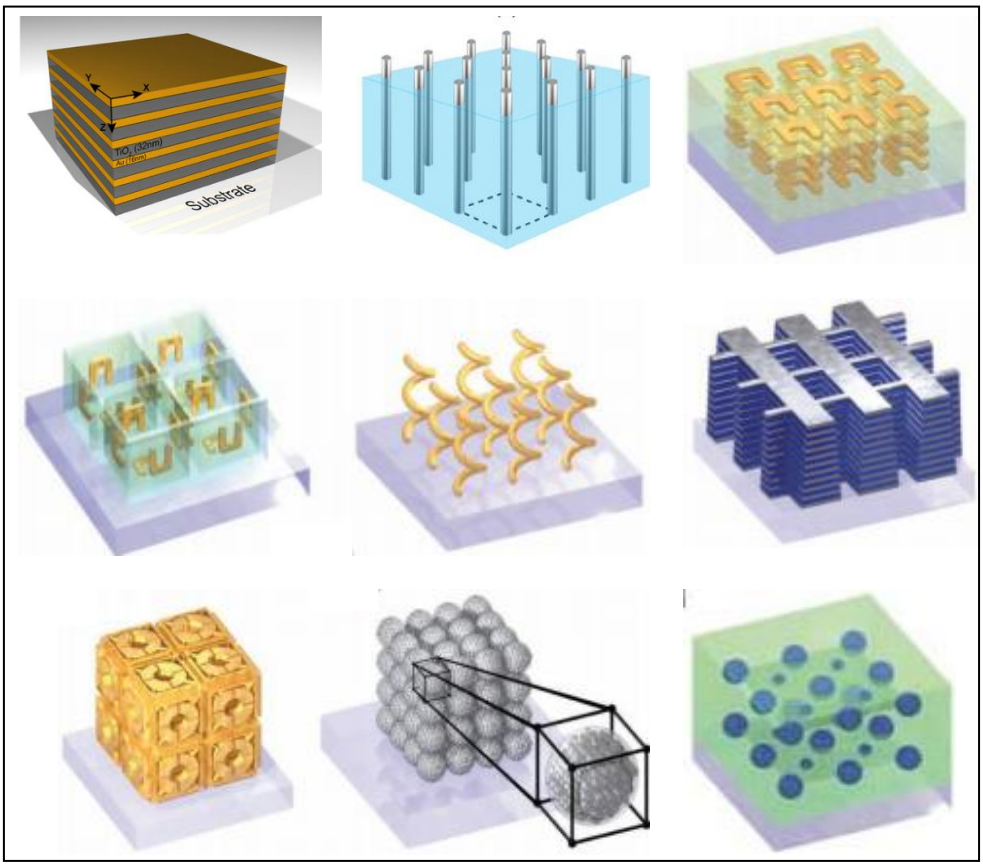


Figure I.2. Different types of metamaterials [31-34]

Now in the following few sections details about some popular metamaterials (HMMs and some anisotropic metamaterial) will be given along with some of the important theory related to those cases. These sections will be useful for the preceding chapters of this part to understand the thesis related works

**Hyperbolic Metamaterials (HMMs):**

Hyperbolic metamaterials (HMMs), a unique class of electromagnetic metamaterials have the hyperbolic dispersion. For these materials one of the principle components of their effective electric and/or magnetic tensor is of opposite sign to other two principle components and for this reason they show the hyperbolic dispersion. HMMs, because of their anisotropic character are useful for many applications such as spontaneous emission enhancement, superlensing, fluorescence management, biosensing and different other applications with the advantage of having high tunability, high figure of merit, ease of fabrication [23-26]. Few relevant and necessary information about the anisotropic mediums and hyperbolic materials (which is one kind of anisotropic metamaterial) are given below.

**Theory Related to Hyperbolic Metamaterials (HMMs):**

In electrically anisotropic media the electric displacement vector, D and the electric field, E are not always supposed to be parallel but the relation $D = \tilde{\varepsilon}(\omega, k)E$ remains always true for any condition. For a uniaxial media, where, $\varepsilon_x = \varepsilon_y = \varepsilon$ and $\varepsilon \neq \varepsilon_z$ we can find hyperbolic dispersion behaviour. If the isofrequency curve of the medium turns out to be hyperbolic, rather than of circular type as can be seen for the case of regular dielectric material, then that unusual anisotropic material can be defined as the hyperbolic metamaterial (HMM).

For HMMs, the electric displacement vector, D and the magnetic induction vector, B follows the following relations

$$D = \varepsilon_0 \tilde{\varepsilon} E \tag{I.2}$$

$$B = \mu_0 \tilde{\mu} H \tag{I.3}$$

Where, E is the electric field, H is the magnetic field, $\varepsilon_0$ is the vacuum permittivity, $\mu_0$ is the vacuum permeability, $\tilde{\varepsilon}$ is the effective permittivity tensor and $\tilde{\mu}$ is the effective permeability tensor. In the optical regime, as already discussed for these material $\mu$ reduces to a unit tensor and thus for these HMMs in the optical regime, the electric permittivity tensor $\tilde{\varepsilon}$ can be written as

$$\tilde{\varepsilon} = \begin{bmatrix} \varepsilon_{xx} & 0 & 0 \\ 0 & \varepsilon_{yy} & 0 \\ 0 & 0 & \varepsilon_{zz} \end{bmatrix} \tag{I.4}$$

Here the Cartesian frame of reference is considered to be oriented along the principle axes of the crystal. Here all the diagonal components depend on the angular frequency $\omega$ and are considered as positive. When we have the condition $\varepsilon_{xx} \neq \varepsilon_{yy} \neq \varepsilon_{zz}$ the medium becomes a

biaxial one. For a uniaxial media the condition reduces to, $\varepsilon_{xx} = \varepsilon_{yy} = \varepsilon$ and$\varepsilon_{zz} \neq \varepsilon$. For an isotropic medium $\varepsilon_{xx} = \varepsilon_{yy} = \varepsilon_{zz}$. Now in order to have the knowledge about the dispersion relation of em waves in any media, in absence of any source, we need to consider the following Maxwell's equation

$$\nabla \times \boldsymbol{E} = -\frac{\partial \boldsymbol{B}}{\partial t} \tag{I.5}$$

$$\nabla \times \boldsymbol{H} = \frac{\partial \boldsymbol{D}}{\partial t} \tag{I.6}$$

Now to solve the above equations, one can consider the electric field and magnetic field components as

$$E = E_0 e^{(\omega t - \boldsymbol{k}.\boldsymbol{r})} \tag{I.7}$$

$$H = H_0 e^{(\omega t - \boldsymbol{k}.\boldsymbol{r})} \tag{I.8}$$

Taking into account the above two electric and magnetic field components the solution of the Maxwell' equations gives the following relations

$$\boldsymbol{k} \times \boldsymbol{E} = \omega \mu \boldsymbol{H} \tag{I.9}$$

$$\boldsymbol{k} \times \boldsymbol{H} = -\omega \varepsilon \boldsymbol{E} \tag{I.10}$$

These two equations are true for isotropic medium and also for anisotropic medium.

For an isotropic medium, the dispersion relation is linear, and the isofrequency surface is of symmetric spherical shape which follows the relation

$$k_x^2 + k_y^2 + k_z^2 = \frac{\omega^2}{c^2} \tag{I.11}$$

Where $\omega$the angular frequency of the em wave and c is is the speed of light in vacuum.

For a uniaxial medium, if one considers the propagation of an extraordinary wave (TM polarization), then the isofrequency relation becomes

$$\left(\frac{k_x^2 + k_y^2}{\varepsilon_\perp} + \frac{k_z^2}{\varepsilon_{||}}\right) = \frac{\omega^2}{c^2} \tag{I.12}$$

Here $\varepsilon_{xx} = \varepsilon_{yy} = \varepsilon_{||}$ and $\varepsilon_{zz} = \varepsilon_\perp$. The isofrequency surface of such type of anisotropic material (uniaxial medium) is ellipsoid. For extreme anisotropy, $\varepsilon_{||}.\varepsilon_\perp < 0$, the isofrequency surface changes from the ellipsoid shape to an open hyperboloid. In this case, that anisotropic material behaves like a metal in one direction and in the other direction it acts like a dielectric or an insulator [23].

**Categorization of different materials:**

Based on the sign of components of the dielectric tensor of a material, it can belong to one of the following categories.

1. **Dielectric and metals**: When all the three diagonal components of the dielectric tensor ($\varepsilon_{xx}, \varepsilon_{yy}, \varepsilon_{zz}$) are negative, then the material is considered as a metal through which propagating wave are not allowed to travel. If all the three diagonal components of the dielectric tensor are positive, then the material is considered to be a dielectric material. The isofrequency surface of a dielectric material is of spherical shape.
2. **Type I HMMs:** When one of the diagonal components of the dielectric tensor is negative and the other two are positive, i.e., $\varepsilon_{zz} < 0$ and $\varepsilon_{xx}, \varepsilon_{yy} > 0$, then the material is known as a Type I hyperbolic metamaterials. These materials have the advantage of having low-loss because of their dominated dielectric nature.
3. **Type II HMMs:** If two of the diagonal components of the dielectric tensor are negative and the third one is positive, i.e., $\varepsilon_{xx}, \varepsilon_{yy} < 0$ and $\varepsilon_{zz} > 0$ then the material is known as the type II hyperbolic metamaterials. These metamaterials have higher optical losses and high impedance mismatch with respect to the vacuum due to their dominated metallic behaviour [24].

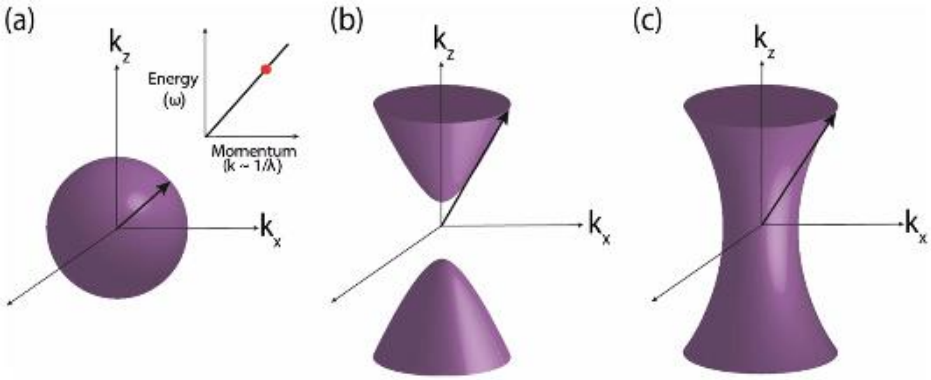


Figure I.3. (a) Spherical isofrequency surface for an isotropic dielectric. Inset shows energy versus momentum relationship with the red dot indicating the operating frequency for the derived isofrequency surface. (b) Hyperboloid isofrequency surface for a uniaxial medium with an extremely anisotropic dielectric response ($\varepsilon_{zz} < 0$; $\varepsilon_{xx}, \varepsilon_{yy} > 0$) (c) Hyperboloid isofrequency surface for an extremely anisotropic uniaxial medium with two negative components of the dielectric tensor ($\varepsilon_{xx}, \varepsilon_{yy} < 0$; $\varepsilon_{zz} > 0$). The (b) Type I and (c) Type II metamaterials can support waves with infinitely large wavevectors in the effective medium limit. Such waves are evanescent and decay away exponentially in vacuum [33].

The above figure I.3 is showing the isofrequency surfaces of dielectrics, type I HMMs and type II HMMs.

As already written HMMs can be fabricated both by top-down and bottom-up approaches. The two very popular style of designing these artificial HMMs are –

i) Multilayer structure containing alternating metal and dielectric layers

ii) Metallic nanowire (or nanorods) structures submerged in a dielectric host.

These two kinds of HMMs are depicted in the figure below.

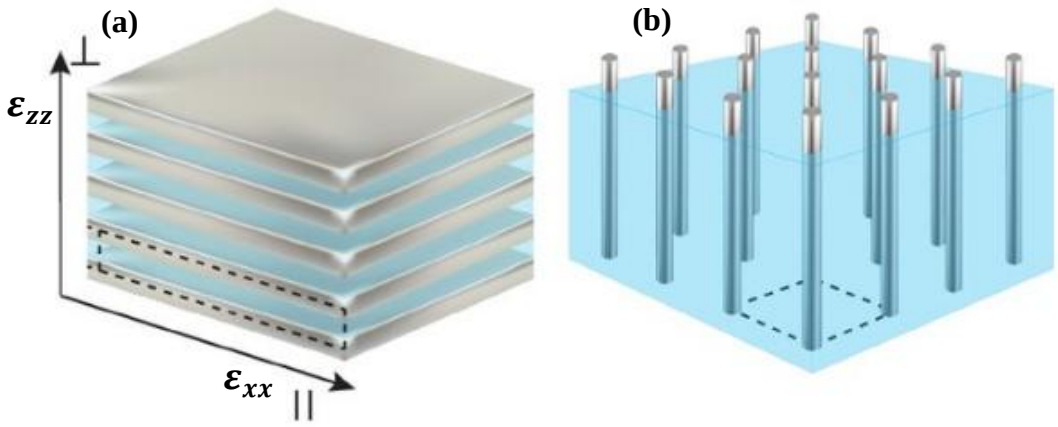


Figure I.4. (a) Multilayer structure containing alternating metal and dielectric layers. (b) Metallic nanowire (or nanorods) structures submerged in a dielectric host [33].

Type I and type II HMMs can support modes with infinitely large wavevectors if we consider the effective medium approximation which is valid for wavelengths below a certain limit [28-29]. These high k modes originate from the coupled surface plasmon polaritons from the metal dielectric multilayers [28-29].

After this general discussion of metamaterials the very important concept regarding the metamaterials is discussed below – which is about the anisotropic medium. Metamaterials belongs to this category of "anisotropic medium" and thus deserve a brief discussion.

**Anisotropic medium:**

According to Landau, the permeability (μ) is equal to unity in the optical regime. For an isotropic medium, permeability

$$\mu = 1 + 4\pi\left(\frac{M}{H}\right) \qquad \text{(I.13)}$$

Where, M and H are the magnetic dipole moment per unit volume and the externally applied magnetic field respectively.

It's well known that M≃0 at optical frequencies [21]. Furthermore, it is a well-known fact that the propagation of wave in any media (linear/non-linear) can be described by electric permittivity (ε) only and there is no requirement of μ, and H in this case. Thus a system can be described by the following relation, where the electric displacement vector, D is defined as,

$$D = \tilde{\varepsilon}(\omega, k)E \qquad \text{(I.14)}$$

Where, the dielectric tensor $\tilde{\varepsilon}(\omega, k)$ contains the materials' magnetic response. These systems, due to their spatial dispersion are categorized as the anisotropic materials [22]. According to Agranovich, for a left-handed anisotropic material as we know, $\varepsilon < 0$, and $\mu < 0$, evaluation of $\tilde{\varepsilon}(\omega, k)$ reveals that there is no magnetic dipole resonance in these materials. This conclusion helps to develop a special group of metamaterials – the Hyperbolic Metamaterials (HMMs).

This completes the required details of the metamaterials. A brief discussion about the metasurface and meta-atoms is given below.

**I.3. Metasurface:** A metasurface is an artificially fabricated sheet of materials (confinement in one dimension) with sub-wavelength thickness. Metasurface can also be considered as the two-dimensional counterpart of the metamaterial [35-36].

The various ways for defining a metasurface is

1. "An alternative approach that has gained increasing attention in recent years deals with one- and two-dimensional (1D and 2D) plasmonic arrays with subwavelength periodicity, also known as metasurfaces. Due to their negligible thickness compared to the wavelength of operation, metasurfaces can (near resonances of unit cell constituents) be considered as an interface of discontinuity enforcing an abrupt change in both the amplitude and phase of the impinging light" [37].
2. , "Our results can be understood using the concept of a metasurface, a periodic array of scattering elements whose dimensions and periods are small compared with the operating wavelength" [38].
3. "Metasurfaces based on thin films". A highly absorbing ultrathin film on a substrate can be also considered as a metasurface, if the properties are not similar to the natural materials [36]. A thin metallic film which can be seen in superlens can be considered as the early type of metasurface [39].

Recently metasurfaces have been fabricated in many different ways such as plasmonic metasurfaces [35, 37, 40], geometric phase based metasurface [41, 42], impedance sheet based metasurfaces [43, 44], even a thin film can also be treated as a metasurface in certain cases.

The metasurfaces can be used in many different areas of application such as – superlens, planar lens or flat lens [36, 39, 40], vortex generator [37], anti-reflective coatings, sensing [35], perfect light absorber [43], beam deflector, axicon and so on [42] and several others.

**I.4. Meta-atoms:** Meta-atoms are considered to be the smallest building blocks of the 2D metasurfaces or the 3D metamaterials. These structures are of sub wavelength size. The meta-atoms being the unit blocks of a metasurface or a metamaterial, can tailor the amplitude and phase of the incident wave which helps to manipulate the em wave inside those materials [45]. This can be done by controlling their geometry. Thus these meta-atoms are suitable for all those kinds of applications which fit the metasurface and the metamaterial that has been already written in previous sections.

With all these discussion these chapter is complete and will be helpful for understanding the features of the comings chapters.

**I.5. Reference:**

[1] V. M. Shalaev. Optical negative-index metamaterial. Nat. Photon. 2007, 1, 41-48.

[2] H. Liu, K. J. Webb. Resonance cones in cylindrically anisotropic metamaterials: a green function analysis. Opt. Lett. 2011, 36, 379-381.

[3] V. G. Vaselago. The electrodynamics of substances with simultaneously negative values of Eps and Mu. Sov. Phys. Usp. 1968, 10, 509.

[4] J. B. Pendry. Negative Refraction Makes a Perfect Lens. Phys. Rev. Lett. 2000, 85, 3966-3969.

[5] J. B. Pendry, A. J. Holden, W. J. Stewart, and I. Youngs. Extremely low frequency plasmons in metallic mesostructures. Phys. Rev. Lett. 1996, 76, 4773-4776.

[6] D. R. Smith, W. J. Padilla, D. C. Vier, S. C. Nemat-Nasser, and S. Schultz. Composite medium with simultaneously negative permeability and permittivity. Phys. Rev. Lett. 2000, 84, 4184-4187.

[7] R. A. Shelby, D. R. Smith, and S. Schultz. Experimental verification of a negative index of refraction. Science, 2001, 292 (5514), 77-79.

[8] S. Zhang, W. Fan, N. C. Panoiu, K. J. Malloy, R. M. Osgood, and S. R. J. Brueck. Experimental demonstration of near-infrared negative-index metamaterials. Phys. Rev. Lett. 2005, 95, 137404.

[9] M. C. K. Wiltshire, J. B. Pendry, I. R. Young, D. J. Larkman, D. J. Gilderdale and J. V. Hajnal. Microstructured magnetic materials for RF flux guides in magnetic resonance imaging. Science 2001, 291, 849-851.

[10] V. M. Shalaev, W. Cai, U. K. Chettiar, H. –K. Yuan, A. K. Sarychev, V. P. Drachev, and A. V. Kildishev. Negative index of refraction in optical metamaterials. Opt. Lett. 2005, 30 (24), 3356-3358.

[11] G. Dolling, C. Enkrich, M. Wegener, C. M. Soukoulis, and S. Linden. Low-loss negative-index metamaterial at telecommunication wavelengths. Opt. Lett. 2006, 31(12), 1800-1802.

[12] V. A. Podolskiy, and E. E. Narimanov. Near-sighted superlens. Opt. Lett. 2005, 30 (1), 75-77.

[13] V. P. Drachev, U. K. Chettiar, A. V. Kildishev. H. –K. Yuan, W. Cai, and V. M. Shalaev. The ag dielectric function in plasmonic metamaterials. Opt. Express 2008, 16 (2), 1186-1195.

[14] S. Xiao, V. P. Drachev, A. V. Kildishev, X. Ni, U. K. Chettiar, H. –k. Yuan, and V. M. Shalaev. Loss-free and active optical negative-index metamaterials Nature 2010, 466 (7307) 735-738.

[15] A. D. Boardman, V. V. Grimalsky, Y. S. Kivshar, S. V. Koshevaya, M. Lapine, N. M. Litchinitser, V. N. Malnev, M. Noginov, Y. G. Rapoport, and V. M. Shalaev. Active and tunable metamaterials. Laser & Photonics Review 2011, 5 (2), 287-307.

[16] S. A. Ramakrishna, and J. B. Pendry. Removal of absorption and increase in resolution in a near-field lens via optical gain. Phys. Rev. B 2003, 67, 201101.

[17] A. Boltasseva, and V. M. Shalaev. Fabrication of optical negative-index metamaterials: Recent advances and outlook. Metamaterials 2008, 2 (1) 1-17.

[18] X. Zhao. Bottom-up fabrication methods of optical metamaterials. J. Mater. Chem. 2012, 22, 9439-9449.

[19] C. R. Simovski, and S. A. Tretyakov. Model of isotropic resonant magnetism in the visible range based on core-shell clusters. Phys. Rev. B 2009, 79, 045111.

[20] A. Alu, A. Salandrino, and N. Engheta. Negative effective permeability and left-handed materials at optical frequencies. Opt. Express 2006, 14 (4), 1557-1567.

[21] L. D. Landau, and E. M. Lifshitz. Chapter V – "Ferromagnetism and Antiferromagnetism" In L. D. Landau, and E. M. Lifshitz, editors, Electrodynamics of Continuous Media (Second Edition Revised and Enlarged), volume 8 of Course of Theoretical Physics, pages 130-179. Pergamon, Amsterdam, second edition revised and enlarged edition, 1984. ISBN 978-0-08-030275-1.

[22] V. M. Agranovich, Y. R. Shen, R. H. Baughman, and A. A. Zakhidov. Linear and nonlinear wave propagation in negative refraction metamaterials. Phys. Rev. B 2004, 69, 165112.

[23] P. Shekhar, J. Atkinson, and Z. Jacob. Hyperbolic metamaterials: fundamentals and applications. Nano Convergence 2014, 1(1), 14.

[24] A. Poddubny, I. Iorsh, P. Belov, and Y. Kivshar. Hyperbolic metamaterials. Nat. Photon 2013, 7(12), 948-957.

[25] D. Lu, and Z. Liu. Hyperlenses and metalenses for far-field super-resolution imaging. Nat. Commun. 2012, 3, 1205.

[26] Y. Guo, and Z. Jacob. Thermal hyperbolic metamaterials. Opt. Express 2013, 21 (12), 15014-15019.

[27] T. Taubner, D. Korobkin, Y. Urzhumov, G. Shvets, and R. Hillenbrand. Near-field microscopy through a SiC superlens. Science 2006, 313 (5793), 1595-1595.

[28] A. J. Hoffman, L. Alekseyev, S. S. Howard, K. J. Franz, D. Wasserman, V. A. Podolskiy, E. E. Narimanov, D. L. Sivco, and C. Gmachl. Negative refraction in semiconductor metamaterials. Nat. Mater. 2007, 6 (12), 946-950.

[29] J. Elser, V. A. Podolskiy, I. Salakhutdinov, and I. Avrutsky, Nonlocal effects in effective-medium response of nanolayered metamaterials. Appl. Phys. Lett. 2007, 90 (19), 191109.

[30] Vehmas J (2015) Transmission-line metamaterials, bianisotropy, and transmission-line bianisotropy. Doctoral Dissertations, Aalto University, Unigrafia Oy, Helsinki.

[31] K. V. Sreekanth, A. De Luca , G. Strangi, Experimental demonstration of surface and bulk plasmon polaritons in hypergrating. Sci Rep. 2013, 3, 3291.

[32] S. Molesky, C. J. Dewalt, Z. Jacob. High Temperature Epsilon-Near-Zero and Epsilon-Near-Pole Metamaterial Emitters for Thermophotovoltaics. Optics Express 2012, 21, A96-A110.

[33] P. Shekhar, J. Atkinson, Z. Jacob. Hyperbolic metamaterials: Fundamentals and applications. Nano Convergence 2014, 1, 1-17.

[34] C. M. Soukoulis, M. Wegener. Optical Metamaterials - More Bulky and Less Lossy. Science 2010, 330 (17), 1633-1634.

[35] Zeng, S. et al. Graphene-gold metasurface architectures for ultrasensitive plasmonic biosensing. Advanced Materials. 2015, 27: 6163–6169.

[36] N. Yu, F. Capasso. Flat optics with designer metasurfaces. Nat. Mater. 2014, 13, 139–150.

[37] A. Pors, I. S. Bozhevolnyi. Plasmonic metasurfaces for efficient phase control in reflection. Optics Express. 2013, 21: 27438.

[38] P. –C. Li, Y. Zhao, A. Alu, T. E. Yu, Experimental realization and modeling of a subwavelength frequency-selective plasmonic metasurface. Appl. Phys. Lett. 2011, 99: 221106.

[39] Pendry, J. B. Negative Refraction Makes a Perfect Lens. Physical Review Letters. 2000, 85 (18): 3966–9.

[40] Verslegers, Lieven; Fan, Shanhui. Planar Lenses Based on Nanoscale Slit Arrays in a Metallic Film. Nano Lett. 2009, 9, 235–238.

[41] Yu, Nanfang; Genevet, Patrice; Kats, Mikhail A.; Aieta, Francesco; Tetienne, Jean-Philippe; Capasso, Federico; Gaburro, Zeno. Light Propagation with Phase Discontinuities: Generalized Laws of Reflection and Refraction. Science. 2011, 334, 333–337.

[42] Lin, Dianmin; Fan, Pengyu; Hasman, Erez; Brongersma, Mark L. Dielectric gradient metasurface optical elements. Science. 2014, 345, 298–302.

[43] Pfeiffer, Carl; Grbic, Anthony. Metamaterial Huygens' Surfaces: Tailoring Wave Fronts with Reflectionless Sheets. Phys. Rev. Lett. 2013, 110, 197401.

[44] Felbacq, Didier Impedance operator description of a metasurface Mathematical Problems in Engineering. 2015: 473079.

[45] J. Ding, S. An, B. Zheng, H. Zhang, Multiwavelength Metasurfaces Based on Single-Layer DualWavelength Meta-Atoms: Toward Complete Phase and Amplitude Modulations at Two Wavelengths. Advanced Optical Materials 5, 1700079 (2017).

# CHAPTER II

# ALUMINIUM DOPED ZNO NANOPILLARS ARRAYS

# Chapter IIA

# Aluminium doped ZnO hollow nanopillars arrays for gas sensing

**IIA.1. Introduction:** Hydrogen ($H_2$) gas is a highly combustible diatomic gas with low ignition energy and therefore, when hydrogen gas leaks into external air, it may spontaneously ignite the environment and can cause an explosion, which is extremely hazardous. Hydrogen gas can set into fire within its concentration range of 4 to 75 % [1]. As $H_2$ is a tasteless, non-toxic, non-metallic gas, it is hard to detect by human sense. Apart from the danger of explosion, hydrogen possesses a number of threats, such as detonations and fires when mixed with air, asphyxiation in its pure, oxygen-free form, [2] frostbite ability associated with very cold liquid cryogenic hydrogen [3]. Therefore, for safety, the detection of a low concentration of hydrogen within a very short time is crucial in industries where it is considered as an obvious component or a by-product.

For large scale industrial $H_2$ Gas sensing chromatography and mass spectrometer are very well-known techniques. But these techniques cannot be applicable in the miniaturized systems such as in the food industries and for various disease detection where the detection of ultra-low concentration of exhaling hydrogen has to be detected over a smaller area [4-6]. Until now, many groups reported some nanophotonic and nanoplasmonic system-based optical hydrogen sensors which work by controlling light at the sub-wavelength scale using their metallic components [5, 7-8]. However in most of the cases the metallic system posses a disadvantage of having high optical losses while metallic hydride photonic systems are relatively selective. Moreover, the fabrication of those sensing systems is not only based on lithography but they also possess a lot of limitations such as high cost, low throughput, and inclined to imperfections, which prohibits those systems to become one of the promising commercialized miniaturized hydrogen sensors [9-10].

As losses are inherent to the plasmonic substance, alternative materials with lower optical losses should be adopted. Zinc oxide (ZnO)-based nanostructures, as a dielectric material, have been studied extensively for highly sensitive, selective and efficient gas sensors for the detection of various hazardous and toxic gases such as NO, $NO_2$ [11-12], $H_2$ [13-14], ammonia ($NH_3$) [15], methane ($CH_4$) [15-16] acetone [17], ethanol [18-21], humidity [22], CO [15, 23-25], volatile organic compound (VOCs) [26], and hydrogen [16, 27-37] Up to now zinc oxide (ZnO) is considered as one of the promising resistive-type gas sensing

material. But the high operating temperature, slow response time, poor selectivity and stability limit its extensive applications in the field of dissolved gases monitoring. These are electrical detection where the presence of $H_2$ gas is detected by monitoring the change of the resistivity of ZnO structures. However, for safety optical detection system is desirable.

In this work, we experimentally demonstrate hydrogen sensing using aluminium-doped zinc oxide (AZO) nanotubes (hollow pillars). We also have conducted the comparative study on the gas sensing property of the solid AZO pillars. All these high aspect ratio AZO pillars and nanotubes were fabricated using a combination of advanced reactive ion etching and atomic layer deposition (ALD) techniques [38]. The solid AZO pillars do not respond to the $H_2$ gas of concentration 0.7 % - 4 % at room temperature and pressure even after long time. On the other hand, the AZO nanotubes shows a wavelength shift of ~ 13 nm upon exposure to hydrogen gas of concentration of 4 % in ambient temperature and pressure and a simultaneous decrease in the reflectance intensity of ~ 0.4 % is also detected within 10 minutes. This structure can even sense the presence of a low concentration (0.7 %) of hydrogen gas with a smaller response time. For the better understanding of these AZO nanotubes based gas sensing system, along with the experimental results Numerical simulation also have been reported here.

## IIA.2. Results and discussion:

**IIA.2.a. Theoretical analysis method:** Theoretical analysis has been done based on Finite element Method (FEM) to support the experimental findings and to better understand the structure specially for gas sensing. FEM based Comsol simulation is carried out to find the interaction between light and AZO nanotubes with 400 nm periodicity in square lattice arrangement. In order to map out the electric field pattern in the nanotubes structures interacting with light the Radio Frequency (RF) module of FEM based COMSOL 5.4 software package has been used. During this theoretical study, all the specifications about the size, shape, substrates of AZO nanotubes are obtained from the SEM studies. Moreover, the COMSOL material library is used for the optical properties of air as surrounding medium, $SiO_2$ layer, and Si substrate. The wavelength dependent complex permittivity with both real and imaginary parts of AZO is taken from the experimental data obtained from spectroscopic ellipsometry measurements and a proper fitting [38]. Linearly polarized plane waves are used as the excitation source. Electric field of incident light is perpendicular to the semi major axis of the nanotubes (TE-polarized light) which is identical to the experimental framework. Physics controlled free triangular and tetrahedral meshes (depending on different layers) are

used for these analysis to calculate the electromagnetic power loss density ($W/m^3$) and the electric field enhancement with a suitable and variable mesh size where the lowest mesh size is kept at 1.6 nm.

**IIA.2.b. Fabrication method of AZO nanotubes (hollow pillars) and AZO solid pillars:** Two types of samples were fabricated: AZO solid pillars and nanotubes structures on Si substrate with thermally grown 200 nm silica layer (see figure IIA.1). The external diameter, thickness, and height of the AZO nanotubes are 300 nm, 20 nm, and 2 $\mu$m respectively and a pitch of 400 nm is maintained over $1\times1$ $cm^2$.

On the other hand, the diameter and height of the AZO solid pillars are 300 nm and 2 $\mu$m, respectively, and a pitch of 400 nm is also maintained here over the same area. For both types of structures, air acts as the host material. Elemental analysis by transmission electron microscopy (TEM) and other characterization methods as well as extended details on fabrication of AZO pillars and nanotubes can be found elsewhere [38].

Deep-UV lithography was used to define grating patterns on standard silicon <100> wafers. DRIE was implemented with a standard Bosch process [39] in order to fabricate a Si template with the 2 $\mu$m-deep air hole arrays. Afterwards, the processed structures were cleaned in $N_2/O_2$ plasma in order to get rid of resist remaining and other organic contaminants. Then, the silicon templates were coated by AZO (using trimethylaluminum, diethylzinc, and water as precursors) by means of atomic layer deposition (ALD), until the air holes were filled entirely. ALD is based on the self-limiting, sequential surface chemical reactions which allows conform deposition on complex structures with sub-thickness control [40]. For the final step, the AZO filling needs to be isolated, and for that purpose, the samples were subjected to Ar+ sputtering for removal of the top AZO layer and exposing the silicon template. Afterwards, the silicon template in-between cavities coated with AZO, has been removed using $SF_6$ plasma in conventional isotropic reactive ion etching process without interference with functional ALD material, resulting in the formation of AZO pillars and tubes as shown in figure IIA.1. The more detailed description of the fabrication method for different structures, such as, AZO trenches [41-42], TiN trenches [43], dielectric trenches [44], can be found elsewhere. The optical properties of AZO films fabricated by ALD have been measured by ellipsometer for the wavelength range of interests [38, 41].

**IIA.2.c. Fabrication of microfluidic channel:** The microfluidic channel is made up of poly (methyl methacrylate) (PMMA) plastic window which is surrounded by the micromachined

inlets and outlets. Along with that a double-sided adhesive film is attached there which defines the outlines and thickness of the microfluidic channels. The diameter of inlets and outlets of the PMMA top is 0.61 mm and separation distance of 12.4 mm is maintained here.

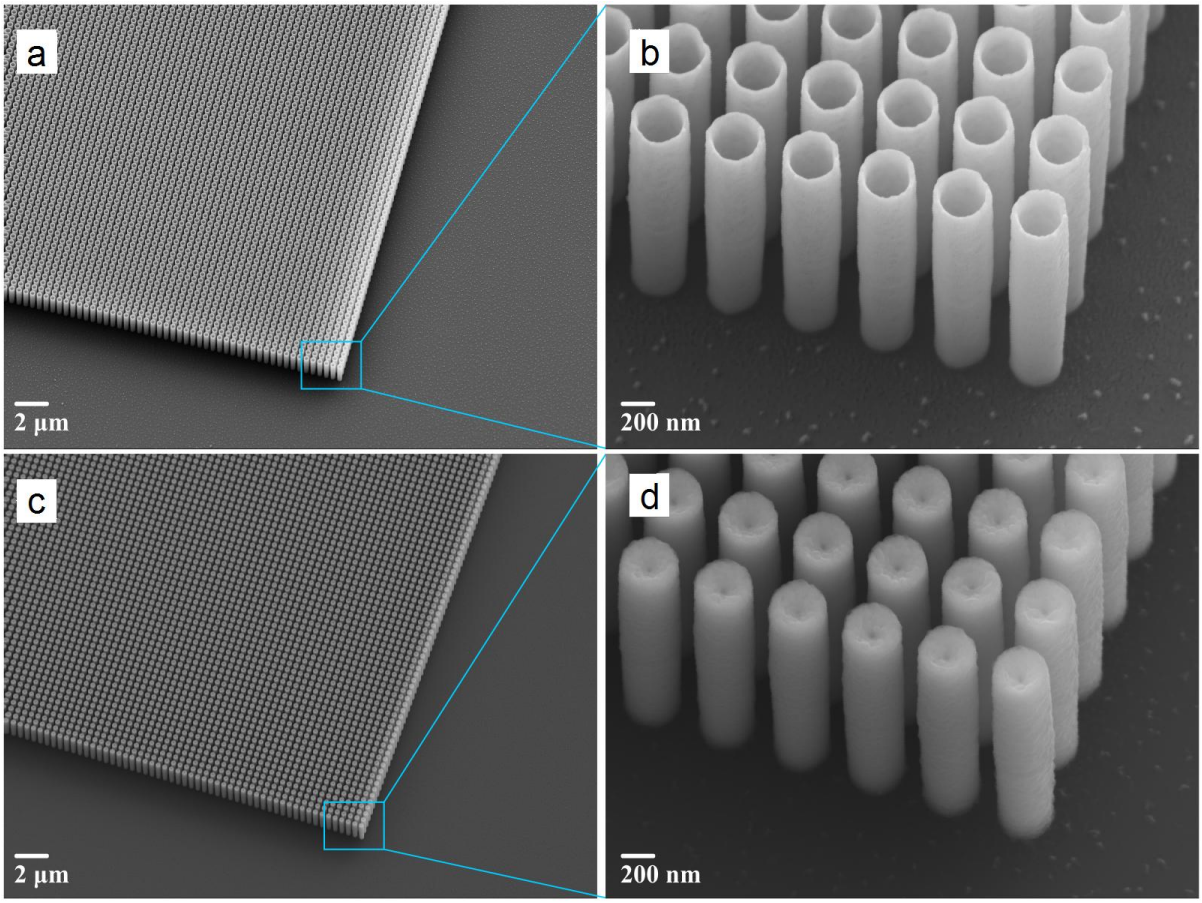


Figure IIA.1. Scanning electron microscope (SEM) images of fabricated AZO (a, b) nanotubes and (c, d) solid pillar structures with a pitch of 400 nm, diameter of 300 nm, and height of 2 $\mu$m. The wall thickness of nanotubes is approximately 20 nm.

The PMMA top is fabricated by laser micromachining using a VersaLASER system (Universal Laser Systems). A double-sided adhesive film (iTapestore, 100 $\mu$m in height) has been cut by laser to have the same precise size of PMMA top and is placed within the 14 × 2 mm microchannels. Here the adhesive film is connected to the PMMA top to include the inlet and outlet within the outline of the channel. To connect the gas sources with the microfluidic channel fluorinated ethylene propylene (FEP) tubing (Cole-Parmer) is used. All the tubing and their connections between gas sources and channels are fastened using a 5 min epoxy (Devcon). For clarity a picture of our sensor is given below.

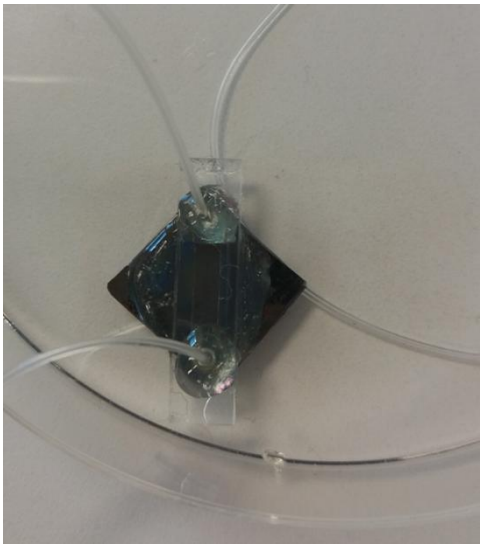

Figure IIA.2. A picture of the AZO nanotubes hydrogen gas sensor.

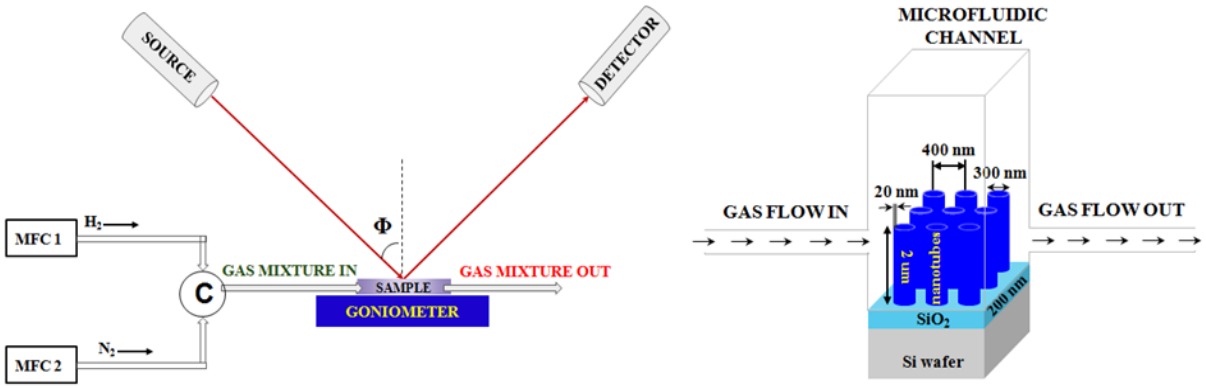


Figure IIA.3. (a) Schematic diagram of the experimental set-up. (b) Schematic diagram of the AZO nanotubes sensing system where air acts as the host material.

**IIA.2.d. Ellipsometric reflection measurement method for gas sensing:** A high-resolution variable-angle spectroscopic ellipsometry (SE) (J. A. Woollam Co., Inc., V-VASE) is used to experimentally measure all types of angular reflection data as illustrated in figure IIA.3 (a). The low-power spectroscopic ellipsometer has high precision and it is non-destructive and thus preferable for the optical characterization of nanostructures and gas sensing. In order to characterize the performance of our gas sensing system, AZO nanotubes are exposed to $H_2$ gas of different concentrations. The channel inlet was connected to a tank of nitrogen mixed with 4 % volume concentration of $H_2$ and with pure nitrogen. The gas flow from both the tanks was controlled separately using two separate mass flow controllers (MFCs). By adjusting those MFCs, we could control the hydrogen concentration (between 0 and 4 %)

introduced to the sample as illustrated in panel (b) of the figure above. After adjusting all these parameters the sensor was placed on the variable angle ellipsometer to measure the reflectivity R ($\lambda$, $\phi$) at different angle of incidence, $\phi$, in the wavelength range of $\lambda$ = 300 - 1500 nm. The maximum resolution of this ellipsometer is 0.03 nm but for our measurements 1 nm resolution is maintained throughout all the experiments. Note that, all around the paper, we present experimental results of TE-polarized incident light because TM-polarized light does not show any sensitivity toward hydrogen gas. The comparison between both the polarizations is given below.

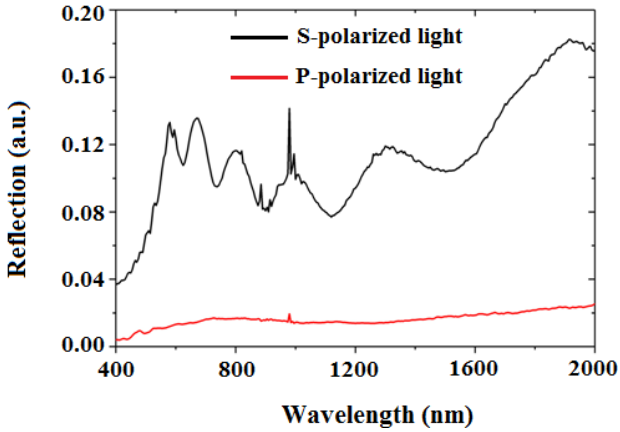


Figure IIA.4. The response of both S- and P-polarized light is shown here. For AZO nanotube system we chose S-polarized light for all the gas sensing experimental measurements because that shows the presence of different modes. The P-polarized light shows almost no variation and thus not useful for gas sensing. Here the measurement angle is $45^{o}$. These measurements are taken in absence of $H_2$ gas to only figure out which mode will be the best mode for gas sensing measurements.

During gas sensing experiment, because of the PMMA window on top of the channel, the incident beam splits into two reflected beams at the interfaces of Air-PMMA window and PMMA window-microfluidic channel, causing Fabry-Perot oscillation in the reflection spectra. In order to minimize the effect and keep the associated error minimum, a particular suitable incident angle for the sensing set-up needs to be optimized. Here in our case the measurement angle is kept below or equal to $\phi = 45^{o}$. Moreover, the iris of the ellipsometer detector helps to block the additional reflected beam during the sensing measurement, an unavoidable source of experimental error which originates from the insertion of the microfluidic channel. After fixing the measurement angle to see the response of the AZO sensing system for $H_2$ gas of a particular concentration, the reflectance has been continuously

measured over a wavelength range (selected based on the minima of reflectance) for 90 minutes keeping a constant time interval between each measurement.

**IIA.2.e. Discussion about the theoretical results:** Finite Element Method (FEM) based Comsol software was used for the theoretical analysis of the AZO nanotubes gas sensing system. Figure IIA.5 shows all the simulation results. Panel (a) shows the simulated reflection from AZO nanotubes. The incident angle is taken as $\phi$ = 45$^{o}$, similar to the experimental case. Here 400 nm periodicity, 20 nm thick tube wall, and 2 $\mu$m height are considered. Electric field is taken along the x-axis (TE-polarized incident light). The electromagnetic power loss density (W/m$^3$) associated with the AZO nanotubes for plane incident waves are shown in panel (b) at 1100 nm, which is one of the reflection minima mode in the theoretical reflectance spectra of AZO nanotubes shown in panel (a). Here, it is clear that the optical loss is concentrated mostly within the AZO nanotubes. The light absorption in the AZO tubes layer suggests that the AZO tubes absorption properties can be strongly modify due to slight changes in the environment. Note that during our measurements for $H_2$ gas sensing, reflectance minima around 1100 nm in wavelength was used.

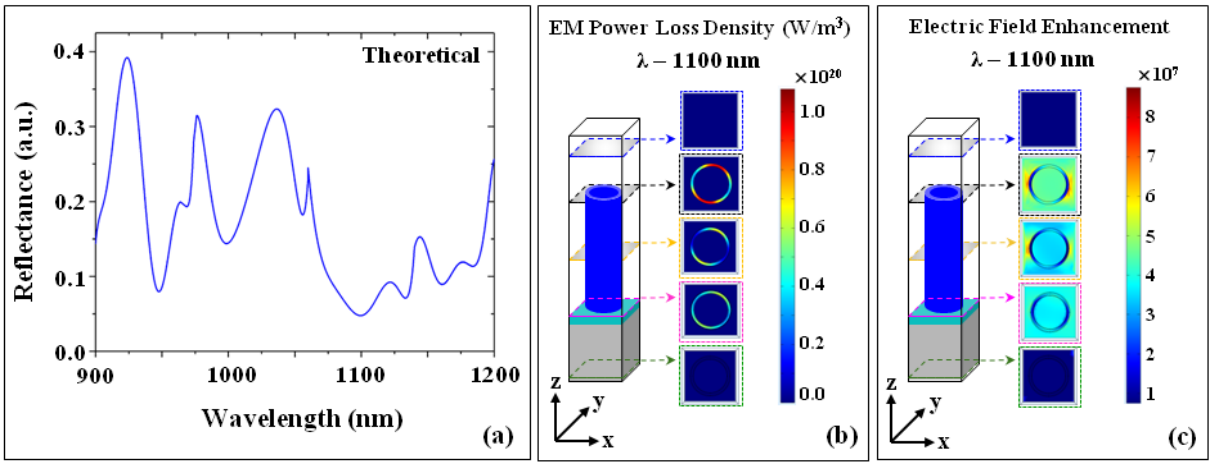


Figure IIA.5. Simulation results. (a) Reflection spectra. (b) The electromagnetic power loss density (W/m$^3$) and (c) Electric field profile at 1100 nm in wavelength. Simulation was conducted for linearly polarized plane wave (TE-polarized light with electric field parallel to the surface of tubes along x-axis) is investigated. The periodicity, thickness of wall, and height of tubes are 400 nm, 20 nm, and 2 $\mu$m, respectively. The incident angle is $\phi$ = 45$^{o}$.

In the above figure, the simulated electric field profile at the wavelength of 1100 nm is shown in panel (c) which depicts the high electric field enhancement near the surface of AZO nanotubes, useful for the detection of any changes of AZO nanotubes optical properties.

**IIA.2.f. Hydrogen sensing by AZO nanotubes:** We study the spectral shift, Δλ, for different hydrogen concentrations. Figure IIA.6 (a) shows the response of AZO nanotubes system for 0.7 % $H_2$ gas at $\phi$ = 45° over a wavelength range of λ = 300 nm - 1500 nm. This plot shows that for a particular measurement angle the wavelength shift, Δλ, is larger for longer wavelengths, giving higher sensitivity. For example for $\phi$ = 45°, the wavelength shift of reflectance minima around λ = 900 nm is Δλ = 0 nm, while reflectance minima at λ = 1126 nm shifts by Δλ = 2.6 nm for 0.7 % $H_2$ gas. Depending on the measurement angle, the sensitivity can also be tuned.

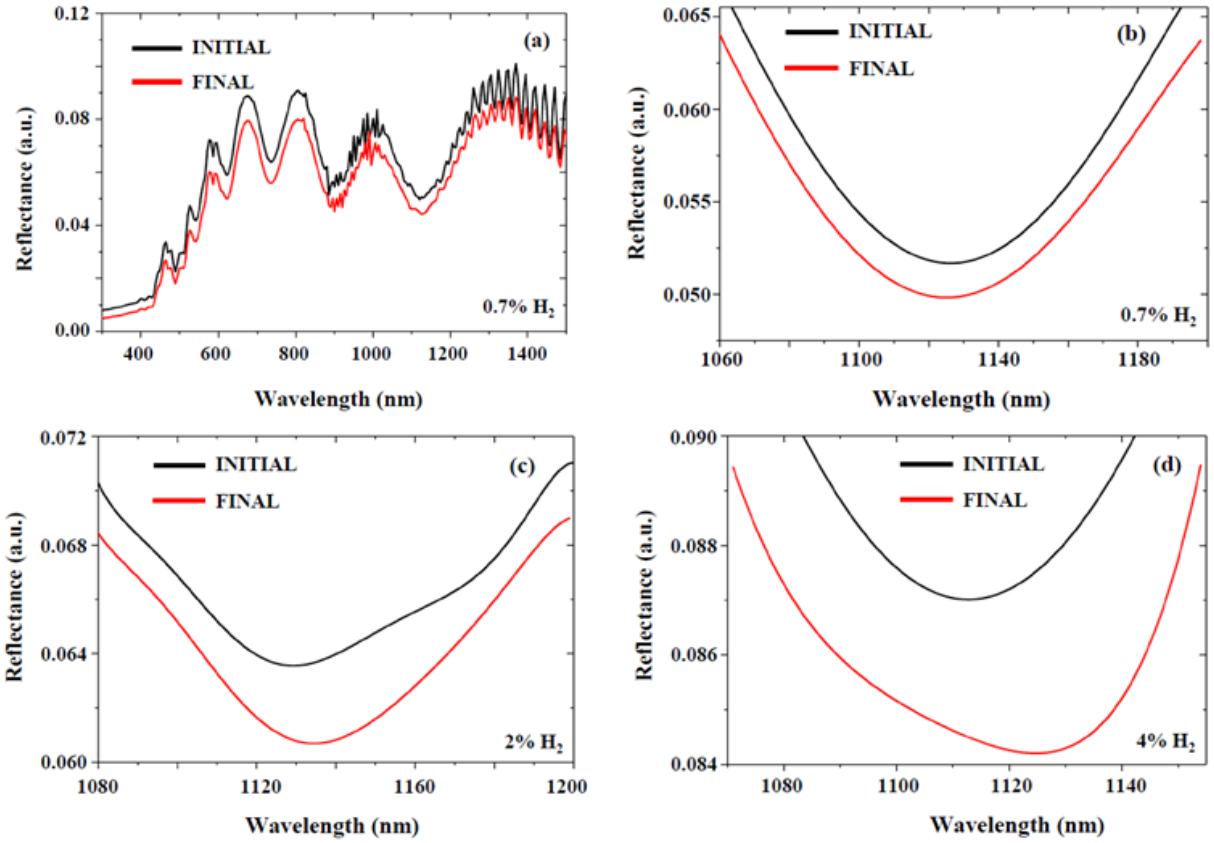


Figure IIA.6. The response of AZO nanotubes in presence of hydrogen gas. (a) The response of AZO nanotubes sensing system before and after intercalation of 0.7 % $H_2$ gas measured at the incident angle, $\phi$ = 45° over a wavelength range of λ = 300 nm - 1500 nm. Using this plot one can choose the suitable mode for $H_2$ gas detection with higher sensitivity. (b) 0.7 % $H_2$, (c) 2 % $H_2$, and (d) 4 % $H_2$ gas sensing results. For all these measurements, the response time is 10 min.

An example containing more detailed information about the dependence of wavelength shift and sensitivity on the measurement angle and mode wavelength variation is given in the figure IIA.7. We note that for longer wavelengths the fluctuation in reflectance increases due to Fabry-Perot interference originated from the microfluidic channel. Taking these factors

into account, we focus on the reflection minima around 1100 nm in wavelengths for hydrogen sensing throughout this paper. In the above figure, panel (b – d) are showing the properly fitted gas sensing response of AZO nanotubes array system for $H_2$ gas of concentration 0.7 %, 2 %, and 4 %, respectively. For all these measurements the response time was 10 minutes. Here, the system shows wavelength shift, $\Delta\lambda$, as well as reflectance intensity change, $\Delta I$, even for the lowest concentration 0.7 % of $H_2$ gas. The wavelength shift is 2.6 nm for 0.7 % $H_2$ and the change in reflectance intensity is 0.2 %. Similarly, the wavelength shift is 5 nm for 2 % $H_2$ and the change in reflectance intensity is nearly 0.3 %. For 4 % $H_2$ gas the wavelength shift is 13 nm and the reflectance intensity change is 0.4 %. If one considers the wavelength shift as the measurement parameter, the signal to noise ratio (S/N) becomes 16.7 % which is equivalent to the wavelength shift / FWHM (Full Width at Half Maxima) of the mode. In order to characterize the sensitivity in terms of reflectance change, the figure of merit (FOM) is defined as FOM = $R(AZO_{air})/R(AZO_{H2})$ [8] where $R(AZO_{air})$ is the reflectance of the sensor in $N_2$ (which is equivalent to air media) without hydrogen and $R(AZO_{H2})$ is the reflectance of the sensor in presence of hydrogen gas. According to the figure shown in panel (d) for 4 % $H_2$ gas, the calculated FOM of our sensor is FOM ≈ 104. Note that we also conducted reflectance measurement for AZO solid pillar in presence of 4 % $H_2$ gas over 90 minutes. However, even after such a long time, one cannot see any clear wavelength shift or reflectance intensity change for such gas sensing with those solid AZO pillars. The response of solid AZO pillars in presence of $H_2$ gas is shown in figure IIA.8. This indicates that the ultra thin wall thickness of AZO nanotubes and their hollowness play an important role in sensing for its large surface area [45].

Figure IIA.9 (a) and (b) display the wavelength shift and the intensity change in the reflectance minima of AZO nanotubes array after exposure to $H_2$ gas with different concentration. Based on the measurement of wavelength shift, here the limit of detection (LOD) is nearly 0.3 % $H_2$ for 10 minutes of response time considering the fact that the maximum possible resolution of the used spectroscopic ellipsometer is 0.03 nm. The graph depicting the LOD is shown in figure IIA.10. It is well-known that practical hydrogen sensors must be able to respond to hydrogen at concentrations approximately an order of magnitude lower than the explosive limit of $H_2$ (4 %) [8, 46]. The previous work shows Pd-based optical $H_2$ gas sensor with high FOM in room temperature [8]. However, the response time was nearly 60 minutes, which can be an issue for the safety in the industrial field.

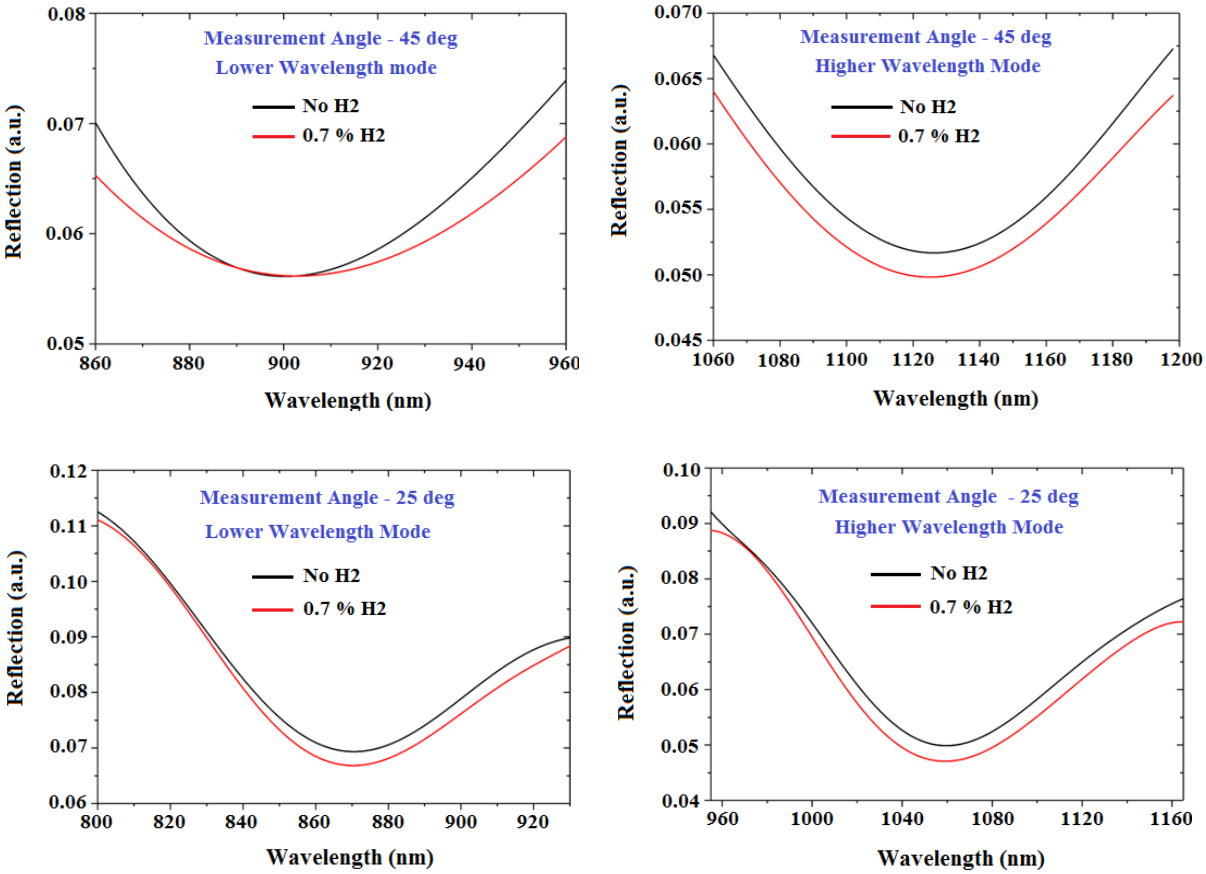


Figure IIA.7. Here the response of the AZO nanotubes sensing system is shown for 0.7% $H_2$ gas. For all these cases, the response time is 10 min. Panel (a) describes the case for a lower wavelength mode when the measurement angle is 45°. In this case no wavelength shift is seen. Panel (b) describes the case for a higher wavelength mode when the measurement angle is 45°. In this case wavelength shift as well as the reflection intensity change has been observed. Panel (c) describes the case for a lower wavelength mode when the measurement angle is 25°. In this case variation is observed. While panel (d) describes the case for a higher wavelength mode when the measurement angle is 25°. In this case also the shift in mode is seen. One can choose any mode and any measurement angle based on these variations. The only restriction for our set-up is the measurement angle should be less or equal to 45° to minimize the interference effect introduced by the microfluidic channel and maximize the signal intensity.

Our AZO nanotubes array system could achieve the requirement in terms of FOM and fast response time of 10 minutes in room temperature by means of safe optical measurement. The results of gas sensing response over time up to 90 minutes for 4 % $H_2$ gas is shown in figure IIA.11 (a) from which we can see the fast response nature of the AZO nanotubes sensor. Here it can be seen that 10 minutes is sufficient to detect 4 % $H_2$ gas concentration. This response time is also valid for 2 % and 0.7 % of $H_2$ gas.

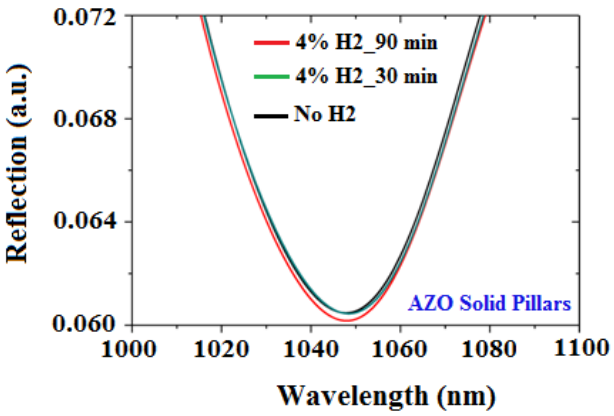


Figure IIA.8. The response of AZO solid pillars for 4% hydrogen gas is shown here. Almost no change in the reflectance mode is observed here for 4% $H_2$ after 90 min which signifies the incompatibility of these solid pillars for hydrogen gas sensing.

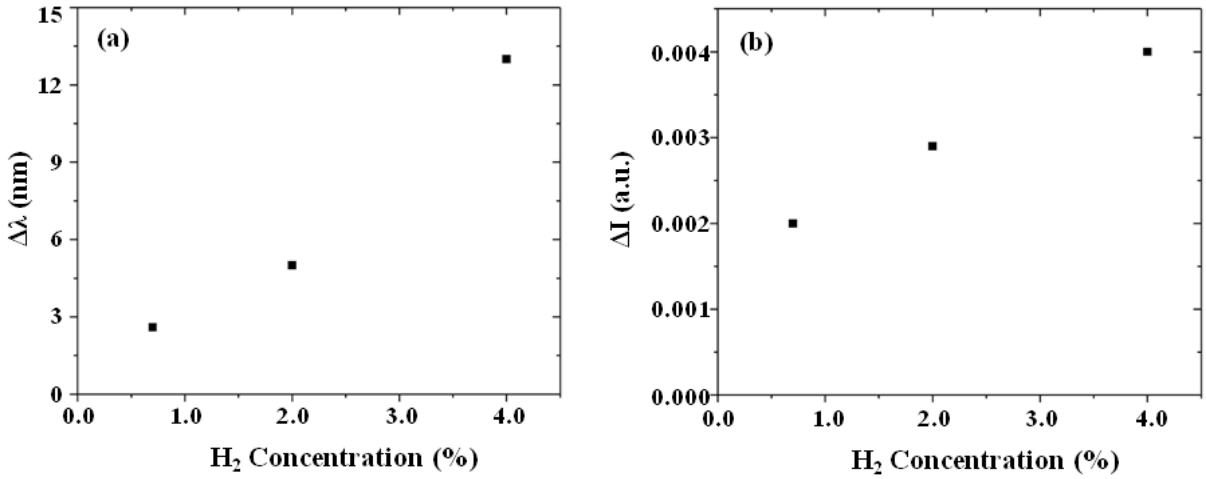


Figure IIA.9. Variation of (a) wavelength shift, Δλ, and (b) Reflectance intensity change of reflection minima, ΔI, observed in AZO nanotubes sensing system in presence of $H_2$ gas of different concentration (0.7 %, 2 %, and 4 %).

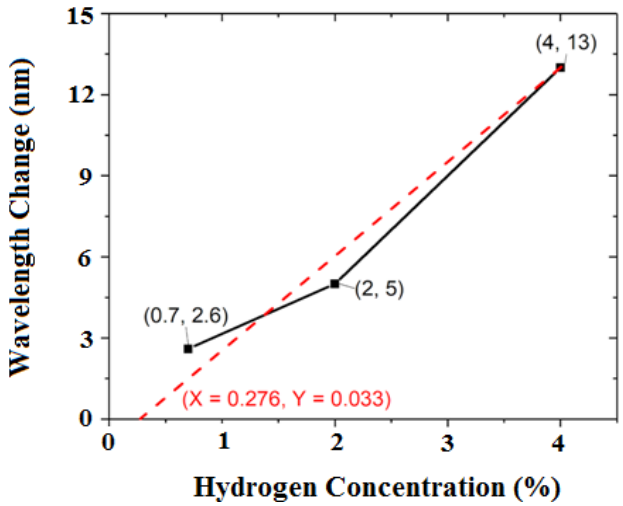


Figure IIA.10. The Limit of Detection (LOD) measurement is shown here. If one considers wavelength change as the parameter to detect the presence of hydrogen gas with the help of AZO nanotubes sensing system then the LOD is measured as nearly 0.3% $H_2$ gas considering the fact that the maximum resolution of the used ellipsometer in our case is 0.03 nm. Here the black curve is showing the experimentally measured wavelength shift variation of reflection minima, observed for AZO nanotubes sensing system in presence of $H_2$ gas of different concentration (0.7 %, 2 %, and 4 %) and the red dashed curve is the fitted curve drawn to see the LOD.

Figure IIA.11 (b) shows the response of AZO nanotubes in different ambient conditions. Here the ellipsometric response of the AZO nanotubes system with PMMA channel in absence of any gas as well as in presence of pure $N_2$ gas and 4 % $H_2$ gas are shown. In this plot, we do not observe any wavelength shift in reflection after introducing pure $N_2$ gas to the sensor (dashed red curve) compared to the reflectance when the sample is not exposed to any gas (black curve). In comparison, after introducing $N_2$ mixed with 4 % of $H_2$ (cyan curve), we observe a clear red shift in the reflection minimum, as well as a change in the reflection amplitude due to the intercalation of hydrogen atoms in the sensing system as expected. By introducing pure N2 to the channel again, the reflectance did not go back to its primary position. However, the absorption properties of the AZO nanotubes system remain same for a longer time afterward. Here different cycles of introducing N2 mixed with 4 % of H2, and pure N2, show almost no change in the spectral properties of the absorption mode of AZO nanotubes sensor.

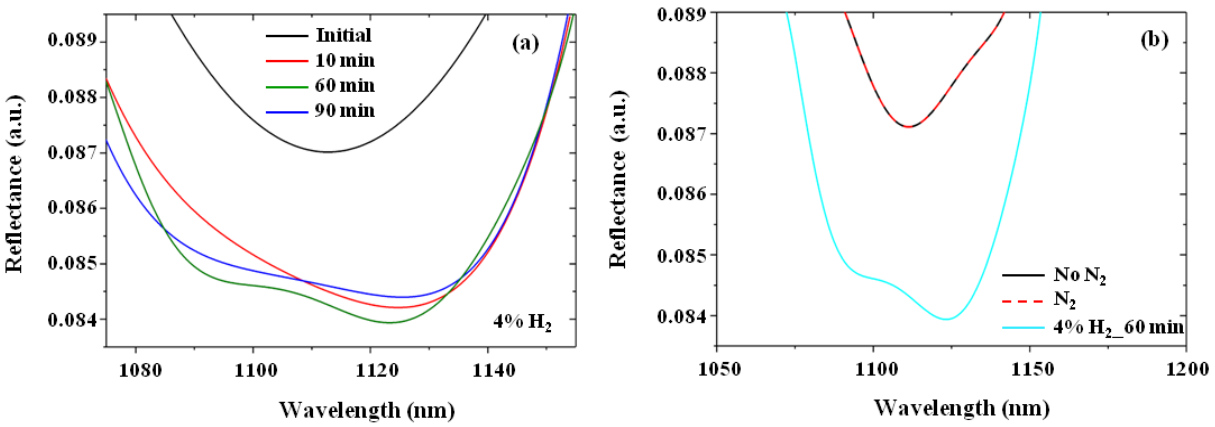


Figure IIA.11. (a) Response of AZO nanotubes sensing system overtime in presence of 4 % $H_2$ gas. It is very clear that 10 min is enough to detect the presence of 4 % $H_2$ gas. (b) The response of AZO nanotubes sensing system (with PMMA channel) in presence and absence of $N_2$ gas where there is almost no variation in the mode. But a clear shift of the mode is observed in presence of 4 % $H_2$ gas after 60 min.

## IIA.3. Conclusion

In summary, we report the study of $H_2$ gas sensing properties of highly ordered aluminium-doped zinc oxide (AZO) nanotubes for near-infrared wavelengths around 1100 nm. While AZO solid pillars do not respond to $H_2$ gas, AZO nanotubes show a wavelength shift as well as a significant decrease in the reflectance intensity after exposing them to $H_2$ gas. This response not only we have seen in the room temperature and pressure, but also quickly, within 10 minutes. Therefore, the possibility of having a two-level room-temperature $H_2$ gas sensor, with all the advantages of low-response time, capability to detect low concentration of $H_2$, a good figure of merit, possibility of fabricating a large area sensor with high precision and reliability can make these tubes as one of the promising $H_2$ gas sensors for industrial applications. Moreover, the sensitivity of nanotubes may be further enhanced by controlling the doping level of ZnO by aluminium. In Future, AZO based room temperature gas sensor can be realized which will enable monitoring hydrogen gas by looking at color changes in the visible range.

## IIA.4. References

[1] Fong, N. R.; Berini, P.; Tait, R. N. Hydrogen sensing with Pd-coated long-range surface plasmon membrane waveguides. Nanoscale 2016, 8, 4284 - 4290.

[2] Brown, W. J. National Aeronautics and Space Administration, NASA; 1997.

[3] Overview, E. Liquid Hydrogen MSDS (PDF). Praxair, Inc. 2004, 1985 - 1986.

[4] Wilkins, J. R.; Stoner, G. E.; Boykin, E. H. Microbial detection method based on sensing molecular hydrogen. Applied microbiology 1974, 27, 949 - 94952.

[5] Tittl, A.; Mai, P.; Taubert, R.; Dregely, D.; Liu, N.; Giessen, H. Palladium-based plasmonic perfect absorber in the visible wavelength range and its application to hydrogen sensing. Nano letters 2011, 11, 4366 - 4369.

[6] Wadell, C.; Syrenova, S.; Langhammer, C. Plasmonic hydrogen sensing with nanostructured metal hydrides. ACS Nano 2014, 8, 11925 - 11940.

[7] Liu, N. tailored nanofocus. Nature Materials 2011, 10, 631 - 636.

[8] ElKabbash, M.; Sreekanth, K. V.; Alapan, Y.; Kim, M.; Cole, J.; Fraiwan, A.; Letsou, T.; Li, Y.; Guo, C.; Sankaran, R. M.; Gurkan, U. A.; Hinczewski, M.; Strangi, G. Hydrogen Sensing Using Thin-Film Perfect Light Absorber. ACS Photonics 2019, 6, 1889 - 1894.

[9] Ngene, P.; Radeva, T.; Slaman, M.; Westerwaal, R. J.; Schreuders, H.; Dam, B. Seeing hydrogen in colors: Low-cost and highly sensitive eye readable hydrogen detectors. Advanced Functional Materials 2014, 24, 2374 - 2382.

[10] Li, Z.; Butun, S.; Aydin, K. Large-area, Lithography-free super absorbers and color filters at visible frequencies using ultrathin metallic films. ACS Photonics 2015, 2, 183 - 188.

[11] Ahn, M. W.; Park, K. S.; Heo, J. H.; Park, J. G.; Kim, D. W.; Choi, K. J.; Lee, J. H.; Hong, S. H. Gas sensing properties of defect-controlled ZnO-nanowire gas sensor. Applied Physics Letters 2008, 93, 263103.

[12] Kumar, R.; Al-Dossary, O.; Kumar, G.; Umar, A. Zinc oxide nanostructures for $NO_2$

Gas-sensor applications: A review. Nano-Micro Letters 2015, 7, 97-120.

[13] Narayan, T. C.; Hayee, F.; Baldi, A.; Koh, A. L.; Sinclair, R.; Dionne, J. A. Dynamics in individual palladium nanoparticles. Nature Communications 2017, 8, 14020.

[14] Choo, T. F.; Saidin, N. U.; Kok, K. Y. Hydrogen sensing enhancement of zinc oxide nanorods via voltage biasing. Royal Society Open Science 2018, 5, 172372.

[15] Ryong Ryu, S.; Ram, S. D.; Cho, H. D.; Lee, D. J.; Won Kang, T.; Woo, Y. Single ZnO nanocactus gas sensor formed by etching of ZnO nanorod. Nanoscale 2015, 7, 11115 - 11122.

[16] Lupan, O.; Postica, V.; Gr□ottrup, J.; Mishra, A. K.; De Leeuw, N. H.; Carreira, J. F.; Rodrigues, J.; Ben Sedrine, N.; Correia, M. R.; Monteiro, T.; Cretu, V.; Tiginyanu, I.;

Smazna, D.; Mishra, Y. K.; Adelung, R. Hybridization of zinc oxide tetrapods for selective gas sensing applications. ACS Applied Materials and Interfaces 2017, 9, 4084 - 4099.

[17] Morisot, F.; Zuliani, C.; Luque, J.; Ali, Z.; Mouis, M.; Nguyen, V. H.; Munoz-Rojas, D.; Lourhzal, O.; Texier, M.; Cornelius, T. W.; Ternon, C. ZnO based nanowire network for gas sensing applications. Materials Research Express 2019, 6, 084004.

[18] Wan, Q.; Li, Q. H.; Chen, Y. J.; Wang, T. H.; He, X. L.; Li, J. P.; Lin, C. L. Fabrication and ethanol sensing characteristics of ZnO nanowire gas sensors. Applied Physics Letters 2004, 84, 3654 - 3656.

[19] Hsueh, T. J.; Chang, S. J.; Hsu, C. L.; Lin, Y. R.; Chen, I. C. Highly sensitive ZnO nanowire ethanol sensor with Pd adsorption. Applied Physics Letters 2007, 91, 053111.

[20] Son, J. Y.; Lim, S. J.; Cho, J. H.; Seong, W. K.; Kim, H. Synthesis of horizontally aligned ZnO nanowires localized at terrace edges and application for high sensitivity gas sensor. Applied Physics Letters 2008, 93, 053109.

[21] Wang, C.; Wang, Z.-g.; Xi, R.; Zhang, L.; Zhang, S.-h.; Wang, L.-j. Sensors and Actuators B: Chemical In situ synthesis of flower-like ZnO on GaN using electrodeposition and its application as ethanol gas sensor at room temperature. Sensors & Actuators: B. Chemical 2019, 292, 270 - 276.

[22] Majithia, R.; Ritter, S.; Meissner, K. E. Heterogeneous nucleation for synthesis of sub-20nm ZnO nanopods and their application to optical humidity sensing. Analytica Chimica Acta 2014, 812, 206 - 214.

[23] Katoch, A.; Choi, S.-w.; Kim, S. S. Effect of the wall thickness on the gas-sensing properties of ZnO hollow fibers. Nanotechnology 2014, 25, 455504.

[24] Paliwal, A.; Sharma, A.; Tomar, M.; Gupta, V. Sensors and Actuators B: Chemical Carbon monoxide (CO) optical gas sensor based on ZnO thin films. Sensors & Actuators: B. Chemical 2017, 250, 679 - 685.

[25] Kim, J.-h.; Mirzaei, A.; Woo, H.; Sub, S. Sensors and Actuators B: Chemical Low power-consumption CO gas sensors based on Au-functionalized $SnO_2$-ZnO core-shell nanowires. Sensors & Actuators: B. Chemical 2018, 267, 597 - 607.

[26] Ozturk, S.; Kosemen, A.; Alpaslan, Z.; Kilinc, N.; Ozturk, Z. Z.; Penza, M. Sensors and Actuators B : Chemical Electrochemically growth of Pd doped ZnO nanorods on QCM for room temperature VOC sensors. 2016, 222, 280 - 289.

[27] Wang, H. T.; Kang, B. S.; Ren, F.; Tien, L. C.; Sadik, P. W.; Norton, D. P.; Pearton, S. J.; Lin, J. Hydrogen-selective sensing at room temperature with ZnO nanorods. Applied Physics Letters 2005, 86, 243503.

[28] Das, S. N.; Kar, J. P.; Choi, J. H.; Lee, T.; Moon, K. J.; Myoung, J. M. Fabrication and characterization of ZnO single nanowire-based hydrogen sensor. Journal of Physical Chemistry C 2010, 114, 1689 - 1693.

[29] Lim, M. A.; Kim, D. H.; Park, C. O.; Lee, Y. W.; Han, S. W.; Li, Z.; Williams, R. S.; Park, I. A new route toward ultrasensitive, flexible chemical sensors: Metal nanotubes by wet-chemical synthesis along sacrificial nanowire templates. ACS Nano 2012, 6, 598 - 608.

[30] Kashif, M.; Ali, M. E.; Usman, S. M.; Hashim, U. Sol-gel synthesis of Pd doped ZnO nanorods for room temperature hydrogen sensing applications. Ceramics International 2013, 39, 6461 - 6466.

[31] Ranwa, S.; Kulriya, P. K.; Sahu, V. K.; Kukreja, L. M.; Kumar, M. Defect-free ZnO nanorods for low temperature hydrogen sensor applications. Applied Physics Letters 2014, 105, 213103.

[32] Katoch, A.; Choi, S. -W.; Woo, H.; Sub, S. Highly sensitive and selective $H_2$ sensing by ZnO nanofibers and the underlying sensing mechanism. Journal of Hazardous Materials 2015, 286, 229 - 235.

[33] Faisal, M.; Alam, B.; Phan, D. -T.; Chung, G. -S. Palladium nanocubes decorated on a one-dimensional ZnO nanorods array for use as a hydrogen gas sensor. Materials Letters 2015, 156, 113 - 117.

[34] Kathiravan, D.; Huang, B. R.; Saravanan, A. Self-Assembled Hierarchical Interfaces of ZnO Nanotubes/Graphene Heterostructures for Efficient Room Temperature Hydrogen Sensors. ACS Applied Materials and Interfaces 2017, 9, 12064 - 12072.

[35] Zhao, M.; Hon, M.; Chung, H.; Wo, C. Sensors and Actuators B: Chemical Resistive hydrogen sensing response of Pd-decorated ZnO “nanosponge” film. Sensors & Actuators: B. Chemical 2017, 249, 624 - 631.

[36] Bhati, V. S.; Ranwa, S.; Rajamani, S.; Kumari, K.; Raliya, R.; Biswas, P.; Kumar, M. Improved Sensitivity with Low Limit of Detection of a Hydrogen Gas Sensor Based on rGO-Loaded Ni-Doped ZnO Nanostructures. ACS Applied Materials and Interfaces 2018, 10, 11116 - 11124.

[37] Kim, J.-h.; Mirzaei, A.; Woo, H.; Wu, P.; Sub, S. Sensors and Actuators B: Chemical Design of supersensitive and selective ZnO-nano fiber-based sensors for $H_2$ gas sensing by electron-beam irradiation. Sensors & Actuators: B. Chemical 2019, 293, 210 - 223.

[38] Shkondin, E.; Takayama, O.; Panah, M. E. A.; Liu, P.; Larsen, P. V.; Mar, M. D.; Jensen, F.; Lavrinenko, A. V. Large-scale high aspect ratio Al-doped ZnO nanopillars arrays as anisotropic metamaterials. Optical Materials Express 2017, 7, 1606 - 1627.

[39] Lindroos, V.; Tilli, M.; Lehto, A.; Motooka, T.; Veijola, T. Handbook of silicon based MEMS materials and technologies. Micro & Nano Technologies Series 2010.

[40] George, S. Atomic layer deposition: an overview. Chem. Rev. 2010, 110, 111 - 131.

[41] Takayama, O.; Shkondin, E.; Bogdanov, A.; Aryaee Pahah, M. E.; Golenitskii, K.; Dmitriev, P. A.; Repan, T.; Malreanu, R.; Belov, P.; Jensen, F.; Lavrinenko, A. V. Mid-infrared surface waves on a high aspect ratio nano-trench platform. ACS Photonics 2017, 4, 2899 - 2907.

[42] Shkondin, E.; Repan, T.; Aryaee Panah, M. E.; Lavrinenko, A. V.; Takayama, O. High Aspect Ratio Plasmonic Nano-trench Structures with Large Active Surface Area for Label-Free Mid-Infrared Molecular Absorption Sensing. ACS Applied Nano Materials 2018, 1, 1212 - 1218.

[43] Shkondin, E.; Repan, T.; Takayama, O.; Lavrinenko, A. V. High aspect ratio titanium nitride trench structures as plasmonic biosensor. Optical Materials Express 2017, 7, 4171 - 4182.

[44] Shkondin, E.; Takayama, O.; Lindhard, J. M.; Larsen, P. V.; Mar, M. D.; Jensen, F.; Lavrinenko, A. V. Fabrication of high aspect ratio TiO2 and Al2O3 nano-gratings by atomic layer deposition. Journal of Vacuum Science & Technology A: Vacuum, Surfaces, and Films 2016, 34, 031605.

[45] Katoch, A.; Abideen, Z. U.; Kim, J.-H.; Kim, S. S. Sensors and Actuators B: Chemical Influence of hollowness variation on the gas-sensing properties of ZnO hollow nano-fibers. Sensors & Actuators: B. Chemical 2016, 232, 698 - 704.

[46] Pitts, J. R.; Liu, P.; Lee, S.; Tracy, C. E.; Hopkins, A. Interfacial Stability of Thin Film Hydrogen Sensors. Proceedings of the 2000 DOE Hydrogen Program Review 2000, 1 - 16.

# CHAPTER IIB

# ALUMINIUM DOPED ZnO SOLID NANOPILLARS ARRAYS AND THEIR USEFULNESS

**IIB.1. Introduction:** In the previous chapter it has been seen that the aluminium doped ZnO (AZO) solid nanopillars arrays are not good for the hydrogen gas sensing. But it can find many other different applications. Here it has been explored that the AZO solid pillars can be a very good optical switch. When air acts as the host material for these solid pillars it shows also the generalized Brewster phenomena which is very useful for many applications such as sunglasses, Polaroid, holograms and many more. These two very important characteristics of AZO solid pillars - Generalized Brewster phenomena and the optical switching characteristics – is discussed in the following sections of this chapter. For all these experimentations the high aspect ratio AZO solid nanopillars were fabricated using a combination of advanced reactive ion etching technique and atomic layer deposition (ALD) techniques as described in the previous chapter along with their SEM characterization [1].

## IIB.2. Generalized Brewster phenomena and Perfect light absorption observed in aluminium doped ZnO (AZO) solid nanopillars arrays and their usefulness:

For this section one should know about the generalized Brewster phenomena first. Then all the details about the experimental and theoretical results will be descried to explain how our AZO solid pillars show this effect.

### IIB.2.a. Generalized Brewster Phenomena:

Brewster's angle, $\theta_B$ which is also known as polarization angle is nothing but an angle of incidence at which light with a particular polarization is perfectly transmitted without any reflection through a transparent dielectric surface. When unpolarized light strikes a surface at $\theta_B$ then the reflected light from the surface becomes perfectly polarized. This special angle of incidence is named after the Scottish physicist Sir David Brewster [2-3].

When light interacts with a boundary of two media having two different refractive indices, one part of it gets reflected and the other part gets transmitted. The figure below is describing this fact. This reflected light depends on the incoming light's polarization and angle of incidence and the rule of this dependence can be found from the Fresnel equations.

According to the Fresnel equations, p-polarized light for which the electric field polarization is in the same plane of the incident ray and the surface normal at the point of incidence, will not be reflected, if the angle of incidence is

$$\theta = \theta_B = arctan\left(\frac{n_2}{n_1}\right) \qquad \text{(IIB.2.1)}$$

Where, $n_1$ is the refractive index of the first medium through which light is propagating (as shown in the figure below), and $n_2$ is that of the other medium. The above equation is popularly known as Brewster's law, and the angle by the Brewster's angle.

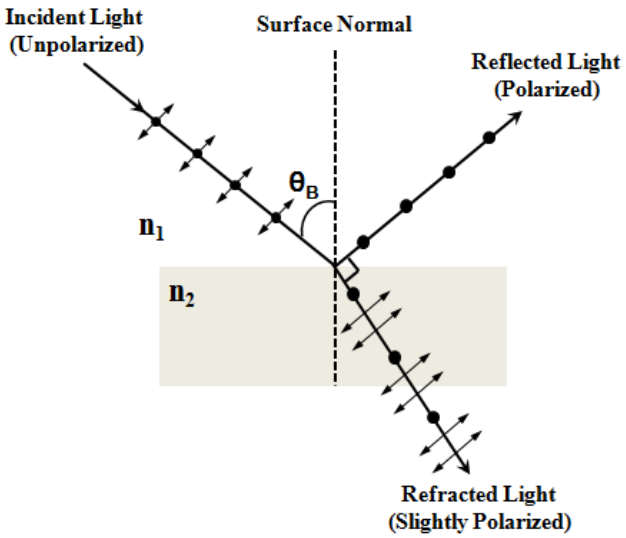


Figure IIB.1. An illustration of the light reflection when the incident angle is Brewster angle.

To qualitatively understand the mechanism behind this phenomena one should focus on the behaviour of the electric dipoles of the media in presence of p-polarized light. As the incident light gets absorbed on the surface, the electric dipoles start oscillating at the interface between two media and then they re-radiate. It's a very well-known fact that the freely propagating light polarization is always perpendicular to the light propagation direction. Now the dipoles re-radiating at the interface produce the refracted or the transmitted light which oscillate in the same polarization direction of that light. These dipoles also create the reflected light but they don't radiate energy in the direction of the dipole moment. As shown in the figure above when the refracted light is p-polarized light and it propagates perpendicularly to the direction of the reflected light, the dipoles point along the specular reflection direction and therefore no light can be reflected. In this way, the Fresnel reflection coefficients for p-polarized light vanish and the Brewster phenomenon takes place. For most of the materials this phenomena occurs only for p-polarized light.

If we consider, $\Theta_1$ as the angle of reflection (or the angle of incidence) and $\Theta_2$ as the angle of refraction, then for the condition

$$\Theta_1 + \Theta_2 = 90^o$$

Using the Snell's law,

$$n_1 \sin\Theta_1 = n_2 \sin\Theta_2$$

It can be found that, no light will be reflected if the incident angle $\Theta_1 = \Theta_B$. Thus for this condition,

$$n_1 \sin \Theta_B = n_2 \sin (90^o - \Theta_B) = n_2 \cos \Theta_B$$

This gives,

$$\theta = \theta_B = arctan\left(\frac{n_2}{n_1}\right)$$

Here it is worth to mention that, as the refractive index of a medium depends on the wavelength of the incident light, Brewster's angle also vary with the chosen wavelength. Brewster showed in his popular Brewster law that the angle for which there will be no p-polarized reflected light will be a function of the refractive indices of the material used. Brewster's angle is also known as the polarizing angle as the reflected light from a surface at this angle is completely a polarized light which has polarization perpendicular to the plane of incidence, i.e., s-polarized light. The Brewster angle concept is useful for many practical applications such as polarized sunglasses, polarizing filter cameras, for reducing glare of sun reflecting off horizontal surfaces, holograms, Brewster angle prisms to minimize reflection losses useful for laser physics [4], Brewster windows for gas lasers, in high-performance terahertz modulators [5], Brewster angle microscopes, useful in the study of surface science [6-7] and many more.

Till this point, for all the discussion of Brewster angle we have assumed that the reflection is taking place from a homogeneous, non-magnetic, achiral, and isotropic material. Generally Brewster effect is seen to occur either for s-polarized light or for p-polarized light. For a normal dielectric material, the Brewster phenomenon of p-polarized light is a common event. On the other hand, a Brewster angle for s-polarized light generally can be seen in a magnetic material with permeability $\mu \neq 1$. For some magnetic materials, $\Theta_B$ for s-polarized light ($\theta_B^{s-pol}$, in which angle the reflectance for s-polarized light is zero) is not same as the $\Theta_B$ for the p-polarized light ($\theta_B^{p-pol}$, in which angle the reflectance for p-polarized light is zero) for

non-normal incidence angle [8]. In this case, the condition $\Theta_1 + \Theta_2 = 90^o$ does not need to be satisfied (where $\Theta_1$ = angle of reflection = angle of incidence = $\Theta_B$ and $\Theta_2$ = angle of refraction) if the total destructive interference of the magnetic and/or electric dipoles of the magnetic material occurs at $\theta_B^{s,p-pol}$. Here the only necessary and sufficient condition is that the vector resultant radiation field should vanish in the reflection due to the above mentioned destructive interference [9]. For normal magnetic materials, the Brewster's angle exists only for one polarization either s- or p- , which is controlled by the relative strengths of the dielectric permittivity and magnetic permeability [21]. This fact is very useful for finding the explanation of generalized Brewster angles for dielectric metasurfaces [22] and other systems.

The generalized Brewster angle (GBA) is the incidence angle at which one can see the Brewster effect for both the polarization which means, at that particular incidence angle reflection for p- as well as s-polarized light vanishes. To have the generalized Brewster angle phenomena in a particular material along with the p-polarization Brewster effect, s-polarization Brewster effect is also needed which is only possible in case if the material has dielectric as well as magnetic response. Moreover, to realize the GBA effect in visible and NIR region, material should have magnetic response at those required frequencies to have s-polarization Brewster effect, which is quite challenging as the magnetic features become extremely weak ($\mu \approx 1$) there. Metamaterials, as they have negative permeability and thus a magnetic response are seen to have the GBA effect [10-12]. The generalized Brewster effect has also been observed experimentally in microwave region using the split-ring resonators [13-14] and in the optical frequency using all-dielectric metamaterials [15]. However, the GBA effect represented in those work did not realize the complete polarization of the reflected light, especially for the s-polarized light [15]. There, unequal reflection for p- and s-polarized light is seen which is quite normal for non-magnetic material and therefore, cannot be considered as a true Brewster effect as this is obvious according to the Fresnel equations. In addition, s-polarized Brewster effect was seen in stratified metal-dielectric metamaterial [16] and in graphene layer [4, 17]. The GBA effect was also experimentally evidenced in anisotropic material [18], Graphene combined with thin film absorber [4], chiral materials [19], and in a multilayer structure [20]. However an experimental demonstration of GBA phenomena in case of aluminium doped ZnO (AZO) nanopillars arrays was not given. AZO which is a very popular transparent conductive oxide (TCO) material, has the benefit of having low-loss compared to the conventional noble metals, such as gold, silver, platinum,

rhodium, iridium, palladium etc. Thus the realization of the GBA effect in AZO structures will be very useful for many applications as already discussed especially for the sensing applications if they will provide the strong field localization which is possible for certain kind of structure.

Here in the following sections all the experimental results will be discussed about the presence of the generalized Brewster angle effect in the high aspect ratio highly ordered aluminium doped ZnO (AZO) solid pillar structures. These low-loss AZO structures satisfy both the p- and s- polarization Brewster condition experimentally at multiple wavelengths in the NIR region. The wavelength range at which these GBA effect occurs can also be tuned by tuning the angle of incidence which is adding one more advantage of these structures for sensing. Because of the high aspect ratio of these TCO structures, it is also expected to have strong field localization near their surface and thus a high sensitivity during protein sensing.

**IIB.2.b. Results and discussions regarding the GBA effect in AZO solid pillars:**

Here in this section, the experimental and theoretical details regarding the GBA effect of AZO pillars will be given. The fabrication method of these AZO nanopillars is already explained in the previous chapter along with their SEM characterization details. From the SEM study it has been seen that these high aspect ratio AZO nanopillars structures are highly ordered. All of their structure parameters can be found from that study (of previous chapter). The diameter and height of the AZO solid pillars are 300 nm and 2 $\mu$m, respectively, and a pitch of either 400 nm or 500 nm in the square lattice is maintained over the area $1\times1cm^2$. For these structures air and Si acts as the host-material on which the AZO pillars are submerged. All the AZO solid pillars structures are standing on thermally grown 200 nm silica layer over a Si substrate. To explore the GBA effect of these structures the optical properties of AZO pillars fabricated by ALD have been measured by spectroscopic ellipsometer for the wavelength range of interests. The method of these optical measurements is given below.

**Ellipsometric reflection measurement method:** A high-resolution variable-angle spectroscopic ellipsometry (SE) (J. A. Woollam Co., Inc., V-VASE) is used to experimentally measure all types of angular reflection data. The low-power spectroscopic ellipsometer has high precision and it is non-destructive and thus preferable for the optical characterization of nanostructures. The measurements are taken using the variable angle ellipsometer to have the reflectivity R ($\lambda$, $\phi$) at different angle of incidence, $\phi$, in the

wavelength range of λ = 300 - 3300 nm. The maximum resolution of this ellipsometer is 0.03 nm but for our measurements 1 nm resolution is maintained throughout all the experiments.

**Experimental Results and related Discussions:** The experimental results for both s- and p-polarized light are given to claim the GBA effect of these nanopillars arrays. For all types of the AZO solid nanopillars arrays (with 400/500 nm pitch in the square lattice and for both air/Si host material) the transmission is measured to be zero for all wavelengths and angles. The figure below shows transmission feature for both kinds of polarization of the AZO solid pillars where air acts as the host material and 400 nm pitch is maintained. Here $1\times10^{-3}$ in the transmission scale is considered as the zero transmission. The zero transmission feature is true for lower (0 - 40 deg) as well as higher angles. The same characteristic has been seen for the other solid pillar samples – where 500 nm pitch is maintained for air host and 400 nm/500 nm pitch is maintained for Si host. Since all the AZO solid pillars arrays are opaque (Transmission, T = 0) we can consider for those samples absorbance (A) is complementary to the reflectance (R), i.e., A = (1 – R) (as it is well-known that A + R + T = 1). So for these AZO solid pillars array system whenever we will see R ≃ 0, we can consider that as a perfect light absorption.

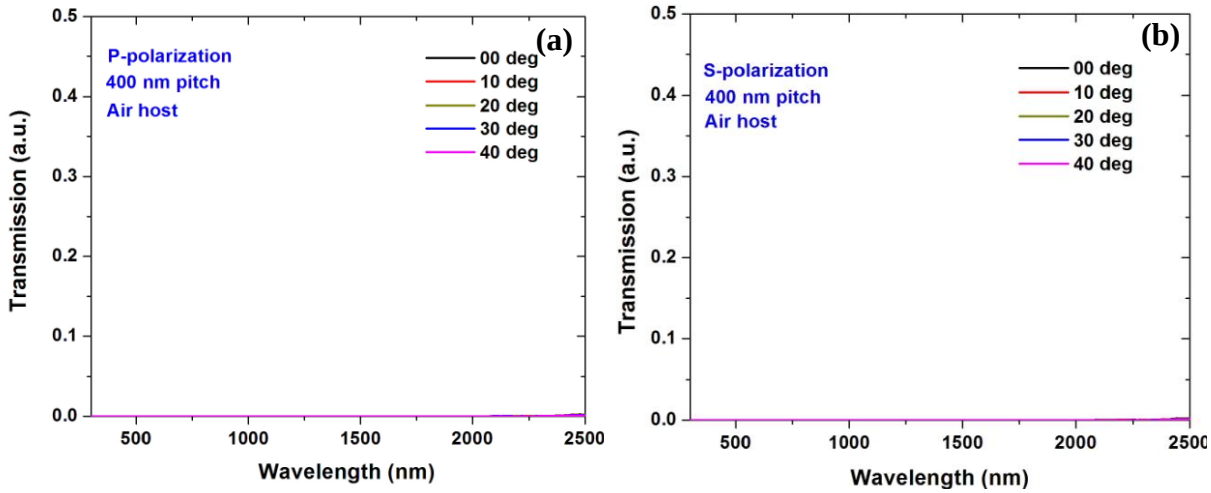


Figure IIB.2. The transmission characteristics of the AZO solid nanopillars arrays for both (a) P-polarization and (b) S-polarization are shown. In this case air is acting as the host material and pitch is 400 nm. The angle of measurement in this case is from 0 deg to 40 deg but this kind of zero transmission features of the AZO solid pillars is true for higher angles too. Moreover, the zero transmission is applicable to all the other three kind of solid AZO nanopillar system – where 500 nm pitch is maintained for air host and for Si host where 400 nm and 500 nm pitch is maintained over 1×1 $cm^2$ area. Here $1\times10^{-3}$ in the transmission scale is considered as the zero transmission.

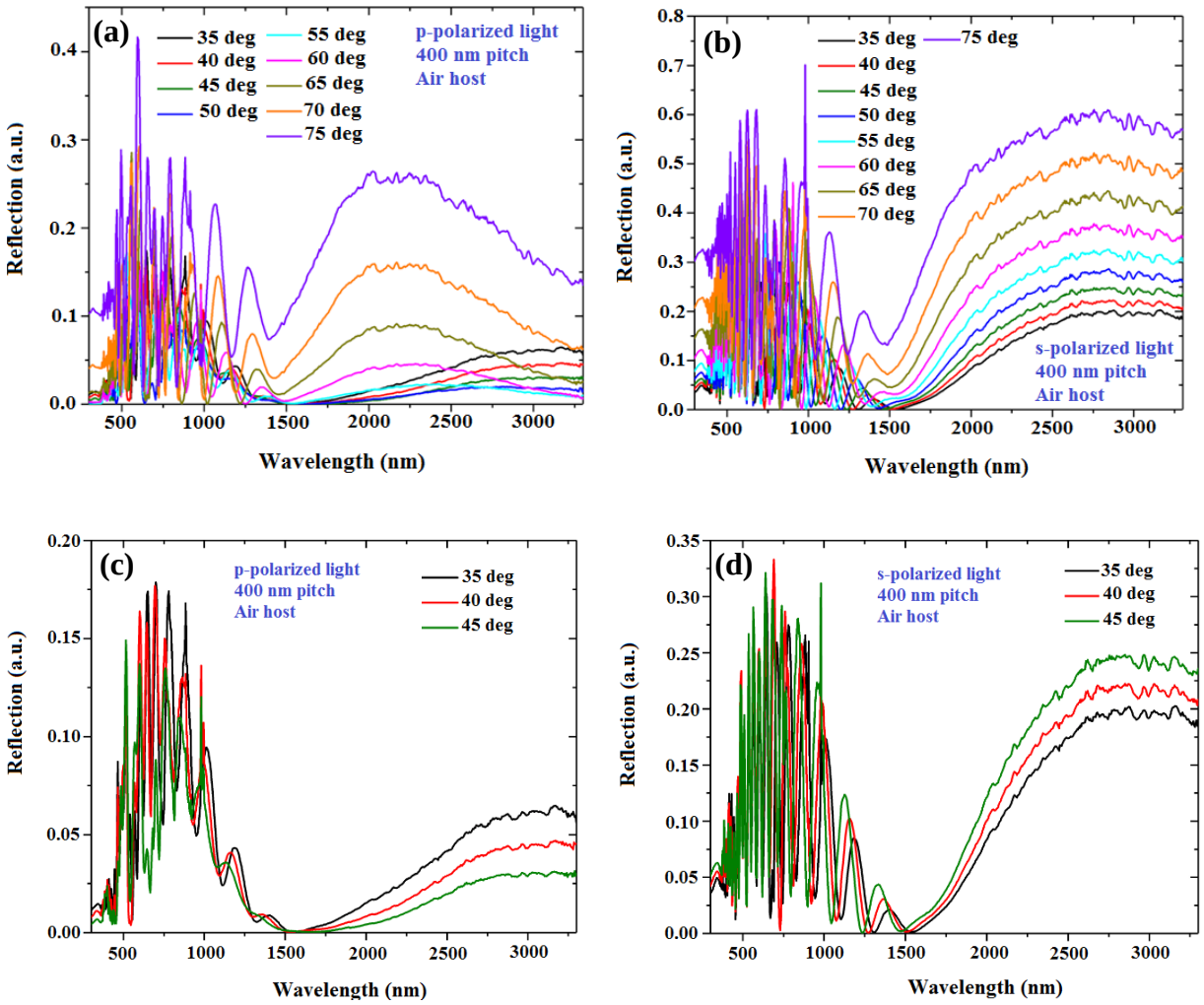


Figure IIB.3. The reflection characteristics of the AZO solid nanopillars arrays for both (a, c) P-polarization and (b, d) S-polarization are shown here. In this case air is acting as the host material and pitch is 400 nm. The angle of measurement is varied from 35 deg to 75 deg in panel (a) and (b) showing reflection characteristics for p- and s- polarization respectively for a higher angular range. There the GBA effect for this structure is found near 1500 nm and over an angular range of 35 deg to 45 deg. In panel (c) and (d) the zero reflection for both s- and p- polarization is shown. The wavelength at which this GBA effect is occurring is seen to have a blue shift when the measurement angle increases.

The angular reflection characteristics of the AZO solid pillar arrays with 400 nm pitch and air host is shown in the figure IIB.3 for both (a) p- and (b) s- polarization where the measurement angle is varied from 35 deg to 75 deg by 5 deg. Here it's clear that for 35 deg, 40 deg and 45 deg incident angle we can have both p- and s- Brewster phenomena. From panel (c) and (d) the zero reflection phenomena for both p- and s- polarization is very clear for those three angles. Here one can notice that the Brewster wavelength gets blue-shifted for higher incident angle.

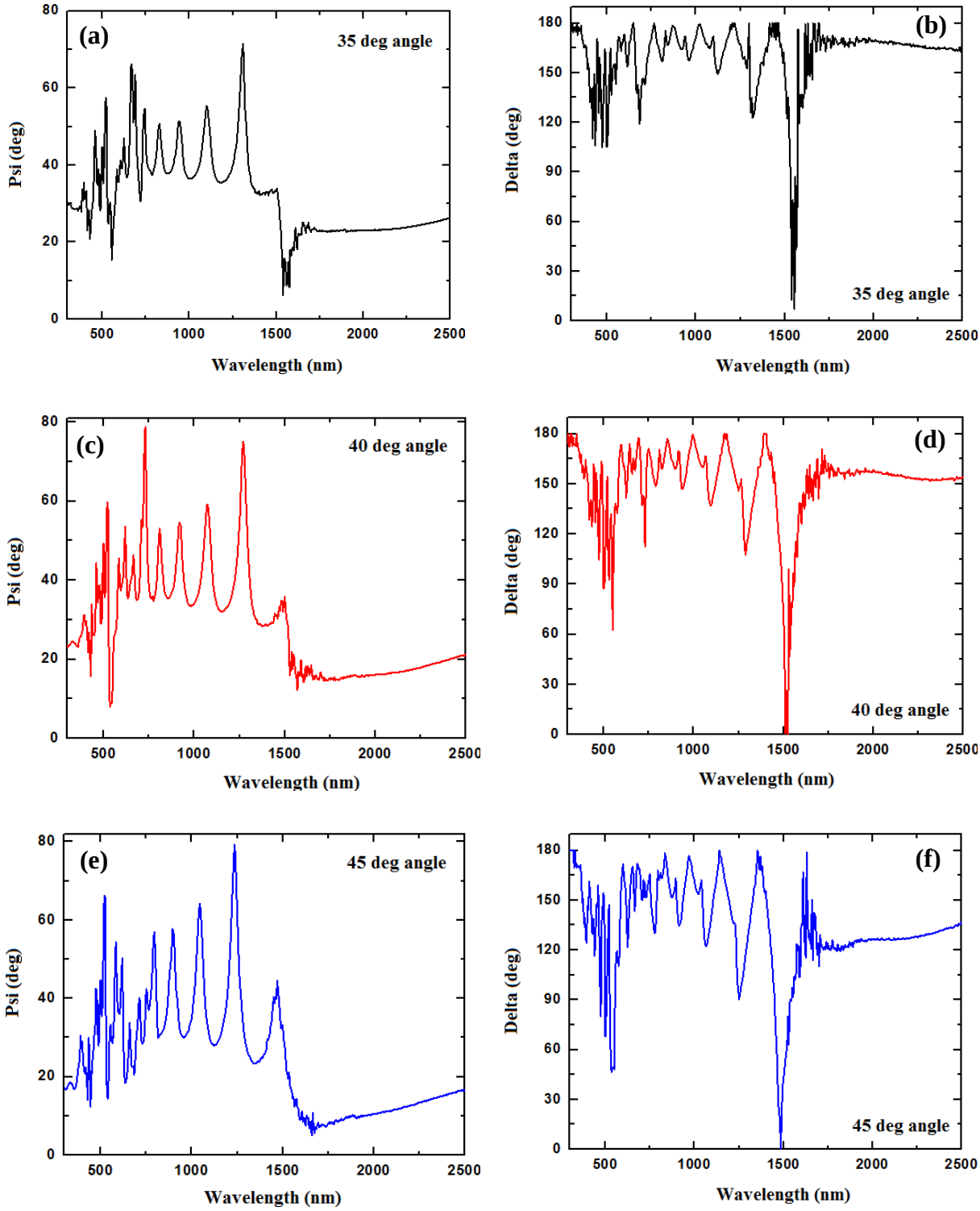


Figure IIB.4. Spectroscopic parameters of the AZO solid pillars arrays system with 400 nm pitch and air host for three different measurement angle. (a) Psi for 35 deg angle, (b) Delta for 35 deg angle, (c) Psi for 40 deg angle, (d) Delta for 40 deg angle, (e) Psi for 45 deg angle, and (f) Delta for 45 deg angle is shown.

The wavelength at which the generalized Brewster angle (GBA) phenomena is taking place for 35 deg, 40 deg, and 45 deg incident angle in case of AZO solid pillars arrays system with

air host and 400 nm pitch can be better understood from their spectroscopic parameter study, measured with the help of ellipsometer at those incident angles. The figure IIB.4 is showing both psi and delta characteristics at 35 deg, 40 deg and 45 deg angle measured with the help of spectroscopic ellipsometer. In panel (b), (d), and (f) the particular wavelength at which the GBA effect is occurring can be figured out by pointing out the wavelength at which delta is changing by 180 deg. So the comparison among all the GBA wavelengths for 35 deg, 40 deg and 45 deg informs that the GBA wavelength shows a blue shifting for higher incident angle as already seen in the figure IIB.3. Panel (a), (c) and (e) are showing the variation of the parameter Psi for this AZO structure for 35 deg, 40 deg, and 45 deg respectively. At the GBA wavelength in each case (35 deg/40 deg/ 45 deg incident angle) the Psi parameter goes from minimum to maximum for 35 deg (panel a), maximum to minimum for 40 deg (panel b), and also maximum to minimum for 45 deg (panel c) incident angle.

The AZO solid pillars with Air host and 500 nm pitch also shows this kind of GBA effect. Here in the figure IIB.5 the reflection characteristics of these AZO pillars for both p- and s-polarization are shown for variable angle. Panel (a) and (b) are showing the reflection for p- and s- polarized light where the incident angle is varied from 35 deg to 75 deg by 5 deg. For no angles from 35 deg to 75 deg, the GBA effect is seen here with zero reflectance for both p- and s- polarization. But the reflection measurements for lower incident angles (15 deg to 25 deg by 5 deg) shown in panel (c) and (d) for p- and s- polarization respectively reveals that this structure also has the GBA effect. Here GBA effect is seen to occur around 1600 nm for 15 deg, 20 deg, and 25 deg incident angle. The blue shifting of the GBA wavelength for higher incident angle can also be verified here. It is worth to mention here that, compared to the case of AZO solid pillars with air host and 400 nm pitch here for 500 nm pitch, the GBA effect is seen to occur at smaller angular range because for 400 nm pitch the GBA is seen for 35 deg - 45 deg angular range and for 500 nm pitch the GBA is seen for 15 deg - 25 deg angular range.

At this point, it is very clear that the AZO solid pillars array system with air as the host material has the GBA effect for both the 400 nm and 500 nm pitch. These structures are thus able to behave as the perfect light absorber at those particular wavelength and incident angle range. Therefore these AZO solid pillars structures will be useful for many applications such as polarized sunglasses, polarizing filter cameras, holograms, Brewster angle prisms, Brewster windows, Brewster angle microscopes and many more as already discussed in the introduction. As the AZO is a low-loss TCO material, thus this high aspect ratio, highly

ordered AZO solid pillars array nanostructures having GBA effect will also be useful for protein sensing as these high aspect ratio structures are able to have a high electric field intensity enhancement at their surface. For the GBA and thus perfect light absorption property of these structures one may use them also as the optical switch where incident angle and the operating wavelength can be used to switch from one optical state (ON state) to the other optical (OFF state).

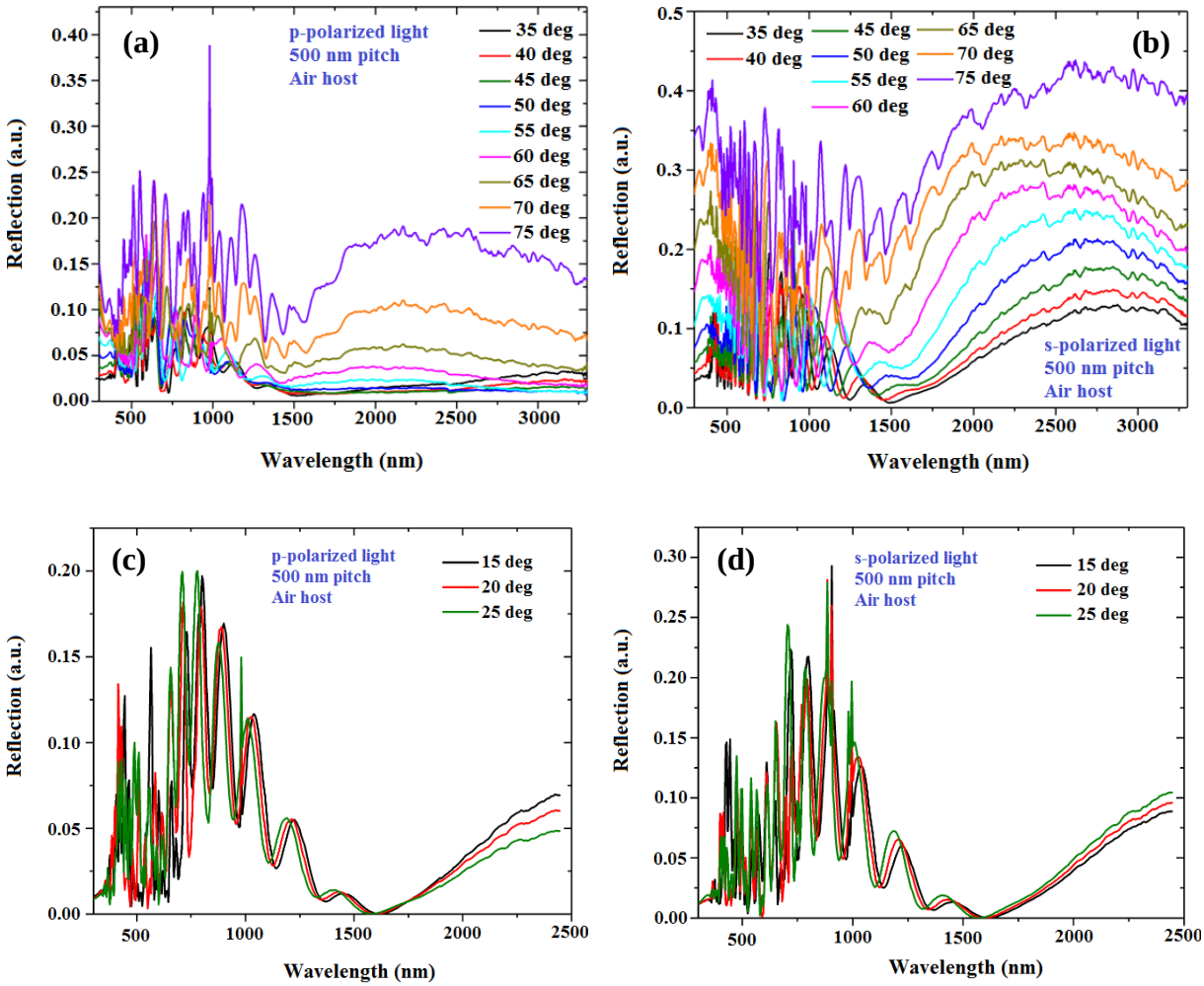


Figure IIB.5. The reflection characteristics of the AZO solid nanopillars arrays for both (a, c) P-polarization and (b, d) S-polarization are shown here. In this case air is acting as the host material and pitch is 500 nm. The angle of measurement is varied from 35 deg to 75 deg in panel (a) and (b) showing reflection characteristics for p- and s- polarization respectively for a higher angular range. There the GBA effect for this structure is found near 1600 nm and over an angular range of 35 deg to 45 deg. In panel (c) and (d) the zero reflection for both s- and p- polarization is shown. The wavelength at which this GBA effect is occurring is seen to have a blue shift when the measurement angle increases.

**IIB.3. AZO solid pillars as optical switch:** The optical switches are better than the electronic switches for many reasons and recently a lot of research groups have introduced different types of optical switches to apply in different areas [21-33]. In the previous section the AZO solid pillars with air host are seen to be useful as optical switches for their GBA effect and their perfect light absorption capability.

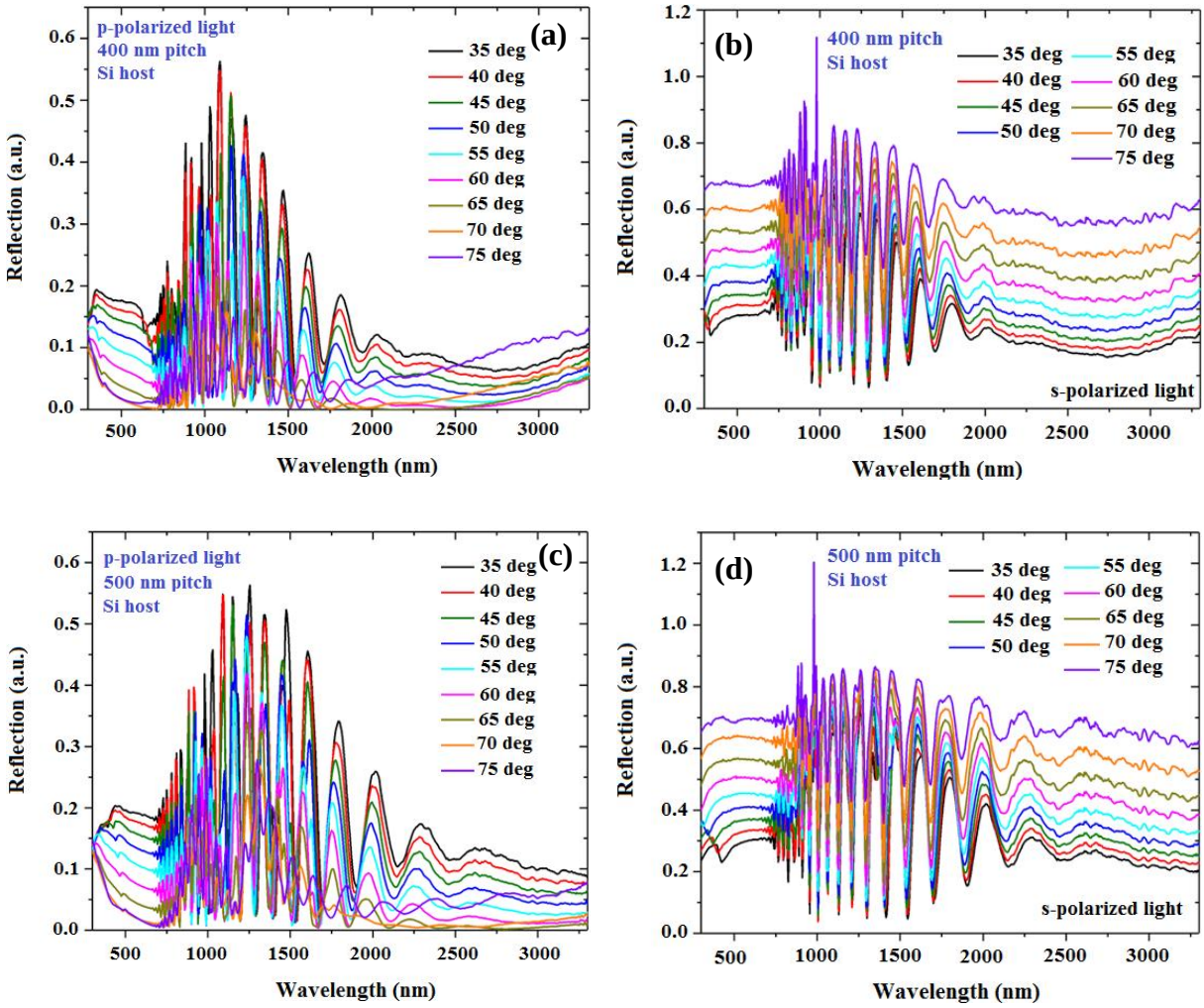


Figure IIB.6. The reflection characteristics of the AZO solid nanopillars arrays where Si acts as the host material. (a) Reflection for p-polarized light, (b) Reflection for s-polarized light is shown. For both (a) and (b) AZO solid pillars with 400 nm pitch is chosen. (c) Reflection for p-polarized light from AZO solid pillars array system with 500 nm pitch, (d) Reflection for s-polarized light from AZO solid pillars array system with 500 nm pitch, is shown. For all the angular reflection measurements the incident angle is varied from 35 deg to 75 deg by 5 deg.

The reflection properties for both p- and s- polarization of the Si host AZO solid structures with 400 nm and 500 nm pitches are shown in the figure above. Here the reflection properties for different measurement angles are shown. It is quite evident here that the refection properties of these Si host structures are way more different than that of the air host case and

they don’t show any GBA effect. But these structures are also useful to build optical switches based on the variation of the reflection intensity for different angles, polarization, and operating wavelength.

**IIB.4. Conclusion:** In summary, here from all the experiments, it has been seen that the AZO solid pillars structures with Air host have the GBA effect and thus they behave as perfect light absorber over a particular range of wavelength and incident angle which makes them useful as optical switches. Although, the Si host structures did not show any GBA effect like the air host structures yet their unique reflection properties for both polarization helps to use them as optical switches by controlling the light polarization, incident angle and operating wavelength.

**IIB.5. Reference:**

[1] Shkondin, E.; Takayama, O.; Panah, M. E. A.; Liu, P.; Larsen, P. V.; Mar, M. D.; Jensen, F.; Lavrinenko, A. V. Large-scale high aspect ratio Al-doped ZnO nanopillars arrays as anisotropic metamaterials. Optical Materials Express 2017, 7, 1606 - 1627.

[2] Brewster, D. On the laws which regulate the polarisation of light by reflexion from transparent bodies. Philosophical Transactions of the Royal Society of London. 1815, 105, 125–159.

[3] Lakhtakia, A. Would Brewster recognize today's Brewster angle. Optics News. 1989, 15, 14–18.

[4] Sreekanth, K. V.; ElKabbash,E.; Medwal, R.; Zhang, J.; Letsou, T.; Strangi, G.; Hinczewski, M.; Rawat, R. S.; Guo, C.; Singh, R. Generalized Brewster Angle Effect in Thin-Film Optical Absorbers and Its Application for Graphene Hydrogen Sensing. ACS Photonics 2019, 6, 1610−1617.

[5] Chen, Z.; Chen, X.; Tao, L.; Chen, K.; Long, M.; Liu, X.; Yan, K.; Stantchev, R. I.; Pickwell-MacPherson, E.; Xu, J.-B. Graphene controlled Brewster angle device for ultra-broadband terahertz modulation. Nat. Commun. 2018, 9, 4909.

[6] Hoenig, D.; Moebius, D. Direct visualization of monolayers at the air−water interface by Brewster angle microscopy. J. Phys. Chem. 1991, 95, 4590−4592.

[7] Kravets, V. G.; Schedin, F.; Jalil, R.; Britnell, L.; Gorbachev, R. V.; Ansell, D.; Thackray, B.; Novoselov, K. S.; Geim, A. K.; Kabashin, A. V.; Grigorenko, A. N. Singular phase nano optics in plasmonic metamaterials for label-free single-molecule detection. Nat. Mater. 2013,

12, 304−309.

[8] Giles, C. L.; Wild, W. J. Brewster angles for magnetic media. Int. J. Infrared Millimeter Waves 1985, 6, 187−197.

[9] Heading, J. Generalized Investigations into the Brewster Angle. Opt. Acta 1986, 33, 755−770.

[10] Shalaev, V. M. Optical negative-index metamaterials. Nat. Photonics 2007, 1, 41−48.

[11] Zheludev, N. I. The road ahead for metamaterials. Science 2010, 328, 582−583.

[12] Fu, C.; Zhang, Z. M.; First, P. N. Brewster angle with a negative index material. Appl. Opt. 2005, 44, 3716−3724.

[13] Tamayama, Y.; Nakanishi, T.; Sugiyama, K.; Kitano, M. Observation of Brewster's effect for transverse-electric electromagnetic waves in metamaterials: Experiment and theory. Phys. Rev. B: Condens. Matter Mater. Phys. 2006, 73, 193104.

[14] Tamayama, Y. Brewster effect in metafilms composed of bi-anisotropic split-ring resonators. Opt. Lett. 2015, 40, 1382−1385.

[15] Paniagua- Domínguez, R.; Yu, Y. F.; Miroshnichenko, A. E.; Krivitsky, L. A.; Fu, Y. H.; Valuckas, V.; Gonzaga, L.; Toh, Y. T.; Kay, A. Y. S.; Luk'yanchuk, B.; Kuznetsov, A. I. Generalized Brewster effect in dielectric metasurfaces. Nat. Commun. 2016, 7, 10362.

[16] Watanabe, R.; Iwanaga, M.; Ishihara, T. s-polarization Brewster's angle of stratified metal−dielectric metamaterial in optical regime. Phys. Status Solidi B 2008, 245, 2696−2701.

[17] Lin, X.; Shen, Y.; Kaminer, I.; Chen, H.; Soljačić, M. Transverse-electric Brewster effect enabled by nonmagnetic two dimensional materials. Phys. Rev. A: At., Mol., Opt. Phys. 2016, 94, 023836.

[18] Lakhtakia, A. Would Brewster recognize today's Brewster angle. Optics News 1989, 15, 14−18.

[19] Bassiri, S.; Papas, C. H.; Engheta, N. Electromagnetic wave propagation through a dielectric−chiral interface and through a chiral slab. J. Opt. Soc. Am. A 1988, 5, 1450−1459.

[20] Mahlein, H. F. Generalized Brewster-angle conditions for quarter-wave multilayers at non-normal incidence. J. Opt. Soc. Am. 1974, 64, 647−653.

[21] Giles, C. L.; Wild, W. J. Brewster angles for magnetic media. International Journal of

Infrared and Millimeter Waves 1985, 6, 187–197.

[22] Paniagua-Domínguez, R.; Feng, Y. Y.; Miroshnichenko, A. E.; Krivitsky, L. A.; Fu, Y. H.; Valuckas, V.; Gonzaga, L. et al. Generalized Brewster effect in dielectric metasurfaces". Nature Communications. 2016, 7, 10362.

[23] Chilwell, J.; Hodgkinson, I. Thin films field-transfer matrix theory of planar multilayer waveguides and reflection from prismloaded waveguides. J. Opt. Soc. Am. A 1984, 1, 742.

[24] Yang, Y.; Kelley, K.; Sachet, E.; Campione, S.; Luk, S. T.; Maria, J.-P.; Sinclair, M. B.; Berner, I. Femtosecond optical polarization switching using a cadmium oxide-based perfect absorber. Nat. Photonics 2017, 11, 390−395.

[25] Banon, J. –P.; Hetland, Q. S.; Simonsen, I. Physics of polarized light scattering from weakly rough dielectric surfaces: Yoneda and Brewster scattering phenomena. Phys. Rev. A 2019, 99, 023834.

[26] Smith, P. W. Application of all-optical switching and logic. Phil. Trans. R. Soc. Lond. A 1984, 313, 349-355.

[27] Tucker, R. S. Optical packet switching: A reality check. Opt. Switch. Netw. 2008, 5, 2-9.

[28] Fork, R. L. Physics of optical switching. Phys. Rev. A 1982, 26, 2049-2064.

[29] K. Asakawa, Y. Sugimoto, Y. Watanabe, N. Ozaki, A. Mizutani, Y. Takata, Y. Kitagawa, H. Ishikawa, N. Ikeda, K. Awazu, X. Wang, A. Watanabe, S. Nakamura, S. Ohkouchi, K. Inoue, M. Kristensen, O. Sigmund, P. I. Borel, and R. Baets, Photonic crystal and quantum dot technologies for all-optical switch and logic device. New J. Phys. 2006, 8, 208, 126.

[30] Jin, C.-Y.; Wada, O. Photonic switching devices based on semiconductor nano-structures. Journal of Physics D. 2014, 47, 133001.

[31] Paniagua-Dominguez, R.; Yu, Y. F.; Miroshnichenko, A. E.; Krivitsky, L. A.; Fu, Y. H.; Valuckas, V.; Gonzaga, L.; Toh, Y. T.; Kay, A. Y. S.; Lukyanchuk, B.; Kuznetsov, A. I. Generalized Brewster effect in dielectric metasurfaces. Nature Communications 2016, 7, 10362.

[32] Paniagua-Dominguez, R.; Yu, Y. F.; Miroshnichenko, A. E.; Krivitsky, L. A.; Fu, Y. H.; Valuckas, V.; Gonzaga, L.; Toh, Y. T.; Kay, A. Y. S.; Lukyanchuk, B.; Kuznetsov, A. I. Generalized Brewster-Kerker effect in dielectric metasurfaces.

[33] Abujetas, D. R.; Sánchez-Gil, J. A.; Sáenz, J. J. Generalized Brewster effect in high refractive-index nanorod-based metasurfaces. Optics Express 2018, 26, 31523.

# PART III

# FEW ADDITIONAL PROJECTS DONE

# Chapter I

## Twin Photonic Nanojet

**Introduction:** Photonic nanojet (PNJ) is an em beam coming out from the shadow side of a lossless dielectric microstructure (seen in microsphere and in micro-cylinder) when illuminated by a non-resonant Gaussian wave or a plane wave [1-2]. This kind of beam is much focused and thus is narrow and capable of having high electric field intensity [1-5]. The PNJ originates from the constructive interference of the incident em wave and the strong Mie scattered light wave coming out of the microstructures [3-10]. The maximum intensity enhancement by the PNJ has been reported to be around 500 times the incident em field intensity [2]. This kind of electric field manipulation using PNJ can be used in many applications especially to enhance the surface enhanced Raman scattering (SERS) signal [11-14].

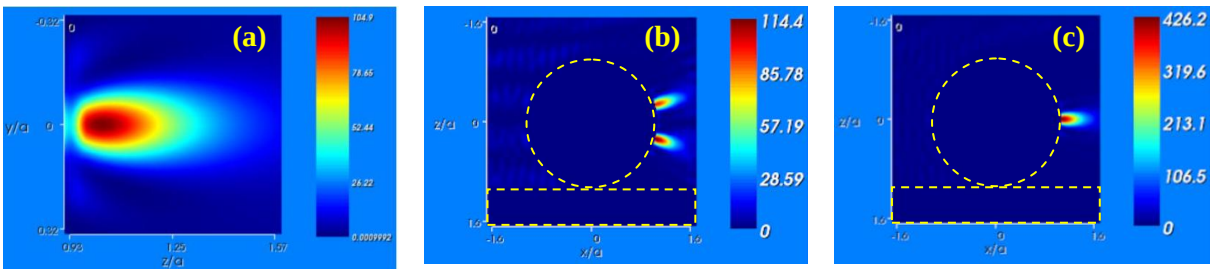


Figure I.1. (a) Photonic nanojet created by a bare microsphere. Photonic nanojet created by a microsphere with a substrate (b) for lower angle, (c) higher angle. Here the radius, the refractive index of microsphere and the surrounding medium is considered to be 2 μm, 1.6, and 1.0 respectively. Incident wavelength of light is 632.8 nm.

**Results and Discussions:** The figure I.1 (a) shows PNJ of a bare microsphere of 2 um radius and refractive index 1.6 in air. For PNJ, the length, width, the maximum possible intensity enhancement factor, and the distance of the highest intensity area from the surface of the microstructure can be tuned by varying the size, shape, and refractive index of the microstructure, and the refractive index of the dielectric medium. One advantage of this PNJ is the possibility of tuning the distance of the highest intensity area from the surface of the microstructure which is not possible for the plasmonic hot-spots – seen always adjacent to the nanoparticle surface. Therefore with PNJ one can excite some areas which are far from the micro particle surface. Here PNJ related theoretical work has been done. In this work it has been seen that with the proper arrangement of a micro-particle along with a substrate one can have two parts of PNJ easily (fig. I.1 (b)). The direction of these twins PNJ is tunable

depending on the angle of incidence for a particular polarization (I.1 (c)). Till now no theoretical and experimental proof is present to show this kind of behaviour. The intensity enhancement in this case is larger with respect to the bare microstructure (I.1 (c)). Not only the presence of two PNJs is seen here but also in this work one can tune the distance of the highest intensity area of both the PNJs from the surface of the microstructure and the angle between those two PNJs. Here all the theoretical analysis on PNJs of the dielectric microsphere with a substrate has been done by DSIMie software, [15] which is developed based on Lorenz–Mie scattering theory of a single microsphere.

**Reference:**


[1] G. M. Das, A. B. Ringne, V. R. Dantham, R. K. Easwaran, R. Laha, Optics Express. 2017, 25, 19822-19831.

[2] G. M. Das, R. Laha, V. R. Dantham, J. Raman Spectrosc. 2016, 47, 895–900.

[3] Z. Chen, A. Taflove, V. Backman, Opt. Express 2004, 12, 1214.

[4] X. Li, Z. Chen, A. Taflove, V. Backman, Opt. Express 2005, 13, 526.

[5] A. V. Itagi, W. A. Challener, J. Opt. Soc. Am. A 2005, 22, 2847.

[6] A. Heifetz, J. J. Simpson, S. C. Kong, A. Taflove, V. Backman, Opt. Express 2007, 15, 17334.

[7] S. Lecler, S. Haacke, N. Lecong, O. Crégut, J. L. Rehspringer, C. Hirlimann, C. Opt. Express 2007, 15, 4935.

[8] P. Ferrand, J. Wenger, A. Devilez, M. Pianta, B. Stout, N. Bonod, H. Rigneault, Opt. Express 2008, 16, 6930.

[9] D. Gérard, J. Wenger, A. Devilez, D. Gachet, B. Stout, N. Bonod, H. Rigneault, Opt. Express 2008, 16, 15297.

[10] A. Devilez, N. Bonod, J. Wenger, D. Gérard, B. Stout, H. Rigneault, E. Popov, Opt. Express 2009, 17, 2089.

[11] K. J. Yi, H. Wang, Y. F. Lu, Z. Y. Yang, J. Appl. Phys. 2007, 101, 063528.

[12] C. L. Du, J. Kasim, Y. M. You, D. N. Shi, Z. X. Shen, J. Raman. Spectrosc. 2011, 42, 145.

[13] V. R. Dantham, P. B. Bisht, C. K. R. Namboodiri, J. Appl. Phys. 2011, 109, 103103.

[14] J. F. Cardenas, J. Raman Spec. 2013, 44, 540.

[15] S. Lee, L. Li, Z. Wang, J. Opt. 2014, 16, 015704.

# Chapter II

# Acoustic Metamaterial

**Introduction:** An acoustic metamaterial (AMM) is an artificially designed material which can control, direct or manipulate the incoming sound waves. The AMM belongs to the class of conventional metamaterials and therefore obeys the same basic principle like the metamaterials in general. These types of materials usually acquire their unique properties from their structure due to the cleverly implanted inhomogeneities rather than composition. Similar to electromagnetic metamaterial, AMM also get their unique properties from its negative index character, which can be achieved by adjusting the effective bulk modulus, $\beta$, mass density, $\rho$, and chirality. Here it is worth to mention that the mass density and bulk modulus in the case of AMM are parallel to the electric permittivity, $\varepsilon$, and magnetic permeability, $\mu$ in the case of em metamaterials. The first AMM has been reported in 2000 using sonic crystals in a liquid [2]. After that a lot of AMMs have been reported [3-6]. These AMMs can find applications in many areas such as – acoustic superlens, acoustic diodes, medical imaging, acoustic cloak, acoustic rectification, acoustic near-zero index [5-9]. In this chapter (following paragraph) a brief idea about our 3D printed AMM will be given.

**Results and Discussions:** Here AMMs have been fabricated by 3D printing. The structures are shown in the figure II.1. Based on the number of unit cells present in a structure those are marked as “0 dimensional (0D)”, “1 dimensional (1D)”, “2 dimensional (2D)”, and “3 dimensional (3D)”, according to the convention we know. These structures are fabricated with and without a neck section (along with its rhombus shaped cavity). The necked ones show a peculiar behaviour because of their inhomogeneities. A particular frequency of sound waves was swallowed up by these necked AMM structures when they face the sound generator in a specific way. This asymmetric behaviour of the sound wave coming out from the necked AMM structure in presence of a continuous sound wave generator is shown in the figure II.1 (b). Here it is worth to mention that this kind of behaviour does not vary with the distances from the sound generator provided a sound wave interact with the AMM with a good intensity level. Furthermore, these 3D printed AMM structures show shift in their characteristic frequency dip when one will consider the response from 0D to 3D (for either necked structures or without neck) which is very common feature of an AMM.

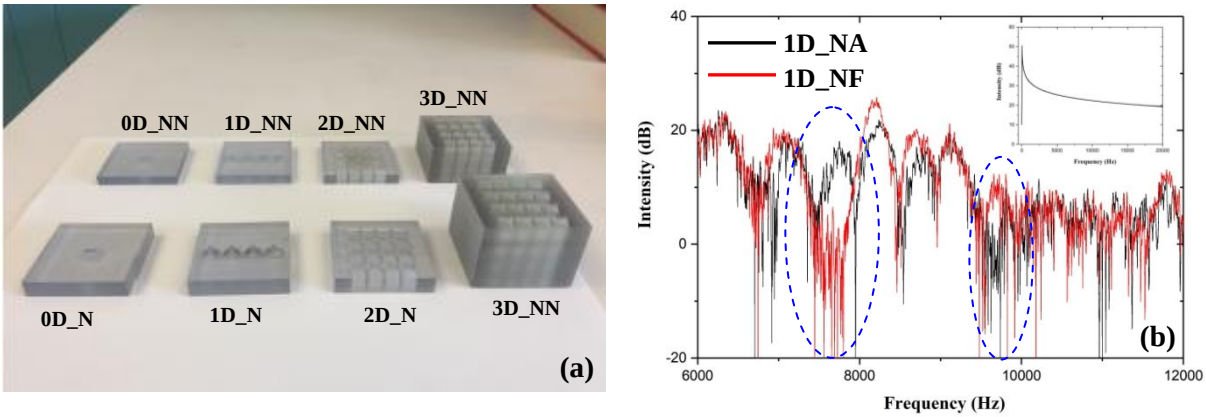


Figure II.1 (a) Different 3D printed AMMs are shown (0D, 1D, 2D, and 3D) which are fabricated with (N) and without neck (NN). (b) The asymmetric behaviour is shown. Here the measurement has been done with 1D necked AMM structure, but this character is maintained also for 0D and 2D necked AMM structure. Here NA and NF denote respectively the neck away and neck facing case from the sound source. The inset is showing the input sound signal where almost 25 dB is maintained from 4000-20000 Hz.

**Reference:**

[1] Guenneau, Sébastien; Alexander Movchan; Gunnar Pétursson; S. Anantha Ramakrishna (2007). "Acoustic metamaterials for sound focusing and confinement" (PDF). New Journal of Physics. 9 (399): 1367–2630.

[2] Zhengyou Liu, Liu; Xixiang Zhang; Yiwei Mao; Y. Y. Zhu; Zhiyu Yang; C. T. Chan; Ping Sheng (2000). "Locally Resonant Sonic Materials". Science. 289 (5485): 1734–1736.

[3] Smith, D. R.; Padilla, WJ; Vier, DC; Nemat-Nasser, SC; Schultz, S (2000). "Composite Medium with Simultaneously Negative Permeability and Permittivity" (PDF). Physical Review Letters. 84 (18): 4184–4187.

[4] Li, Jensen; C. T. Chan (2004). "Double-negative acoustic metamaterial". Phys. Rev. E. 70 (5): 055602.

[5] Thomas, Jessica; Yin, Leilei; Fang, Nicholas (2009). "Metamaterial brings sound into focus". Physics. 102 (19): 194301.

[6] Shuang Chen, Yuancheng Fan, Quanhong Fu, Hongjing Wu, Yabin Jin, Jianbang Zheng, and Fuli Zhang. A Review of Tunable Acoustic Metamaterials.

[7] Zhang, Shu; Leilei Yin; Nicholas Fang (2009). "Focusing Ultrasound with Acoustic Metamaterial Network". Phys. Rev. Lett. 102 (19): 194301.

[8] Li, Baowen; Wang, L; Casati, G (2004). "Thermal Diode: Rectification of Heat Flux". Physical Review Letters. 93 (18): 184301.

[9] Ding, Yiqun, Liu, Zhengyou; Qiu, Chunyin; Shi, Jing (2007). Metamaterial with Simultaneously Negative Bulk Modulus and Mass Density. Phys. Rev. Lett. 99 (9), 093904.

# Chapter III

## Plasmonic Nanoantenna for Cancer Therapy

**Introduction:** Photodynamic therapy (PDT), an emerging technique for cancer therapy is better than the traditional therapies such as chemotherapy, surgery, or radiotherapy because of its less side-effect and other issues. PDT, a non invasive treatment with spatio-temporal selectivity has three components - a photosensitizer molecule, tissue oxygen and light. When the photosensitizer illuminated with a light of specific wavelength it gets excited to a singlet state. After that during the intersystem crossing it can reach to the long-lived triplet excited state which eventually helps to generate the singlet oxygen ($^1O_2$). This singlet oxygen helps to damage the tumor cell irreversibly and is the reason why PDT is considered as safer and more effective. Cyclometalated iridium (III) complexes due to many reasons seem to be a good candidate for bio-imaging and sensing [3-5] and furthermore, it gets extended even in the field of PDT for many advantages [6-8]. But recently it has been seen that the application of nanoparticle in PDT could make the conventional bare PDT more powerful because of many inherent advantages of nanoparticles [3]. Silica-based NPs are one of the promising candidates for this extended PDT [3, 9-10]. Recently Loredana et al reported the synthesis of water soluble iridium (III) complex ($Ir_1$), a photosensitizer and luminescent probe coupled with a gold core which can act as a very good PDT agent. These $Ir_1$-embedded silica NPs with a gold core has several advantages – high emission quantum yield, water solubility, possibility of simultaneous cellular imaging, photodynamic and photo thermal therapies, combined photodynamic–photo thermal effect (introduced due to the presence of the nanoparticle) [3]. The research group reported very promising in-vitro photo-cytotoxicity study results using these nanocomposites on human glioblastoma tumor cells (U87MG) and proposed as one of the promising Theranostics agents in cancer therapy. That impressive result poked us to do some in-vivo study to evaluate the capability of that Ir based nanocomposites for treating the brain cancer (glioblastoma tumor cells) in real environment. The theme of this work is written in the following paragraph.

**Results and Discussions:** For this project immune-suppressed mice are used where every mouse has a pea sized tumor (containing glioblastoma tumor cells). For therapy at first, the aqueous solution containing $Ir_1$-embedded silica NPs with a gold core injected locally at the tumor of a mouse. The amount has been fixed based on the size of the tumor. Then the tumor area is illuminated with the UV-light (decided based on the extinction characteristics of the

probe) for certain time. This step has been done only once for each mice and then kept at normal condition. After certain days (around 1 month) the tumor is seen to disappear completely. Monitoring those treated mice for quite a long time help us to conclude that the re-appearance of the tumor has not been seen here (re-appearance of the tumor is a known problem in case of brain cancer). To confirm about the successful treatment with this probe more than one mouse are treated and monitored. Here in-vivo imaging has also been done to see the reactivity of the drug.

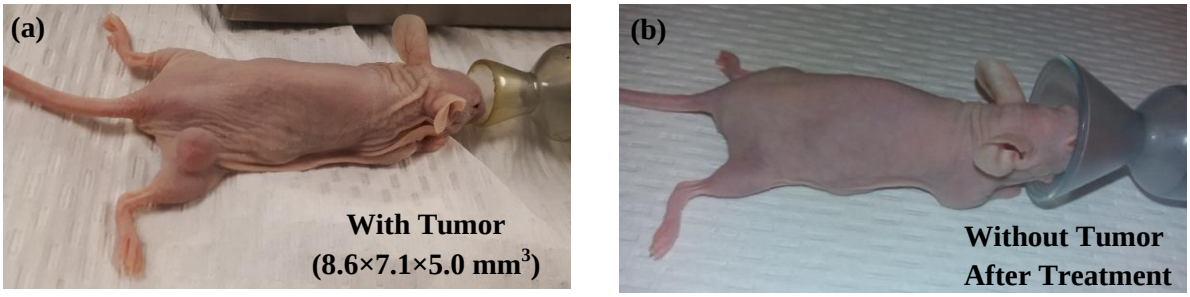


Figure III.1 (a) A mouse with tumor. (b) The mouse after treatment without tumor.

**Reference:**

[1] D. E. Dolmans, D. Fukumura and R. K. Jain, Nat. Rev. Cancer, 2003, 3, 380.

[2] C. A. Robertson, D. Hawkins Evans and H. Abrahamse, J. Photochem. Photobiol., B, 2009, 96, 1.

[3] L. Ricciardi, L. Sancey, G. Palermo, R. Termine, A. De Luca, E. I. Szerb, I. Aiello, M. Ghedini, G. Strangi, and M. La Deda, Nanoscale, 2017, 9, 19279.

[4] Y. You, S. Cho and W. Nam, Inorg. Chem., 2014, 53, 1804.

[5] E. Baggaley, J. A. Weinstein and J. A. G. Williams, Coord. Chem. Rev., 2012, 256, 1762.

[6] L. He, Y. Li, C.-P. Tan, R.-R. Ye, M.-H. Chen, J.-J. Cao, L.-N. Ji and Z.-W. Mao, Chem. Sci., 2015, 6, 5409.

[7] D. Maggioni, M. Galli, L. D'Alfonso, D. Inverso, M. V. Dozzi, L. Sironi, M. Iannacone, M. Collini, P. Ferruti, E. Ranucci and G. D'Alfonso, Inorg. Chem., 2015, 54, 544.

[8] F. Xue, Y. Lu, Z. Zhou, M. Shi, Y. Yan, H. Yang and S. Yang, Organometallics, 2015, 34, 73.

[9] J. M. Ageitos, J. A. Chuah and K. Numata, Design Considerations for Properties of Nanocarriers on Disposition and Efficiency of Drug and Gene Delivery, in Nanomedicines: Design, Delivery and Detection, ed. M. Braddock, The Royal Society of Chemistry, 2016, 1.

[10] P. Couleaud, V. Morosini, C. Frochot, S. Richeter, L. Raehm and J. O. Durand, Nanoscale, 2012, 2, 1083.

# Chapter IV

# Optical focal length tunability of Meta-lens: Effect of implanting liquid crystal into Meta-lens

**Introduction:** As already written in the chapter I of part II that a metasurface is an artificially fabricated sheet of materials (confinement in one dimension) with sub-wavelength thickness. Metasurface can also be considered as the two-dimensional counterpart of the metamaterial [1]. A metalens (a flat lens) is a kind of metasurface [2-6]. Metalens act as a flat kind of lens with a specific focal length for a specific wavelength. The light focusing by metalens does not follow the conventional way of the optical lens. When light interacts with metalens, its subunits interact uniquely and independently with the incoming light and their outcomes interfere in far field which generates a focal spot, the focal spot of metalens.

**Results and Discussions:** Metalens has a specific focal length for a specific wavelength. But the focal length of metalens for that specific wavelength of the incoming light can be tuned. The tuning of the focal length of a flat lens will be very useful for many applications. One can tune the focal length of metalens by using liquid crystal (LCs). This work is for the optical focal length tuning by implanting the liquid crystal into metalens. Here metalens has been fabricated via a known way [3]. Then Nematic Liquid Crystal (NLC) have been infiltrated

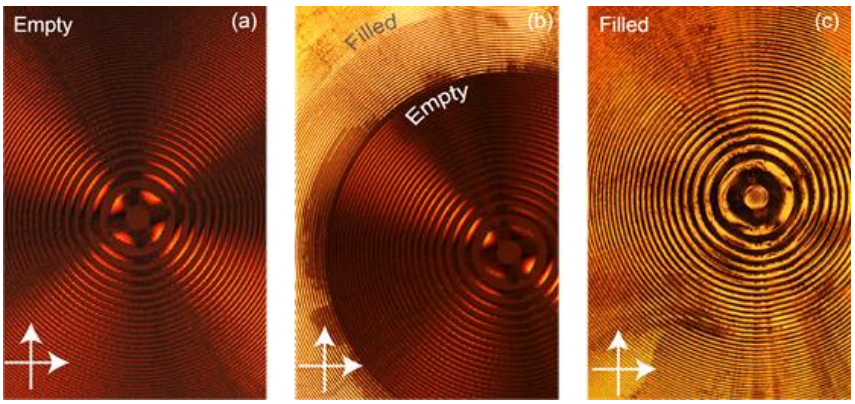


Figure IV.1 Polarized Optical Microscopy images for cross polarization. (a) Un-infiltrated metalens (b) Partially filtrated metalens (c) Completely infiltrated metalens.

Here it is worth to mention that the liquid crystal does not sit on top of the metasurface. (Sub-units of metalens have 2um) rather it goes inside metalens (verification has been done). The polarized optical microscopy images of metalens during infiltration process have been taken

under cross-polarization (for better visualization of the LCs during infiltration) and has been shown in the figure IV.1. Here the difference in the brightness is telling about the progress of the infiltration process. The homogeneous brightness in case of the infiltrated metalens is helping us to safely conclude that the depth of the LCs into metalens can be considered as nearly homogeneous. After infiltration optical focal length measurement has been done for both the empty metalens and the fully infiltrated metalens. For this optical measurement, the specific wavelength of the incoming light has been chosen based on metalens used [3]. The focal length measurement of both the empty and filled metalens help us to conclude that with the proper implantation of the LC molecule and using an external stimuli (here light) by using the properties of LCs, focal length of a particular metalens can be tuned.

**References:**

[1] Pendry, J. B. Phys. Rev. Lett. 2000 85, 3966-3969.

[2] Aieta, Francesco; Genevet, Patrice; Kats, Mikhail; Yu, Nanfang; Blanchard, Romain; Gaburro, Zeno; Capasso, Federico Aberration-free ultra-thin flat lenses and axicons at telecom wavelengths based on plasmonic metasurfaces. Nano Letters. 2012, 12, 4932–4936.

[3] Yu, Nanfang, Capasso, Federico. Flat optics with designer metasurfaces. Nat. Mater. 2014, 13, 139–150.

[4] Yu, Nanfang; Genevet, Patrice; Kats, Mikhail A.; Aieta, Francesco; Tetienne, Jean-Philippe; Capasso, Federico; Gaburro, Zeno. Light Propagation with Phase Discontinuities: Generalized Laws of Reflection and Refraction. Science. 2011, 334, 333–337.

[5] Genevet, Patrice; Yu, Nanfang; Aieta, Francesco; Lin, Jiao; Kats, Mikhail; Blanchard, Romain; Scully, Marlan; Gaburro, Zeno; Capasso, Federico. Ultra-thin plasmonic optical vortex plate based on phase discontinuities. Applied Physics Letters. 2012, 100, 013101.

[6] Yu, Nanfang; Genevet, Patrice; Kats, Mikhail A.; Aieta, Francesco; Tetienne, Jean-Philippe; Capasso, Federico; Gaburro, Zeno. Light Propagation with Phase Discontinuities: Generalized Laws of Reflection and Refraction". Science. 2011, 334 (6054), 333.

# CONCLUSION

Here in this thesis, different kinds of plasmonic nanostructures and their optical activities have been discussed. The thesis is divided into three parts and the summary of the works are given below.

In the 1st part of the thesis the light harvesting plasmonic nanoantennas were discussed which is divided into many sections containing the study of gold nanostar (AuNS) antenna, a heterodimeric antenna based on AuNS, the breathing modes observed in the single AuNS and the thermo-responsive Fano system.

In the first chapter of part I a brief discussion about the plasmonic nanoantenna related processes are described.

In the following chapter stable AuNSs and their optical properties have been discussed along with the synthesis process. A surfactant-free, simple, one step wet-chemistry method has been used to synthesize these spiky AuNSs. The AuNSs has been seen to be stable in aqueous media for more than five months. The characterization and the numerical analysis done here indicate that these nanoantennas could be efficient for the real time and label-free detection of protein markers at ultra-low concentration, useful for the disease detection at its early stage.

In the third chapter, a heterodimeric nanogap, created between a nanostar antenna tip and a gold nanosphere was introduced. These hybrid nanoantennas were seen to have more efficiency than a single gold nanostar antenna because of their higher intensity enhancement capability at the hot-spots and also the optimum electric field map in the binding site area of a molecule. It is worth to mention here that the attachment of suitable anti-bodies on the surface of the nanoantenna could easily convert both of these hybrid antenna and AuNS antenna to a promising biosensor useful for clinical diagnostics.

Later, breathing modes of AuNSs have been discussed. The AuNS antennas were seen to have both the non-edge breathing modes and the plasmonic edge dipolar mode. The plasmonic edge dipolar mode is useful to detect the protein molecules by using their localized surface plasmon resonance (LSPR) effect like a conventional plasmonic biosensor. On the other hand the non-edge acoustic breathing modes of AuNSs are helpful to determine the mass of adsorbed analyte based on the cantilever principle. The mass evaluation, which carries the information about the polarizability and the size of the biomarker, is essential to have the information about the number of amino acids present in that molecule which is

further necessary for the complete understanding of the molecular structure and to design the anti-agent. Finite element method (FEM) simulations also verify here the presence of both types of modes in these spiky nanoantennas.

In the last chapter of this part, a Fano system has been described. The reported Fano line-shape arose from the coupling of the gold nanorod antennas dipped in a thermo-responsive polymer matrix and a silver thin film. The study has also been extended with a spacer $SiO_2$ dielectric layer with variable thickness. This Fano line-shape has been seen to respond to both the change in external temperature and the refractive index. This will be help the system to detect the foreign molecule in real-time with high efficiency and also to identify the marker's thermodynamic condition which is crucial for protein engineering. Here numerical analysis has also been done for this system which verifies its Fano response as well as its capability to have higher intensity enhancement at the hot-spots. With all these discussion part I of the thesis get completed.

In the second part of the thesis plasmonic metasurfaces and their optical activities were discussed. This part is majorly about the aluminium doped zinc oxide (AZO) nanopillars of both hollow and solid nature.

In the first chapter of this part a general discussion about the metamaterials and metasurfaces has been given.

For the second chapter, the metasurface composed of highly ordered high aspect ratio AZO nanotubes (hollow pillars) were considered. AZO, because of its low-loss property is getting popular as an alternate plasmonic material. These AZO nanotubes array system has seen to have here $H_2$ gas sensing capability with low response time in room temperature. The low-power optical measurement regarding these $H_2$ gas sensing indicates that this system could find applications in industries. These nanostructures could also detect the presence of bacteria by detecting their exhaled $H_2$ gas of lower concentration. Here, the gas sensing experimentation with the solid AZO nanopillar structure establishes the importance of the hollowness for gas sensing. In this section the FEM analysis is done to help ourselves to understand clearly about the gas sensing process.

In the third chapter of this part AZO solid nanopillars arrays system was considered. For these systems with air as the host material generalized Brewster angle (GBA) phenomena has been realized for a particular range of angles which could be useful for many applications including optical switch. Here the optical activity of these solid pillars is also discussed for

the silicon (Si) host. In this case of Si host the GBA effect is not seen for any angle and in any wavelength range but their optical activities is suitable to use them as polarization based optical switches and other optical switches using different other optical parameters.

After these discussions, part III (last part) begins with a brief discussion about some of the important additional projects done during my PhD. These projects are – twin photonic nanojet (PNJ) related theoretical study, asymmetric sound transmission behaviour seen in 3D printed acoustics metamaterials, focal-length tunability of metalens by properly implanting the liquid crystals (LCs), and plasmon assisted cancer therapy.